UNIVERSIDAD DE A CORUÑA

Departamento de Métodos Matemáticos y de Representación

Programa de doctorado en Ingeniería Civil

TESIS DOCTORAL

An unstructured finite volume model for unsteady turbulent shallow water flow with wet-dry fronts: Numerical solver and experimental validation

AUTOR:	Luis Cea Gómez
DIRECTORES:	Jerónimo Puertas Agudo
	María-Elena Vázquez Cendón

Tesis doctoral depositada en Abril 2005, y defendida el 23 de Junio de 2005 ante el jurado:

Presidente:	D. Tomás Chacón Rebollo	Universidad de Sevilla
Vocales:	D. Manuel Gómez Valentín	Universidad Politécnica de Cataluña
	D^{a}. Pilar García Navarro	Universidad de Zaragoza
	D. Jon R. French	University College London
Secretario:	D. Vicente Navarro Gámir	Universidad de Castilla la Mancha

Agradecimientos

Muchas son las personas que me han ayudado, enseñado y apoyado durante los años de elaboración de este trabajo. Todas ellas han contribuido de manera importante al desarrollo del mismo, por lo que quiero mostrarles aquí mi agradecimiento.

En primer lugar doy las gracias a los dos directores de esta tesis, Jerónimo Puertas y Elena Vázquez, que en todo momento me han dado su apoyo y ayuda. Con su guía, conocimiento y estímulo he conseguido superar las dificultades que se presentan en todo trabajo de investigación. Generosamente han puesto a mi disposición esfuerzos personales y medios materiales. Sin todo ello la realización de esta tesis no habría sido posible.

Hace cuatro años comencé este trabajo de investigación en el Centro de Innovación Tecnolóxica en Edificación e Enxeñería Civil (CITEEC), en donde durante un año compartí trabajo y amistad con Gonzalo, Esteban, Jose, Paula, Blanca, Juan, Félix, Pili y Quique.

Durante mi estancia en el CITEEC conocí a Luis Pena, con el que desde entonces he compartido amistad, trabajo, ilusiones y buenos momentos (además de despacho, mesa y ordenador). Sus resultados en la escala de peces han sido de gran ayuda, al igual que su compañía y consejos. Gracias por todo.

Una gran parte del contenido de esta tesis se debe a los conocimientos que adquirí en la Universidad de Chalmers. Gracias a William George por la ilusión y motivación transmitidas, a Gunnar Johansson por tener siempre la respuesta adecuada, y a Lars Davidson por sus explicaciones y consejos en la modelización de la turbulencia. Todos mis profesores y compañeros hicieron con su cálida acogida que mi estancia en Göteborg haya sido una experiencia inolvidable.

Todo el trabajo realizado en el estuario Crouch lo llevé a cabo en la UCL (University College of London), con la inestimable ayuda de Jon French y Helene Burningham, a los que agradezco mi incorporación al grupo CERU, así como el haber puesto a mi disposición todo el material y medios necesarios. Gracias también a todos mis compañeros en Londres con los que compartí despacho durante un año, por su compañía y ayuda.

Debo agradecerle aquí a la Fundación Barrié la ayuda económica concedida, con la que financié mi etapa en Suecia. Agradezco igualmente a la Fundación Caixa Galicia el haberme concedido la ayuda económica necesaria para realizar la estancia en el University College de Londres. Gracias a Montse Orta y a Almudena Cúns.

Doy las gracias también a aquellas personas con las que durante estos años he intercambiado discusiones, comentarios e ideas. A Ana Ferreiro, a Pilar García, a Tomás Chacón, a Pilar Brufau y a Manuel Castro. Sin olvidarme de todos mis compañeros en el ONERA, especialmente de Damien (le ppb qui a toujours des calculs a faire), de Fred y de Robert.

Gracias a Sergio, y no es la primera vez, por tener siempre la paciencia y el tiempo necesarios para resolver los problemas informáticos que me han ido surgiendo.

Gracias sobre todo a mis padres, a mi familia y a Marie-Paule por estar siempre a mi lado.

Acknowledgments

Many people have greatly contributed to the development of this thesis during the last four years. I want to express now my most sincere acknowledgements to them all.

First of all I would like to gratefully acknowledge my two supervisors, Jerónimo Puertas and Elena Vázquez, for their expert guidance, advice, support and encouragement. They have generously provided me with everything I needed. Without their help this work would never have been possible.

I began this research four years ago in the CITEEC (Centro de Innovación Tecnolóxica en Edificación e Enxeñería Civil), where I enjoyed working with my mates and friends Gonzalo, Esteban, Jose, Paula, Blanca, Juan, Félix, Pili and Quique. With their company I spent a really good year.

During my stay in the CITEEC I met Luis Pena, with whom I shared illusions, work and friendship. His results on the fishway have been very helpful. Thanks for everything.

An important part of the contents of this research is due to the knowledge I acquired at Chalmers University. I am specially grateful to William George for the illusion and motivation he transmits, to Gunnar Johansson for his continuous advice, and to Lars Davidson for his numerous suggestions and much-needed advice in the turbulence modelling.

All my research on the Crouch estuary was done at the University College of London. The continuous support and technical discussions with Jon French and Helene Burningham have contributed significantly to my work. They put everything necessary at my disposal, making my work much easier. I also want to thank all my mates in London for their sympathy and help.

I have to express my gratitude to Fundación Barrié and Fundación Caixa Galicia, that provided generous financial support for my stays in Sweden and in London. Many thanks to Montse Orta and Almudena Cúns.

I would like to offer special thanks to the following, for their much valuable comments and ideas: Ana Ferreiro, Pilar García, Tomás Chacón, Pilar Brufau and Manuel Castro. Also to all my colleagues at ONERA, specially to Damien, Fred and Robert.

I wish to say 'thank-you' to Sergio, for solving all the computer problems, specially for reviving this computer a couple of times.

Thanks to my parents, to my family and to Marie-Paule for being always by my side.

MEMORIA

Introducción

Esta tesis se centra en la modelización numérica de flujos superficiales en aguas someras. Dichos flujos se caracterizan por un comportamiento fuertemente bidimensional, que generalmente viene impuesto por una separación entre las escalas horizontales y verticales que definen el problema. Esta separación entre escalas permite realizar ciertas aproximaciones en las ecuaciones de Navier-Stokes, para obtener así las ecuaciones de aguas someras bidimensionales. Existen numerosos flujos en ingeniería hidráulica que pueden considerarse poco profundos, como por ejemplo el flujo en ríos, canales o estuarios. La mayor parte de dichos flujos son turbulentos, siendo necesario para su correcta modelización un adecuado tratamiento de la turbulencia. Al mismo tiempo, en numerosas situaciones de interés práctico las fronteras que definen la extensión espacial del flujo son una incógnita adicional del problema, que además puede variar con el tiempo. En dichos casos es necesario realizar un adecuado tratamiento numérico del frente seco-mojado que permita obtener soluciones estables y precisas. Algunos ejemplos en los que es necesario considerar el frente seco-mojado son el flujo inducido por la marea en estuarios, el flujo en ríos con llanuras inundables, o la modelización de oleaje de onda larga en zonas costeras.

El principal objetivo de esta tesis es aplicar las ecuaciones de aguas someras bidimensionales a diferentes flujos en lámina libre, centrándose especialmente en aquellos problemas en los que o bien el tratamiento de la turbulencia o bien el tratamiento del frente seco-mojado son de especial relevancia. Para ello se ha desarrollado un código de volúmenes finitos que resuelve las ecuaciones de aguas someras acopladas con diferentes modelos de turbulencia. El código incluye un modelo parabólico de viscosidad turbulenta, un modelo algebraico de longitud de mezcla y 3 versiones del modelo $k - \varepsilon$ para aguas someras. Al mismo tiempo se ha propuesto e incluido un modelo de tensiones algebraicas para aguas someras.

El código desarrollado se ha utilizado para simular el flujo en 4 aplicaciones prácticas diferentes que incluyen el oleaje de onda larga, el flujo inducido por la marea en un estuario, el flujo en canal con un codo de 90^o, y el flujo en escalas de peces de hendidura vertical. En todos los casos los resultados numéricos se han comparado con datos experimentales, algunos de ellos proporcionados por otros investigadores, otros obtenidos específicamente para este trabajo.

Metodología

El método de volúmenes finitos es probablemente el más comúnmente utilizado en Dinámica de Fluidos Computacional (CFD), debido principalmente a sus propiedades de conservación y a su

intuitiva interpretación física, que lo hacen especialmente adecuado para resolver ecuaciones diferenciales de transporte. Por ello ha sido el método elegido en este trabajo para resolver tanto las ecuaciones de aguas someras como las ecuaciones de transporte de los modelos de turbulencia. Los esquemas de volúmenes finitos más adecuados para la resolución de las ecuaciones de aguas someras han sido estudiados en profundidad por numerosos investigadores. Como discretización del flujo convectivo, en este trabajo se han utilizado las extensiones de orden 2 de los esquemas descentrados de van Leer y de Roe. Se ha utilizado asimismo una discretización descentrada del término fuente pendiente del fondo, la cual proporciona esquemas más estables y precisos. El tratamiento de los frentes seco-mojado utilizado es no-difusivo, numéricamente estable, y proporciona un balance exacto de las ecuaciones del flujo en el caso hidrostático. Se han implementado 3 tipos de tratamiento para los contornos de tipo pared: condición de deslizamiento libre, funciones de pared (wall functions) y condición de no-deslizamiento. El tipo de condición a aplicar depende del tamaño de malla en la pared. En las aplicaciones prácticas presentadas en esta tesis únicamente se han utilizado las funciones de pared y la condición de deslizamiento libre.

La verificación de los esquemas numéricos incluidos en el código se ha realizado para diferentes flujos sencillos que incluyen condiciones hidrostáticas con fondo irregular (discretización del término fuente pendiente fondo), frente seco-mojado estacionario (condición seco-mojado), flujo laminar en canal (término difusivo en las ecuaciones de aguas someras) y flujo turbulento en canal (modelos de turbulencia).

En la primera de las aplicaciones prácticas las ecuaciones de aguas someras unidimensionales se han utilizado para modelar la generación, propagación y reflexión de ondas largas generadas por movimientos del fondo. Numéricamente, la generación de la ola se consigue mediante un movimiento del fondo, excepto en el caso de generación mediante una pala vertical, en el que se utiliza una condición de contorno móvil. Al mismo tiempo la condición seco-mojado participa implícitamente en el proceso de generación. El muro rebasable se modela con la condición seco-mojado, introduciendo una discontinuidad en el fondo. Las diferencias entre los resultados numéricos y experimentales se deben principalmente a la existencia de aceleraciones verticales cerca de las paredes con pendiente muy elevada. Estas aceleraciones invalidan la hipótesis de presión hidrostática asumida en las ecuaciones de aguas someras.

La capacidad del código para modelar flujos en regiones costeras con extensas zonas inundables se prueba en la segunda aplicación práctica, en la que se calcula el flujo inducido por la marea en el estuario Crouch (Reino Unido). Las numerosas zonas inundables existentes en dicho estuario se anegan y drenan con cada ciclo de marea. Una gran parte son llanuras de inundación con un drenaje relativamente lento, mientras que en otras zonas la pendiente del terreno es considerable. Los campos de velocidad y profundidad en el estuario son prácticamente insensibles al modelo de turbulencia utilizado. Los resultados numéricos se comparan con datos experimentales de profundidad y velocidad obtenidos en varios puntos del estuario por el grupo CERU de la Universidad de

Londres (UCL).

El flujo en un canal con un codo de 90^o se ha utilizado para comparar el comportamiento de los modelos de turbulencia en zonas de recirculación. A pesar de la relativa simplicidad geométrica, el flujo presenta zonas de recirculación secundarias cuyos efectos no son tenidos en cuenta en el modelo bidimensional de aguas someras. A pesar de ello el modelo es capaz de ajustar los resultados experimentales y de evaluar correctamente el tamaño de la zona de recirculación.

En la última aplicación práctica se estudia el flujo en dos diseños diferentes de escalas de peces de hendidura vertical. El flujo en este tipo de estructuras hidráulicas es marcadamente bidimensional excepto en la hendidura vertical. El nivel de turbulencia en el flujo es muy alto, y la correcta modelización de esta es fundamental para obtener una buena predicción del campo de velocidades, así como de la energía turbulenta. La turbulencia es fuertemente anisótropa, lo cual es tenido en cuenta únicamente en el modelo ASM. Las simulaciones numéricas se han realizado con diferentes caudales, cubriendo el rango de aplicación práctica en este tipo de escalas. Las resultados y el comportamiento de los diferentes modelos de turbulencia se ha analizado poniéndolo en relación con las características del flujo.

Conclusiones y aportaciones más relevantes

Como resultado de este trabajo se ha desarrollado un código de volúmenes finitos para resolver las ecuaciones de aguas someras bidimensionales acopladas a diferentes modelos de turbulencia en régimen no estacionario, con especial atención a la modelización de la turbulencia y al tratamiento de los frentes seco-mojado.

Se ha propuesto un modelo de tensiones algebraicas para aguas someras como una extensión del modelo de tensiones algebraicas bidimensional, con términos adicionales que tienen en cuenta la producción de tensiones turbulentas debido al rozamiento del fondo. En los casos estudiados en esta tesis, el modelo de tensiones algebraicas proporciona resultados similares al modelo $k - \varepsilon$, mejorando ligeramente la predicción de las tensiones de Reynolds.

La condición seco-mojado utilizada es numéricamente estable y ha proporcionado resultados satisfactorios en la simulación de ondas largas generadas por movimientos del fondo, así como en la simulación del flujo de marea en estuarios con topografía irregular. El hecho de que la condición seco-mojado sea no-difusiva permite utilizarla para modelar muros verticales rebasables mediante una discontinuidad en la altura del fondo. A pesar de ello, en dicho caso debe tenerse en cuenta que las ecuaciones de aguas someras asumen una distribución de presión hidrostática, lo cual no es correcto en el caso de existir fuertes aceleraciones verticales. Una posible futura línea de trabajo es la inclusión de términos fuente que tengan en cuenta la distribución de presión no hidrostática en las proximidades de muros con pendientes muy elevadas.

Se ha comprobado la importancia de utilizar esquemas descentrados de orden 2, especialmente en flujos con gradientes de velocidad elevados. Un esquema de orden 1 produce soluciones excesivamente difusivas, en las que la difusión numérica interfiere con la difusión turbulenta, dificultando de esta manera la comparación de diferentes modelos de turbulencia. En este contexto se ha propuesto un esquema híbrido, que simplemente utiliza una discretización de orden 2 para los caudales unitarios, mientras que mantiene una discretización de orden 1 para el calado. El esquema híbrido ha proporcionado resultados muy satisfactorios en las aplicaciones prácticas estudiadas.

Los resultados obtenidos en la escala de peces muestran que las ecuaciones de aguas someras bidimensionales con un modelo adecuado de turbulencia proporcionan una buena representación del flujo en escalas de hendidura vertical. Este resultado es especialmente interesante, ya que debido a la naturaleza del flujo en la escala, podría parecer que solamente un modelo tridimensional puede proporcionar resultados precisos. El modelo numérico reproduce con un nivel de precisión satisfactorio las características más importantes del flujo (velocidad máxima, tamaño de las zonas de recirculación, nivel de turbulencia, ...). En este caso el modelo de turbulencia utilizado tiene una gran importancia en los resultados numéricos. Si bien los modelos ASM y $k-\varepsilon$ proporcionan campos de velocidad y profundidad ligeramente diferentes, la comparación con los datos experimentales no permite afirmar cual de ellos es más preciso. Por otro lado, las tensiones turbulentas proporcionadas por el modelo ASM ajustan mejor los resultados experimentales.

Como suele ocurrir en la dinámica de fluidos computacional, es difícil establecer cual es el modelo más adecuado en términos generales. El modelo de tensiones algebraicas proporciona una representación más precisa de las tensiones de Reynolds que el modelo $k-\varepsilon$, lo cual puede ser interesante en problemas de transporte de contaminantes o de sedimentos. Ambos modelos proporcionan campos de velocidad similares, y a la vez más fiables y precisos que los proporcionados por el modelo de longitud de mezcla. Sin embargo, en flujos en los que la turbulencia está generada por las tensiones de fondo, los tres modelos proporcionan resultados parecidos. La principal ventaja del modelo de longitud de mezcla es su robustez, simplicidad y su bajo coste computacional. Por ello puede resultar más conveniente en determinadas situaciones en las cuales el campo de turbulencia no influye excesivamente en el flujo medio. Por otro lado, en flujos fuertemente turbulentos, como en la escala de peces, es necesario utilizar un modelo complejo para obtener resultados fiables y precisos.

Contents

List of Figures

Introduction

This thesis is a study on the numerical modelling of quasi-2D free surface turbulent flows. The two-dimensional character of a free surface flow is usually enforced by a horizontal length scale much larger than the vertical one, and by an homogeneous behaviour along the vertical coordinate. Under these conditions certain approximations can be done in the governing equations of the fluid in order to obtain the shallow water equations. Here, the term *shallow* refers to a small vertical length scale compared to the horizontal length scale.

There are many free surface flows in environmental hydraulic and coastal engineering which can be considered shallow water flows. The ability to accurately compute those flows is of great importance in the placement of waste outfalls, in the evaluation of sediment transport, in the location of fisheries and in the computation of water currents inside harbours, just to cite some examples.

Almost every free surface flow is turbulent. Considering the usual length scales in engineering practise, and the small kinematic viscosity of water, in most cases the Reynolds number is large enough in order to consider the flow as fully turbulent. Even in the simplest river flow we can observe small eddies that appear and disappear with an apparently chaotic movement, showing the complexity of turbulent motion. In coastal regions, large eddies often occur due to the separation of the flow past a headland, a breakwater or an island. These eddies are very important in environmental engineering problems, and they have a great influence on solute and sediment trapping. Figure 1(a) shows a Von Kármán's vortex street formed in the clouds in the leeward flow from the island of Guadalupe. A similar wake occurs in the water flow, being the sediment and pollutant transport behind the island very dependent on these eddies. A sadly famous recent example of unstable wake in a marine environment is given by the photographs of the oil spilt from the Prestige tanker (Figure 1(b)) which sank in the Galician coast in November 2002.

The interaction between tidal currents and the coastline can create strong and large turbulent structures. Figure 2(a) shows a photograph of the tidal whirlpools generated in the Naruto-Strait, in the Japan islands chain. As the tidal flow passes through the strait, which is about $1Km$ wide, a high speed tidal turbulent jet is formed. Whirlpools of different sizes appear and interact between each other producing complex turbulent patterns. Some of the eddies generated are even larger than a cargo ship (Figure 2(b)), and do present a real problem for navigation along the strait.

(a) von Kármán vortex street in the clouds wake behind the island of Guadalupe (picture taken from the webpage of the Atmospheric Sciences Data Centre. http://eosweb.larc.nasa.gov).

(b) Oil wake behind the Prestige tanker in the Galician coast (picture taken from the webpage of the European Space Agency. http://earth.esa.int/ew/oil_slicks/).

Figure 1: Turbulent wakes in nature.

(a) Naruto strait.

(b) Cargo ship inside the whirlpools.

Figure 2: Whirlpools generated in the Naruto-Strait by tidal currents (pictures taken from http://133.31.110.195/D/inetpub/wwwroot/www/eddy.htm).

Turbulence is a state of fluid motion in which the flow seems to behave in a chaotic way, both in space and time. It is difficult to give a precise definition of turbulence, but every turbulent flow has a number of characteristics that distinguish it: (1) the flow seems chaotic and random; (2) small oscillations upstream may lead to large perturbations downstream; (3) turbulence fluctuations are always three-dimensional and unsteady; (4) in turbulent flow there are different length scales of motion which differ by several orders of magnitude.

Fluid motion is governed by the Navier-Stokes equations, which are derived from Newton's laws of motion, and thus, they are deterministic. So why does turbulence seem chaotic and random? A new insight into the problem was given by the development of the chaos theory, which shows that even very simple non-linear equations can produce apparently random results. One of the most famous and simplest equations which is able to produce a chaotic result is the model

called *logistic map*, which is given by:

$$x_{n+1} = \lambda x_n (1 - x_n) \tag{1}$$

Depending on the value of its single parameter λ, this apparently simple equation can produce a chaotic sequence of values x_n. For $\lambda = 2$ the equation converges to $x_n = 0.5$, while for $\lambda = 4$ there is not convergence at all, not even a periodic behaviour. Furthermore, a small change in the initial conditions changes the results completely. The values of x_n seem to have a random behaviour, even though they are deterministic and given by the simple Equation 1.

If we think now about the Navier-Stokes equations, which are much more complex, we should not be surprised to find apparently chaotic solutions. Even if they are deterministic laws, the high non-linearity of the equations and their extreme sensitivity to the initial conditions produce random results. In a similar way as the behaviour of Equation 1 depends on the parameter λ, the solution to the Navier-Stokes equations depends on the geometry, on the boundary conditions and on the Reynolds number. It is well known that for small Reynolds numbers the fluid flow is laminar, while for large Reynolds numbers it is turbulent. It is also well known that the Reynolds number limit where the flow changes from laminar to turbulent depends on the geometry and boundary conditions of the problem (pipe, channel, boundary layer, ...).

It has been said by many authors that turbulence is probably the last unsolved problem in classical physics. Certainly it is one of the most important problems in physics and engineering nowadays, since it appears in almost all fluid flows. Many turbulence models have been developed and used in practical calculations. Each day the understanding of turbulence increases, and more sophisticated models appear. But we should not forget that they are still models, and so, turbulent motions are not being resolved, but approximated by a model which was developed under some simplifying hypotheses. Nowadays, with the increase in computers power, turbulence is starting to be simulated rather than modelled, which means that the *real* equations which govern the fluid motion, including turbulent motion, are being solved. But it is still not possible to perform these kind of calculations in practical engineering flows. And, even considering that the computer's speed doubles every 18 months, it will not be possible for at least a hundred years. Thus, turbulence modelling is, and will be necessary for many years.

Goals and Summary

The main goal of this thesis is to apply the depth averaged shallow water equations (2D-SWE) to several free surface flows in which the turbulence modelling and the treatment of wet-dry fronts are of special interest. In this context, four different flows have been studied: the generation, propagation and reflection of shallow waves in a 1D flume (wet-dry fronts), the tidal flow in a coastal estuary (wet-dry fronts and turbulence modelling), the flow in an open channel with a

90^o bend (turbulence modelling), and the flow in vertical slot fishways (turbulence modelling). The treatment of wet-dry fronts is specially important in the modelling of long waves and tidal flow in coastal regions. The turbulence modelling is much more important when computing the flow over a 90^o bend and in vertical slot fishways. The numerical models based on the shallow water equations include a number of assumptions concerning the flow conditions. As it is pointed out by Lloyd and Stansby [84], due to these assumptions, and considering the numerical dissipation inherent to the numerical schemes, the accuracy of the results is problem dependent and usually uncertain. The aim of this work is to investigate, for the considered applications, which flow features can be resolved by a depth averaged model and which features are beyond the capabilities of the 2D-SWE. In order to do so, a finite volume solver for the 2D-SWE, coupled with several depth averaged RANS (Reynolds Averaged Navier-Stokes) turbulence models, has been developed as a result of this work. A depth averaged mixing length model and a $k-\varepsilon$ model for shallow waters have been included in the code, and a depth averaged algebraic stress model has been proposed. Additional limiters to the production of turbulence proposed by Menter [88] and Durbin [45], which are generally used in aerodynamic models but not in shallow water models, have been introduced in the $k-\varepsilon$ model. At the same time experimental data has been used to analyse the characteristics of the flow as well as to compare with the numerical results. The experimental data permits us to evaluate the degree to which the shallow water hypotheses are fulfilled in the considered flow. Some of the experimental data has been obtained specifically for this thesis, and the rest has been taken from other researchers.

In chapter 1 the general governing equations for 3D incompressible fluid flow are presented. Several approaches for turbulence simulation are briefly described, with special emphasis on the RANS turbulence modelling.

Chapter 2 summarises some previous theoretical, experimental and numerical studies about turbulent shallow water flows. Since shallow water flows have a strong two-dimensional character, some basic notions about 2D turbulence are included. It has been considered appropriate to derive the shallow water equations starting from the 3D incompressible Navier-Stokes equations. This derivation has not only an academical interest, but it also serves to show all the approximations that are made in the derivation process. This is very helpful in order to understand the limitations of the resulting equations, and to be able to asses the numerical results. Chapter 2 is also dedicated to turbulence modelling in shallow waters. The models which have been implemented in the numerical solver are presented and discussed. In order to account for anisotropic turbulence without a significant decrease in the numerical stability, a depth averaged algebraic stress model has been proposed as an extension of the 2D algebraic stress model, with additional terms which account for the production of turbulence due to bed friction.

After a brief introduction to the finite volume method, the numerical solver is presented in chapter 3. The numerical schemes and discretisation techniques used in the solver are described

in detail. The solver includes the first and second order upwind schemes of van Leer and Roe, an upwind discretisation of the source terms with second order corrections for the bed slope term, and a special treatment of the wet-dry fronts. An hybrid first/second order discretisation of the convective flux free of spurious oscillations is proposed and included in the solver. The $k - \varepsilon$ equations are solved with either an hybrid or a second order scheme. The validation of the solver is done in chapter 4 for some simple flow conditions which include hydrostatic flow, steady wet-dry fronts, laminar channel flow and turbulent channel flow.

In chapter 5 the 1D-SWE are used to model the generation, propagation and reflection of long shallow waves in a 1D flume. This test case is specially suitable to validate the treatment of wet-dry fronts in unsteady computations, and at the same time it allows us to check the solutions given by the model in problems with a moving bed. The experimental results obtained in a 1D flume are compared with the predictions given by the numerical solver.

In chapter 6 the numerical solver is used to compute the tidal flow in the Crouch estuary (Essex, England). The estuary has extensive flat marsh areas which flood and dry periodically due to the tidal driven flow. This makes it possible to test the treatment of the wet-dry fronts in complex two-dimensional geometries with a very irregular bathimetry. The numerical results are compared with experimental water depth and velocity data obtained at several points in the estuary by the Coastal and Estuarine Research Unit (UCL, London).

In chapter 7 the free surface flow around a channel with a 90^o bend is computed with several turbulence models, and compared with experimental results obtained by Bonillo [13]. The aim is to compare the flow in the recirculation region predicted by each turbulence model.

Finally, chapter 8 is dedicated to the computation of the flow field in two different designs of vertical slot fishways. Statistical techniques are used to analyse the turbulent characteristics of the flow field, using the experimental data obtained by Pena, who pointed out in recent works the need of developing a numerical model of the flow in the fishway [105]. The results obtained with the mixing length, the $k - \varepsilon$ and the ASM models are discussed and compared with the experimental data.

Part I

The Equations

Chapter 1

Numerical modelling of turbulent flows

1.1 Governing equations

1.1.1 The Navier-Stokes equations

The equations governing the behaviour of a fluid are the well known Navier-Stokes equations. For an incompressible fluid, they form a system of 4 equations which account for the conservation of mass and momentum:

$$\frac{\partial u_j}{\partial x_j} = 0 \tag{1.1}$$

$$\frac{\partial u_i}{\partial t} + \frac{\partial u_i u_j}{\partial x_j} = -\frac{1}{\rho}\frac{\partial p}{\partial x_i} + \frac{1}{\rho}\frac{\partial \tau_{ij}}{\partial x_j} + F_i$$

where u_i ($i = 1, 2, 3$) are the instantaneous velocity components, τ_{ij} is the viscous stress tensor, p is the pressure, and F_i are the volume forces. For a Newtonian fluid the viscous stress tensor can be expressed as:

$$\tau_{ij} = \mu\left(\frac{\partial u_i}{\partial x_j} + \frac{\partial u_j}{\partial x_i} - \frac{2}{3}\delta_{ij}\frac{\partial u_k}{\partial x_k}\right) = 2\mu\left(s_{ij} - \frac{1}{3}\delta_{ij}\frac{\partial u_k}{\partial x_k}\right) \tag{1.2}$$

where s_{ij} is the strain-rate tensor and μ is the dynamic viscosity. For an incompressible fluid, Equation 1.2 reduces to:

$$\tau_{ij} = 2\mu s_{ij} \tag{1.3}$$

The Navier-Stokes equations are a highly non-linear system. The strong non-linearity of the equations produces high frequency oscillations when the Reynolds number is increased, and the flow becomes unstable and turbulent. It is computationally very expensive to solve the equations directly, which makes that presently, only in very simple geometry configurations it is possible to solve the Navier-Stokes equations using direct methods (DNS). The most common approach at the moment in hydraulic engineering practise is to solve the Reynolds Averaged Navier-Stokes

equations, in which the effect of turbulence is modelled rather than resolved.

1.1.2 The Reynolds Averaged Navier-Stokes equations (RANS)

The Reynolds Averaged Navier-Stokes equations are obtained after decomposing the instantaneous variable values in a mean value ($\overline{u}$) and a fluctuating value ($\overline{u'}$) (Reynolds decomposition):

$$u = \overline{u} + u' \tag{1.4}$$

where the overbar accounts for ensemble average. Introducing the Reynolds decomposition given by expression 1.4 in the Navier-Stokes equations, averaging the equations (ensemble average), and taking into account that the ensemble average of the fluctuation velocity is zero ($\overline{u'} = 0$), the following system of equations is obtained for incompressible flow:

$$\frac{\partial \overline{u_j}}{\partial x_j} = 0 \tag{1.5}$$

$$\frac{\partial \overline{u_i}}{\partial t} + \frac{\partial \overline{u_i}\,\overline{u_j}}{\partial x_j} = -\frac{1}{\rho}\frac{\partial \overline{p}}{\partial x_i} + \frac{\partial}{\partial x_j}\left[\overline{\tau_{ij}} - \overline{u_i' u_j'}\right]$$

$$\overline{\tau_{ij}} = \mu\left(\frac{\partial \overline{u_i}}{\partial x_j} + \frac{\partial \overline{u_j}}{\partial x_i}\right)$$

The terms $\overline{u_i' u_j'}$, which appear due to the non-linearity of the convective flux, are known as the Reynolds stresses or turbulent stresses. Only the 3 normal Reynolds stresses contribute to the turbulent kinetic energy (k) of the flow, which is defined as:

$$k = \frac{1}{2}\left(\overline{u'^2} + \overline{v'^2} + \overline{w'^2}\right) \tag{1.6}$$

The Reynolds stresses are 6 new unknowns which need to be calculated. This is known as the closure problem of turbulence, since there are more unknowns than equations, and thus, it is necessary to close the problem with additional equations. The most common approach is to relate the Reynolds stresses to the mean strain tensor by the Boussinesq assumption. A more accurate approach, but computationally more expensive, is to solve 6 new transport equations, one for each Reynolds stress (Reynolds Stress Turbulence Models).

1.1.3 The non-dimensional Navier-Stokes equations

In order to obtain the non-dimensional Navier-Stokes equations, the following non-dimensional variables are defined:

$$\tilde{x_i} = \frac{x_i}{L_s} \qquad \tilde{u_i} = \frac{u_i}{U_s} \qquad \tilde{\rho} = \frac{\rho}{\rho_s} \tag{1.7}$$

where L_s, U_s and ρ_s are respectively, the characteristic length, velocity and density scales, which are chosen in order to characterise the geometry, the velocity field and the density field of the problem. Any variable is referred to them via relation 1.7. Other non-dimensional variables can be obtained as a combination of the three basic characteristic variables. The non-dimensional pressure, for example, is evaluated as:

$$\tilde{p} = \frac{p}{\rho_s U_s^2} \tag{1.8}$$

and the non-dimensional time is computed as:

$$\tilde{t} = t\frac{U_s}{L_s} \tag{1.9}$$

If the relations 1.7 are introduced in the Navier-Stokes equations, the non-dimensional equations are obtained as:

$$\frac{\partial \tilde{u_j}}{\partial \tilde{x_j}} = 0 \tag{1.10}$$

$$\frac{\partial \tilde{u_i}}{\partial \tilde{t}} + \frac{\partial \tilde{u_i}\tilde{u_j}}{\partial \tilde{x_j}} = -\frac{1}{\tilde{\rho}}\frac{\partial \tilde{p}}{\partial \tilde{x_i}} + \frac{1}{Re}\frac{\partial \tilde{u_i}}{\partial \tilde{x_j}\partial \tilde{x_j}} + \tilde{F_i}$$

where the viscosity has been assumed to be constant, and the Reynolds number has been defined as:

$$Re = \frac{U_s L_s}{\nu} \tag{1.11}$$

The resulting equations depend only on the Reynolds number, which is the ratio between the convective and the viscous forces in the flow. This means that, for a given problem, i.e. given geometry, initial and boundary conditions, the non-dimensional velocity field depends only on the ratio $\frac{U_s L_s}{\nu}$. In fact, it is the Reynolds number which gives the laminar or turbulent character of the flow. For low Reynolds numbers the flow is laminar, while for large Reynolds numbers the flow becomes turbulent. The transition from laminar to turbulent depends on the geometry and boundary conditions of each particular problem (jet, wake, boundary layer, pipe, ...).

In the compressible Navier-Stokes equations another non-dimensional number appears, the Mach number, which is a ratio between the velocity and the celerity at which pressure waves propagate in the flow. For ideal incompressible flow the pressure waves celerity is infinity, and thus, the Mach number is always zero, and it does not appear in the equations.

1.2 Turbulence simulation in engineering flows

With the great development of computer capabilities in the last decades, the numerical computation of fluid flows, generally known as Computational Fluid Dynamics (CFD), has become a common practise in engineering. Since most of the practical engineering flows are high Reynolds flows, the simulation of turbulence is of great importance in order to obtain accurate numerical results. Several approaches exist which permit accounting for the turbulent effects in the flow.

The most straightforward approach is to solve the instantaneous Navier-Stokes equations. This technique is known as Direct Numerical Simulation (DNS). The main problem of DNS is that it is necessary to resolve all the frequency and spatial oscillations in the flow. In high Reynolds number flows this is very expensive computationally, requiring extremely small spatial and time steps in the computations. With the computer power available nowadays it is only possible to apply DNS to very simple geometry configurations at very low Reynolds numbers.

A second approach consists in resolving the large scale fluctuations, while modelling the high frequency motions. This kind of methods have been developed in the last 10 years by many researchers, obtaining very good results in flows dominated by large fluctuations. In this group of methods we can include the Large Eddy Simulation (LES), which resolves the large and medium turbulent fluctuations and models the dissipative scales; the Very Large Eddy Simulation (VLES), which resolves only the largest turbulent structures; and the Detached Eddy Simulation (DES), which models all the turbulence near the walls and resolves the large scales in the rest of the flow. These methods are computationally less expensive than DNS. DES starts to be used in engineering computations, but they cannot be used yet in general engineering practise.

The most common approach at the moment in practical engineering problems is to solve the Reynolds Averaged Navier-Stokes equations (RANS), in which all the effects of turbulence are modelled. This is the less expensive approach, but all the accuracy obtained in the simulation depends on the turbulence model used. Many RANS turbulence models exist, most of them semi-empirical, some of them for specific flow conditions. But there is not a universal model with universal constants. Usually all the models are calibrated for fully developed turbulence and trained in a small range of simple shear flows. Hence, there is not any strong theoretical reason to think that their performance can be generalised to complex flows. Some of the common handicaps to RANS models are separated flows and transition flows. Nevertheless, the RANS approach is commonly used in engineering practise, giving a good compromise between numerical accuracy and computational cost.

1.2.1 Direct Numerical Simulation (DNS)

In DNS the instantaneous Navier-Stokes equations are solved. All the turbulence spectrum is simulated, and therefore, no turbulence model is needed. Since turbulence is a three-dimensional

unsteady phenomenon, it is always necessary to solve the 3D Navier-Stokes equations in time.

The main problem of DNS is that it is necessary to resolve all the scales of motion appearing in the flow, since they interact between each other. In order to do that, the computational mesh size must be smaller than the smallest significant scale of motion, and the time step must be small enough to resolve the highest frequency oscillations appearing in the flow. The smallest significant scale of motion (Kolmogorov's microscale) is usually several orders of magnitude smaller than the computational domain, specially for large Reynold numbers. Since DNS calculations are always three-dimensional, the size of the numerical mesh increases very fast as the Reynolds number increases. Rodi [117] estimates that for a plane channel flow at $Re = 10^5$, the number of grid points should be of the order of 10^9. If the Reynolds number is increased to $Re = 10^6$, the number of point increases to 10^{12}.

This behaviour can also be illustrated by the estimation of the Kolmogorov microscale. Assuming a fully developed turbulent flow with separation between the large and small turbulent scales, the ratio between the Kolmogorov's microscale and the large length scale can be approximated as:

$$\frac{\eta_k}{l_s} = \frac{1}{l_s}\left(\frac{\nu^3}{\varepsilon}\right)^{1/4} \approx \left(\frac{\nu}{u_s l_s}\right)^{3/4} \tag{1.12}$$

where η_k is the Kolmogorov's microscale, l_s is the large length scale, u_s is the fluctuating velocity scale, ν is the kinematic viscosity, and ε is the dissipation rate of turbulent energy. Considering the viscosity of water ($\nu \approx 10^{-6} m^2/s$), a fluctuating velocity scale of $u_s = 10^{-1} m/s$, and a length scale of $10m$, which are typical values in hydraulic engineering flows, the Kolmogorov microscale obtained is $\frac{\eta_k}{l_s} \approx 3.\,10^{-5}$. In order to obtain this resolution in a 3D mesh, around 10^{16} grid points would be required. These calculations can take several months even in the fastest computers available at the moment. For this reason, at the present time and in the near future it will not be possible to use DNS for practical engineering calculations.

However, DNS plays an important role in turbulence research. DNS is applied nowadays for low Reynolds number calculations in simple geometries like boundary layers, channel flow, flow around a cylinder, etc, providing very exhaustive and high quality data. These simple flows are the base of more realistic conditions, and their analysis makes it possible to understand more complex phenomena.

1.2.2 Large Eddy Simulation (LES)

The idea of LES is to simulate the large and medium scales of motion while modelling the small scales, also called subgrid scales (SGS). This is a good approach in flows which are mainly driven by large turbulent structures.

In LES, the Navier-Stokes equations are filtered (averaged over a volume). The resulting equa-

tions depend on time and space. Thus, LES calculations, as happens with DNS, are always 3D and unsteady. However, the mesh size in LES is much larger than in DNS (except in the near wall region), which makes it computationally less expensive. The cut-off between the modelled scales (SGS) and the resolved scales should ideally be placed somewhere in the Kolmogorov's inertial subrange of the spectrum. In this way only the dissipative scales are modelled, which are assumed to be isotropic an homogeneous. This removes much responsibility from the turbulence model, which permits to obtain good results with relatively simple turbulence models.

The main problem of LES is the simulation of the near wall region. Close to the walls the size of the turbulent structures becomes very small. In order to have a well resolved LES it is necessary to have a very fine mesh in the near wall region in order to be able to capture those structures. This makes that in practise the near wall grid size should be almost as small as in DNS. This requirement precludes the use of fully LES for industrial applications at the present time. Spalart [126] estimates that until later than 2050 the computer's power will not be enough to apply fully LES and DNS techniques to aerodynamic industrial applications. A common solution is to solve the RANS equations near the wall and the LES equations far away from the wall. This approach is called Detached Eddy Simulation (DES), and it is presently more commonly used than LES.

1.2.3 RANS models

The most commonly used approach in engineering practise nowadays is to solve the Reynolds Averaged Navier-Stokes equations coupled with a turbulence model. Here, all the turbulent structures occurring in the flow are modelled. The RANS turbulence models are usually derived for fully turbulent flow, and their constants are obtained from experimental data on boundary layers or other simple shear flows. While the turbulence models used in LES are only responsible for modelling the subgrid scales, in RANS they are responsible for modelling the whole turbulence spectrum.

Several kinds of RANS turbulence models exist. The most used in practise are the linear eddy viscosity models, in which the Boussinesq assumption is used to compute the Reynolds stresses from the mean velocity gradients via a linear relation. There are also non-linear eddy viscosity models, in which the Reynolds stresses and the mean velocity gradients are linked by a non-linear relation. None of the eddy viscosity models can be considered clearly superior to the other ones. The most popular RANS model is the $k-\varepsilon$ model of Jones and Launder [67] (with all its low-Reynolds versions), which was proposed in the early seventies, and it is still widely used in all fluid dynamics areas, including aerodynamic, hydraulic and environmental flows. Other popular models are the SST, the $k-\omega$ and the Spalart-Allmaras models [127], which are mainly used in aerodynamic flows. New versions of the models are still appearing, and much work is still being done in order to improve the existing models introducing correction terms which account for

specific flow conditions (near wall terms, curvature and rotation corrections, anisotropy effects, ...). The fact of the original $k - \varepsilon$ model being one of the most commonly used two-equation models, shows that there has not yet appeared any clearly superior model. A possible reason for the similar results given by the different models under some flow conditions was pointed out by Hunt [63], who considers that the influence of the turbulence model may be smeared in regions where the time scale of the mean flow distortions is smaller than the characteristic turbulent time scale.

In the Reynolds Stress Turbulence Models (RSTM), instead of using the Boussinesq assumption, a transport equation is solved for each Reynolds stress. The fact of solving one equation for each Reynolds stress permits accounting for curvature effects and anisotropy. In the Algebraic Stress Models (ASM) the Reynolds stresses are approximated with non-linear algebraic expressions. The ASM can be thought of either as a simplification of the RSTM or as an extension of Boussinesq eddy viscosity models. Nevertheless, the fact that the equations for the Reynolds stresses still contain modelled terms, and the higher complexity of RSTM compared with eddy viscosity models, make the latter be more commonly used in engineering practise.

1.2.4 Unsteady RANS (URANS)

The purpose of unsteady RANS (URANS) is to simulate the largest eddies present in the flow and their non-linear interaction. Therefore, URANS solutions are unsteady in time even with steady boundary conditions. Durbin [44] found that the Reynolds stresses created behind a bluff body by time averaging of URANS are larger than those given by the turbulence model, removing in such a way much responsibility from the model.

In principle, URANS is an intermediate approach between steady RANS and LES. The main difference between URANS and LES is that in LES the eddy viscosity of the subgrid model depends explicitly on the grid size, while URANS is mesh independent by definition. Nonetheless, there are many facts about URANS simulations that are still not clear, which makes LES/DES a more common approach at the present time. A 3D-URANS computation is able to produce 3D solutions over 2D geometries, like LES, but they appear to be much more dependent on the spanwise size of the domain, which is chosen arbitrarily in the computations [126]. In addition, the accuracy of the results depends on the kind of flow, and the solutions have been found to be quite sensitive to the turbulence model [135]. Although URANS solutions should be mesh independent by definition, there are some recently formulations [91, 135] which reduce the value of the eddy viscosity in some regions of the flow in order to be able to resolve smaller turbulent structures, obtaining in such a way an LES-like behaviour. These facts show that there is not yet a complete understanding of the results given by URANS simulations [135].

1.3 Turbulence models for the RANS equations

This section presents some of the most commonly used turbulence models for general 3D-RANS computations. These models, as presented here, are not valid to be used with the depth averaged shallow water equations. Nevertheless, it has been considered useful to present the original models in order to account for their main features and limitations. The depth averaged versions of the models are presented and discussed in chapter 2.

As it has been said, in the RANS equations the effect of turbulence is included in the mean momentum equations via the Reynolds stresses. There are a great number of turbulence models which are based on the Boussinesq assumption. These models are known as eddy viscosity models. Other models do not rely directly on the Boussinesq approximation, as for example the Reynolds Stress Turbulence Models, the Algebraic Stress Models or the non-linear eddy viscosity models, although all of them use at some point the concept of eddy viscosity.

1.3.1 Linear eddy viscosity models

The Boussinesq assumption

The Boussinesq assumption is the base of all the eddy viscosity models. It relates the Reynolds stresses with the mean velocity gradients via the eddy viscosity as:

$$\overline{u_i' u_j'} = -2\nu_t \left(\overline{s}_{ij} - \frac{1}{3}\overline{s}_{kk}\delta_{ij} \right) + \frac{2}{3}k\delta_{ij} \tag{1.13}$$

where u_i' $(i = 1, 3)$ is the fluctuating velocity, ν_t is the eddy viscosity, $\overline{s}_{ij}$ is the mean strain-rate tensor, and k is the turbulent kinetic energy defined as $k = \dfrac{\overline{u_k' u_k'}}{2}$. The evaluation of the eddy viscosity, which is assumed to be isotropic, is left to the turbulence model. For a long time simple turbulence models based on algebraic formulations have been used due to their simplicity and robustness. More sophisticated models exist, which solve one or more transport equations for different turbulent quantities, as the turbulent kinetic energy or the dissipation rate.

Algebraic turbulence models

Algebraic models, also called mixing length models, are the simplest models. An algebraic expression is used in order to evaluate the eddy viscosity at each point. They do not account for the production, transport and dissipation of turbulence. Turbulence is assumed to be in local equilibrium. Due to their simplicity they are very easy to implement, but the results obtained should not be expected to be highly accurate. Nevertheless, they can still give results comparable to those of more sophisticated models in some simple flows.

From dimensional analysis, the eddy viscosity is computed as the product of a turbulent length scale l_s, and a turbulent velocity scale v_s, as:

$$\nu_t \sim l_s v_s \tag{1.14}$$

Some well known mixing length models are the Cebeci-Smith model [22] and the Baldwin-Lomax model [6], which were frequently used in boundary layer codes to compute the flow around airfoils and in turbo machinery. Shirazi and Truman [122] have extensively studied the Baldwin-Lomax model, founding that it produces very poor results when used in separated flows or in flows with a complicated geometry. An extension of the Cebeci-Smith model for non-boundary layer flows can be expressed as:

$$\nu_t = l_s^2 |\overline{s}| = l_s^2 \sqrt{2\overline{s}_{ij}\,\overline{s}_{ij}} \tag{1.15}$$

For simple boundary layer flows the expression of the eddy viscosity reduces to:

$$\nu_t = l_s^2 \left| \frac{\partial \overline{u}}{\partial y} \right| \tag{1.16}$$

where y is the normal direction to the wall, and $\overline{u}$ is the tangential velocity to the wall. The main problem of the mixing length models is the evaluation of the length scale, which is usually done under empirical basis for each specific flow. Some often used length scales are given by Wilcox [148]:

$l_s = 0.090l$	plane jet
$l_s = 0.075l$	circular jet
$l_s = 0.090l$	mixing layer

where l is the half width of the flow structure (the radius in the circular jet).

One-equation models

In order to be able to account for the physical processes occurring in turbulent flows, i.e. production, transport and destruction of turbulence, models which solve a transport equation for a given turbulent quantity were proposed. The most representative quantity is the turbulent kinetic energy, but there are also models which solve directly a transport equation for the eddy viscosity, like the Spalart-Allmaras model [127].

From the turbulent kinetic energy equation, the velocity scale is computed as $v_s \sim \sqrt{k}$, where k is the turbulent kinetic energy. The length scale still needs to be determined empirically depending on the nature of the flow, i.e. wake, jet or boundary layer. The modelled k equation for

incompressible flow reads:

$$\frac{\partial k}{\partial t} + \frac{\partial k\overline{u}_j}{\partial x_j} = \underbrace{\frac{\partial}{\partial x_j}\left[(\nu + \frac{\nu_t}{\sigma_k})\frac{\partial k}{\partial x_j}\right]}_{Diffusion} + \underbrace{2\nu_t\overline{s}_{ij}\,\overline{s}_{ij}}_{Production} - \underbrace{\frac{k^{3/2}}{l_s}}_{Dissipation} \tag{1.17}$$

where σ_k is a model constant with a usual value of 1, and l_s is the length scale, which should be determined empirically. Usually an algebraic expression is used to evaluate the length scale [16]. The k-equation model is not very often used in practise, except in the near-wall region, where the length scale is easier to determine. On the other hand, the Spalart-Allmaras model for the eddy viscosity is often used in aerospace applications with good results.

Two-equation models

As an extension of the one-equation models, the two-equation models compute both the length and the velocity scales from transport equations. Usually the velocity scale is determined from the modelled k equation, while different equations have been proposed for evaluating the length scale. Some of the most frequently used two-equation models are the $k-\varepsilon$ model of Jones and Launder [67], the Wilcox $k-\omega$ model [147, 148], and the Smith's $k-l$ model [124, 125]. Each of them is more suitable for different flow conditions. There have been some attempts to combine the best features of each model, as the SST model of Menter [89], which combines the best features of the $k-\omega$ model in the near wall region and the $k-\varepsilon$ model in the outer region.

The $k-\varepsilon$ model was originally proposed by Jones and Launder [67] in 1972. The length scale in Equation 1.14 is computed from the turbulent kinetic energy k and the dissipation rate ε as:

$$l_s = \frac{k^{3/2}}{\varepsilon} \tag{1.18}$$

Introducing the length scale given by Equation 1.18 into Equation 1.14, and computing the velocity scale as $v_s \sim \sqrt{k}$, the turbulent viscosity is evaluated as:

$$\nu_t = c_\mu \frac{k^2}{\varepsilon} \tag{1.19}$$

where $c_\mu = 0.09$ is an empirical constant. The modelled k and ε transport equations read:

$$\begin{aligned}
\frac{Dk}{Dt} &= \underbrace{\frac{\partial}{\partial x_j}\left[(\nu + \frac{\nu_t}{\sigma_k})\frac{\partial k}{\partial x_j}\right]}_{Diffusion} + \underbrace{2\nu_t\overline{s}_{ij}\,\overline{s}_{ij}}_{Production} - \underbrace{\varepsilon}_{Dissipation} \\
\frac{D\varepsilon}{Dt} &= \underbrace{\frac{\partial}{\partial x_j}\left[(\nu + \frac{\nu_t}{\sigma_\varepsilon})\frac{\partial \varepsilon}{\partial x_j}\right]}_{Diffusion} + \underbrace{c_{1\varepsilon}\frac{\varepsilon}{k}2\overline{s}_{ij}\,\overline{s}_{ij}}_{Production} - \underbrace{c_{2\varepsilon}\frac{\varepsilon^2}{k}}_{Dissipation}
\end{aligned} \tag{1.20}$$

$$c_\mu = 0.09 \quad c_{1\varepsilon} = 1.44 \quad c_{2\varepsilon} = 1.92 \quad \sigma_k = 1.0 \quad \sigma_\varepsilon = 1.31$$

The five constants of the model are obtained from experimental results. Three of them, c_μ, $c_{1\varepsilon}$ and $c_{2\varepsilon}$, have been obtained from experimental data on turbulent boundary layer flow and homogeneous decaying turbulence behind a grid. The other two constants, σ_k and σ_ε, have been optimised by applying the model to various fundamental flows, such as flow in channel, pipes, jets, wakes, etc.

The $k - \varepsilon$ model as formulated in Equation 1.20 cannot be applied through the viscous layer down to the wall, since it would lead to erroneous results, because the model was developed for fully turbulent flow. If all the boundary layer wants to be resolved, it is necessary to use the low-Reynolds version of the model, in which a damping function is used in order to diminish the turbulence level near the wall. Many low-Reynolds versions of the $k - \varepsilon$ model exist, which will not be treated here. Some of them were proposed by Launder and Sharma [78] and Chien [27], but many more exist in the literature. Patel et al. [103] give a review of low-Reynolds turbulence models.

Limitations of the eddy viscosity models

The eddy viscosity models have some limitations which should be considered when analysing the results given by them, specially in impinging regions, in swirling flows, or when buoyancy effects are important.

In general, the performance of eddy viscosity models decreases when the turbulence is highly non-isotropic. This is due to the fact that the Boussinesq assumption assumes an isotropic eddy viscosity. Nevertheless, this kind of models can still give rather good predictions of the mean flow variables in non-isotropic flows. On the other hand, they usually give poor predictions of the turbulence field. The main flow conditions that the eddy viscosity models cannot account accurately for are: (1) strong curvature; (2) impingement regions; (3) separation; (4) buoyancy forces; (5) strong adverse pressure gradients. Despite these limitations, eddy viscosity models are widely used in engineering calculations due to their robustness and simplicity compared to other more sophisticated models. They have a good balance between accuracy, robustness and complexity. When more accuracy is required it is necessary to use a non-linear eddy viscosity model or a Reynolds Stress Model.

1.3.2 Reynolds Stress Turbulence Models (RSTM)

In the RSTM a transport equation is solved for each Reynolds stress. This means that, in 3D flow, six new transport equations must be solved. The modelled equations for the turbulent stresses read:

$$\begin{aligned}\frac{D\overline{u_i'u_j'}}{Dt} = \; & \Phi_{ij} + \underbrace{\frac{\partial}{\partial x_k}\left[(\nu + C_k\overline{u_k'u_m'}\frac{k}{\varepsilon})\frac{\partial\overline{u_i'u_j'}}{\partial x_m}\right]}_{Diffusion} \\ & \underbrace{-\overline{u_i'u_k'}\frac{\partial\overline{u_j}}{\partial x_k} - \overline{u_j'u_k'}\frac{\partial\overline{u_i}}{\partial x_k}}_{Production} - \underbrace{\frac{2}{3}\varepsilon\delta_{ij}}_{Dissipation}\end{aligned} \tag{1.21}$$

The term Φ_{ij} accounts for the modelling of the pressure strain term, which is responsible of redistributing the turbulent kinetic energy among the normal Reynolds stresses. It transports the energy from the most energetic stresses to the less energetic ones. Its trace is zero, and thus, it does not create neither destroy turbulence, it just redistributes it. For modelling purposes, the pressure strain term is divided into a slow part and a rapid part. The effect of the wall is introduced by a slow and a rapid wall terms. In this way, Φ_{ij} is split as:

$$\Phi_{ij} = \Phi_{ij,R} + \Phi_{ij,S} + \Phi^w_{ij,R} + \Phi^w_{ij,S} \tag{1.22}$$

where the subindex R refers to the rapid part, the subindex S to the slow part, and the superindex w to the wall-correction terms. The expressions for the slow and the rapid part are:

$$\begin{aligned}\Phi_{ij,S} &= -c_1\frac{\varepsilon}{k}\left(\overline{u_i'u_j'} - \frac{2}{3}k\delta_{ij}\right) \\ \Phi_{ij,R} &= -c_2\left(P_{ij} - \frac{2}{3}P_k\delta_{ij}\right)\end{aligned} \tag{1.23}$$

$$c_1 = 1.8 \qquad\qquad c_2 = 0.6$$

A modelled expression for the wall-correction terms can be found in [77]. The diffusion term in Equation 1.21 accounts for the viscous and turbulent diffusion. Davidson [33] proposes an alternative expression to model this term, which is more stable and produces similar results:

$$D_{ij} = \frac{\partial}{\partial x_k}\left[(\nu + \frac{\nu_t}{\sigma_k})\frac{\partial\overline{u_i'u_j'}}{\partial x_k}\right] \tag{1.24}$$

One of the most important differences between RSTM and eddy viscosity models is that in the former ones the production term does not need to be modelled, since the Reynolds stresses are directly computed. Hence, its value is much more accurate than in the eddy viscosity models,

where the Boussinesq assumption is used to model the production of turbulent kinetic energy.

Equation 1.21 assumes an isotropic dissipation. This is a reasonable hypothesis since the small turbulent scales, where dissipation occurs, can be assumed to be isotropic for large Reynolds numbers.

1.3.3 Algebraic Stress Models (ASM)

In order to avoid solving six new differential equations, the ASM use algebraic expressions to model the Reynolds stresses. They can be considered either as a simplification of the RSTM or as an extension of the $k-\varepsilon$ model.

The transport equations which model the Reynolds stresses (Equation 1.21) and the turbulent kinetic energy (Equation 1.20) can be written in symbolic form as:

$$C_{ij} = D_{ij} + P_{ij} + \Phi_{ij} - \varepsilon_{ij} \tag{1.25}$$

$$C_k = D_k + P_k - \varepsilon$$

where the subindex ij accounts for the Reynolds stress $\overline{u_i' u_j'}$, C_{ij} represents the convection terms, D_{ij} the diffusion terms, P_{ij} the production terms, and Φ_{ij} the pressure strain terms. The basic approximation in ASM is that the convection and diffusion terms in the Reynolds stress equations are proportional to those in the turbulent kinetic energy equation, which can be expressed mathematically as:

$$C_{ij} - D_{ij} = \frac{\overline{u_i' u_j'}}{k}(C_k - D_k) \tag{1.26}$$

Combining Equations 1.25 and 1.26 gives:

$$P_{ij} + \Phi_{ij} - \varepsilon_{ij} = \frac{\overline{u_i' u_j'}}{k}(P_k - \varepsilon) \tag{1.27}$$

Introducing into Equation 1.27 the modelled expressions for the production and pressure strain terms, and considering an isotropic dissipation ($\varepsilon_{ij} = \frac{2}{3}\varepsilon$), yields:

$$\overline{u_i' u_j'} = \frac{2}{3}k\delta_{ij} + \frac{k}{\varepsilon}\frac{(1-c_2)(P_{ij} - \frac{2}{3}P_k\delta_{ij}) + \Phi_{ij,R}^w + \Phi_{ij,S}^w}{c_1 + \frac{P_k}{\varepsilon} - 1} \tag{1.28}$$

Equation 1.28 is highly non-linear and implicit in the Reynolds stresses, which appear both in the left and in the right hand side of the equation. The production terms P_k and P_{ij}, as well as the wall-correction pressure strain terms, $\Phi_{ij,R}^w$ and $\Phi_{ij,R}^w$, depend on $\overline{u_i' u_j'}$. This strong non-linear relation between the different Reynolds stresses promotes the instability of the model, being

the numerical convergence usually more difficult than in RSTM. Some explicit expressions have been derived for the ASM for 2D [109] and 3D flow [52]. The expressions for the Reynolds stresses in the explicit ASM are more complex, specially in 3D flow, but the numerical stability is improved [34].

1.4 Wall boundary condition

The interaction between the fluid and the boundary walls is of great importance in turbulent flows. Due to the strong velocity gradients occurring near the walls, a large amount of turbulence is generated. This turbulence plays a very important role in physical phenomena as heat exchange and reattachment of separated regions.

The structure of the flow near the wall is called boundary layer. It is divided in an outer region, where the convective and turbulent stresses are much more important than the viscous effects, and an inner region, where the convection terms in the Navier-Stokes equations can be neglected. At the same time, the inner region is divided in a viscous linear layer and a mesolayer, linked by a transition buffer layer [54].

The viscous sublayer is dominated by viscous diffusion. It extends from the wall up to a distance of around 5 wall units ($y^+ \approx 5$, as defined in Equation 1.29). The fluctuating velocity is damped by the wall and by the viscous forces, and the turbulence level is low. In the viscous sublayer occur the strongest velocity gradients in the flow. In the buffer layer the viscous forces diminish and the turbulent forces increase as the distance from the wall increases. It is a transition layer linking the viscous layer and the mesolayer. The mesolayer, starts around $y^+ \approx 30$, and it extends up to $y^+ \approx 100 - 200$. The main force in the Navier-Stokes equations is the turbulent shear stress. The velocity profile is almost logarithmic and the velocity gradients are much lower than they are in the viscous layer. The total shear stress (viscous plus turbulent stresses) is approximately constant from the wall up to the outer part of the logarithmic layer. It can be expressed as $\tau_w = \rho u_*^2$, where u_* is the wall friction velocity. The limits between the viscous layer, the mesolayer and the outer layer depend on the Reynolds number and on the flow configuration.

Due to this rather complicated structure of the flow near the walls, the numerical modelling of the wall region is not straightforward. Different boundary conditions must be used depending on the size of the numerical mesh near the wall. The strong gradients occurring near the wall oblige to use a very fine mesh if we want to resolve all the boundary layer down to the wall. An alternative approach is the use of wall functions, which allow to have a coarser mesh near the wall. In some cases in hydraulic engineering, due to the large size of the spatial domain, the mesh near the walls is very coarse. In these situations a slip condition is often used.

The boundary condition to be used depends on the distance from the first computational inner

node to the wall, expressed in wall units (y^+):

$$y^+ = \frac{yu_*}{\nu} \tag{1.29}$$

where the superindex $+$ refers to wall units, u_* is the wall friction velocity and ν is the cinematic viscosity.

1.4.1 No-slip condition

The no-slip condition at the wall is given by:

$$\overline{u}_w = \overline{v}_w = \overline{w}_w = 0 \qquad k_w = 0 \qquad \varepsilon_w = \nu\frac{\partial^2 k}{\partial y^2} \tag{1.30}$$

where the subindex w refers to wall values, and y is the normal direction to the wall. As it has been said, this boundary condition needs a very fine mesh near the walls. The first inner node of the numerical mesh must be located at a distance of approximately 1 wall units ($y^+ \approx 1$) or smaller. Which is a strong limitation in the mesh size.

If the no-slip condition is applied, a low Reynolds turbulence model should be used. This is because the original models were developed for fully turbulent flow conditions, which do not apply close to the wall.

1.4.2 Wall functions

An alternative approach to the no-slip condition are the wall functions. In this case the first inner node should be located in the logarithmic boundary layer, which typically extends from $y^+ \approx 30$ up to $y^+ \approx 100$. The velocity field near the wall is not resolved, and therefore, the wall shear stress cannot be computed from the velocity gradient at the wall. Instead it is computed from the wall friction velocity as $\tau_w = \rho u_*^2$. From the velocity field, the wall friction velocity u_* is computed from the logarithmic law of the wall as:

$$\overline{u}_t = \frac{u_*}{\kappa}\ln\left(\frac{yu_*E}{\nu}\right) \tag{1.31}$$

where $\overline{u}_t$ is the velocity component parallel to the wall, y is the normal distance to the wall, u_* is the friction velocity, κ is the von Kármán's constant ($\kappa = 0.41$), and E is the roughness parameter. For smooth walls $E = 9.0$. In environmental hydraulic problems, like river flow, the bed surface is not smooth, and the value of E should be modified. For rough surfaces the roughness parameter

depends on the non-dimensional roughness, which is defined as:

$$K_s^+ = \frac{K_s u_*}{\nu} \tag{1.32}$$

where K_s is the roughness height. The dependence of the roughness parameter on the non-dimensional roughness is given by [43]:

$$E = \begin{cases} 9.0 & \text{if} \quad K_s^+ \leq 5 \\ \dfrac{1}{0.11 + 0.033 K_s^+} & \text{if} \quad 5 < K_s^+ < 70 \\ \dfrac{30}{K_s^+} & \text{if} \quad K_s^+ \geq 70 \end{cases} \tag{1.33}$$

Other formulations for evaluating the roughness parameter exist (see for example [153]). For smooth walls $K_s = 0$. For rough sand beds K_s is taken usually as the median diameter of the bed material ($K_s = d_{50}$). Other expressions for K_s are given by van Rijn [142].

Equation 1.31 must be solved iteratively at each first inner node of the numerical mesh. The wall shear stress τ_w, the turbulent kinetic energy k, and the dissipation rate ε at the first inner node are computed from the logarithmic law as:

$$\begin{array}{lll} \tau_w = \rho u_*^2 & k = c_\mu^{-0.25} u_*^2 & \varepsilon = \dfrac{u_*^3}{\kappa y} \\ \overline{u'^2} = 3.63 u_*^2 & \overline{u'v'} = -u_*^2 & \overline{v'^2} = 0.825 u_*^2 \end{array} \tag{1.34}$$

where $\overline{u'^2}$ and $\overline{v'^2}$ are, respectively, the Reynolds stresses tangential and perpendicular to the wall, and $c_\mu = 0.09$ is the same constant as in Equation 1.19. With this formulation, the k and ε equations are not solved at the first inner node, but their value is imposed from Equation 1.34, as well as the values of the Reynolds stresses if a RSTM or ASM is used.

1.4.3 Slip condition

In some situations in which the spatial domain is very large (rivers, estuaries, coastal domains, ...) the first inner node of the numerical mesh is located far away from the wall, lying outside of the logarithmic layer. In these situations it is generally used a slip condition. The normal velocity at the wall is set to zero, and the tangential velocity is left free. Concerning the turbulent variables, the diffusion is neglected at the wall, and the value of k and ε is left free:

$$\overline{u}_n = 0 \qquad D_k = 0 \qquad D_\varepsilon = 0 \tag{1.35}$$

where $\overline{u}_n$ is the velocity component normal to the wall, D_k is the diffusion of turbulent energy, and D_ε is the diffusion of ε.

This approach is less accurate than the wall functions formulation, special near the solid walls. On the other hand, the computational cost is smaller and it can be a relatively good approach when the walls do not play an important role in the flow patterns. Quite often in shallow water flows the turbulence is mainly generated by the bed friction or by velocity gradients inside the flow, and thus, the flow far away from the walls is barely influenced by the wall friction.

An attempt to improve the results near the wall when the slip condition is applied, is to overestimate the bed friction in the nodes adjacent to the walls, in order to account partially for the wall friction effect. If the Manning's formula is used to estimate the bed friction, the Manning's coefficient can be overestimated as [13]:

$$n_c = n_i \left(1 + \frac{h}{B}\right)^{1/6} \tag{1.36}$$

where n_c is the Manning's coefficient in the wall boundary nodes, n_i is the Manning's coefficient in the inner nodes, h is the water depth, and B is a measure of the cell width.

1.4.4 Mesh independent wall functions

A typical problem when dealing with large and complex spatial domains is the difficulty to adjust the wall mesh size to the values required by the wall function formulation, mainly for two reasons: first, because it is difficult to make a previous estimation of the wall friction velocity at each point; and second, because the friction velocity may vary a lot from one point to another, and thus, it is difficult to place the first inner node always in the range of the logarithmic law.

An efficient way to solve this problem is to use scalable wall functions. Menter [90] proposed a formulation independent of the mesh size near the wall which permits using wall functions even if the first node is located between the viscous and the logarithmic layer. In this formulation the friction velocity is computed as:

$$\begin{aligned} \overline{u}_t &= \frac{u_*}{\kappa} \ln\left(y^+ E\right) \\ y^+ &= \max\left(11.067, \frac{y u_*}{\nu}\right) \end{aligned} \tag{1.37}$$

The lower limit for y^+ gives a linear relation between $\overline{u}_t$ and u_* when the first node is very close to the wall ($y_1^+ < 11.067$). When $y_1^+ > 11.067$, the usual logarithmic law applies. Menter obtained good results, almost independent of the wall mesh size, with this approach [90]. Menter's formulation is valid in meshes where the grid size is always smaller than the upper limit of the logarithmic law ($y^+ \approx 100$).

Chapter 2

Shallow water turbulent flows

2.1 Quasi-2D turbulent flows

Several kind of flows are often studied and modelled as shallow water flows. A few examples are coastal and estuarine tidal flow, tsunami propagation and dam break problems, among others. This section presents a brief review of previous experimental and theoretical studies on shallow water flows and 2D turbulence.

The study of shallow water flows is strongly linked with 2D flow and turbulence. Shallow water flows are those in which the vertical characteristic length is much smaller than the horizontal one. The water depth limits the development of the large 3D turbulent structures. At the same time, the production of vorticity due to stretching of vortex lines in the vertical direction is also limited by the water depth, and the 2D state is approached as the water depth diminishes. However, this is not always the case in real flow conditions. The possibility of distinguishing between 2D and 3D turbulent structures depends on the ratio between the horizontal and the vertical turbulent length scales. Nevertheless, no matter how small the water depth is, there is always some interactions between the quasi-2D and the 3D structures.

The possibility of assuming quasi-2D turbulence, at least on the large scales, is of great appealing, since it reduces the degrees of freedom of the problem. The main differences between 2D and 3D turbulence lay in the fact that in two dimensions there is no production of turbulence due to vortex stretching, and therefore, the vorticity of a fluid element is conserved in the inviscid case limit. Some of the first researchers studying 2D turbulence were Kraichnan and Batchelor in the final sixties. Kraichnan [75] studied the behaviour of the energy spectrum in the inertial subrange in quasi-steady forced 2D turbulence, while Batchelor [7] studied the energy spectrum in homogeneous decaying 2D turbulence. They obtained scalings of the 2D energy spectra different from, but compatible with, Kolmogorov's $-5/3$ power law for the inertial subrange. It was proposed by Kraichnan [75], and it is generally accepted, that if energy is injected in the flow at a characteristic length scale l_i, there exists an inverse energy cascade from the small to the large scales for wave

numbers smaller than $\mathrm{k}_i < \dfrac{2\pi}{l_i}$, with the energy spectra scaling as $E(\mathrm{k}) \sim \varepsilon^{2/3}\mathrm{k}^{-5/3}$, where ε is the energy transfer rate. At the same time, and for wave numbers larger than $\mathrm{k}_i > \dfrac{2\pi}{l_i}$, there is an enstrophy transfer to the small scales (the enstrophy is defined as the fluctuating vorticity energy $\dfrac{\overline{w_i' w_i'}}{2}$, where w_i is the vorticity). In this range the spectrum scales as $E(\mathrm{k}) \sim \eta^{2/3}\mathrm{k}^{-3}$, being η the enstrophy transfer rate. It has been argued by Benzi et al. [9] that the scaling of the spectrum depends on the initial conditions, being the previous scenario a marginal case. One of the few experiments in which the two inertial subranges proposed by Kraichnan have been observed has been presented by Rutgers [119]. In any case, an important point derived from the theory is that under certain flow conditions it may exist an inverse energy cascade from the small to the large scales. This phenomenon can be often observed in shallow water wakes behind a body, where small whirlpools join together in order to form a larger eddy. The spectral analysis of shallow water flows often reveals the -3 power law proposed by Kraichnan [75] and Batchelor [7], as well as strong energy peaks which show the existence of large 2D structures in the flow [141, 66, 138, 137].

There are several studies which reveal that the large horizontal quasi-2D coherent structures play an important role in shallow water flows. Plane turbulent jets in shallow waters have been extensively studied experimentally by Dracos et al. [42], Giger et al. [56], Thomas et al. [132] and Chen et al. [26]. Shallow water wakes around circular cylinders and conical islands were studied by Lloyd et al. [86, 84, 85] as well as by Chen and Jirka [24, 25]. The homogeneous decaying turbulence produced by a grid in shallow flows was investigated by Uijttewaal and Jirka [137], who found the merging of vortex which characterises the inverse energy transfer. There are several studies by Uijttewaal et al. [138, 136] and by Chu et al. [28] about the shallowness and bed friction effects in the development of 2D turbulent structures in free surface mixing layers. The turbulence characteristics in open shallow channels were measured and analysed by Prooijen et al. [141] and simulated numerically with a DNS approach by Pan et al. [100]. Different generation mechanisms of large coherent structures in shallow jets, wakes and mixing layers were proposed by Jirka [66]. All these theoretical, experimental and numerical studies reveal the critical role which large 2D turbulent structures play in shallow water flows, as well as the importance of the bottom and free surface boundary conditions, which confine the flow and modify the turbulence properties. The no-slip bottom condition enhances the 3D turbulence production, while the free slip condition at the free surface promotes 2D turbulence [138]. The confinement of the flow by the bottom and free surface prevents the generation of vorticity by the vortex stretching mechanism, which is an important difference between quasi-2D shallow water flows and 3D flows over 2D geometries, since the vortex stretching process is present in the latter.

The 2D properties are not always present in shallow water flows. The stability of the 2D large structures depends on the balance between the effect of horizontal shear, which produces 2D structures, the effect of shallowness, which damps the 3D instabilities, and the effect of bed

friction and vertical shear, which damp and stabilise the large 2D eddies [138, 29] and create 3D turbulence. Wolanski et al. [151] studied the wakes formed behind islands and defined an island wake parameter P as:

$$P = \frac{UH^2}{\nu_z D} \tag{2.1}$$

where U is the free stream velocity, H is the water depth, D is the island characteristic diameter and ν_z is the vertical eddy viscosity. According to their study, when the island wake parameter is very small ($P << 1$) the flow is stable and no bubble appears in the wake, for $P \approx 1$ a stable turbulent wake is formed behind the island, and for $P >> 1$ the bed friction becomes negligible and an unsteady wake appears. Further theoretical and experimental studies on the shallow water flow around islands have been made by Chen and Jirka [24, 25]. In order to classify the shallow wake behind a cylinder they used a wake stability parameter S defined by Ingram and Chu [64] as:

$$S = 2c_f \frac{D}{H} \tag{2.2}$$

where c_f is the bed friction coefficient, defined as $c_f = \frac{\tau_b}{U^2}$, where τ_b is the bed shear stress. Chen and Jirka found that above a critical vertical Reynolds number of $R_v = \frac{UH}{\nu} > 1500$, the flow structures depend mainly on the wake stability parameter S, being quite insensitive to the horizontal Reynolds number ($R_h = \frac{UD}{\nu}$). For small values of the stability parameter ($S < 0.2$) a von Kármán's vortex street appears behind the body. This is the case of a small bed friction and a large water depth. As the bed friction increases and the water depth diminishes, an unsteady bubble appears in the wake for values of the wake stability parameter in the range $0.2 < S < 0.5$. For larger values of S the wake is stable and the bubble becomes steady. Similar results were obtained by Lloyd et al. [84, 86] in flows around conical islands.

The results of Wolanski [151], Chen and Jirka [24, 25], and Lloyd [84, 86], show clearly that unlike in unbounded flows, where the flow patterns are classified according to the Reynolds number, in shallow waters the flow patterns depend strongly on the water depth and on the bed friction. These parameters establish the differences between 2D unbounded flow and 2D shallow water flow.

2.2 Numerical models in hydraulic engineering

The most general approach to model a free surface flow, although not the most often used, is to compute the fully 3D flow with a specific treatment of the free surface boundary. The main drawback to a fully 3D approach is its computational cost, specially in environmental problems, where the size of the spatial domain is very large and there are flow patterns of very different length scales involved in the flow. For this reason, it is not yet efficient to use the fully 3D approach in

river engineering applications, as it is pointed out in recent works by Duan [43] and Minh-Duc [92]. Still, the 3D approach can be used to compute the flow in hydraulic structures. Olsen [99, 98] used a 3D Navier-Stokes model to compute the flow in a spillway, where the vertical velocity is important and the extension of the spatial domain is small. Wu et al. [153] used the same approach to compute the flow and sediment transport in open channels.

In shallow water flows it is possible to simplify the governing equations assuming an hydrostatic pressure distribution in the vertical direction. In such a case the vertical momentum equation is simplified to the hydrostatic pressure equation, and therefore, only the two horizontal momentum equations need to be solved in a 3D mesh. The continuity equation is used in order to compute the free surface level. The numerical mesh is often built as a 2D horizontal mesh with several layers in the vertical direction, being the number of layers dependent on the expected complexity of the vertical velocity profile. This approach is called 3D shallow water computations, and it has been used by Bijvelds et al. [12] to compute the turbulent flow in square harbours, by Lloyd and Stansby [84, 85] to model the shallow flow around conical islands, and by Stansby and Lloyd [128] to compute the wake around islands in oscillatory laminar shallow flow.

Further simplifications can be done in order to derive the depth averaged shallow water equations, also known as St. Venant equations or 2D shallow water equations, which are obtained after vertical integration of the 3D shallow water equations. The depth averaged formulation, which is the one adopted in this thesis, has been successfully applied to different problems, obtaining rather accurate results with a relatively low computational cost when compared with the fully 3D approach. It has also the advantage of being very robust for computing accurately the water depth, even in unsteady problems with large free surface gradients, as it happens in the shocks appearing in hydraulic jumps or in the dam break simulations. The treatment of unsteady wet-dry fronts, which appear typically in coastal regions and in flooding problems, is also much simpler and stable than in the 3D approach. The 2D depth averaged formulation has been extensively used to model the dam break problem (Bellos et al. [8], Brufau and García-Navarro [18]), the propagation and runup of shallow water waves (Cea et al. [20], Dodd [40], Hubbard and Dodd [61]), flooding and drying problems (Brufau et al. [19], Bradford and Sanders [15], Playán et al. [108]), free surface flow in hydraulic structures (Bonillo [13], Molls and Chaudry [93]), flow in rivers and estuaries (Sleigh et al. [123], Wilson et al. [149], Winterwerp et al. [150], Yoon and Kong [155], Ding et al. [39]), flow in coastal regions (Sauvaget et al. [120]), and sediment transport in open channels and reservoirs (Wu [152], Olsen [97]). Some well known 2D shallow water models are the finite difference model MIKE21, developed at the Danish Hydraulic Institute [38], the finite element model TELEMAC2D [104], and the CCHE2D model [65]. Another simplification step can still be given in order to obtain the 1D St. Venant equations, which can be applied to channels, hydraulic structures or rivers, when the transversal effects are of little importance.

Due to the physical assumptions done in the shallow water models, the accuracy of the results is

problem dependent. Lloyd and Stansby [84] used both the 2D-SWE and the 3D-SWE to compute the shallow water flow around conical islands, and found that in some cases the 2D model gave more accurate results than the 3D model. The authors attributed those results to the fact that in a 2D model the vertical mixing is instantaneous, while in a 3D model it depends on the turbulence model used.

Regarding turbulence, simple models are often used in hydraulic and coastal engineering. The extension of the spatial domain and the different scales involved preclude the use of fully 3D LES and DNS techniques in practical problems at the present time. The 2D features which are present in most shallow water flows have induced Uittenbogaard and van Vossen to simulate the turbulent scales larger than the water depth, rather than modelling them [139]. This approach leads to 2D-LES computations. This may seem contradictory with the idea of LES being always three dimensional, but it is justified by using a filter size approximately equal to the water depth, and by the fact that the horizontal large scales have 2D characteristics.

Two-equation RANS models, specially $k - \varepsilon$ models, are usually the more advanced models used with both the 3D as well the 2D shallow water equations. Uijttewaal and Tukker [138] studied the development of quasi-2D structures in a shallow free-surface mixing layer, concluding that the turbulence model used should account for both, the 3D turbulent structures created by bed friction and the quasi-2D large structures originated by horizontal strain. A classical shallow water turbulence model proposed by Rastogi and Rodi [116] is a depth averaged version of the famous $k - \varepsilon$ model of Jones and Launder [67], with additional source terms which account for the bed generated turbulence. Booij [14] proposed the modification of some constants in the bed friction production terms of the Rastogi and Rodi model. Babarutsi and Chu [3] proposed a two-length-scale depth averaged version of the $k - \varepsilon$ model which accounts in a different way for the 3D bed generated turbulence. The same two-length-scale model, but with a slight modification on the dissipation equation, was used by Babarutsi and Chu in [4]. All these models will be presented and discussed later on in this chapter. A simplified 2D algebraic stress model was used by Ni [95] in order to simulate the non-isotropic transport and dispersion when heated water or pollutant are side-discharged into a large water body. The model of Ni does not account for the production of turbulence due to bed friction, and it uses simplified expressions for the Reynolds stresses in order to improve the stability of the numerical scheme.

2.3 The shallow water equations

Most environmental hydraulic flows are turbulent free surface flows which extend over relatively large spatial domains like estuaries, rivers, basins, channels, etc. Some of the complications that arise when doing a numerical simulation of these kind of flows are the complex geometry, the size of the domain, the computation of the free surface, and the treatment of wet-dry fronts. The

complex geometry makes very convenient the use of unstructured meshes. The size of the domain and the different length scales involved, make it difficult and expensive to have a high spatial resolution in boundary layers and shear layers. In order to cope with the uneven and unknown free surface, the water depth is treated as a new unknown. If the 3D-version of the shallow water equations is solved, the σ-coordinates introduced by Phillips [107] are often used in order to have a constant number of cells in the vertical direction throughout the computation. Other different numerical approaches exist to track the free surface moving boundary which will not be treated here. In many problems, some regions of the spatial domain may become wet and dry depending on the water depth. In those cases the wet-dry front must be computed by the numerical model.

In this section a complete derivation of the shallow water equations is done, starting from the general Navier-Stokes equations for incompressible flow, following with the 3D shallow water equations, and finally obtaining the depth averaged shallow water equations. The purpose of this derivation is not only academic, but also to show and summarise all the hypotheses and simplifications that are made in the process, in order to know and understand the limitations of the resulting equations, when they can be applied and what we can expect from the numerical results.

2.3.1 Notation

When deriving the shallow water equations starting from the Navier-Stokes equations several definitions of the flow variables appear (instantaneous, vertical average, fluctuation, vertical fluctuation, ensemble average), which might lead to confusion if the notation is not clear. In order to avoid misleading, a complete definition of the different variables is made below:

$u(x,y,z,t):$	instantaneous
$\overline{u}(x,y,z,t):$	ensemble average of u
$u'(x,y,z,t):$	fluctuation of u respect to $\overline{u}$
$< u > (x,y,t):$	vertical average of u
$u''(x,y,z,t):$	fluctuation of u respect to $< u > (x,y,t)$
$U =< \overline{u} > (x,y,t):$	vertical average of $\overline{u}$
$U'(x,y,z,t):$	fluctuation of $\overline{u}$ respect to U

It should be remarked that in a general case the ensemble average may be time dependent. In steady flows the ensemble average is equivalent to the time average, and therefore, it is not time dependent:

$$\overline{u} = \overline{u}(x,y,z) \qquad\qquad U = U(x,y) \tag{2.3}$$

On the other hand, the instantaneous velocity u is always time dependent even in steady flows. For the sake of simplicity in the notation, the vertical average of the ensemble average will be

addressed as U:

$$U = \frac{1}{h}\int_{z_b}^{z_s} \overline{u}\, dz \tag{2.4}$$

where $h = z_s - z_b$ is the water depth, z_b is the bed elevation, and z_s is the free surface elevation. With the previous definitions any variable can be decomposed into its average and fluctuating values as:

$$u = \overline{u} + u' \qquad u =< u > +u'' \qquad \overline{u} = U + U' \qquad < u >= U+ < u' > \tag{2.5}$$

The forth equation in 2.5 is just the vertical average of the first one, while the third one is just the ensemble average of the second one. Considering the previous definitions, the following relations apply:

$$\overline{u'} = 0 \qquad < u'' >= 0 \tag{2.6}$$

2.3.2 Computation of the free surface

When computing free surface flows a new unknown appears: the location of the free surface boundary, i.e. the water depth. This is usually computed by either the depth averaged mass continuity equation or by the kinematic free surface condition. The depth averaged mass continuity equation is obtained after vertical integration of the mass continuity equation as:

$$\int_{z_b}^{z_s} \frac{\partial \overline{u}}{\partial x} + \frac{\partial \overline{v}}{\partial y} + \frac{\partial \overline{w}}{\partial z}\, dz = 0 \tag{2.7}$$

Applying Leibnitz's rule yields:

$$\frac{\partial}{\partial x}\int_{z_b}^{z_s} \overline{u}\, dz - \frac{\partial z_s}{\partial x}\overline{u}_s + \frac{\partial z_b}{\partial x}\overline{u}_b + \frac{\partial}{\partial y}\int_{z_b}^{z_s} \overline{v}\, dz - \frac{\partial z_s}{\partial y}\overline{v}_s + \frac{\partial z_b}{\partial y}\overline{v}_b + \overline{w}_s - \overline{w}_b = 0 \tag{2.8}$$

where the subindex s refers to free surface variables, and the subindex b refers to bed variables. Notice that the bed velocities ($\overline{u}_b, \overline{v}_b, \overline{w}_b$) are allowed to be different from zero. In the hypothetical case that the bed moves, due to the no-slip condition the fluid velocity is equal to the bed velocity. The free surface and bed kinematic conditions are given by:

$$\begin{aligned} \overline{w}_s &= \frac{\partial z_s}{\partial t} + \frac{\partial z_s}{\partial x}\overline{u}_s + \frac{\partial z_s}{\partial y}\overline{v}_s \\ \overline{w}_b &= \frac{\partial z_b}{\partial t} + \frac{\partial z_b}{\partial x}\overline{u}_b + \frac{\partial z_b}{\partial y}\overline{v}_b \end{aligned} \tag{2.9}$$

Using Equation 2.9 in Equation 2.8 gives the depth averaged mass continuity equation, which

reads:

$$\frac{\partial h}{\partial t} + \frac{\partial hU}{\partial x} + \frac{\partial hV}{\partial y} = 0 \tag{2.10}$$

It should be noticed that no approximation has been done in the derivation of Equation 2.10. Notice also that it is valid even for moving beds.

2.3.3 The 3D shallow water equations. The shallow water approximation

For the sake of simplicity, only one horizontal dimension will be considered in the following derivation of the shallow water equations. The extension to the second horizontal dimension is straightforward.

The RANS vertical momentum equation for steady flow reads:

$$\frac{\partial \overline{u}\,\overline{w}}{\partial x} + \frac{\partial \overline{w}\,\overline{w}}{\partial z} = -\frac{1}{\rho}\frac{\partial \overline{p}}{\partial z} + \nu\left(\frac{\partial^2 \overline{w}}{\partial x^2} + \frac{\partial^2 \overline{w}}{\partial z^2}\right) - \frac{\partial \overline{u'w'}}{\partial x} - \frac{\partial \overline{w'^2}}{\partial z} - g \tag{2.11}$$

The total pressure p can be split into an hydrostatic pressure p_h and a dynamic pressure p_d. Assuming a constant density yields:

$$\begin{aligned} p &= p_h + p_d \\ p_h &= \rho g(z_s - z) + p_a \end{aligned} \tag{2.12}$$

where z_s is the free surface elevation, and p_a is the atmospheric pressure. The hydrostatic pressure term p_h is balanced by the gravity acceleration $-g$ in Equation 2.11. The scales defined in Table 2.1 will be considered in the derivation.

Variable	Scale
$\overline{u}, \overline{v}$	U_n
$\overline{w}$	W_n
x, y	L_n
z	H_n
P_d	ρU_n^2
$\overline{u'w'}, \overline{w'^2}$	u_n^2

Table 2.1: Characteristic scales involved in the shallow water approximation

The separation of length scales is the main hypothesis that will be done. It implies that the horizontal length scale L_n is much larger than the vertical length scale H_n. From the mass continuity

equation, the relation between the horizontal and vertical velocity scales is obtained as:

$$\begin{aligned} \frac{\partial \overline{u}}{\partial x} &+ \frac{\partial \overline{w}}{\partial z} = 0 \\ \frac{U_n}{L_n} &\sim \frac{W_n}{H_n} \end{aligned} \tag{2.13}$$

where the symbol $\sim$ accounts for proportional relation. An analysis of the characteristic scales of the different terms in the vertical momentum equation yields:

$$\begin{aligned} \frac{\partial \overline{u}\,\overline{w}}{\partial x} &+ \frac{\partial \overline{w}\,\overline{w}}{\partial z} = -\frac{1}{\rho}\frac{\partial \overline{p_d}}{\partial z} + \nu\left(\frac{\partial^2 \overline{w}}{\partial x^2} + \frac{\partial^2 \overline{w}}{\partial z^2}\right) - \frac{\partial \overline{u'w'}}{\partial x} - \frac{\partial \overline{w'^2}}{\partial z} \\ \frac{U_n W_n}{L_n} &\sim \frac{W_n^2}{H_n} \sim \frac{U_n^2}{H_n} \sim \nu\frac{W_n}{L_n^2} \sim \nu\frac{W_n}{H_n^2} \sim \frac{u_n^2}{L_n} \sim \frac{u_n^2}{H_n} \end{aligned} \tag{2.14}$$

Multiplying Equation 2.14 by $\frac{H_n}{U_n^2}$ and using the relation between the velocity scales given by Equation 2.13, the following relations between the characteristic scales are obtained:

$$\frac{H_n^2}{L_n^2} \sim \frac{H_n^2}{L_n^2} \sim 1 \sim \frac{\nu H_n^2}{U_n L_n^3} \sim \frac{\nu}{U_n L_n} \sim \frac{u_n^2}{U_n^2} \sim \frac{u_n^2 H_n}{U_n^2 L_n} \tag{2.15}$$

The order of magnitude 1 corresponds to the dynamic pressure term. Now lets assume that the horizontal Reynolds number ($R_h = \frac{U_n L_n}{\nu}$) is much larger than 1, that the turbulence intensity ($\frac{u_n}{U_n}$) is much smaller than 1, and, as it has been previously assumed, that the horizontal length scale is much larger than the vertical one. These assumptions are represented mathematically by the following relations:

$$R_h >> 1 \qquad U_n >> u_n \qquad L_n >> H_n \tag{2.16}$$

Under these hypotheses, the leading term in the vertical momentum equation is the pressure term. The order of magnitude of the other terms (convection, viscous diffusion and turbulent stresses) depends on the degree to which the relations 2.16 are fulfilled in the considered flow. Considering that the assumptions 2.16 apply, the vertical momentum equation reduces to:

$$\frac{\partial p_d}{\partial z} \approx 0 \tag{2.17}$$

Since the pressure at the free surface is equal to the atmospheric pressure p_a, it follows directly from Equations 2.12 and 2.17 an hydrostatic pressure distribution, which is the main shallow water

hypothesis:

$$p \approx p_h = \rho g(z_s - z) + p_a \tag{2.18}$$

It should be noticed that this approximation is just a result of the hypotheses made on the characteristic scales (Equation 2.16), which are fulfilled in many free surface flows. The horizontal Reynolds number is almost always much larger than one. The separation between the horizontal and vertical length scales is actually a limitation on the bed and free surface slopes, which are usually of the order 0.01, and in very rare situations are larger than 0.1. Finally, the turbulence intensity is generally smaller than 1. Hence, in many cases it is quite reasonable to assume an hydrostatic pressure distribution.

Inserting the pressure term given by Equation 2.18 into the horizontal momentum equations gives the 3D shallow water equations, which read:

$$\frac{\partial \overline{u}}{\partial x} + \frac{\partial \overline{v}}{\partial y} + \frac{\partial \overline{w}}{\partial z} = 0 \tag{2.19}$$

$$\frac{\partial \overline{u}}{\partial t} + \frac{\partial \overline{u}\,\overline{u}}{\partial x} + \frac{\partial \overline{v}\,\overline{u}}{\partial y} + \frac{\partial \overline{w}\,\overline{u}}{\partial z} = -g\frac{\partial z_s}{\partial x} - \frac{1}{\rho}\frac{\partial p_a}{\partial x} + \nu\left(\frac{\partial^2 \overline{u}}{\partial x^2} + \frac{\partial^2 \overline{u}}{\partial y^2} + \frac{\partial^2 \overline{u}}{\partial z^2}\right) - \frac{\partial \overline{u'^2}}{\partial x} - \frac{\partial \overline{u'v'}}{\partial y} - \frac{\partial \overline{u'w'}}{\partial z}$$

$$\frac{\partial \overline{v}}{\partial t} + \frac{\partial \overline{u}\,\overline{v}}{\partial x} + \frac{\partial \overline{v}\,\overline{v}}{\partial y} + \frac{\partial \overline{w}\,\overline{v}}{\partial z} = -g\frac{\partial z_s}{\partial y} - \frac{1}{\rho}\frac{\partial p_a}{\partial y} + \nu\left(\frac{\partial^2 \overline{v}}{\partial x^2} + \frac{\partial^2 \overline{v}}{\partial y^2} + \frac{\partial^2 \overline{v}}{\partial z^2}\right) - \frac{\partial \overline{v'u'}}{\partial x} - \frac{\partial \overline{v'^2}}{\partial y} - \frac{\partial \overline{v'w'}}{\partial z}$$

The evaluation of the free surface z_s can be done from the depth averaged mass continuity (Equation 2.10).

2.3.4 The 2D depth averaged shallow water equations

The main hypothesis which has been done in order to derive the 3D shallow water equations is the assumption of an hydrostatic pressure distribution. Now, some more simplifications will be done in order to obtain the depth averaged version of the shallow water equations. Only the x-momentum equation will be considered, being the derivation for the y-momentum equation completely analogous. The derivation process consists basically in integrating the x-momentum equation over the vertical direction, applying Leibnitz's rule, and using the kinematic free surface and bed surface conditions. For derivation purposes, the different terms in Equation 2.19 will be classified in convection, pressure gradient, viscous and turbulent diffusion in x-direction, viscous and turbulent diffusion in z-direction.

Convection

The integration of the convection terms over the water depth gives:

$$\begin{aligned}\int_{z_b}^{z_s}\left(\frac{\partial\overline{u}}{\partial t}+\frac{\partial\overline{u}\,\overline{u}}{\partial x}+\frac{\partial\overline{v}\,\overline{u}}{\partial y}+\frac{\partial\overline{w}\,\overline{u}}{\partial z}\right)dz &= \frac{\partial}{\partial t}\int_{z_b}^{z_s}\overline{u}\,dz-\overline{u_s}\,\overline{w_s}+\overline{u_b}\,\overline{w_b} \\ &+ \frac{\partial}{\partial x}\int_{z_b}^{z_s}\overline{u}^2\,dz-\overline{u_s}^2\frac{\partial z_s}{\partial x}+\overline{u_b}^2\frac{\partial z_b}{\partial x} \\ &+ \frac{\partial}{\partial y}\int_{z_b}^{z_s}\overline{v}\,\overline{u}\,dz-\overline{v_s}\,\overline{u_s}\frac{\partial z_s}{\partial y}+\overline{v_b}\,\overline{u_b}\frac{\partial z_b}{\partial y} \\ &+ \frac{\partial}{\partial z}\int_{z_b}^{z_s}\overline{w}\,\overline{u}\,dz-\overline{w_s}\,\overline{u_s}\frac{\partial z_s}{\partial z}+\overline{w_b}\,\overline{u_b}\frac{\partial z_b}{\partial z}\end{aligned} \tag{2.20}$$

Applying the kinematic conditions at the bed and free surface (Equation 2.9), the depth integrated convection term (Equation 2.20) can be rewritten as:

$$\frac{\partial}{\partial t}\int_{z_b}^{z_s}\overline{u}\,dz+\frac{\partial}{\partial x}\int_{z_b}^{z_s}\overline{u}^2\,dz+\frac{\partial}{\partial y}\int_{z_b}^{z_s}\overline{u}\,\overline{v}\,dz \tag{2.21}$$

In order to solve the integrals in Equation 2.21, a shape function f is defined as:

$$\overline{u}(x,y,z)=U(x,y)f(x,y,z) \tag{2.22}$$

The shape function f is allowed to vary not only in z, but also in x and y, since the vertical profile of the horizontal velocity varies in shape from one point to another. Considering the definition of the depth averaged velocity U given by Equation 2.4, and defining a sigma coordinate as $\sigma=\frac{z}{h}$, the following condition applies to the shape function f:

$$\int_0^1 f(x,y,\sigma)\,d\sigma=1 \tag{2.23}$$

In shallow water flows with a strong homogeneous behaviour in the vertical direction the shape function is almost constant, with a value near to 1. In those situations the following approximation can be done:

$$\int_0^1 f^2\,d\sigma\approx 1 \tag{2.24}$$

Assuming approximation 2.24, and using Equation 2.22 in Equation 2.21, gives the final form of the depth averaged convection terms in the x-momentum equation as:

$$\frac{\partial hU}{\partial t}+\frac{\partial hU^2}{\partial x}+\frac{\partial hUV}{\partial y} \tag{2.25}$$

An alternative way to compute the integrals in Equation 2.21 is to split the horizontal velocity

into its depth averaged value plus a fluctuation which depends on the vertical coordinate as:

$$\overline{u} = U + U' \qquad\qquad \overline{v} = V + V' \tag{2.26}$$

where $U' = U'(z)$, while U is z independent. Using decomposition 2.26 into Equation 2.21 yields:

$$\frac{\partial hU}{\partial t} + \frac{\partial hU^2}{\partial x} + \frac{\partial hUV}{\partial y} + \frac{\partial D_{uu}}{\partial x} + \frac{\partial D_{uv}}{\partial y} \tag{2.27}$$

with:

$$D_{uu} = \int_{z_b}^{z_s} U'^2 dz \qquad\qquad D_{uv} = \int_{z_b}^{z_s} U'V' dz \tag{2.28}$$

The terms involving D_{uu} and D_{uv} are often called longitudinal and lateral dispersion stresses respectively. Their relative importance respect to the convective and turbulent stress fluxes depends on the magnitude of the fluctuating velocities U' and V'. In the limit case of a complete uniform velocity profile over the vertical coordinate, the dispersion terms vanish. In a general case their value is strongly dependent on the existence of vertical secondary currents, which appear typically when the curvature effects in the velocity field are important. These secondary flows create non-uniformities in the vertical profile of the horizontal velocities $\overline{u}$ and $\overline{v}$. Rastogi and Rodi [116] computed the shallow water flow in a longitudinal channel with secondary flows due to buoyancy effects, and found that the bed friction tends to damp the secondary flows, diminishing in this way the relative importance of the dispersion terms. Hence, a better agreement between a 2D and a 3D model is obtained for rough beds rather than for smooth beds.

The dispersion terms D_{uu} and D_{uv} are generally neglected in the depth averaged equations, which is equivalent to assume the approximation given by Equation 2.24. In recent works, Duan [43] and Lien at al. [81] proposed approximated expressions for the dispersion terms, based on experimental velocity profiles obtained in curved channels. Both formulations are specially suitable for bend channels for two reasons: first, due to the specific vertical velocity profile assumed; and second, because they need the definition of a streamwise direction, as well as an inner and outer bank. Both formulations are quite recent and, to our knowledge, have only been tested in bend channels, but not in general flow conditions. An alternative way to account for the dispersion terms is to increase the effective eddy viscosity. However, the value of the effective viscosity is empirical and it depends on the problem geometry, as well as on the flow conditions. Molls and Chaudry [93] use and effective stress including the laminar stress, the turbulent stress and the dispersion stress. The same idea is used by Minh-Duc et al. [92], which introduces a coefficient in the $k - \varepsilon$ model in order to increase or decrease the eddy viscosity value.

Pressure gradient

The integral of the pressure gradient over the water depth is given by:

$$-\int_{z_b}^{z_s} g\frac{\partial z_s}{\partial x}\,dz = -g\frac{\partial z_s}{\partial x}(z_s - z_b) = -gh\frac{\partial z_b}{\partial x} - gh\frac{\partial h}{\partial x} \tag{2.29}$$

Viscous and turbulent diffusion in x-direction

Considering an effective stress $\overline{t}_{xx}$, which includes the viscous and turbulent stresses in the x-direction, the integral of the viscous and turbulent diffusion terms can be expressed as:

$$\int_{z_b}^{z_s} \frac{\partial \overline{t}_{xx}}{\partial x}\,dz = \frac{\partial}{\partial x}\int_{z_b}^{z_s} \overline{t}_{xx}\,dz - \frac{\partial z_s}{\partial x}\overline{t}_{xx}(z_s) + \frac{\partial z_b}{\partial x}\overline{t}_{xx}(z_b) \tag{2.30}$$

with:

$$\overline{t}_{xx} = \nu\frac{\partial \overline{u}}{\partial x} - \overline{u'^2} \tag{2.31}$$

The longitudinal stress at the bed is zero ($\overline{t}_{xx}(z_b) = 0$). Considering that at the free surface the longitudinal stress is rather small (specially when compared with the vertical stress $\overline{t}_{xz}$), the term $\overline{t}_{xx}(z_s)$ can be neglected in Equation 2.30. With this approximation, using Equation 2.22 into Equation 2.30 gives:

$$\int_{z_b}^{z_s} \frac{\partial \overline{t}_{xx}}{\partial x}\,dz = \frac{\partial}{\partial x}\int_{z_b}^{z_s} \nu f\frac{\partial U}{\partial x}\,dz + \frac{\partial}{\partial x}\int_{z_b}^{z_s} \nu U\frac{\partial f}{\partial x}\,dz - \frac{\partial}{\partial x}\int_{z_b}^{z_s} \overline{u'^2}\,dz \tag{2.32}$$

If it is assumed, as it has been done in Equation 2.24, that the variations of the shape function f are smaller than its value, i.e. the variations of the horizontal velocity in the z-direction are small, then, the second term in the right hand side of Equation 2.32 can be neglected:

$$\frac{\partial}{\partial x}\int_{z_b}^{z_s} \nu U\frac{\partial f}{\partial x}\,dz \approx 0 \tag{2.33}$$

With this new approximation, and using Equation 2.23, the final form of the depth averaged viscous and turbulent diffusion terms in the x-direction is obtained as:

$$\frac{\partial}{\partial x}\left(\nu h\frac{\partial U}{\partial x}\right) - \frac{\partial h < \overline{u'^2} >}{\partial x} \tag{2.34}$$

where $< \overline{u'^2} >$ represents the depth averaged value of the Reynolds stress $\overline{u'^2}$.

Viscous and turbulent diffusion in z-direction

The integral of the vertical diffusion term gives:

$$\begin{aligned}\int_{z_b}^{z_s} \nu \frac{\partial^2 \overline{u}}{\partial z^2}\, dz + \int_{z_b}^{z_s} \frac{\partial \overline{u'w'}}{\partial z}\, dz &= \nu \frac{\partial \overline{u}}{\partial z}\bigg|_{z_s} - \nu \frac{\partial \overline{u}}{\partial z}\bigg|_{z_b} + (\overline{u'w'})_{z_s} - (\overline{u'w'})_{z_b} \\ &= \tau_{s,x} - \tau_{b,x}\end{aligned} \tag{2.35}$$

where $\tau_{s,x}$ and $\tau_{b,x}$ are respectively the free surface and bed shear stresses in the x-direction.

The depth averaged equations

With the former approximations, the final form of the depth averaged shallow water equations is obtained as:

$$\frac{\partial h}{\partial t} + \frac{\partial h U_j}{\partial x_j} = 0 \tag{2.36}$$

$$\frac{\partial h U_i}{\partial t} + \frac{\partial h U_i U_j}{\partial x_j} = -gh\frac{\partial h}{\partial x_i} - gh\frac{\partial z_b}{\partial x_i} - \frac{h}{\rho}\frac{\partial p_a}{\partial x_i} - \frac{\tau_{b,i}}{\rho} + \frac{\tau_{s,i}}{\rho} + \frac{\partial}{\partial x_j}\left(\nu h \frac{\partial U_i}{\partial x_j}\right) - \frac{\partial h < \overline{u_i' u_j'} >}{\partial x_j}$$

The Reynolds stresses must be computed by means of a turbulence model. Leaving the turbulent terms apart, the depth averaged equations are a system of 3 partial differential equations with 3 unknowns (U, V, h), which are defined over a two-dimensional spatial domain. This is an important reduction in the computational cost with respect to the original RANS equations, which are 4 equations defined over a 3D spatial domain, with the additional inconvenience of the free surface moving boundary. On the other hand, the approximations made when deriving Equations 2.36 reduce their range of application. Nevertheless, when applied to shallow water flows they keep a good compromise between accuracy and computational cost.

2.3.5 Summary of the derivation hypotheses

Through the derivation of the depth averaged shallow water equations several assumptions have been done. It is very important to have in mind the approximations made in each different term, in order to know the limitations of the equations, when they can be applied, and to understand and interpret the results obtained from them. The different hypotheses made are summarised below, and both a physical and a mathematical interpretation are done.

- Constant density:
  The incompressible RANS equations have been taken as the base for the derivation. By assuming incompressible flow the density variations with the pressure gradients are neglected, which is a reasonable hypothesis in water flows.

- Hydrostatic pressure:
  The hydrostatic pressure distribution is mainly a consequence of assuming a separation of the vertical and horizontal characteristic scales. This occurs when both the horizontal length and the horizontal velocity are larger than the vertical ones. This is a typical characteristic of quasi-2D flows. The definition of the horizontal and vertical scales is not trivial, and depends on the flow conditions and geometry. In a long shallow wave propagation problem the horizontal scale is given by the wave length, while the vertical scale is given by the water depth, since it is over those distances that the velocity and pressure changes occur. In some cases the vertical length scale is given by the variations in the bed and free surface elevation rather than by the water depth, and therefore, the condition $\frac{H_n}{L_n} << 1$ is actually a restriction on the free surface and bed slopes. Therefore, the shallow water equations may be applied to flows with a large water depth if the bed slope is small. Some researchers make a distinction between shallow water flow and deep water flow depending on the ratio between the inertial and bed friction forces [5], although the shallow water equations may be used in both situations. Apart from the separation of scales, there are another two conditions which must be fulfilled in order to assure an hydrostatic pressure distribution: the Reynolds number must be much larger than 1, and the turbulence intensity must be smaller than 1. Both conditions are usually fulfilled in shallow water flows. Finally, it should be noted that the fact of assuming a separation of length scales does not mean that the vertical velocity is neglected, as it is clearly shown in the 3D shallow water model (Equation 2.19).

- Homogeneous behaviour in the vertical direction:
  The physical meaning of this hypothesis is that the values of both the velocity and the Reynolds stresses, are almost independent of the vertical coordinate. This cannot be assumed as frequently as the previous hypothesis. Mathematically it can be expressed in 3 conditions which affect the convection and the diffusion terms in the equations:

$$\int_{z_b}^{z_s} f^2\, dz \approx 0 \qquad \frac{\partial}{\partial x}\int_{z_b}^{z_s} \nu U \frac{\partial f}{\partial x}\, dz \approx 0 \qquad -\frac{\partial z_s}{\partial x}\overline{t}_{xx}(z_s) + \frac{\partial z_b}{\partial x}\overline{t}_{xx}(z_b) \approx 0$$

  where f is the shape function as defined in Equation 2.22.

2.3.6 The non-dimensional depth averaged shallow water equations

One important difference between the shallow water equations and the Navier-Stokes equations is that in the former ones the vertical dimension plays a different role than the horizontal dimension. This is in direct relation with the assumption of an hydrostatic pressure distribution. For this reason, different non-dimensional variables should be defined for the horizontal and the vertical

length scales. The non-dimensional variables for the shallow water equations are defined as:

$$\tilde{x} = \frac{x}{L_s} \qquad \tilde{y} = \frac{y}{L_s} \qquad \tilde{z} = \frac{z}{Z_s} \qquad \tilde{h} = \frac{h}{H_s} \qquad \tilde{U} = \frac{U}{U_s} \qquad \tilde{\rho} = \frac{\rho}{\rho_s} \tag{2.37}$$

The non-dimensional time is defined with the horizontal velocity scale and the horizontal length scale. In order to avoid imposing additional constraints, different length scales have been defined for the vertical coordinate and for the water depth. Introducing the non-dimensional variables in the depth averaged equations 2.36 gives:

$$\frac{\partial \tilde{h}}{\partial \tilde{t}} + \frac{\partial \tilde{h}\tilde{U}_j}{\partial \tilde{x}_j} = 0 \tag{2.38}$$

$$\frac{\partial \tilde{h}\tilde{U}_i}{\partial \tilde{t}} + \frac{\partial \tilde{h}\tilde{U}_i\tilde{U}_j}{\partial \tilde{x}_j} = -g\frac{H_s}{U_s^2}\tilde{h}\frac{\partial \tilde{h}}{\partial \tilde{x}_i} - g\frac{Z_s}{U_s^2}\tilde{h}\frac{\partial \tilde{z}_b}{\partial \tilde{x}_i} + \frac{L_s c_f}{H_s}\tilde{U}_i + \frac{1}{Re}\frac{\partial}{\partial \tilde{x}_j}\left(\tilde{h}\frac{\partial \tilde{U}_i}{\partial \tilde{x}_j}\right) - \frac{\partial \tilde{h} < \widetilde{\overline{u_i' u_j'}} >}{\partial \tilde{x}_j}$$

where the free surface shear and the variations in atmospheric pressure have not been considered. From the non-dimensional equations it is obvious that, in order to have fully similarity solutions, the water depth scale must be equal to the vertical scale ($Z_s = H_s$). In other case the hydrostatic pressure term and the bed slope term would not be proportional. With this condition the equations depend on three non-dimensional parameters:

$$Fr = \frac{U_s}{\sqrt{gH_s}} \qquad Re = \frac{U_s L_s}{\nu} \qquad T = \frac{H_s}{c_f L_s} \tag{2.39}$$

While the non-dimensional incompressible Navier-Stokes equations depend only on the Reynolds number, the depth averaged shallow water equations depend on three parameters. The parameter T appears because different length scales have been chosen for the vertical and horizontal dimensions, and also because a logarithmic profile has been assumed in order to compute the bed friction. In the case that $H_s = L_s$, the non-dimensional number T becomes just a restriction on the bed friction coefficient $T = \dfrac{1}{c_f}$. The Froude number appears from the assumption of hydrostatic pressure distribution, which is a simplification of the vertical momentum equation. The Froude number is equivalent to the Mach number in the compressible Navier-Stokes equations. Both of them are the ratio between the fluid speed and the celerity of pressure waves. If the Froude number is greater than 1 the flow is supercritical and the information travels only in the downstream direction. In the case of the shallow water equations, since the pressure is hydrostatic, the pressure waves are also called gravity waves.

2.3.7 Bed friction

The bed friction has a double effect on the depth averaged shallow water equations. First, it produces a friction force ($\boldsymbol{\tau}_b = (\tau_{b,x}, \tau_{b,y})$) opposite to the mean velocity, and second, it produces turbulence. Both effects can be characterised by the bed friction velocity u_f, which is the wall friction velocity (u_*) of the bed surface. However, in the depth averaged equations the bed friction velocity cannot be computed from a wall function approach (section 1.4), since the equations are not resolved in the vertical direction. Instead, it is related to the depth averaged velocity by a bed friction coefficient.

The bed shear stress can be expressed as:

$$|\boldsymbol{\tau}_b| = \rho u_f^2 = \rho c_f |\mathbf{U}|^2 \tag{2.40}$$

where $c_f = \dfrac{u_f^2}{|\mathbf{U}|^2}$ is the bed friction coefficient. There are several expressions which permit to approximate the bed friction coefficient. Most of them assume fully developed channel flow, and all the water depth is approximated as a logarithmic boundary layer. In this case the horizontal velocity can be expressed as a function of the friction velocity and the roughness height (K_s) as (see Equation 1.33 for $K_s^+ > 70$):

$$|\overline{\mathbf{u}}| = \frac{u_f}{\kappa} \ln\left(30\frac{z}{K_s}\right) \tag{2.41}$$

where $|\overline{\mathbf{u}}|$ is the module of the mean velocity. The roughness height K_s is a measure of the bed surface rugosity. It has length dimensions. Equation 2.41 should only be applied for $z \geq \dfrac{K_s}{30}$. For lower values of z Equation 2.41 gives a negative velocity. The depth averaged horizontal velocity can be obtained after integration of Equation 2.41 over the water depth as:

$$|\mathbf{U}| = \frac{1}{h}\int_{z_b}^{z_s} |\overline{\mathbf{u}}|\, dz = \frac{u_f}{\kappa}\left[\ln\frac{30h}{K_s} - 1 + \frac{K_s}{30h}\right] \tag{2.42}$$

Assuming that the water depth is much larger than the roughness height, Equation 2.42 is simplified as:

$$|\mathbf{U}| = \frac{u_f}{\kappa} \ln\frac{11h}{K_s} \tag{2.43}$$

which is known as Keulegan's law. From Equation 2.43 it is obvious that for the same depth averaged velocity $|\mathbf{U}|$, the friction velocity diminishes as the water depth increases. The friction coefficient c_f is then obtained as:

$$c_f^{-1/2} = \frac{|\mathbf{U}|}{u_f} = 2.5 \ln\frac{11h}{K_s} \tag{2.44}$$

An approximation of Keulegan's law was proposed by Manning and Strickler as:

$$c_f^{-1/2} = 8.1 \left(\frac{h}{K_s} \right)^{1/6} \tag{2.45}$$

An alternative way to evaluate the bed friction which is widely used in hydraulic engineering is the Manning's formula, which uses the Manning's coefficient n instead of the roughness height. The friction coefficient is given by:

$$c_f = g \frac{n^2}{h^{1/3}} \tag{2.46}$$

Comparing the friction coefficients given by Manning's formula (Equation 2.46) and by the Manning-Strickler approximation (Equation 2.45), the following relation between the Manning's coefficient and the roughness height is obtained:

$$n \approx \frac{K_s^{1/6}}{25} \tag{2.47}$$

Manning's formula is specially suited for rough river beds. Schlichting [121] proposed an alternative formula for evaluating the bed friction coefficient in smooth river beds:

$$c_f = 0.027 \left(\frac{\nu}{|\mathbf{U}| R_h} \right)^{1/4} \tag{2.48}$$

where R_h is the hydraulic radius.

2.3.8 Boundary conditions

There are two main kind of boundaries in the shallow water models: open boundaries and wall boundaries. The treatment of wall boundaries has been already presented in section 1.4.

The number of boundary conditions that must be specified at any open boundary depends on the direction in which information travels across that boundary. In shallow water flows the direction in which information propagates depends on the sign of the eigenvalues of the Jacobian matrix of the normal flux, which are given by (see chapter 3):

$$\lambda_1 = U n_x + V n_y \qquad \lambda_2 = \lambda_1 + c\sqrt{n_x^2 + n_y^2} \qquad \lambda_3 = \lambda_1 - c\sqrt{n_x^2 + n_y^2} \tag{2.49}$$

where $\mathbf{n} = (n_x, n_y)$ is the normal vector to the surface, and $c = \sqrt{gh}$ is the wave celerity. It will be assumed that the normal vector to an open boundary points outward. Four possible open boundary conditions arise depending on the sign of the eigenvalues: supercritical inlet, subcritical inlet, subcritical outlet and supercritical outlet. If all the eigenvalues are negative the three characteristic lines are entering the domain, and three boundary conditions must be imposed. This is the case

of supercritical inlet. It occurs when the flow enters the domain ($\lambda_1 < 0$) and the wave celerity is smaller than the normal velocity to the boundary ($\lambda_2, \lambda_3 < 0$). If the flow enters the domain but the wave celerity is larger than the normal velocity, there are two negative eigenvalues (λ_1, λ_3) and one positive (λ_2). In this case only two characteristic lines enter the domain, and therefore, two boundary conditions must be imposed. This is the subcritical inlet boundary condition. The subcritical outlet occurs when the flow exits the domain and the wave celerity is larger than the normal velocity. In this case two eigenvalues are positive (λ_1, λ_2), only one characteristic line enters the domain, and thus, only one boundary condition must be imposed, generally the water depth. Finally, if all the eigenvalues are positive all the information travels outward the domain, and no boundary condition is needed (supercritical outlet).

2.4 Turbulence modelling in shallow water flows

2.4.1 Turbulent length scales in shallow flows

It has already been discussed in section 2.1 the 2D character of the large turbulent structures in shallow water flows. As it is pointed out by Uijttewaal and Tukker [138], the turbulence model must account for both, the 3D structures produced by bed friction and the quasi-2D large structures produced by horizontal strain. If a depth averaged model is used, the 2D character of the flow is already taken into account in the transport equations by assuming a uniform vertical profile of the velocity, while the 3D production is usually included via a source term which depends on the bed friction velocity. In the same way, even when a 3D shallow water approach is used, the turbulence model should account for the anisotropy of turbulence in the vertical and horizontal directions. Bijvelds et al. [12] modelled the flow in a square harbour using the 3D shallow water equations. The turbulence generated by bed friction was modelled with the standard 3D $k-\varepsilon$ model, while the horizontal turbulent stresses were computed with a 2D depth averaged $k-\varepsilon$ model. The results obtained were better than those given by the standard 3D $k-\varepsilon$ model.

Several depth averaged turbulence models are discussed in this section, and a depth averaged algebraic stress model is proposed in the next section. All the models presented in this chapter have been included in the numerical solver described in chapter 3. Three of them, the mixing length model, the $k-\varepsilon$ model of Rastogi and Rodi, and the algebraic stress model, have been systematically used in the practical applications studied in this thesis.

2.4.2 The Boussinesq assumption in shallow flows

In section 1.3 it was presented the Boussinesq assumption, which is used in the eddy viscosity models in order to relate the Reynolds stresses and the mean velocity gradients as:

$$\overline{u_i' u_j'} = -2\nu_t \left(\overline{s}_{ij} - \frac{1}{3}\overline{s}_{kk}\delta_{ij} \right) + \frac{2}{3}k\delta_{ij} \tag{2.50}$$

From the six Reynolds stresses ($\overline{u_i' u_j'}$), only 3 of them ($\overline{u'^2}, \overline{u'v'}$ and $\overline{v'^2}$) appear in the depth averaged equations. Assuming incompressible flow, they can be approximated as:

$$\begin{aligned} -\overline{u'^2} &= 2\nu_t \frac{\partial \overline{u}}{\partial x} - \frac{2}{3}k \\ -\overline{u'v'} &= \nu_t \left(\frac{\partial \overline{u}}{\partial y} + \frac{\partial \overline{v}}{\partial x} \right) \\ -\overline{v'^2} &= 2\nu_t \frac{\partial \overline{v}}{\partial y} - \frac{2}{3}k \end{aligned} \tag{2.51}$$

What actually appears in the equations is the depth averaged value of the Reynolds stresses. In shallow flows the eddy viscosity can be assumed to be homogeneous in the vertical direction, except in the bed boundary layer and in a thin layer near the free surface. With this approximation the vertical average of Equations 2.51 yields:

$$\begin{aligned} -<\overline{u'^2}> &= 2\nu_t \frac{\partial U}{\partial x} - \frac{2}{3} < k > -\overline{u}_s \frac{\partial z_s}{\partial x} + \overline{u}_b \frac{\partial z_b}{\partial x} \\ -<\overline{u'v'}> &= \nu_t \frac{\partial U}{\partial y} + \frac{\partial V}{\partial x} - \overline{u}_s \frac{\partial z_s}{\partial y} + \overline{u}_b \frac{\partial z_b}{\partial y} - \overline{v}_s \frac{\partial z_s}{\partial x} + \overline{v}_b \frac{\partial z_b}{\partial x} \\ -<\overline{v'^2}> &= 2\nu_t \frac{\partial V}{\partial y} - \frac{2}{3} < k > -\overline{v}_s \frac{\partial z_s}{\partial y} + \overline{v}_b \frac{\partial z_b}{\partial y} \end{aligned} \tag{2.52}$$

Assuming a separation between the horizontal and vertical scales ($L_s >> H_s$), Equations 2.52 can be approximated as:

$$\begin{aligned} -<\overline{u'^2}> &= 2\nu_t \frac{\partial U}{\partial x} - \frac{2}{3} < k > \\ -<\overline{u'v'}> &= \nu_t \left(\frac{\partial U}{\partial y} + \frac{\partial V}{\partial x} \right) \\ -<\overline{v'^2}> &= 2\nu_t \frac{\partial V}{\partial y} - \frac{2}{3} < k > \end{aligned} \tag{2.53}$$

which is an analogous expression to the original Boussinesq approximation, with the only difference that now all the variables are depth averaged. In order to simplify the notation, hereafter the symbols $<>$ will be omitted when referring to depth averaged values.

2.4.3 The depth averaged parabolic eddy viscosity model

This is the simplest turbulence model for shallow flows. Assuming an equilibrium state of the flow, the shear and the pressure forces in the fluid element of Figure 2.1 should be balanced. By assuming an equilibrium state of the flow the convection terms in the momentum equation can be neglected. The only mass force is the gravity acceleration, which acts in the vertical direction.

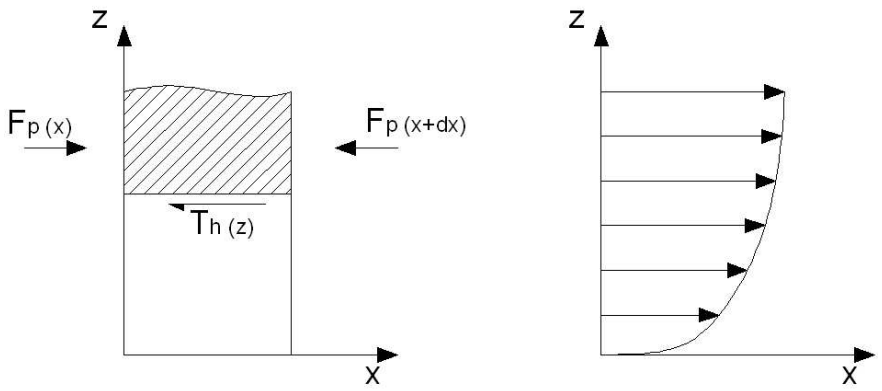

Figure 2.1: Balance of forces in a fluid element in uniform channel flow.

The equilibrium of forces in the x-direction gives:

$$\tau_h(z) = -\frac{\partial F_p}{\partial x} = -\rho g(h-z)\frac{\partial h}{\partial x} \tag{2.54}$$

where $F_p = \rho g \dfrac{(h-z)^2}{2}$ is the total pressure force on each side of the fluid element. For $z = z_b = 0$, the friction force is equal to the bed friction $\tau_{b,x}$:

$$\tau_{b,x} = \tau_h(z=0) = -\rho g h \frac{\partial h}{\partial x} \tag{2.55}$$

With this condition Equation 2.54 can be rewritten as:

$$\tau_h(z) = \tau_{b,x}(1-\frac{z}{h}) = \rho u_f^2(1-\frac{z}{h}) \tag{2.56}$$

Equation 2.56 predicts a linear relation between the shear stress and the vertical coordinate z. The shear stress in a turbulent boundary layer can be expressed in function of the eddy viscosity as:

$$\tau_h(z) = \rho \nu_t'(z)\frac{\partial \overline{u}}{\partial z} \tag{2.57}$$

where $\nu_t'(z)$ is the eddy viscosity as a functions of z, and not its depth averaged value. Assuming a logarithmic velocity profile, which is a sensible approximation in fully developed turbulent

boundary layer flows, Equation 2.57 becomes:

$$\tau_h(z) = \rho\nu_t'(z)\frac{u_f}{\kappa z} \tag{2.58}$$

From Equations 2.56 and 2.58, a parabolic profile for the eddy viscosity is obtained as:

$$\nu_t'(z) = u_f\kappa z(1 - \frac{z}{h}) \tag{2.59}$$

Finally, the depth averaged eddy viscosity is obtained after vertical integration of Equation 2.59, which yields.

$$\nu_t = \frac{1}{h}\int_{z_b}^{z_s} u_f\kappa z(1 - \frac{z}{h})\, dz = \frac{1}{6}\kappa u_f h \tag{2.60}$$

The eddy viscosity $\nu_t'(z)$ can be expressed as the product of a velocity scale $u_s'(z)$ and a length scale $l_s'(z)$ as:

$$\nu_t'(z) = l_s'(z)u_s'(z) \tag{2.61}$$

The velocity scale is defined in a boundary layer basis as:

$$u_s'(z) = l_s'(z)\frac{\partial\overline{u}}{\partial z} = l_s'(z)\frac{u_f}{\kappa z} \tag{2.62}$$

From Equations 2.62, 2.61 and 2.59, a turbulent length scale can be defined as a function of the vertical coordinate z:

$$l_s'(z) = \kappa z\sqrt{1 - \frac{z}{h}} \tag{2.63}$$

The parabolic eddy viscosity model is very simple. It does not account for the effect of horizontal velocity gradients, but only for the turbulence generated by bed friction. It leads to very low eddy viscosity values when the turbulent production due to horizontal shear is large. It does not account for transport and dissipation processes. Despite its simplicity, it is sometimes used in simple channel flows. It has been used to model channel bend flows by Hsieh and Yang [59], Lien et al. [81] and Duan [43].

2.4.4 The depth averaged mixing length model

This is a depth averaged version of the original mixing length model presented in chapter 1. In order to account for both the horizontal and the vertical production of turbulence, the total eddy viscosity is split into an horizontal ν_t^h and a vertical ν_t^v component. The horizontal eddy viscosity accounts for the turbulence produced by horizontal shear. It is computed as:

$$\nu_t^h = l_s^2\sqrt{2S_{ij}S_{ij}} = l_s^2\sqrt{2(S_{uu}^2 + S_{vv}^2 + 2S_{uv}^2)} \tag{2.64}$$

where l_s is the characteristic turbulent length scale, and S_{ij} is the horizontal mean strain-rate tensor computed from the depth averaged velocity as:

$$S_{ij} = \frac{1}{2}\left(\frac{\partial U_i}{\partial x_j} + \frac{\partial U_j}{\partial x_i}\right) \tag{2.65}$$

The vertical eddy viscosity is generated by the vertical velocity gradients produced by bed friction. Therefore, it is computed from the parabolic eddy viscosity model as:

$$\nu_t^v = \frac{1}{6}\kappa u_f h \tag{2.66}$$

The total eddy viscosity is evaluated from the horizontal and vertical values as:

$$\nu_t = \sqrt{(\nu_t^h)^2 + (\nu_t^v)^2} = l_s^2\sqrt{2\left(\frac{\partial U}{\partial x}\right)^2 + 2\left(\frac{\partial V}{\partial y}\right)^2 + \left(\frac{\partial U}{\partial y} + \frac{\partial V}{\partial x}\right)^2 + \left(\frac{1}{6}\frac{\kappa u_f h}{l_s^2}\right)^2} \tag{2.67}$$

In the inner part of the domain the turbulent length scale is assumed to be dependent on the water depth, since it is a restriction on the size of the turbulent eddies. In order to estimate its value, the turbulent length given by the parabolic eddy viscosity model (Equation 2.63) is averaged over the vertical coordinate, which yields:

$$l_s = \frac{1}{h}\int_{z_b}^{z_s} \kappa z\sqrt{1 - \frac{z}{h}}\, dz \approx 0.267\kappa h \tag{2.68}$$

Equation 2.68 is not valid near the walls, as it would predict very large length scales. Instead, the wall distance is used as the length scale in the near wall regions. The final expression for the eddy viscosity given by the model is:

$$\nu_t = l_s^2\sqrt{2\left(\frac{\partial U}{\partial x}\right)^2 + 2\left(\frac{\partial V}{\partial y}\right)^2 + \left(\frac{\partial U}{\partial y} + \frac{\partial V}{\partial x}\right)^2 + \left(2.34\frac{u_f}{\kappa h}\right)^2} \tag{2.69}$$

$$l_s = \min\left(0.267\kappa h, \kappa d_{wall}\right)$$

where d_{wall} is the distance to the nearest wall. In the absence of horizontal velocity gradients, Equations 2.69 and 2.60 are equal. Hence, the depth averaged mixing length model tends to the parabolic eddy viscosity model when the turbulence is mainly produced by bed friction. This is the case of flows with a very low water depth, a relatively rough bed surface, and small horizontal velocity gradients. The depth averaged mixing length model was used in channel flow computations by Jia and Wang [65], among others.

2.4.5 Some depth averaged $k-\varepsilon$ models

The $k-\varepsilon$ model of Rastogi and Rodi

The first $k-\varepsilon$ model for shallow water flows was proposed by Rastogi and Rodi [116] as a depth averaged version for quasi-2D flows of the original $k-\varepsilon$ model of Jones and Launder [67]. Instead of solving for the three-dimensional turbulence and dissipation, it solves for their depth averaged value $< k >$ and $< \varepsilon >$. The symbols $<>$ referring to depth averaged values will be omitted for the sake of simplicity in the notation.

Since an homogeneous behaviour in the vertical direction is assumed in shallow flows, the modelled equations are very similar to those of the 2D standard $k-\varepsilon$ model. Nevertheless, it is necessary to introduce a production term in order to account for the production of turbulence due to bed friction. The equations of the model are given by:

$$\begin{aligned}
\frac{\partial hk}{\partial t}+\frac{\partial U_j hk}{\partial x_j} &= \frac{\partial}{\partial x_j}\left((\nu+\frac{\nu_t}{\sigma_k})h\frac{\partial k}{\partial x_j}\right)+hP_k+hP_{kv}-h\varepsilon \\
\frac{\partial h\varepsilon}{\partial t}+\frac{\partial U_j h\varepsilon}{\partial x_j} &= \frac{\partial}{\partial x_j}\left((\nu+\frac{\nu_t}{\sigma_\varepsilon})h\frac{\partial \varepsilon}{\partial x_j}\right)+hc_{1\varepsilon}\frac{\varepsilon}{k}P_k+hP_{\varepsilon v}-hc_{2\varepsilon}\frac{\varepsilon^2}{k}
\end{aligned} \tag{2.70}$$

$$\begin{aligned}
\nu_t &= c_\mu\frac{k^2}{\varepsilon} & P_k &= 2\nu_t(S_{uu}^2+S_{vv}^2+2S_{uv}^2) \\
P_{kv} &= c_k\frac{u_f^3}{h} & c_k &= \frac{1}{c_f^{1/2}} \\
P_{\varepsilon v} &= c_\varepsilon\frac{u_f^4}{h^2} & c_\varepsilon &= 3.6\frac{c_{2\varepsilon}c_\mu^{1/2}}{c_f^{3/4}}
\end{aligned}$$

$$c_\mu = 0.09 \quad c_{1\varepsilon} = 1.44 \quad c_{2\varepsilon} = 1.92 \quad \sigma_k = 1.0 \quad \sigma_\varepsilon = 1.31$$

where c_f is the bed friction coefficient as defined in Equation 2.40 ($c_f = \dfrac{|\boldsymbol{\tau}_b|}{\rho|\mathbf{U}|^2} = \dfrac{u_f^2}{|\mathbf{U}|^2}$). The five constants of the model ($c_\mu, \sigma_k, \sigma_\varepsilon, c_{1\varepsilon}, c_{2\varepsilon}$) are assumed to have the same values as in the original $k-\varepsilon$ model (Equation 1.20). The term P_k accounts for the production of turbulent energy due to horizontal velocity gradients. The effect of the bed is included via the production terms P_{kv} and $P_{\varepsilon v}$. These source terms are responsible for modelling the 3D turbulence generated by bed friction.

In uniform channel flow conditions, all the production of turbulent kinetic energy is due to bed friction. Turbulence is in an equilibrium state, and the $k-\varepsilon$ equations reduce to:

$$P_{kv} = \varepsilon \qquad P_{\varepsilon v} = c_{2\varepsilon}\frac{\varepsilon^2}{k} \tag{2.71}$$

Using the expressions for P_{kv} and $P_{\varepsilon v}$ given by Equation 2.70, it is straightforward to show

that the values of the turbulent energy and dissipation predicted by the model in uniform channel flow are given by:

$$k_u = \frac{c_{2\varepsilon}}{c_\varepsilon} c_k^2 u_f^2 = \frac{|\mathbf{U}|^{1/2} u_f^{3/2}}{1.08} \qquad \varepsilon_u = c_k \frac{u_f^3}{h} = \frac{|\mathbf{U}| u_f^2}{h} \tag{2.72}$$

With these values the eddy viscosity is equal to:

$$\nu_{t,u} = c_\mu c_k^3 \frac{c_{2\varepsilon}^2}{c_\varepsilon^2} u_f h = 0.08 u_f h \tag{2.73}$$

which actually is a very similar value to that one given by the depth averaged parabolic model (Equation 2.60). On the other hand, when the horizontal shear is much larger than the vertical shear, the vertical production terms are negligible compared to the horizontal shear production ($P_{kv} \approx 0$, $P_{\varepsilon v} \approx 0$), and the model reduces to the standard 2D $k - \varepsilon$ model.

A slight modification of the coefficient c_ε has been used in recent works by Minh-Duc et al. [92]. The expression used is given by:

$$c_\varepsilon = \frac{1}{(e_* \sigma_t)^{1/2}} \frac{c_{2\varepsilon} c_\mu^{1/2}}{c_f^{3/4}} \tag{2.74}$$

where σ_t is a Prandtl/Schmidt number relating the eddy viscosity and diffusivity for the transport of scalars ($\sigma_t = 0.7$ in [92]), and e_* is an adjustable empirical parameter. The value 3.6 in the definition of c_ε in Equation 2.70, corresponds to a value of $e_* = 0.11$ in Equation 2.74. Minh-Duc et al. [92] report values of the parameter e_* ranging from 0.15 in flumes to 0.6 is meandering rivers. In the numerical solver used in this thesis, the original definition of c_ε was used, since Equation 2.74 would need a previous calibration for each practical application.

The modified constants of Booij

The production terms P_{kv} and $P_{\varepsilon v}$ in Equation 2.70 depend on two coefficients, c_k and c_ε. The value of these coefficients determine the turbulence level in uniform channel flow conditions (Equation 2.72). Booij [14] proposed the following modification in the value of c_k and c_ε:

$$c_k^B = \frac{1}{10} c_k \qquad c_\varepsilon^B = \frac{1}{44} c_\varepsilon \tag{2.75}$$

where the superindex B refers to Booij. The effect of diminishing the coefficients c_k and c_ε in such a way is that the production terms due to bed friction (P_{kv} and $P_{\varepsilon v}$) are strongly reduced. Using the modified coefficients of Booij to evaluate the turbulent kinetic energy and dissipation in uniform

channel flow (Equation 2.72) gives:

$$k_u^B = 0.44 k_u \qquad \varepsilon_u^B = 0.10 \varepsilon_u \qquad \nu_{t,u}^B = 1.94 \nu_{t,u} \tag{2.76}$$

where the values $k_u, \varepsilon_u, \nu_{t,u}$ are those given by the Rastogi and Rodi model. Hence, in uniform channel flow conditions, the modification proposed by Booij reduces the turbulent kinetic energy and dissipation by a factor of 0.44 and 0.10 respectively, and increases the eddy viscosity by a factor of 1.94. On the other hand, in flows dominated by horizontal shear the differences with the Rastogi and Rodi model smear, because the term P_{kv} becomes much smaller than P_k in Equation 2.70.

The $k - \varepsilon$ model of Babarutsi and Chu

Babarutsi and Chu [3] proposed a two-length-scale depth averaged $k - \varepsilon$ model. The main difference with Rastogi's model is the way in which the effects of the 3D turbulence produced by bed friction are introduced. Babarutsi and Chu propose to split the total eddy viscosity into a 3D part and a 2D part:

$$\nu_t = \nu_t^{2D} + \nu_t^{3D} \tag{2.77}$$

The 3D eddy viscosity accounts for the small scale bed generated turbulence, and it is computed with a similar equation to that of the depth averaged parabolic eddy viscosity (Equation 2.60). The equation for ν_t^{3D} used by Babarutsi and Chu is given by:

$$\nu_t^{3D} = 0.08 u_f h \tag{2.78}$$

which is the same value given by the Rastogi model for uniform channel flow (Equation 2.73). The 2D part is computed from k' and ε', which account for the large-scale 2D turbulence generated by horizontal shear, as:

$$\nu_t^{2D} = c_\mu \frac{k'^2}{\varepsilon'} \tag{2.79}$$

Notice that the turbulent kinetic energy k' does not include the 3D bed generated turbulence. The transport equations used to compute k' and ε' are similar to those used in Rastogi's model (Equation 2.70), but the vertical production terms are zero ($P_{kv} = P_{\varepsilon v} = 0$) and a new term F' is introduced in order to account for the transfer of energy between the large 2D scales and the small 3D scales. The equations for k' and ε' are given by:

$$\begin{aligned}
\frac{\partial h k'}{\partial t} + \frac{\partial U_j h k'}{\partial x_j} &= \frac{\partial}{\partial x_j}\left((\nu + \frac{\nu_t}{\sigma_k}) h \frac{\partial k'}{\partial x_j} \right) + h P_{k'} - h F' - h \varepsilon' \\
\frac{\partial h \varepsilon'}{\partial t} + \frac{\partial U_j h \varepsilon'}{\partial x_j} &= \frac{\partial}{\partial x_j}\left((\nu + \frac{\nu_t}{\sigma_\varepsilon}) h \frac{\partial \varepsilon'}{\partial x_j} \right) + h c_{1\varepsilon} \frac{\varepsilon'}{k'} (P_{k'} - (1 - c_{3\varepsilon}) F') - h c_{2\varepsilon} \frac{\varepsilon'^2}{k'}
\end{aligned} \tag{2.80}$$

with the constant $c_{3\varepsilon} = 0.8$. Note that in Equation 2.80 the diffusion term is modelled with the total eddy viscosity ν_t. On the other hand, the production term $P_{k'}$ is computed with the expression given in Equation 2.70, but using the 2D part of the eddy viscosity ν_t^{2D}. All the constants of the model are the same as in Rastogi's model. The sink term F' is associated with the negative work done by the large scale turbulent fluctuations against the bed friction forced. It is computed as:

$$F' = \frac{c_f \left[\overline{u'^2}(2U^2 + V^2) + 2\overline{u'v'}UV + \overline{v'^2}(U^2 + 2V^2) \right]}{h\sqrt{U^2 + V^2}} \tag{2.81}$$

where the Reynolds stresses $\overline{u'^2}, \overline{u'v'}, \overline{v'^2}$ are computed from the Boussinesq approximation using the large scale eddy viscosity ν_t^{2D}.

In uniform channel flow, the production of large scale turbulence due to horizontal shear is zero ($P_{k'} = 0$). The large scale turbulent kinetic energy equation reduces to $0 = -F' - \varepsilon'$. Therefore, all the large scale turbulent variables are zero, i.e:

$$k'_u = 0 \qquad \varepsilon'_u = 0 \qquad \nu_{t,u}^{2D} = 0 \qquad \nu_{t,u} = \nu_t^{3D} = 0.08 u_f h \tag{2.82}$$

where the subindex u refers to uniform channel flow values. In this case all the turbulence is 3D, and generated by bed friction. The total eddy viscosity is similar to that one given by the Rastogi model. On the other hand, in a flow dominated by horizontal shear, the bed friction velocity (u_f) tends to zero, and so do the term F' and the 3D eddy viscosity ($F' \approx 0$, $\nu_t^{3D} \approx 0$). In this situation all the turbulence is 2D, and generated by horizontal shear. The equations for k' and ε' reduce to the standard 2D $k - \varepsilon$ model.

This model has been used by Babarutsi et al. in [5], with the constant $c_{3\varepsilon} = 1$, to compute shallow recirculating flows dominated by friction. It has also been used by Babarutsi and Chu to model shallow mixing layers [4], where they obtained the same results with $c_{3\varepsilon=1}$ and with $c_{3\varepsilon} = 0.8$.

Differences between the 3 versions of the $k - \varepsilon$ model

The main differences between the previous depth averaged $k - \varepsilon$ models, appear in friction dominated flows. The modification of Booij increases the turbulent diffusion of the model, reduces the bed generated turbulence, and as a consequence, the large scale turbulence is increased. We have not found concluding results showing that the modification proposed by Booij improves the results of the original model of Rastogi in general flow conditions. Furthermore, the work by Minh-Duc et al. [92] seems to show that the optimum value of the constant c_ε is problem dependent.

The version of Babarutsi and Chu is more interesting from a conceptual point of view, since it distinguish between two different turbulent length scales. The main differences with Rastogi's

model appear in shear flows dominated by friction. Both models converge to the standard 2D $k-\varepsilon$ model for zero bed friction. In uniform channel flow, where all the turbulence is generated by bed friction, both models give the same eddy viscosity (Equations 2.73 and 2.82). It is in shear layers dominated by friction where both models show some differences. Altai et al. [2] estimate that, in order to produce the modelled effects introduced by the term F', the water depth should be approximately 100 times smaller than the horizontal turbulent length scale, i.e. the effects of F' are only significant in flows which are strongly dominated by friction. Babarutsi et al. [5] compared the results given by the models of Babarutsi and Rastogi in a recirculating shallow water flow dominated by friction. Despite the different turbulent energy and eddy viscosity predicted by the models, no significant differences in the mean flow field, neither in the recirculation length, were found, and therefore, no conclusion was obtained regarding which model performs better. Both models were compared again by Babarutsi and Chu [4] to model transverse mixing layers in shallow flows dominated by friction. In this case they found that the results given by the model of Babarutsi were in better agreement with the experimental data.

All the results presented in this work have been done with the original depth averaged model of Rastogi and Rodi. Although the three versions of the models were implemented in the numerical solver, no systematic comparison between models has been done in the practical applications. Nevertheless, in the applications studied in this thesis, no differences are expected to be found in the mean flow field obtained with the different versions of the model. This is because the flow in the vertical slot fishway (chapter 8) and in the 90^o bend (chapter 7) is not dominated by bed friction. In the Crouch estuary (chapter 6) the turbulence is generated by friction, but the turbulence level is low, and it has very little influence on the mean velocity field. In the Crouch estuary some differences in the turbulent energy field would probably be obtained with Booij's and Babarutsi's versions of the model.

The reason of using the original model of Rastogi and Rodi is that it has been used in many river flow and channel simulations, showing a good behaviour [152, 92, 115, 149, 12, 154, 104]. On the other hand, the versions of Booij and Babarutsi have not been so extensively used. In any case, as it has been argued, only in the Crouch estuary some differences between the different versions are expected, and in this case, only in the turbulent kinetic energy field, and not in the mean flow field.

Boundary conditions

While the parabolic and mixing length models assume an equilibrium state of turbulence, the $k-\varepsilon$ model solves the turbulent kinetic energy and dissipation transport equations, and thus, it needs boundary conditions for these two variables. The wall boundary condition has already been discussed in section 1.4. In the same way as in the shallow water equations, the boundary condition at the open boundaries depends on the direction in which information propagates. In this case the

convective direction is given by the depth averaged velocity. Hence, at the inlet boundaries the values of k and ε must be imposed, while at the outlet boundaries no condition is needed.

The turbulent kinetic energy and dissipation at the inlet boundaries can be evaluated in several ways. Sometimes the turbulent energy k or the turbulence intensity T_u can be approximated from experimental values or from previous experience in similar flows. If the turbulence intensity is known, then the turbulent kinetic energy and the dissipation can be approximated at the inlet boundary as:

$$k_i \approx \frac{3}{2}(T_u U_i)^2 \qquad\qquad \varepsilon_i \approx 0.09\frac{k_i^2}{\nu_{t,i}} \tag{2.83}$$

where the subindex i refers to inlet boundary values, and $\nu_{t,i}$ is an approximated value for the eddy viscosity at the inlet boundary. However, in general it may be difficult to estimate the values of ν_t and T_u at the inlet boundary. An alternative method is to assume fully developed uniform channel flow at the inlet. In that case the values of the turbulent energy and dissipation are given by Equation 2.72:

$$k_i = \frac{c_{2\varepsilon}}{c_\varepsilon}c_k^2 u_f^2 \qquad\qquad \varepsilon_i = c_k\frac{u_f^3}{h} \qquad\qquad \nu_{t,i} = 0.19\kappa u_f h \tag{2.84}$$

where the values of c_k and c_ε depend on the version of the $k-\varepsilon$ model used. Notice that the values given by Equations 2.83 and 2.84 refer to the total turbulent energy and dissipation values (2D + 3D).

Limiter to the production of turbulent kinetic energy

It is well known that Boussinesq assumption does not work well under some flow conditions like swirling flow, strong adverse pressure gradients, or near stagnation points. The main cause of these problems is that the eddy viscosity is assumed to be isotropic.

In stagnation points the production of turbulent kinetic energy is overpredicted by the $k-\varepsilon$ model, which gives much larger values of k than the measured ones. This behaviour can be easily explained considering the modelling of the turbulent energy production in the eddy viscosity models. When an impinging jet approaches a wall (Figure 2.2) the sign of the main velocity gradients are:

$$\frac{\partial U}{\partial x} < 0 \qquad\qquad \frac{\partial V}{\partial y} > 0 \tag{2.85}$$

Considering that these ones are the largest velocity gradients, the real production of turbulent kinetic energy is given by:

$$P_k^{real} \approx \underbrace{-\overline{u'^2}\frac{\partial U}{\partial x}}_{Positive}\underbrace{-\overline{v'^2}\frac{\partial V}{\partial y}}_{Negative} \tag{2.86}$$

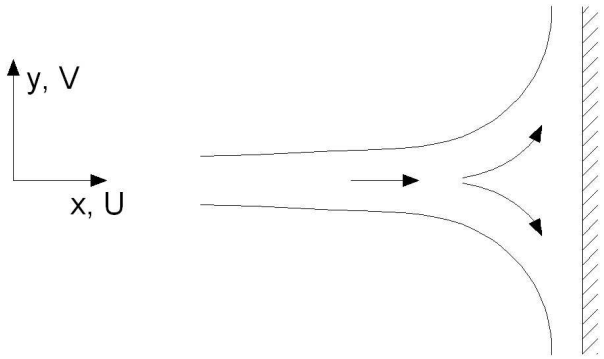

Figure 2.2: Impinging jet.

The positive production of $\overline{u'^2}$ in Equation 2.86 balances partially the negative production of $\overline{v'^2}$. If the Boussinesq assumption is used in Equation 2.86 to model the Reynolds stresses, a much larger production is predicted:

$$P_k^{Boussinesq} \approx 2\nu_t \left[\underbrace{\left(\frac{\partial U}{\partial x}\right)^2}_{Positive} + \underbrace{\left(\frac{\partial V}{\partial y}\right)^2}_{Positive} \right] >> 0 \tag{2.87}$$

For this reason, a limiter in the production term is introduced in almost all the eddy viscosity models in order to avoid too large values of the turbulent energy near stagnation points. Menter [88] limits the ratio between the production and dissipation of turbulence as:

$$P = \min\left(P_k, c_l \varepsilon\right) \tag{2.88}$$

where c_l is a constant which takes a value between 10 and 20. Although limiter 2.88 is a rough estimation which does not imply a good modelling of the stagnation region, it can improve the numerical results, avoiding an extremely large turbulence level which may propagate and affect the solution in the whole numerical domain.

In this thesis, the turbulent production limiter has been applied independently to the horizontal shear production and to the bed friction production as:

$$\begin{aligned} P_k &= \min\left(P_k, c_l \varepsilon\right) \\ P_{kv} &= \min\left(P_{kv}, c_l \varepsilon\right) \end{aligned} \tag{2.89}$$

with a value of $c_l = 10$. The limit imposed in the bed friction production is specially suitable for problems with wet-dry fronts. The term P_{kv} can take very large values when the water depth is very small. In that case, the second limiter in Equation 2.89 avoids instabilities in the solution, and allows using smaller values of the wet-dry tolerance parameter (see section 3.9).

Realizability in the eddy viscosity models

An important drawback to Boussinesq assumption is that it can predict negative values of the normal Reynolds stresses, specially in stagnation regions, as it is pointed out by Durbin in [45]. In order to avoid negative normal stresses a constraint should be used in the eddy viscosity value. This procedure also helps to avoid the excessive turbulent production near stagnation regions. Using Boussinesq assumption, the normal stress $\overline{u'^2}$ is given by:

$$\overline{u'^2} = \frac{2}{3}k - 2\nu_t \frac{\partial U}{\partial x} \tag{2.90}$$

If the turbulence model predicts too large values of ν_t, the normal stress $\overline{u'^2}$ may become negative. From Equation 2.90, the maximum value of ν_t which still gives a positive value of $\overline{u'^2}$ is:

$$\nu_t < \frac{k}{3\dfrac{\partial U}{\partial x}} \tag{2.91}$$

At any given point, the maximum value of $\dfrac{\partial U}{\partial x}$ occurs in the principal axis of the mean strain tensor. Hence, it is in those axis where constraint 2.91 should be imposed. It can be shown [45] that in 3D flow the constraint over the eddy viscosity which assures that all the normal turbulent stresses remain positive is given by:

$$\nu_t < \frac{k}{3}\left(\frac{3}{2\overline{s}_{ij}\overline{s}_{ij}}\right)^{1/2} \tag{2.92}$$

For 2D flow the constraint is slightly different:

$$\nu_t < \frac{k}{3}\left(\frac{2}{S_{ij}S_{ij}}\right)^{1/2} \tag{2.93}$$

The limiter given by Equation 2.93 has been used in all the $k-\varepsilon$ models presented in this section.

2.5 A depth averaged algebraic stress model

The general algebraic stress models (ASM) have been presented in section 1.3.3. Even though they seem simpler than the Reynolds Stress Turbulence Models, they are usually more unstable, specially in 3D flow computations. This is due to the highly non-linear algebraic expressions used in ASM in order to evaluate the Reynolds stresses. The stability of the model is increased if explicit rather than implicit expressions are used to compute the turbulent stresses [34]. In this

section an explicit depth averaged ASM which accounts for the turbulence production due to bed friction is proposed. The model has been used in all the computations done in this thesis, showing a numerical stability similar to the $k-\varepsilon$ model.

2.5.1 Algebraic stresses in 2D shallow flows

Only three Reynolds stresses ($\overline{u'^2}$, $\overline{u'v'}$ and $\overline{v'^2}$) appear in the depth averaged shallow water equations. The production term for each Reynolds stress will be split into an horizontal 2D production ($P_{uu,H}, P_{vv,H}, P_{uv,H}$) and a vertical production due to the bed friction ($P_{uu,V}, P_{vv,V}, P_{uv,V}$). Assuming that the vertical velocity is much smaller than the horizontal one, the expressions for each production term are given by:

$$\begin{aligned}
P_{uu} &= P_{uu,H} + P_{uu,V} = -2\overline{u'^2}\frac{\partial U}{\partial x} - 2\overline{u'v'}\frac{\partial U}{\partial y} + P_{uu,V} \\
P_{vv} &= P_{vv,H} + P_{vv,V} = -2\overline{u'v'}\frac{\partial V}{\partial x} - 2\overline{v'^2}\frac{\partial V}{\partial y} + P_{vv,V} \\
P_{ww} &= 0 \\
P_{uv} &= P_{uv,H} + P_{uv,V} = -\overline{u'^2}\frac{\partial V}{\partial x} - \overline{u'v'}\left(\frac{\partial U}{\partial x} + \frac{\partial V}{\partial y}\right) - \overline{v'^2}\frac{\partial U}{\partial y} + P_{uv,V}
\end{aligned} \tag{2.94}$$

Since the vertical velocity is assumed to be negligible, the production of $\overline{w'^2}$ is zero ($P_{ww} = 0$). The evaluation of the terms $P_{uu,V}, P_{vv,V}, P_{uv,V}$, which account for the production due to vertical shear, will be treated later on in this section. Instead of using the Boussinesq eddy viscosity approximation, in the ASM the production of turbulent kinetic energy is computed directly from the Reynolds stresses as:

$$\begin{aligned}
P_k &= \frac{P_{uu} + P_{vv} + P_{ww}}{2} \\
&= -\overline{u'^2}\frac{\partial U}{\partial x} - \overline{u'v'}\left(\frac{\partial U}{\partial y} + \frac{\partial V}{\partial x}\right) - \overline{v'^2}\frac{\partial V}{\partial y} + \frac{P_{uu,V} + P_{vv,V}}{2}
\end{aligned} \tag{2.95}$$

Introducing Equations 2.94 and 2.95 into the algebraic expressions for the Reynolds stresses (Equation 1.28) yields:

$$\begin{aligned}
\overline{u'v'} &= \frac{k}{\varepsilon}\frac{(1-c_2)}{c_{11}}\left(-\overline{u'^2}\frac{\partial V}{\partial x} - \overline{v'^2}\frac{\partial U}{\partial y} - \overline{u'v'}\frac{\partial U}{\partial x} - \overline{u'v'}\frac{\partial V}{\partial y} + P_{uv,V}\right) \\
\overline{u'^2} &= \frac{2}{3}k + \frac{k}{\varepsilon}\frac{(1-c_2)}{c_{11}}\left(-\frac{4}{3}\overline{u'^2}\frac{\partial U}{\partial x} - \frac{4}{3}\overline{u'v'}\frac{\partial U}{\partial y} + \frac{2}{3}\overline{v'^2}\frac{\partial V}{\partial y} + \frac{2}{3}\overline{u'v'}\frac{\partial V}{\partial x} + \frac{2}{3}P_{uu,V} - \frac{1}{3}P_{vv,V}\right) \\
\overline{v'^2} &= \frac{2}{3}k + \frac{k}{\varepsilon}\frac{(1-c_2)}{c_{11}}\left(-\frac{4}{3}\overline{v'^2}\frac{\partial V}{\partial y} - \frac{4}{3}\overline{u'v'}\frac{\partial V}{\partial x} + \frac{2}{3}\overline{u'^2}\frac{\partial U}{\partial x} + \frac{2}{3}\overline{u'v'}\frac{\partial U}{\partial y} + \frac{2}{3}P_{vv,V} - \frac{1}{3}P_{uu,V}\right)
\end{aligned} \tag{2.96}$$

with the constants:

$$c_1 = 1.8 \qquad c_2 = 0.6 \qquad c_{11} = c_1 + \frac{P_k}{\varepsilon} - 1 \tag{2.97}$$

The system of equations 2.105 can be written in matrix form as:

$$\begin{pmatrix} \overline{u'^2} \\ \overline{v'^2} \\ \overline{u'v'} \end{pmatrix} = \frac{1-c_2}{c_{11}}\frac{k}{\varepsilon} \begin{pmatrix} a_{11} & a_{12} & a_{13} \\ a_{21} & a_{22} & a_{23} \\ a_{31} & a_{32} & a_{33} \end{pmatrix} \begin{pmatrix} \overline{u'^2} \\ \overline{v'^2} \\ \overline{u'v'} \end{pmatrix} + \begin{pmatrix} b_1 \\ b_2 \\ b_3 \end{pmatrix} \tag{2.98}$$

with the coefficients a_{ij} and b_i equal to:

$$\begin{aligned} a_{11} &= -\frac{4}{3}\frac{\partial U}{\partial x} & a_{12} &= \frac{2}{3}\frac{\partial V}{\partial y} & a_{13} &= -\frac{4}{3}\frac{\partial U}{\partial y} + \frac{2}{3}\frac{\partial V}{\partial x} \\ a_{21} &= \frac{2}{3}\frac{\partial U}{\partial x} & a_{22} &= -\frac{4}{3}\frac{\partial V}{\partial y} & a_{23} &= -\frac{4}{3}\frac{\partial V}{\partial x} + \frac{2}{3}\frac{\partial U}{\partial y} \\ a_{31} &= -\frac{\partial V}{\partial x} & a_{32} &= -\frac{\partial U}{\partial y} & a_{33} &= -\left(\frac{\partial U}{\partial x} + \frac{\partial V}{\partial y}\right) \end{aligned} \tag{2.99}$$

$$\begin{aligned} b_1 &= \frac{2}{3}k + \frac{k}{\varepsilon}\frac{(1-c_2)}{c_{11}}\left(\frac{2}{3}P_{uu,V} - \frac{1}{3}P_{vv,V}\right) \\ b_2 &= \frac{2}{3}k + \frac{k}{\varepsilon}\frac{(1-c_2)}{c_{11}}\left(\frac{2}{3}P_{vv,V} - \frac{1}{3}P_{uu,V}\right) \\ b_3 &= \frac{k}{\varepsilon}\frac{(1-c_2)}{c_{11}}P_{uv,V} \end{aligned} \tag{2.100}$$

After simple algebraic manipulation, the system of equations 2.98 can be expressed as:

$$\left[c_{11}\mathbf{I} - (1-c_2)\frac{k}{\varepsilon}\mathbf{A}\right] \begin{pmatrix} \overline{u'^2} \\ \overline{v'^2} \\ \overline{u'v'} \end{pmatrix} = c_{11}\mathbf{b} \tag{2.101}$$

where $\mathbf{A}$ is a matrix whose elements are given by the expressions 2.99, and $\mathbf{b}$ is the vector given by expressions 2.100. The coefficient c_{11} is given by Equation 2.97. At this point two possibilities arise when computing the turbulent kinetic energy production P_k in Equation 2.97. The first option is to compute P_k with Equation 2.95. If this is done the system of equations 2.101 is non-linear, and an iterative procedure is needed to solve it. This leads to a more unstable numerical scheme, because the coupling between Reynolds stresses in very strong. The second possibility is

to compute P_k using the eddy viscosity assumption as:

$$P_k^{\nu_t} = 2\nu_t \left[\left(\frac{\partial U}{\partial x} \right)^2 + \frac{1}{2} \left(\frac{\partial U}{\partial y} + \frac{\partial V}{\partial x} \right)^2 + \left(\frac{\partial V}{\partial y} \right)^2 \right] + P_{kv} \tag{2.102}$$

with the eddy viscosity ν_t computed from the $k - \varepsilon$ model. With this choice, the system of equations 2.101 can be solved exactly without iterating, improving in this way the convergence of the numerical scheme. From now on it will be assumed that the turbulent kinetic energy production term in the coefficient c_{11} (Equation 2.97) is computed from Equation 2.102. The system of equations 2.101 can be written in tensorial form as:

$$m_{ij} r_j = c_{11} b_i \tag{2.103}$$

where r_j ($j = 1, 3$) are the horizontal Reynolds stresses ($\overline{u'^2}, \overline{v'^2}, \overline{u'v'}$), and the tensor m_{ij} is equal to:

$$m_{ij} = c_{11}\delta_{ij} - (1 - c_2)\frac{k}{\varepsilon} a_{ij} \tag{2.104}$$

The Reynolds stresses are obtained after solving the system of equations 2.103. It should be remarked that even if the Reynolds stresses $\overline{u'w'}, \overline{v'w'}$ and $\overline{w'^2}$ do not appear in the depth averaged shallow water equations, that does not mean that their value is assumed to be zero. These turbulent stresses can be evaluated from the general Equation 1.28 in a similar way as it has been done in this section for the horizontal stresses:

$$\begin{aligned}
\overline{u'w'} &= \frac{k}{\varepsilon}\frac{(1-c_2)}{c_{11}} \left(-\overline{u'w'}\frac{\partial U}{\partial x} - \overline{v'w'}\frac{\partial U}{\partial y} + P_{uw,V} \right) \\
\overline{v'w'} &= \frac{k}{\varepsilon}\frac{(1-c_2)}{c_{11}} \left(-\overline{u'w'}\frac{\partial V}{\partial x} - \overline{v'w'}\frac{\partial V}{\partial y} + P_{vw,V} \right) \\
\overline{w'^2} &= \frac{2}{3}k + \frac{k}{\varepsilon}\frac{(1-c_2)}{c_{11}} \left(+\frac{2}{3}\overline{u'^2}\frac{\partial U}{\partial x} + \frac{2}{3}\overline{u'v'}\frac{\partial U}{\partial y} + \frac{2}{3}\overline{u'v'}\frac{\partial V}{\partial x} + \frac{2}{3}\overline{v'^2}\frac{\partial V}{\partial y} - \frac{1}{3}P_{uu,V} - \frac{1}{3}P_{vv,V} \right)
\end{aligned} \tag{2.105}$$

2.5.2 Estimation of the vertical production due to bed friction

The only thing which remains to specify in the present model is the evaluation of the vertical production terms due to bed friction ($P_{uu,V}, P_{vv,V}, P_{uv,V}$). The vertical production of Reynolds stresses in Equation 2.94 is given by:

$$\begin{aligned}
&P_{uu,V} = -2\overline{u'w'}\frac{\partial \overline{u}}{\partial z} \qquad P_{vv,V} = -2\overline{v'w'}\frac{\partial \overline{v}}{\partial z} \qquad P_{ww,V} = 0 \\
&P_{uv,V} = -\overline{u'w'}\frac{\partial \overline{v}}{\partial z} - \overline{v'w'}\frac{\partial \overline{u}}{\partial z} \qquad P_{uw,V} = -\overline{w'^2}\frac{\partial \overline{u}}{\partial z} \qquad P_{vw,V} = -\overline{w'^2}\frac{\partial \overline{v}}{\partial z}
\end{aligned} \tag{2.106}$$

Since the production of $\overline{w'^2}$ is zero, all the generation of turbulent energy is distributed on the horizontal Reynolds stresses $\overline{u'^2}$ and $\overline{v'^2}$. Hence, the vertical production of k is given by:

$$P_{kv} = \frac{P_{uu,V} + P_{vv,V}}{2} \tag{2.107}$$

It should be noticed that even if the production of $\overline{w'^2}$ is zero, this does not mean that its value is zero, since the algebraic expressions 1.28 account for pressure-strain distribution between the normal stresses.

In order to approximate the three vertical production terms ($P_{uu,V}, P_{vv,V}, P_{uv,V}$), uniform channel flow conditions will be assumed. Under these flow conditions the vertical velocity, as well as the horizontal velocity gradients, are zero ($\overline{w} = 0$, $\dfrac{\partial}{\partial x} = \dfrac{\partial}{\partial y} = 0$), and all the production of turbulence is due to vertical shear created by bed friction. A horizontal rotation of the reference coordinate system will be considered, in such a way that in the new coordinate system the transverse velocity is zero ($\overline{v}' = 0$). The relation between the horizontal velocities in both coordinate systems is given by a horizontal rotation of α degrees as:

$$\begin{pmatrix} \overline{u} \\ \overline{v} \\ \overline{w} \end{pmatrix} = \mathbf{N}^T \begin{pmatrix} \overline{u}' \\ \overline{v}' \\ \overline{w}' \end{pmatrix} \tag{2.108}$$

where $\mathbf{N}^T$ is the transposed of the rotation matrix $\mathbf{N}$:

$$\mathbf{N} = \begin{pmatrix} \cos\alpha & -\sin\alpha & 0 \\ \sin\alpha & \cos\alpha & 0 \\ 0 & 0 & 1 \end{pmatrix} \tag{2.109}$$

In a similar way, the relation between the turbulent stresses is obtained by a horizontal rotation of the Reynolds stress tensor as:

$$\mathbf{T} = \mathbf{N}^T \mathbf{T}' \mathbf{N} \qquad\qquad t_{ij} = n_{ki} t'_{kl} n_{lj} \tag{2.110}$$

where $\mathbf{T}$ and $\mathbf{T}'$ are the Reynolds stress tensors in both coordinate systems:

$$\mathbf{T} = \begin{pmatrix} t_{11} & t_{12} & t_{13} \\ t_{21} & t_{22} & t_{23} \\ t_{31} & t_{32} & t_{33} \end{pmatrix} = \begin{pmatrix} \overline{u'^2} & \overline{u'v'} & \overline{u'w'} \\ \overline{u'v'} & \overline{v'^2} & \overline{v'w'} \\ \overline{u'w'} & \overline{v'w'} & \overline{w'^2} \end{pmatrix} \tag{2.111}$$

The main property of the new reference system is that the transverse velocity vanishes ($\overline{v}' = 0$),

and as a consequence the turbulent stress t'_{23} also vanishes:

$$t'_{23} = \frac{k}{\varepsilon}\frac{1-c_2}{c_{11}}\left(-\overline{w'^2}\frac{\partial \overline{v}'}{\partial z}\right) = 0 \tag{2.112}$$

Considering this property, the vertical production of $\overline{u'^2}$ can be computed as:

$$\begin{aligned} P_{uu,V} &= -2t_{13}\frac{\partial \overline{u}}{\partial z} = -2\left(\cos\alpha, \sin\alpha, 0\right)\mathbf{T}'\begin{pmatrix}0\\0\\1\end{pmatrix}\left(\frac{\partial \overline{u}'}{\partial z}\cos\alpha + \frac{\partial \overline{v}'}{\partial z}\sin\alpha\right) \\ &= -2\left(\cos\alpha, \sin\alpha, 0\right)\begin{pmatrix}t'_{13}\\t'_{23}\\t'_{33}\end{pmatrix}\frac{\partial \overline{u}'}{\partial z}\cos\alpha \\ &= -2t'_{13}\frac{\partial \overline{u}'}{\partial z}\cos^2\alpha \end{aligned} \tag{2.113}$$

In a similar way, the vertical productions of $\overline{v'^2}$ and $\overline{u'v'}$ are obtained as:

$$\begin{aligned} P_{vv,V} &= -2t_{23}\frac{\partial \overline{v}}{\partial z} &&= -2t'_{13}\frac{\partial \overline{u}'}{\partial z}\sin^2\alpha \\ P_{uv,V} &= -t_{13}\frac{\partial \overline{v}}{\partial z} - t_{23}\frac{\partial \overline{u}}{\partial z} &&= 2t'_{13}\frac{\partial \overline{u}'}{\partial z}\sin\alpha\cos\alpha \end{aligned} \tag{2.114}$$

From Equations 2.107, 2.113 and 2.114, the vertical production of turbulent kinetic energy is equal to:

$$P_{kv} = \frac{P_{uu,V} + P_{vv,V}}{2} = -t'_{13}\frac{\partial \overline{u}'}{\partial z} \tag{2.115}$$

Using Equation 2.115 in Equations 2.113 and 2.114 yields:

$$\begin{aligned} P_{uu,V} &= 2P_{kv}\cos^2\alpha \\ P_{vv,V} &= 2P_{kv}\sin^2\alpha \\ P_{uv,V} &= -2P_{kv}\sin\alpha\cos\alpha \end{aligned} \tag{2.116}$$

The production of turbulent kinetic energy due to bed friction will be approximated for uniform channel flow in the same way as it has been done in section 2.4.5:

$$P_{kv} = \frac{|\mathbf{U}|u_f^2}{h} \tag{2.117}$$

Finally the vertical production terms are evaluated as:

$$P_{uu,V} = 2\frac{u_f^2 q_x^2}{h^3|\mathbf{U}|} \qquad P_{vv,V} = 2\frac{u_f^2 q_y^2}{h^3|\mathbf{U}|} \qquad P_{uv,V} = -2\frac{u_f^2 q_x q_y}{h^3|\mathbf{U}|} \tag{2.118}$$

2.5.3 Realizability condition in the ASM

In section 2.4.5 a realizability condition over the eddy viscosity was presented in order to avoid the prediction of negative turbulent stresses by the eddy viscosity models. With the ASM a realizability condition is also needed, since there is nothing in the equations of the model which assures that the normal Reynolds stresses will remain positive. Hence, the following restrictions should be imposed in the model:

$$\overline{u'^2} \geq 0 \qquad \overline{v'^2} \geq 0 \qquad \overline{u'^2} + \overline{v'^2} \leq 2k \tag{2.119}$$

The third condition in Equation 2.119 assures that the vertical normal stress $\overline{w'^2}$ remains positive, and avoids excessively large values of the horizontal normal stresses. If any of the normal stresses is negative its value is set to zero. At the same time, in order to keep constant the total turbulent kinetic energy, it is necessary to subtract from the other normal stresses the same amount of energy. This is done, for the stress $\overline{u'^2}$, in the following way:

$$\text{If} \quad \overline{u'^2} = -a^2 < 0 \quad \text{then} \quad \begin{cases} \overline{u'^2} = & 0 \\ \overline{v'^2} = & \overline{v'^2} - a^2 \dfrac{\overline{v'^2}}{\overline{v'^2} + \overline{w'^2}} \\ \overline{w'^2} = & \overline{w'^2} - a^2 \dfrac{\overline{w'^2}}{\overline{v'^2} + \overline{w'^2}} \end{cases} \tag{2.120}$$

It is straightforward to show that using the expressions 2.120 the turbulent kinetic energy is kept constant after imposing the realizability condition. A simple way to implement the realizability condition in the numerical solver is to define the following ratios:

$$R_u = \frac{2k}{2k - \overline{u'^2}} \qquad R_v = \frac{2k}{2k - \overline{v'^2}} \qquad R_w = \frac{2k}{2k - \overline{w'^2}} \tag{2.121}$$

and to recompute the Reynolds stresses as:

$$\begin{aligned} \overline{u'^2} &= \max\{0, \min(\overline{u'^2}, R_v\overline{u'^2}, R_w\overline{u'^2})\} \\ \overline{v'^2} &= \max\{0, \min(\overline{v'^2}, R_u\overline{v'^2}, R_w\overline{v'^2})\} \end{aligned} \tag{2.122}$$

2.5.4 Uniform channel flow

By uniform channel flow we consider the flow in the centre region of a infinitely wide rectilinear channel with constant bed slope. The depth averaged velocity field is given by:

$$U = cte \qquad V = 0 \qquad \frac{\partial}{\partial x} = 0 \qquad \frac{\partial}{\partial y} = 0 \tag{2.123}$$

Under these flow conditions the vertical production of Reynolds stresses is given by:

$$P_{uu,V} = 2P_{kv} \qquad P_{vv,V} = 0 \qquad P_{uv,V} = 0 \qquad P_{kv} = \frac{|U|u_f^2}{h} \tag{2.124}$$

In uniform channel flow the turbulent kinetic energy equation reduces to:

$$P_{kv} = \varepsilon \tag{2.125}$$

and thus, from Equation 2.97, $c_{11} = c_1$. Since all the spatial derivatives vanish, the matrix **A** (Equation 2.99) is an empty matrix, and the solution of the system of equations 2.101 is given by:

$$\begin{aligned} \overline{u'^2} &= \frac{2}{3}k + \frac{k}{\varepsilon}\frac{(1-c_2)}{c_1}\frac{4}{3}P_{kv} \\ \overline{v'^2} &= \frac{2}{3}k - \frac{k}{\varepsilon}\frac{(1-c_2)}{c_1}\frac{2}{3}P_{kv} \\ \overline{u'v'} &= 0 \end{aligned} \tag{2.126}$$

As it should be expected, the largest turbulent stress is $\overline{u'^2}$. If the Boussinesq assumption was used, the three normal turbulent stresses would be equal. It should be noticed that the realizability condition is needed in order to avoid negative values of $\overline{v'^2}$ when the vertical production of turbulent energy is too high.

2.5.5 Boundary layer flow

Near the walls of a channel, the main gradients occur in the normal direction to the wall. If the wall is long enough and the flow is fully developed, the flow field can be approximated by:

$$U = U(y) \qquad V = 0 \qquad \frac{\partial}{\partial x} = 0 \tag{2.127}$$

where U is the velocity component parallel to the wall, V is the velocity normal to the wall, x is the longitudinal direction and y is the normal direction to the wall. Under these flow conditions the vertical turbulence production terms are given, as well as in uniform channel flow, by

Equation 2.124. In this case the matrix $\mathbf{M}$ and the vector $\mathbf{b}$ reduce to:

$$\mathbf{M} = \begin{pmatrix} c_{11} & 0 & (1-c_2)\frac{k}{\varepsilon}\frac{4}{3}\frac{\partial U}{\partial y} \\ 0 & c_{11} & -(1-c_2)\frac{k}{\varepsilon}\frac{2}{3}\frac{\partial U}{\partial y} \\ 0 & (1-c_2)\frac{k}{\varepsilon}\frac{\partial U}{\partial y} & c_{11} \end{pmatrix} \quad \mathbf{b} = \begin{pmatrix} \frac{2}{3}k + \frac{k}{\varepsilon}\frac{(1-c_2)}{c_{11}}\frac{4}{3}P_{kv} \\ \frac{2}{3}k - \frac{k}{\varepsilon}\frac{(1-c_2)}{c_{11}}\frac{1}{3}P_{kv} \\ 0 \end{pmatrix} \quad (2.128)$$

and the Reynolds stresses predicted by the model for shallow water boundary layer flow are:

$$\begin{aligned} \overline{u'^2} &= \frac{c_{11}^3}{|\mathbf{M}|}b_1 + \frac{c_{11}}{|\mathbf{M}|}(1-c_2)^2\frac{k^2}{\varepsilon^2}\frac{2}{3}\left(\frac{\partial U}{\partial y}\right)^2 b_1 + \frac{c_{11}}{|\mathbf{M}|}(1-c_2)^2\frac{k^2}{\varepsilon^2}\frac{4}{3}\left(\frac{\partial U}{\partial y}\right)^2 b_2 \quad (2.129) \\ \overline{v'^2} &= \frac{c_{11}^3}{|\mathbf{M}|}b_2 \\ \overline{u'v'} &= -\frac{c_{11}^2}{|\mathbf{M}|}(1-c_2)\frac{k}{\varepsilon}\frac{\partial U}{\partial y}b_2 \end{aligned}$$

Again, considering that $b_1 > b_2$, the largest normal turbulent stress is $\overline{u'^2}$. If the Boussinesq assumption was used, all the normal turbulent stresses would be equal.

Part II

The Solver

Chapter 3

Numerical solver

3.1 Introduction

The finite volume method is probably the most commonly used numerical method in Computational Fluid Dynamics. The fact of using a conservative formulation, as well as the intuitive physical interpretation of the method, makes it adequate for solving differential equations for conservation laws, as it is the case in fluid dynamics.

In this chapter, after a brief presentation of the finite volume method, an unstructured finite volume solver for the depth averaged shallow water and $k-\varepsilon$ equations is presented. The schemes used, as well as their implementation in the numerical code are described in detail.

The solver is up to second order accurate in space and time. The first order upwind schemes of van Leer and Roe, as well as their second order extension, are used to discretise the convective flux in the shallow water equations. Both a centred and an upwind discretisation of the source terms have been implemented in the solver. Nevertheless, in all the practical applications an upwind discretisation of the bed slope term, and a centred discretisation of the diffusion term and bed friction terms have been used. A specific treatment of the wet-dry fronts is included in the solver, in order to be able to deal with the modelling of flooding and drying processes.

3.2 Numerical methods for the 2D shallow water equations

Several numerical methods exist for solving transport equations which involve convection and diffusion processes. An exhaustive review of all them is out of the scope of this brief introduction. Some of them are the finite volume, the finite element and the finite difference methods, the boundary elements method, the Galerkin-Discontinuous method and the Lagrangian particle method. From all them, the most used nowadays in fluid dynamics are the finite volume and the finite element methods. In order to illustrate briefly both methods, we will consider the scalar

equation $f(u;x,y) = 0$ defined over a 2D domain, where $u(x,y)$ is the unknown variable. Both finite element and finite volume can be considered as particular cases of the weak problem given by:

$$\int_D f(u;x,y) w_i(x,y)\, dA = 0 \qquad i = 1,n \tag{3.1}$$

where D is the spatial domain, and $w_i(x,y)$ are the weight functions.

The finite element method discretises the domain in nodes and elements, and uses a decomposition of the unknown variable $u(x,y)$ in shape functions $\phi_i(x,y)$ defined locally for each node:

$$u(x,y) = \sum_{i=1}^{n} u_i \phi_i(x,y) \tag{3.2}$$

where u_i is the value of $u(x,y)$ at each discrete node. If Equation 3.2 is inserted into Equation 3.1, a system of n equations with n unknowns u_i ($i = 1,n$) is obtained. Several formulations appear depending on the definition of both, the shape and the weight functions. For example, in the Galerkin methods the weight functions are equal to the shape functions. A complete description of the finite element method is given by Zienkiewicz [156], who is one of the first developers of the method. A description of the method applied to turbulent flows can be found in [48].

The formulation of the finite volume method can also be obtained from Equation 3.1, with a piecewise constant definition of the weight functions. The spatial domain is discretised in n cells C_i, or control volumes, where the value of the weight functions is defined as:

$$w_i(x,y) = \begin{cases} 1 & \text{if} \quad (x,y) \in C_i \\ 0 & \text{otherwise} \end{cases} \tag{3.3}$$

This formulation is specially suitable for conservation laws, in which the function $f(u;x,y)$ can be expressed as:

$$f(u;x,y) = \nabla \mathbf{F}(u;x,y) - G(u;x,y) \tag{3.4}$$

where $\mathbf{F}(u;x,y)$ is a vector which accounts for the convective flux in each of the spatial directions, and $G(u;x,y)$ includes any other terms. Introducing Equation 3.4 and the weight functions defined by Equation 3.3 into Equation 3.1, and applying the Gauss theorem, gives the integral form of the equation for the cell C_i:

$$\int_{L_i} \mathbf{F}(u;x,y)\mathbf{n}\, dL = \int_{C_i} G(u;x,y)\, dA \qquad i = 1,n \tag{3.5}$$

where L_i is the boundary of the cell C_i, and $\mathbf{n}$ is the outward normal vector to L_i. This is one of the biggest differences between finite volume and finite element methods. Finite volume works with the flux function $\mathbf{F}(u;x,y)$ in order to establish the conservation of mass and momentum over

each control volume C_i. For this reason it is a specially suitable method for solving conservation laws.

3.3 Finite volume methods for solving the 2D shallow water equations

As it has been said, the finite volume method is very suitable for solving problems involving conservation laws. For that reason, it is the method which has been used in the numerical solver developed in this thesis. Before presenting the specific schemes which have been implemented in the solver, a brief classification of the numerical schemes which are often used in finite volume methods is done in this section.

The main problem when solving a convection-diffusion equation is that a centred discretisation of the convection terms may give unstable schemes, the stability of the numerical method depending on the ratio between diffusive and convective forces. If diffusion dominates, the centred scheme is stable, but if convection is predominant, which is often the case, a centred discretisation is unstable. It should be noticed that the pure convection equation is unconditionally and intrinsically unstable, and thus, regardless of the numerical method used (finite volume, finite element, finite differences, ...), some kind of stabilisation technique is always necessary.

The most common stabilisation methods are the upwind schemes and the centred schemes with artificial diffusion. Both kind of methods can be reduced to the principle of adding an artificial diffusion term of enough magnitude to stabilise the convection term. Some well known centred schemes with artificial viscosity are the first order Lax-Friedrichs scheme and the second order MacCormack scheme. A family of upwind schemes widely used in the solution of hyperbolic conservation laws, as the shallow water equations, are the Godunov's methods, which solve or approximate a 1D Riemann problem at each volume face [133]. Briefly, a Riemann problem consists in solving a conservation equation with an initial condition given by two discontinuous constant states. In the finite volume case, each state depends on the solution in two adjacent control volumes. Two well known Godunov's upwind methods are the Roe's and Van Leer's schemes. The Godunov's schemes are very suitable for capturing shocks [134]. A detailed description of Godunov's methods is given by Toro [134] and Leveque [80, 79]. An attempt to improve the Godunov's methods is proposed by García-Navarro et al. [50], who propose a genuinely multidimensional upwinding method instead of solving a 1D problem in the normal direction to the cell faces.

The stabilisation procedure introduces a non-physical diffusion in the original equations. In order to minimise the error introduced in the numerical solution by this artificial diffusion, upwind discretisations of the source terms have been developed and used by several researchers [144, 51],

and well-balanced properties of the numerical schemes have been defined [101, 23].

Another characteristic of the numerical scheme which is common to any numerical method is the order of accuracy of the spatial and time discretisations. Special care should be taken in the stabilised methods when defining the accuracy of the scheme, due to the introduction of an artificial diffusion term which may modify the global order of accuracy.

Regarding the time discretisation, the numerical method may be explicit, implicit or semi-implicit. Explicit schemes are often used in time marching problems in which the time scales to be resolved are small, and thus, the CFL stability condition is not a great restriction. Fully implicit methods are rarely used in computational fluid dynamics, specially with high order upwind schemes, since the computational cost of solving a non-linear system at each time step is not worth. Alternatively, linearised semi-implicit methods may be used, where a linear system is solved at each time step. A simpler implementation is to implicit only the main diagonal of the coefficients matrix. In this way, it is not necessary to solve any system of equations at each time step, and at the same time the CFL restriction of the explicit scheme is relaxed.

Any of the previous numerical schemes applies to both structured and unstructured meshes. However, the numerical implementation is simpler in structured meshes, specially if a high order scheme is used. In structured meshes it is usual to find spatial discretisations up to third order accurate or even higher, while schemes higher than second order accurate are seldom found in unstructured meshes. Unstructured meshes can be easily adapted to complex geometries. This is a great advantage in environmental hydraulic engineering, where the complexity of the bathimetry and boundaries makes it worth to use a non-structured grid.

3.4 The finite volume method

3.4.1 Discretisation of the convection-diffusion equation

The convection-diffusion equation for a scalar variable w can be written in conservative form as:

$$\frac{\partial w}{\partial t} + \frac{\partial F_k}{\partial x_k}(w) = \frac{\partial}{\partial x_k}\left(\nu \frac{\partial w}{\partial x_k}\right) + G(\mathbf{x}, w) \tag{3.6}$$

where $F_k(w)$ is the k component of the convective flux (which is assumed here to depend only on the variable w), ν is the diffusivity coefficient, and $G(x_k, w)$ accounts for the source terms, which in general can depend on the spatial coordinates as well as on the variable w. The convection-diffusion equation can also be written in non-conservative form as:

$$\frac{\partial w}{\partial t} + c_k(w)\frac{\partial w}{\partial x_k} = \frac{\partial}{\partial x_k}\left(\nu \frac{\partial w}{\partial x_k}\right) + G'(\mathbf{x}, w) \tag{3.7}$$

where $c_k(w)$ is the convective velocity in the k direction ($F_k = c_k w$). In general, from a numerical point of view, it is preferred to work with the conservative form of the equations. It is straightforward to pass from the non-conservative form to the conservative form by introducing an additional source term. Equation 3.7 can be rewritten in conservative form as:

$$\frac{\partial w}{\partial t} + \frac{\partial}{\partial x_k}\left(c_k w\right) = \frac{\partial}{\partial x_k}\left(\nu \frac{\partial w}{\partial x_k}\right) + w\frac{\partial c_k}{\partial x_k} + G' \tag{3.8}$$

Identifying terms in Equations 3.6 and 3.8 yields:

$$G = G' + w\frac{\partial c_k}{\partial x_k} \tag{3.9}$$

From now on, the conservative formulation will be used in order to illustrate the finite volume method. The time discretisation of Equation 3.6 reads:

$$\frac{w^{n+1} - w^n}{\Delta t} + \frac{\partial F_k}{\partial x_k} = \frac{\partial}{\partial x_k}\left(\nu \frac{\partial w}{\partial x_k}\right) + G \tag{3.10}$$

where w^n is the value of the conservative variables at time t^n. The convection and source terms may be evaluated at time t^n (first order explicit scheme), t^{n+1} (first order implicit scheme), $t^{n+1/2}$ (second order implicit scheme), or any other intermediate time.

The spatial domain is discretised in grid cells (or intervals in one dimension) with an arbitrary geometry. Each cell is represented by a node. Integration of Equation 3.10 over a cell C_i gives:

$$\int_{C_i} \frac{w^{n+1} - w^n}{\Delta t}\, dA + \int_{C_i} \frac{\partial F_k}{\partial x_k}\, dA = \int_{C_i} \frac{\partial}{\partial x_k}\left(\nu \frac{\partial w}{\partial x_k}\right) dA + \int_{C_i} G\, dA \tag{3.11}$$

Applying the Gauss theorem to the convective and diffusive flux integrals in Equation 3.11 yields:

$$A_i \frac{w_i^{n+1} - w_i^n}{\Delta t} + \int_{L_i} F_k \tilde{n}_k\, dL = \int_{L_i} \nu \frac{\partial w}{\partial x_k} \tilde{n}_k\, dL + \int_{C_i} G\, dA \tag{3.12}$$

where w_i^n is the mean value of w in the cell C_i at the time t_n, L_i is the boundary of the cell C_i, and $\tilde{n}_k$ (with $k = 1, 2$ in 2D) is the outward normal unit vector to the boundary L_i. In order to evaluate the second term in Equation 3.12, the integral of the normal flux $F_k \tilde{n}_k$ over the cell boundary is computed as a sum of integrals over the cell faces L_{ij}:

$$\int_{L_i} F_k \tilde{n}_k\, dL = \sum_{j \in K_i} \int_{L_{ij}} F_k \tilde{n}_k dL \tag{3.13}$$

where L_{ij} is the common face to the cells C_i and C_j, and K_i accounts for all the cells which share at least one face with the cell C_i. The main difference between finite volume schemes lies

in the way in which the flux over the cell faces is evaluated. The evaluation of the discrete flux brings about concepts such as: centred and upwind schemes, first and second order accuracy, TVD schemes, numerical diffusion, ... A detailed description of several schemes for computing the numerical flux in the shallow water equations can be found in [134, 133].

3.4.2 Upwind discretisation versus centred discretisation

As it has been said, if a centred discretisation is used for both the flux and source terms in the convection-diffusion equation, the numerical scheme may be unstable, and the numerical solution may show non-physical oscillations. One possible way to obtain a stable scheme is to account for the direction in which information propagates. This is the main idea which lies under the upwind schemes, which can be easily understood if the 1D convection-diffusion equation is written in a Lagrangian formulation as:

$$\frac{Dw}{Dt} = \frac{\partial w}{\partial t} + a\frac{\partial w}{\partial x} = G \tag{3.14}$$

where the diffusion term has been included in G. In Equation 3.14, a is defined as:

$$\frac{\partial F}{\partial x} = a\frac{\partial w}{\partial x} \tag{3.15}$$

It should be noticed that a equals c (see Equation 3.7) only if the flux is an homogeneous function, i.e. in the case that $F = \dfrac{\partial F}{\partial w}w$. From Equation 3.14, if the source term G is zero, the conservative variable w is constant along the characteristic line (surface in 2D, or volume in 3D), which (in 1D) is given by:

$$x = at \tag{3.16}$$

The fact that information propagates along the characteristic lines should be taken into account in the numerical scheme. Figure 3.1 shows the characteristic lines for the linear 1D convection equation without source terms. When the source terms appear in the equation, w is not constant along the characteristic lines any more, but the information continues being convected in the same directions. The diffusion term is usually considered as a source term, but it may also be considered as a flux term, in which case the characteristic lines would be modified.

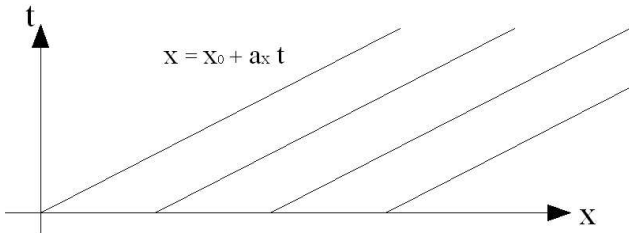

Figure 3.1: Characteristic lines for the 1D linear convection equation.

Upwind discretisation of the convective flux

One way to consider the direction in which information propagates is to evaluate the convection term in the upwind cell face, instead of evaluating it in the cell centre. In 1D, this would lead to the following scheme:

$$\left.\frac{\partial w}{\partial t}\right|_i + \left.\frac{\partial F}{\partial x}\right|_{i\mp 1/2} = G_i \tag{3.17}$$

where the convection term is evaluated at $x_{i-1/2}$ or at $x_{i+1/2}$ depending on the direction in which information propagates, which in 1D is given by the sign of a, as defined in Equation 3.15. In Equation 3.17, a centred discretisation of the source term has been used. The upwind discretisation of the source terms will be treated later on in this chapter. Assuming an equidistant mesh, and using the Taylor's expansion of $\dfrac{\partial F}{\partial x}$ over the point x_i in Equation 3.17, gives:

$$\left.\frac{\partial w}{\partial t}\right|_i + \left.\frac{\partial F}{\partial x}\right|_i - \text{sgn}(a)\frac{\Delta x}{2}\left.\frac{\partial^2 F}{\partial x^2}\right|_i = G_i \tag{3.18}$$

Using Equation 3.15, Equation 3.18 can be rewritten, omitting the subscript i, as:

$$\frac{\partial w}{\partial t} + \frac{\partial}{\partial x}\left(F - |a|\frac{\Delta x}{2}\frac{\partial w}{\partial x}\right) = G \tag{3.19}$$

Identifying terms in Equations 3.19 and 3.6, it is clear that the upwind discretisation of the convection term is equivalent to introducing a diffusion term, with a numerical viscosity ν_n equal to:

$$\nu_n = |a|\frac{\Delta x}{2} \tag{3.20}$$

Equation 3.19 can be discretised in terms of a numerical flux ϕ [57] as:

$$\frac{w_i^{n+1} - w_i^n}{\Delta t}\Delta x + \phi_{i+1/2} - \phi_{i-1/2} = G_i \Delta x \tag{3.21}$$

with the numerical flux $\phi_{i+1/2}$ defined as:

$$\phi_{i+1/2} = \underbrace{\frac{F_i + F_{i+1}}{2}}_{centred} - \underbrace{\nu_{n,i+1/2}\frac{w_{i+1} - w_i}{\Delta x}}_{upwind} \tag{3.22}$$

Upwind discretisation of the source term

It seems logical that, if an upwind discretisation of the convection term is done, the source term should also be treated with an upwind scheme, mainly for two reasons: first, because the physical perturbations introduced by the source term propagate along the characteristic lines, and thus, this should be reflected by the discretisation scheme. Second, because, as it has been shown,

when upwinding the convective flux a diffusion term is introduced in the original equation, which generates a source of error in the solution. The upwind discretisation of the source term should balance, at least in part, the numerical diffusion term, improving in this way the order of accuracy of the scheme [47]. Using an upwind scheme for both the convection and the diffusion terms, yields:

$$\left.\frac{\partial w}{\partial t}\right|_i + \left.\frac{\partial F}{\partial x}\right|_{i\mp 1/2} = G_{i\mp 1/2} \tag{3.23}$$

In a similar way as it has been done with the convective flux, Equation 3.23 can be rewritten using Taylor's polynomial over the point x_i as:

$$\left.\frac{\partial w}{\partial t}\right|_i + \left.\frac{\partial F}{\partial x}\right|_i - \text{sgn}(a)\frac{\Delta x}{2}\left.\frac{\partial^2 F}{\partial x^2}\right|_i = G_i - \text{sgn}(a)\frac{\Delta x}{2}\left.\frac{\partial G}{\partial x}\right|_i \tag{3.24}$$

Using the numerical flux ϕ (Equation 3.22), the discretisation of Equation 3.24 gives:

$$\frac{w_i^{n+1} - w_i^n}{\Delta t}\Delta x + \phi_{i+1/2} - \phi_{i-1/2} = G'_i \tag{3.25}$$

with:

$$G'_i = \underbrace{G_i}_{centred}\underbrace{-\frac{1}{2}\text{sgn}(a_{i+1/2})G_{i+1/2} + \frac{1}{2}\text{sgn}(a_{i-1/2})G_{i-1/2}}_{upwind} \tag{3.26}$$

The function $\text{sgn}(a)$ in Equation 3.26 has been evaluated at each cell face in order to obtain a conservative formulation of the upwind contribution. A conservative discretisation of the whole source term can be obtained if the centred contribution in Equation 3.26 is evaluated as an arithmetic average from the values at the cell faces, which yields:

$$G'_i = \frac{1}{2}\left(1 - \text{sgn}(a)_{i+1/2}\right)G_{i+1/2} + \frac{1}{2}\left(1 + \text{sgn}(a)_{i-1/2}\right)G_{i-1/2} \tag{3.27}$$

from where it is clear that for positive values of a, $G'_i = G_{i-1/2}$, while for negative values of a, $G'_i = G_{i+1/2}$.

3.4.3 Linear stability analysis for the 1D convection-diffusion equation

An important characteristic of any numerical scheme is its stability. Considering a linear 1D convective flux given by $F(w) = cw$ (where c is the constant convective velocity), and a constant diffusivity coefficient ν, Equation 3.6 reads:

$$\frac{\partial w}{\partial t} + c\frac{\partial w}{\partial x} = \nu\frac{\partial^2 w}{\partial x^2} \tag{3.28}$$

Centred discretisation

If an explicit centred discretisation of all the terms in Equation 3.28 is done, the discrete equation reads:

$$w_j^{n+1} = w_j^n - \frac{c\Delta t}{2\Delta x}(w_{j+1}^n - w_{j-1}^n) + \frac{\nu\Delta t}{(\Delta x)^2}(w_{j+1}^n - 2w_j^n + w_{j-1}^n) \tag{3.29}$$

Equation 3.29 can be written in general form as:

$$w_j^{n+1} \quad = a_j w_j^n + a_{j-1} w_{j-1}^n + a_{j+1} w_{j+1}^n \tag{3.30}$$

with the coefficients:

$$a_j = 1 - \frac{2\nu\Delta t}{(\Delta x)^2} \qquad a_{j-1} = \frac{c\Delta t}{2\Delta x} + \frac{\nu\Delta t}{(\Delta x)^2} \qquad a_{j+1} = -\frac{c\Delta t}{2\Delta x} + \frac{\nu\Delta t}{(\Delta x)^2} \tag{3.31}$$

In order to achieve numerical stability all the coefficients a_j, a_{j-1}, a_{j+1} must be positive. Hence, from the coefficient a_{j+1}, the following stability condition over the Peclet number (Pe) is obtained:

$$Pe = \frac{c\Delta x}{\nu} < 2 \tag{3.32}$$

Condition 3.32 is, in general, very restrictive over the spatial step Δx, and usually it is not fulfilled due to the small values of ν in practical calculations. It should be noticed that for $\nu = 0$ the scheme is unconditionally unstable. The fact of using an implicit scheme does not improve the numerical stability, since the coefficient a_{j+1} remains negative if the Peclet condition is not fulfilled.

Upwind discretisation of the convective flux

A way of obtaining a stable numerical scheme when the Peclet number is larger than 2, is to use an upwind discretisation of the convection term. Considering a centred discretisation of the diffusion term, the new numerical scheme is given by:

$$w_j^{n+1} = w_j^n - \frac{c\Delta t}{\Delta x}(w_j^n - w_{j-1}^n) + \frac{\nu\Delta t}{(\Delta x)^2}(w_{j+1}^n - 2w_j^n + w_{j-1}^n) \tag{3.33}$$

where it has been assumed a positive convective velocity ($c > 0$). The new coefficients in the general Equation 3.30 are:

$$a_j = 1 - \frac{c\Delta t}{\Delta x} - \frac{2\nu\Delta t}{(\Delta x)^2} \qquad a_{j-1} = \frac{c\Delta t}{\Delta x} + \frac{\nu\Delta t}{(\Delta x)^2} \qquad a_{j+1} = \frac{\nu\Delta t}{(\Delta x)^2} \tag{3.34}$$

The new stability condition over the time step is given by:

$$\Delta t < \frac{\Delta x}{c + \frac{2\nu}{\Delta x}} \qquad \text{CFL} < \frac{1}{1 + \frac{2\nu}{c\Delta x}} \tag{3.35}$$

The condition over the time step is more restrictive as the diffusivity coefficient ν increases. For $\nu = 0$ the Courant-Friedrich-Levy (CFL) condition is obtained [57].

As it has been shown in the previous section, the fact of using an upwind discretisation of the convection term is equivalent to introduce a diffusion term with a numerical viscosity ν_n equal to:

$$\nu_n = \frac{c\Delta x}{2} \tag{3.36}$$

The artificial viscosity guaranties that the Peclet number is smaller than 2, which is the stability condition for the convection-diffusion equation when a centred discretisation of all the terms is done. The magnitude of the artificial viscosity depends on the numerical scheme used.

Upwind discretisation of the diffusive flux

If an upwind discretisation is used for both the convection and the diffusion terms, the discrete convection-diffusion equation becomes:

$$w_j^{n+1} = w_j^n - \frac{c\Delta t}{\Delta x}(w_j^n - w_{j-1}^n) + \frac{\nu\Delta t}{(2\Delta x)^2}(w_{j+1}^n - w_j^n - w_{j-1}^n + w_{j-2}^n) \tag{3.37}$$

Now the time step condition for numerical stability is:

$$\Delta t < \frac{\Delta x}{c + \frac{\nu}{2\Delta x}} \qquad \text{CFL} < \frac{1}{1 + \frac{\nu}{2c\Delta x}} \tag{3.38}$$

which is somewhat less restrictive than condition 3.35, specially when the diffusivity coefficient ν is high. However, in this case there is another stability condition which limits the spatial step:

$$\Delta x > \frac{\nu}{2c} \qquad Pe > \frac{1}{2} \tag{3.39}$$

Condition 3.39 is not really important because in the case it is not fulfilled ($Pe < 1/2$) the centred scheme can be used for both, the convection and the diffusion terms.

Semi-implicit discretisation of the diffusive flux

No matter whether an upwind or centred discretisation of the diffusion term is done, if the diffusivity coefficient becomes very large the stability condition over the time step becomes very

restrictive. In order to relax the stability condition without additional computational cost, the main diagonal of the diffusive flux can be implicit, giving the following scheme:

$$\left(1+\frac{2\nu\Delta t}{(\Delta x)^2}\right)w_j^{n+1}=w_j^n-\frac{c\Delta t}{\Delta x}(w_j^n-w_{j-1}^n)+\frac{\nu\Delta t}{(\Delta x)^2}(w_{j+1}^n+w_{j-1}^n) \tag{3.40}$$

With this scheme the stability condition over the time step is the usual CFL condition:

$$\Delta t<\frac{\Delta x}{c} \qquad\qquad \text{CFL}<1 \tag{3.41}$$

3.5 Discretisation of the 2D shallow water equations

3.5.1 Discretisation of the spatial domain

Regarding to the discretisation of the spatial domain, the numerical meshes can be classified in two main groups: structured and unstructured. While the latter ones are more suitable for complex geometries, the former ones use simpler and usually higher order numerical algorithms.

Since the shallow water equations are often applied to environmental flow problems with very complex geometries, as rivers and estuaries, it is usually preferred to use unstructured meshes, which are easily adapted to uneven boundaries. On the other hand, more complex algorithms are needed in order to achieve a high order accuracy in space. The numerical schemes for unstructured meshes are usually at most second order accurate in space. In this thesis it has been decided to use unstructured meshes with first and second order upwind schemes.

The main characteristic of unstructured meshes is that the control volumes can have any geometric shape. There are several methodologies to build the numerical mesh. Most of them make use of a previous triangulation of the computational domain (Figure 3.2). The most straightforward approach is to use the original triangulation as the control volumes, and to place the cell nodes in the barycentre of each triangle (triangle-type control volumes). A second possibility is to place the nodes in the vertex of the triangles, and to build the control volumes using the medians of the original triangles. These volumes are known as vertex-type control volumes. The main inconvenience of this approach is that in irregular domains a boundary node may have associated two different normal vectors, as it is pointed out by Dervieux and Desideri in [37].

We will use another kind of control volumes which were introduced by Bermúdez et al. [11] in order to have always only one normal vector associated to each boundary node. The special characteristic of these volumes is that the nodes are placed in the edges of the original triangulation. For this reason they are called edge-type control volumes. This approach permits an easy definition of the normal vector to the boundary faces in irregular geometries. It permits also an easy implementation of the Dirichlet boundary conditions, since the nodes of the boundary cells

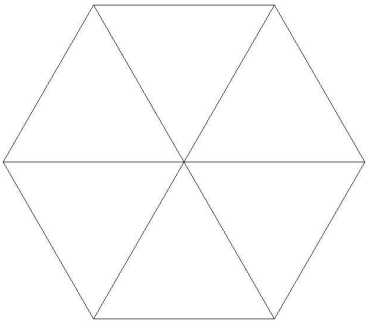

(a) Original triangular mesh

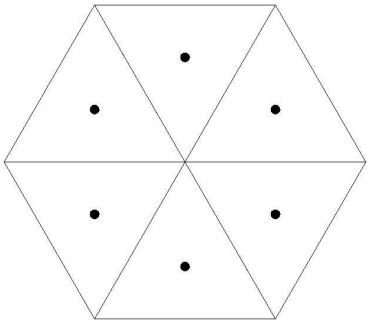

(b) Triangle-type volumes

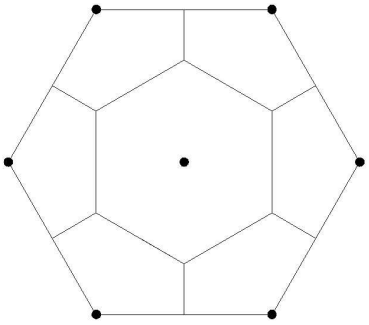

(c) Vertex-type volumes

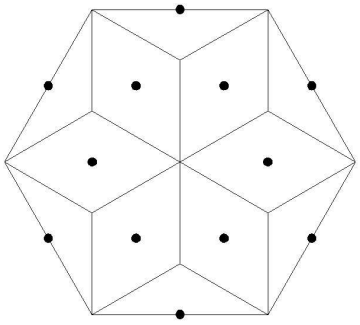

(d) Edge-type volumes

Figure 3.2: Several methods for the generation of control volumes from a triangular mesh.

are placed in the boundary edge. The following steps and definitions are used when creating the edge-type control volumes (Figure 3.3(a)):

- The mesh nodes are placed at the mid-point of the triangles edges.
- Each triangle is subdivided into 6 sub-triangles defined by the 3 medians.
- The cell C_i is formed by all the sub-triangles which have the node N_i as a vertex (4 sub-triangles in the inner nodes and 2 sub-triangles in the boundary nodes).
- The cell face L_{ij} is common to the cells C_i and C_j.
- The normal vector to the face L_{ij} will be addressed as $\mathbf{n}_{ij}$. It points from the node N_i to the node N_j, and it has the same length as the face L_{ij}. In the boundary faces it points outward the domain. The unit normal vector will be addressed as $\tilde{\mathbf{n}}_{ij}$.
- The vector $\mathbf{r}_{ij}$ links the nodes N_i and N_j. The distance between these nodes (d_{ij}) is given by its module ($d_{ij} = |\mathbf{r}_{ij}|$). Notice that the vectors $\mathbf{r}_{ij}$ and $\mathbf{n}_{ij}$ do not necessarily have the same direction.
- The distance $d_{\perp,ij}$ is defined as the projection of $\mathbf{r}_{ij}$ on to the normal direction to the face ($\tilde{\mathbf{n}}_{ij}$), i.e. $d_{\perp,ij} = \mathbf{r}_{ij} \cdot \tilde{\mathbf{n}}_{ij}$.

iar(1,L_{ij})	origin of the face (V)
iar(2,L_{ij})	end of the face (B)
iar(3,L_{ij})	node N_i
iar(4,L_{ij})	node N_j

Table 3.1: Pointer definition for face L_{ij} (see Figure 3.3(a)).

- Due to the way in which the control volumes are generated, the distance from the node N_i to the face L_{ij} is equal to $\frac{d_{\perp,ij}}{2}$.
- The sub-cell T_{ij} is defined as the sub-triangle N_iVB (see Figure 3.3(a)). Its area is given by $A_{T_{ij}} = \frac{|\mathbf{n}_{ij}|d_{\perp,ij}}{4}$.
- The ensemble of cells C_j which share one face with the cell C_i will be denoted by K_i.

The control volumes built in such a way have 4 faces except at the boundaries, where they have only 3 faces. As we are dealing with unstructured meshes, a pointer system is needed in order to store the information about the mesh topology. Since almost all quantities are computed by looping over cell faces, a pointer containing the information on the faces (iar(1:4,L_{ij})) is defined in Table 3.1.

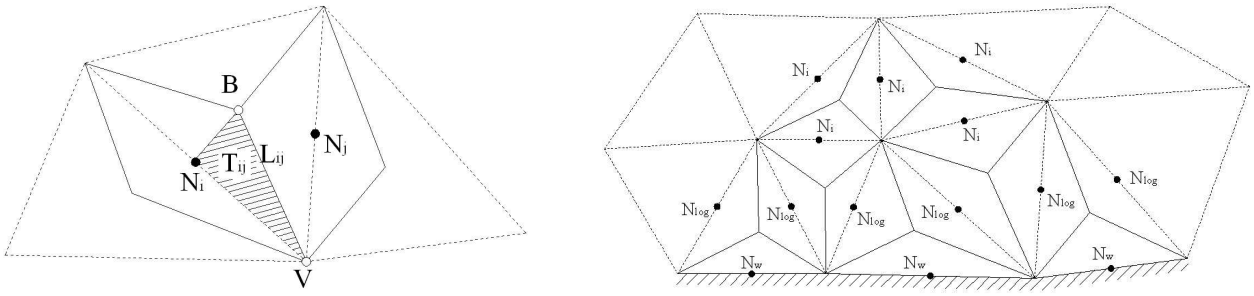

(a) Control volume construction (b) Node classification

Figure 3.3: Definition of edge-type volumes and node classification.

In order to treat the open and wall boundaries the nodes are classified in (Figure 3.3(b)): inner nodes (N_i), open boundary nodes (N_{ob}), wall boundary nodes (N_w) and log-law nodes (N_{log}). Each log-law node has associated only one wall node, while each wall node can be associated to several log-law nodes.

3.5.2 The 2D shallow water equations in conservative and vectorial form

The shallow water equations can be written either in conservative or non-conservative variables. An interesting property of working with conservative variables is the ability to compute shocks in the solution. This is very important if we consider that the solution of the shallow water equations

contains often very steep gradients in the water depth, either in the shape of hydraulic jumps or due to discontinuities in the bed elevation.

The depth averaged shallow water equations in conservative form read:

$$\frac{\partial h}{\partial t} + \frac{\partial q_j}{\partial x_j} = 0 \tag{3.42}$$

$$\frac{\partial q_i}{\partial t} + \frac{\partial}{\partial x_j}\left(\frac{q_i q_j}{h} + \frac{gh^2}{2}\delta_{ij}\right) = -gh\frac{\partial z_b}{\partial x_i} - \frac{\tau_{b,i}}{\rho} + \frac{\partial}{\partial x_j}\left(h\nu\frac{\partial U_i}{\partial x_j}\right) - \frac{\partial}{\partial x_j}\left(h < \overline{u_i' u_j'} >\right), \quad i = 1, 2$$

where the conservative variables are the water depth h, and the unit discharges $q_i = hU_i$ $(i = 1, 2)$. The bed elevation is given by z_b, $\tau_{b,i}$ $(i = 1, 2)$ is the bed friction, ν is the kinematic viscosity, and $< \overline{u_i' u_j'} >$ are the depth averaged horizontal Reynolds stresses. As it has been done in chapter 2, the symbols <> will be omitted for the sake of clarity in the notation. In Equation 3.42 it has been assumed that the Coriolis force and wind stress are negligible, and that the atmospheric pressure is constant in all the domain.

If the Boussinesq assumption is used to model the Reynolds stresses, the diffusive source terms (viscous and turbulent) can be written as:

$$\frac{\partial}{\partial x_j}\left(h\nu_e\frac{\partial U_i}{\partial x_j}\right) \tag{3.43}$$

where ν_e is the effective viscosity, which is defined as the eddy viscosity (ν_t) plus the kinematic viscosity (ν):

$$\nu_e = \nu_t + \nu \tag{3.44}$$

Equations 3.42 can be written in vectorial form as:

$$\frac{\partial \mathbf{w}}{\partial t} + \frac{\partial \mathbf{F_x}}{\partial x} + \frac{\partial \mathbf{F_y}}{\partial y} = \sum_{\mathrm{k}=1}^{3} \mathbf{G_k} \tag{3.45}$$

$$\mathbf{w} = \begin{pmatrix} h \\ q_x \\ q_y \end{pmatrix} \qquad \mathbf{F_x} = \begin{pmatrix} q_x \\ \frac{q_x^2}{h} + \frac{gh^2}{2} \\ \frac{q_x q_y}{h} \end{pmatrix} \qquad \mathbf{F_y} = \begin{pmatrix} q_y \\ \frac{q_x q_y}{h} \\ \frac{q_y^2}{h} + \frac{gh^2}{2} \end{pmatrix}$$

The vectors $\mathbf{F_x}$ and $\mathbf{F_y}$ account for the physical flux in the x and y directions. The vectors $\mathbf{G_k}$ (k $= 1, 3$), account respectively for the bed slope ($\mathbf{G_1}$), the bed friction ($\mathbf{G_2}$), and the turbulent

and viscous diffusion ($\mathbf{G_3}$):

$$\mathbf{G_1} = \begin{pmatrix} 0 \\ -gh\dfrac{\partial z_b}{\partial x} \\ -gh\dfrac{\partial z_b}{\partial y} \end{pmatrix} \qquad \mathbf{G_2} = \begin{pmatrix} 0 \\ -\dfrac{\tau_{b,x}}{\rho} \\ -\dfrac{\tau_{b,y}}{\rho} \end{pmatrix} \qquad \mathbf{G_3} = \begin{pmatrix} 0 \\ \dfrac{\partial}{\partial x_j}\left(\nu_e h\dfrac{\partial U_x}{\partial x_j}\right) \\ \dfrac{\partial}{\partial x_j}\left(\nu_e h\dfrac{\partial U_y}{\partial x_j}\right) \end{pmatrix} \tag{3.46}$$

The general expression for the bed friction $\tau_{b,j}$ is:

$$\tau_{b,j} = \rho c_f U_j |\mathbf{U}| \tag{3.47}$$

where c_f is the bed friction coefficient and $|\mathbf{U}|$ is the module of the velocity vector. Several expressions to evaluate c_f have been presented in chapter 2.

3.5.3 Hyperbolic character of the 2D shallow water equations

In order to study the mathematical character of the shallow water equations, the eigenvalues of the Jacobian matrix of the normal flux must be evaluated. In Equation 3.45 the vector fluxes $\mathbf{F_x}$ and $\mathbf{F_y}$ have been defined, which account for the convective flux in the x and y directions respectively. The total normal flux through a surface defined by the normal vector $\mathbf{n} = (n_x, n_y)$ is computed as:

$$\mathbf{Z} = \mathbf{F_x} n_x + \mathbf{F_y} n_y \tag{3.48}$$

where $\mathbf{Z}$ is the total normal flux to the surface. The length of the normal vector $\mathbf{n}$ is the same as the length of the surface. The Jacobian matrix of the normal flux ($\mathbf{A}$) is given by:

$$\mathbf{A} = \frac{\partial \mathbf{Z}}{\partial \mathbf{w}} = n_x \frac{\partial \mathbf{F_x}}{\partial \mathbf{w}} + n_y \frac{\partial \mathbf{F_y}}{\partial \mathbf{w}} = \tag{3.49}$$

$$= \begin{pmatrix} 0 & n_x & n_y \\ n_x\left(-\dfrac{q_x^2}{h^2} + gh\right) + n_y\left(-\dfrac{q_x q_y}{h^2}\right) & n_x\dfrac{2q_x}{h} + n_y\dfrac{q_y}{h} & n_y\dfrac{q_x}{h} \\ n_x\left(-\dfrac{q_x q_y}{h^2}\right) + n_y\left(-\dfrac{q_y^2}{h^2} + gh\right) & n_x\dfrac{q_y}{h} & n_x\dfrac{q_x}{h} + n_y\dfrac{2q_y}{h} \end{pmatrix}$$

It is straightforward to show that the three eigenvalues of the matrix $\mathbf{A}$ are given by:

$$\lambda_1 = n_x\frac{q_x}{h} + n_y\frac{q_y}{h} \qquad \lambda_2 = \lambda_1 + c\sqrt{n_x^2 + n_y^2} \qquad \lambda_3 = \lambda_1 - c\sqrt{n_x^2 + n_y^2} \tag{3.50}$$

where $c = \sqrt{gh}$ is the wave celerity. For positive water depths ($h > 0$), the three eigenvalues are real and different. In the limit case of zero water depth, the 3 eigenvalues are zero. Hence,

the shallow water equations as defined by Equation 3.45 are an hyperbolic system of conservative laws.

The eigenvectors of the Jacobian matrix $\mathbf{A}$ are given by:

$$\mathbf{v_1} = \begin{pmatrix} 0 \\ -\tilde{n}_y \\ \tilde{n}_x \end{pmatrix} \qquad \mathbf{v_2} = \begin{pmatrix} 1 \\ \frac{q_x}{h} + c\tilde{n}_x \\ \frac{q_y}{h} + c\tilde{n}_y \end{pmatrix} \qquad \mathbf{v_3} = \begin{pmatrix} 1 \\ \frac{q_x}{h} - c\tilde{n}_x \\ \frac{q_y}{h} - c\tilde{n}_y \end{pmatrix} \tag{3.51}$$

3.5.4 Discretisation of the equations

A finite volume solver with upwind discretisation in space has been used to solve Equation 3.45. The solver is explicit in time except for the viscous diagonal, which might be treated either implicitly or explicitly.

Time discretisation

The first order explicit discretisation of Equation 3.45 reads:

$$\frac{\mathbf{w}^{n+1} - \mathbf{w}^n}{\Delta t} + \frac{\partial \mathbf{F_x}}{\partial x}(\mathbf{w}^n) + \frac{\partial \mathbf{F_y}}{\partial y}(\mathbf{w}^n) = \sum_{\mathrm{k}=1}^{3} \mathbf{G_k}^n \tag{3.52}$$

where $\mathbf{w}^n$ is the value of the conservative variables at time t^n. The convective flux and source terms are evaluated at time t^n. The extension of the numerical scheme given by Equation 3.52 to second order in time is straightforward. Different time discretisations may be used. In the numerical solver, the second order in time has been implemented as follows. First, an intermediate state is computed at $t^{n+1/2}$ with a first order scheme:

$$\mathbf{w}^{n+1/2} = \mathbf{w}^n - \frac{\Delta t}{2}\left(\frac{\partial \mathbf{F_x}}{\partial x}(\mathbf{w}^n) + \frac{\partial \mathbf{F_y}}{\partial y}(\mathbf{w}^n)\right) + \frac{\Delta t}{2}\sum_{\mathrm{k}=1}^{3} \mathbf{G_k}^n \tag{3.53}$$

With the new intermediate variables $\mathbf{w}^{n+1/2}$, the flux and source terms are evaluated at $t^{n+1/2}$, and Equation 3.52 is integrated over one complete time step.

$$\mathbf{w}^{n+1} = \mathbf{w}^n - \Delta t\left(\frac{\partial \mathbf{F_x}}{\partial x}(\mathbf{w}^{n+1/2}) + \frac{\partial \mathbf{F_y}}{\partial y}(\mathbf{w}^{n+1/2})\right) + \Delta t\sum_{\mathrm{k}=1}^{3} \mathbf{G_k}^{n+1/2} \tag{3.54}$$

The time step is limited by the CFL condition which, accordingly to the stability analysis presented in section 3.4.3, has been implemented as:

$$\Delta t_i = \mathrm{CFL}\frac{d_i}{|\mathbf{U}|_i + \sqrt{g h_i}} \tag{3.55}$$

where $d_i = \dfrac{A_i}{P_i}$ is the ratio between the area A_i and the perimeter P_i on each cell C_i, and $|\mathbf{U}|_i$ is the module of the velocity vector at the node N_i.

In steady problems condition 3.55 is imposed locally at every node, which means that the time step varies between the different numerical cells in order to improve the convergence speed. In unsteady problems the condition over the time step is imposed globally in all the spatial domain, which means that the time step is the same in all the cells. In this case, in order to obtain global stability, the global time step is equal to the minimum local time step:

$$\Delta t_{unsteady} = \min(\Delta t_i) \tag{3.56}$$

The minimum time step can also be fixed directly by the user, but must always fulfil Equation 3.55.

Spatial discretisation

The integration of Equation 3.52 over a cell C_i gives:

$$\int_{C_i} \frac{\mathbf{w}^{n+1} - \mathbf{w}^n}{\Delta t}\, dA + \int_{C_i} \left(\frac{\partial \mathbf{F_x}}{\partial x} + \frac{\partial \mathbf{F_y}}{\partial y} \right)\, dA = \sum_{\mathrm{k}=1}^{3} \int_{C_i} \mathbf{G_k}\, dA \tag{3.57}$$

where the flux and source terms may be evaluated at t^n or $t^{n+1/2}$ depending on the order of accuracy of the time integration scheme. Applying the Gauss theorem to the convective flux integral in Equation 3.57 gives:

$$A_i \frac{\mathbf{w}_i^{n+1} - \mathbf{w}_i^n}{\Delta t} + \int_{L_i} (\mathbf{F_x}\tilde{n}_x + \mathbf{F_y}\tilde{n}_y)\, dL = \sum_{\mathrm{k}=1}^{3} \int_{C_i} \mathbf{G_k}\, dA \tag{3.58}$$

where $\mathbf{w}_i^n$ is the mean value of $\mathbf{w}$ in the cell C_i at the time t^n, L_i is the boundary of the cell C_i, and $\tilde{\mathbf{n}} = (\tilde{n}_x, \tilde{n}_y)$ is the unit normal vector to L_i. In order to evaluate the second term in Equation 3.58, the integral of the flux over the cell boundary is computed as a sum of integrals over the cell faces L_{ij}, as:

$$\int_{L_i} (\mathbf{F_x}\tilde{n}_x + \mathbf{F_y}\tilde{n}_y)\, dL = \sum_{j \in K_i} \int_{L_{ij}} (\mathbf{F_x}\tilde{n}_x + \mathbf{F_y}\tilde{n}_y)\, dL \tag{3.59}$$

where K_i accounts for all the cells C_j which share one face with the cell C_i. The main difference between numerical schemes lies on how the flux at the cell boundary is evaluated. The first order van Leer's and Roe's schemes, as well as their second order extensions, have been implemented in the numerical solver.

3.5.5 Discretisation of the convective flux

The numerical schemes which have been implemented in the solver belong to the group of upwind methods known as Godunov's methods, which either solve or approximate the solution of a unidimensional Riemann problem at each cell face. A Riemann problem is defined by a set of conservation laws with a discontinuous initial state. The solution permits computing the flux through the cell face. The exact solution of a Riemann problem needs an iterative procedure, which is computationally expensive. For this reason, approximate solutions are generally preferred. In this work the schemes of Roe and van Leer have been used. A detailed description of Riemann solvers for fluid dynamics is given by Toro in [133].

In the first order upwind schemes the left and right states of the Riemann problem are given by the value of the variables at the left and right nodes $\mathbf{w}_i$ and $\mathbf{w}_j$. In order to approximate the real flux $\mathbf{F}$ at the boundaries of the cell C_i, a numerical flux $\boldsymbol{\phi}$ is defined, being the convective flux in Equation 3.59 approximated as:

$$\int_{L_{ij}} (\mathbf{F}_\mathbf{x}\tilde{n}_x + \mathbf{F}_\mathbf{y}\tilde{n}_y)\ dL \approx \boldsymbol{\phi}_{ij}(\mathbf{w}_i, \mathbf{w}_j, \mathbf{n}_{ij}) \tag{3.60}$$

The numerical flux $\boldsymbol{\phi}_{ij}$ depends on the value of the conservative variables at the nodes on each side of the face, and on the normal vector to the face. It is computed at each cell face as:

$$\boldsymbol{\phi}_{ij}(\mathbf{w}_i, \mathbf{w}_j, \mathbf{n}_{ij}) = \underbrace{\frac{\mathbf{Z}(\mathbf{w}_i, \mathbf{n}_{ij}) + \mathbf{Z}(\mathbf{w}_j, \mathbf{n}_{ij})}{2}}_{centred} - \underbrace{\frac{1}{2}|\mathbf{Q}(\mathbf{w}_i, \mathbf{w}_j, \mathbf{n}_{ij})|(\mathbf{w}_j - \mathbf{w}_i)}_{upwind} \tag{3.61}$$

where the centred part is a second order approximation of the normal flux at the cell face, and the upwind part gives stability to the scheme (and accounts for the direction in which information propagates). Note that the definition of the normal flux $\mathbf{Z}$ (Equation 3.48) includes the length of the cell face, which is equal to the module of the normal vector ($|\mathbf{n}_{ij}|$).

The matrix $\mathbf{Q}$ is characteristic of each scheme. For the van Leer's and Roe's schemes it is defined as the Jacobian matrix of the normal flux, evaluated at a mean state ($\tilde{\mathbf{w}}_{ij}$) between nodes N_i and N_j:

$$\mathbf{Q}(\mathbf{w}_i, \mathbf{w}_j, \mathbf{n}_{ij}) = \mathbf{A}\,(\tilde{\mathbf{w}}_{ij}, \mathbf{n}_{ij}) \tag{3.62}$$

where $\mathbf{A}$ is the Jacobian matrix of the normal flux, given by Equation 3.49. The matrix $|\mathbf{Q}|$ in Equation 3.61 is obtained from $\mathbf{Q}$ as:

$$|\mathbf{Q}| = \mathbf{X}|\mathbf{D}|\mathbf{X}^{-1} \tag{3.63}$$

where $\mathbf{X}$ is the matrix formed by the eigenvectors of $\mathbf{Q}$, and $|\mathbf{D}|$ is a diagonal matrix formed by the absolute values of the eigenvalues of $\mathbf{Q}$. Considering the definition of $\mathbf{Q}$ in the schemes of van

Leer and Roe, the matrices $\mathbf{X}, \mathbf{X}^{-1}$ and $|\mathbf{D}|$ are given by:

$$|\mathbf{D}| = \begin{pmatrix} |\tilde{\lambda}_1| & 0 & 0 \\ 0 & |\tilde{\lambda}_2| & 0 \\ 0 & 0 & |\tilde{\lambda}_3| \end{pmatrix} \qquad \mathbf{X} = \begin{pmatrix} 0 & 1 & 1 \\ -\tilde{n}_y & \tilde{U}_x + \tilde{c}\tilde{n}_x & \tilde{U}_x - \tilde{c}\tilde{n}_x \\ \tilde{n}_x & \tilde{U}_y + \tilde{c}\tilde{n}_y & \tilde{U}_y - \tilde{c}\tilde{n}_y \end{pmatrix} \tag{3.64}$$

$$\mathbf{X}^{-1} = \frac{1}{2\tilde{c}} \begin{pmatrix} 2\tilde{c}(\tilde{U}_x\tilde{n}_y - \tilde{U}_y\tilde{n}_x) & -2\tilde{c}\tilde{n}_y & 2\tilde{c}\tilde{n}_x \\ \tilde{c} - \tilde{U}_x\tilde{n}_x - \tilde{U}_y\tilde{n}_y & \tilde{n}_x & \tilde{n}_y \\ \tilde{c} + \tilde{U}_x\tilde{n}_x + \tilde{U}_y\tilde{n}_y & -\tilde{n}_x & -\tilde{n}_y \end{pmatrix}$$

where all the variables are evaluated at the mean state $\tilde{\mathbf{w}}_{ij}$, which is defined by $(\tilde{h}, \tilde{q}_x, \tilde{q}_y, \tilde{c})$. The eigenvalues of $\mathbf{Q}$ are computed as:

$$\tilde{\lambda}_1 = n_x\tilde{U}_x + n_y\tilde{U}_y \qquad \tilde{\lambda}_2 = \tilde{\lambda}_1 + \tilde{c}\sqrt{n_x^2 + n_y^2} \qquad \tilde{\lambda}_3 = \tilde{\lambda}_1 - \tilde{c}\sqrt{n_x^2 + n_y^2} \tag{3.65}$$

The first order upwind van Leer's scheme

In the first order upwind van Leer's scheme [140] the mean state $\tilde{\mathbf{w}}_{ij}$ is given by the arithmetic average of $\mathbf{w}_i$ and $\mathbf{w}_j$, as:

$$\tilde{h} = \frac{h_i + h_j}{2} \qquad \tilde{c} = \sqrt{g\tilde{h}} \qquad \tilde{q}_x = \frac{q_{x,i} + q_{x,j}}{2} \qquad \tilde{q}_y = \frac{q_{y,i} + q_{y,j}}{2} \tag{3.66}$$

The first order upwind Roe's scheme

The scheme of Roe [118] solves an exact linearised Riemann problem at the cell interfaces. In order to do so, the mean state of Roe ($\tilde{\mathbf{w}}_{Roe}$) is chosen in such a way that the following expression is fulfilled:

$$\mathbf{F}_j - \mathbf{F}_i = \mathbf{A}\left(\tilde{\mathbf{w}}_{Roe}\right)\left(\mathbf{w}_j - \mathbf{w}_i\right) \tag{3.67}$$

It can be shown that, in order to verify Equation 3.67, the mean state of Roe is given by:

$$\tilde{h} = \sqrt{h_i h_j} \quad \tilde{c} = \sqrt{g\frac{h_i + h_j}{2}} \quad \tilde{U}_x = \frac{\sqrt{h_i}U_{x,i} + \sqrt{h_j}U_{x,j}}{\sqrt{h_i} + \sqrt{h_j}} \quad \tilde{U}_y = \frac{\sqrt{h_i}U_{y,i} + \sqrt{h_j}U_{y,j}}{\sqrt{h_i} + \sqrt{h_j}} \tag{3.68}$$

and $\tilde{q}_x = \tilde{h}\tilde{U}_x$. Notice that in this case $\tilde{c} \neq \sqrt{g\tilde{h}}$. As a consequence of fulfilling Equation 3.67, Roe's scheme has the property of computing exactly shocks when no source terms are present in the equations, being in those cases superior to van Leer's scheme.

Second order extension of van Leer's and Roe's schemes

Both van Leer's and Roe's schemes are first order accurate in space, since a piecewise constant distribution of the conservative variables is assumed when defining the Riemann's problem at each cell face. The approximate Riemann's problem solution given by Equations 3.61, 3.66 and 3.68, depends on the values of the conservative variables at the nodes N_i and N_j. A first order scheme is not enough to compute accurately the velocity profiles, since it introduces too much numerical diffusion.

In order to improve the accuracy of the scheme more nodes must be considered when computing the numerical flux on the cell faces. In structured meshes it is easy to obtain third order of accuracy or even more. On the other hand, in unstructured meshes more complex algorithms are required in order to obtain more than second order accuracy, since it is difficult to identify which cells should be used to approximate the cell boundary flux. Several schemes exist which permit to obtain second order accuracy. The scheme implemented in the numerical solver is based on a MUSCL (Monotonic Upstream Scheme for Conservation Laws) reconstruction of the conservative variables, using a slope limiter in order to control the total variation of the reconstructed field (Total Variation Diminishing schemes [80]).

The extrapolation of the conservative variables from the nodes to the cell faces is done as:

$$\begin{aligned} \mathbf{w}_{Ij} &= \mathbf{w}_i + \nabla \mathbf{w}_i \frac{\mathbf{r}_{ij}}{2} \\ \mathbf{w}_{iJ} &= \mathbf{w}_j - \nabla \mathbf{w}_j \frac{\mathbf{r}_{ij}}{2} \end{aligned} \tag{3.69}$$

where $\mathbf{w}_{Ij}$ is the extrapolated value of $\mathbf{w}_i$ to the cell face L_{ij}, $\mathbf{w}_{iJ}$ is the extrapolated value of $\mathbf{w}_j$ to the cell face L_{ij}, $\mathbf{r}_{ij}$ is the distance vector between the nodes N_i and N_j, and $\nabla \mathbf{w}$ is an approximation of the gradient of the conservative variables.

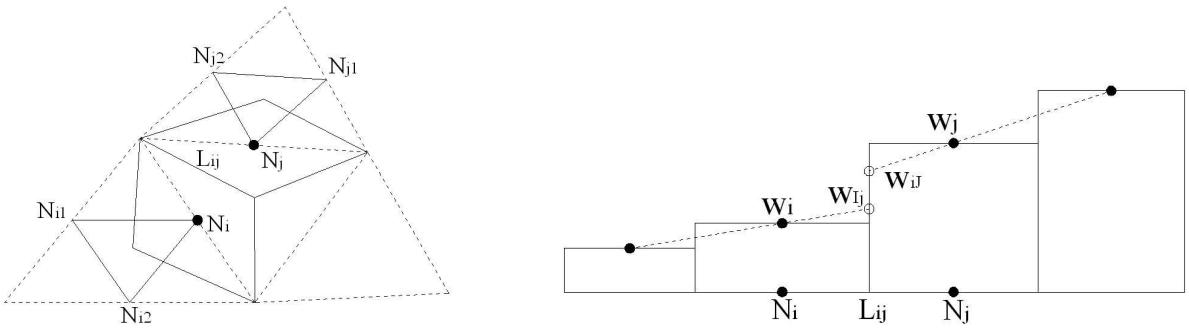

(a) Triangles used to compute the gradients.

(b) Linear extrapolation from nodes to faces.

Figure 3.4: Extrapolation of the conservative variables from the cell nodes to the cell faces in the second order scheme.

In order to keep the upwind character of the scheme, the gradient $\nabla \mathbf{w}_i$ is computed from the values of $\mathbf{w}$ at the nodes N_i, N_{i1}, N_{i2} (Figure 3.4). The way in which the gradient is computed is

described in section 3.5.6. Figure 3.4 shows schematically how the extrapolated face values are computed. In order to avoid under and over-shoots in regions with steep gradients, a limiter for the values of $\nabla \mathbf{w}_i \frac{\mathbf{r}_{ij}}{2}$ and $\nabla \mathbf{w}_j \frac{\mathbf{r}_{ij}}{2}$ in Equation 3.69 must be applied. In order to do so, Equation 3.69 is rewritten as:

$$\mathbf{w}_{Ij} = \mathbf{w}_i + \frac{1}{2}\boldsymbol{\Delta}_i^* \qquad\qquad \mathbf{w}_{iJ} = \mathbf{w}_j + \frac{1}{2}\boldsymbol{\Delta}_j^* \tag{3.70}$$

where $\boldsymbol{\Delta}_i^*$ and $\boldsymbol{\Delta}_j^*$ are the limited slopes [134] at the nodes N_i and N_j, which in the solver are computed as:

$$\boldsymbol{\Delta}_i^* = \begin{cases} \max\left[0,\, \min\left(\beta\nabla\mathbf{w}_i\mathbf{r}_{ij},\, \boldsymbol{\Delta}_{ij}\right),\, \min\left(\nabla\mathbf{w}_i\mathbf{r}_{ij},\, \beta\boldsymbol{\Delta}_{ij}\right)\right] & \text{if} \quad \boldsymbol{\Delta}_{ij} > 0 \\ \min\left[0,\, \max\left(\beta\nabla\mathbf{w}_i\mathbf{r}_{ij},\, \boldsymbol{\Delta}_{ij}\right),\, \max\left(\nabla\mathbf{w}_i\mathbf{r}_{ij},\, \beta\boldsymbol{\Delta}_{ij}\right)\right] & \text{if} \quad \boldsymbol{\Delta}_{ij} < 0 \end{cases} \tag{3.71}$$

with an analogous expression for $\boldsymbol{\Delta}_j^*$. In Equation (3.71), $\boldsymbol{\Delta}_{ij} = \mathbf{w}_j - \mathbf{w}_i$. The limited slopes computed from Equation (3.71) reproduce the Minmod limiter for $\beta = 1$ and the Superbee limiter for $\beta = 2$ [134]. The Superbee limiter has been used in all the second order simulations in this thesis, unless otherwise stated.

Finally, the extrapolated values $\mathbf{w}_{Ij}$ and $\mathbf{w}_{iJ}$ are used in Equation 3.61 instead of $\mathbf{w}_i$ and $\mathbf{w}_j$ in order to compute the numerical flux at the cell faces.

Regularisation of the eigenvalues

The numerical schemes of van Leer and Roe do not give the correct numerical flux at the cell faces when any of the eigenvalues given by Equation 3.65 is zero. Harten [57] proposed that in these situations the absolute value of the eigenvalues should be modified as:

$$|\lambda|_r = \begin{cases} |\lambda| & \text{if} \qquad |\lambda| > \epsilon \\ \dfrac{\lambda^2 + \epsilon^2}{2\epsilon} & \text{if} \qquad |\lambda| \leq \epsilon \end{cases} \tag{3.72}$$

where ϵ is any small value. Although other possible regularisations of the eigenvalues exist, Harten's regularisation has been the one used in this thesis, since it has been widely used and tested in many solvers providing very satisfactory results. In the numerical solver the value of ϵ has been set locally at each cell face as $\epsilon_{ij} = 0.1\sqrt{gh_{ij}}|\mathbf{n}_{ij}|$. Another possible definition of ϵ_{ij} is given by:

$$\epsilon_{ij} = \max\left[0,\, \tilde{\lambda}_{ij} - \lambda_i,\, \lambda_j - \tilde{\lambda}_{ij}\right] \tag{3.73}$$

where $\tilde{\lambda}_{ij}$ is the eigenvalue computed at the mean state between cells C_i and C_j (Equation 3.65), and λ_i, λ_j are the values of the eigenvalues at the nodes N_i and N_j.

It should be remarked that only the absolute value of the eigenvalues is modified in the numerical scheme, and therefore, it only affects the upwind part of the numerical flux in Equation 3.61.

3.5.6 Estimation of the gradient in a triangular mesh

In the second order extension of the van Leer's and Roe's schemes it is necessary to compute the gradient of the conservative variables ($\nabla \mathbf{w}$) on the associated triangular mesh. In order to do so, a shape function approach has been used. A transformation from real coordinates (x, y) to local coordinates (χ, η) is done in each triangle (Figure 3.5) using the shape functions $N_1(\chi,\eta), N_2(\chi,\eta), N_3(\chi,\eta)$. In this way, any variable w can be expressed in local coordinates as:

$$\begin{array}{c} w(\chi,\eta) = w_1 N_1(\chi,\eta) + w_2 N_2(\chi,\eta) + w_3 N_3(\chi,\eta) \\ N_1 = 1-\chi-\eta \qquad\qquad N_2 = \chi \qquad\qquad N_3 = \eta \end{array} \tag{3.74}$$

where w is any variable, w_1, w_2, w_3 are the values of w at each vertex of the triangle, and N_1, N_2, N_3 are the shape functions associated to each vertex.

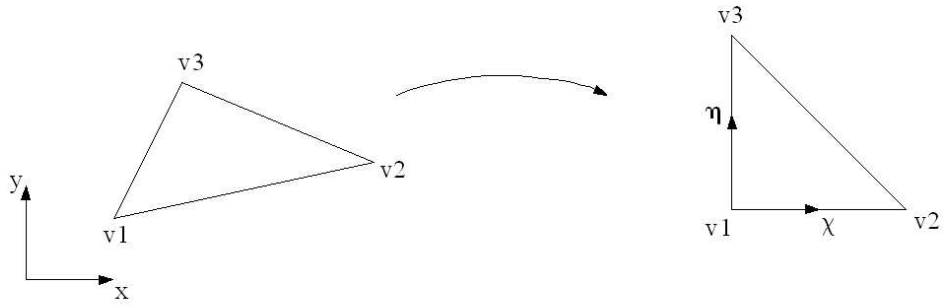

Figure 3.5: Local transformation of coordinates for the evaluation of spatial derivatives.

Using Equation 3.74 to obtain the relation between real and local coordinates yields:

$$\begin{pmatrix} x \\ y \end{pmatrix} = \begin{pmatrix} x_1 \\ y_1 \end{pmatrix} + \begin{pmatrix} x_2-x_1 & x_3-x_1 \\ y_2-y_1 & y_3-y_1 \end{pmatrix} \begin{pmatrix} \chi \\ \eta \end{pmatrix} \tag{3.75}$$

After some mathematical manipulation the gradient of w is obtained using expressions 3.74 and 3.75 as:

$$\begin{array}{rcl} \dfrac{\partial w}{\partial x} & = & \dfrac{w_1(y_2-y_3) + w_2(y_3-y_1) - w_3(y_2-y_1)}{(x_2-x_1)(y_3-y_1) - (x_3-x_1)(y_2-y_1)} \\ \dfrac{\partial w}{\partial y} & = & \dfrac{w_1(x_3-x_2) - w_2(x_3-x_1) + w_3(x_2-x_1)}{(x_2-x_1)(y_3-y_1) - (x_3-x_1)(y_2-y_1)} \end{array} \tag{3.76}$$

Equation 3.76 gives the gradient ∇w in the triangular mesh associated to the finite volume mesh. When the gradient is needed at the nodes of the finite volume mesh, it is simply computed as the average of the gradients in the two triangles to which the node belongs (Figure 3.6):

$$(\nabla w)_i = 0.5 \left((\nabla w)_{\underset{ij_1j_2}{\triangle}} + (\nabla w)_{\underset{ij_3j_4}{\triangle}} \right) \tag{3.77}$$

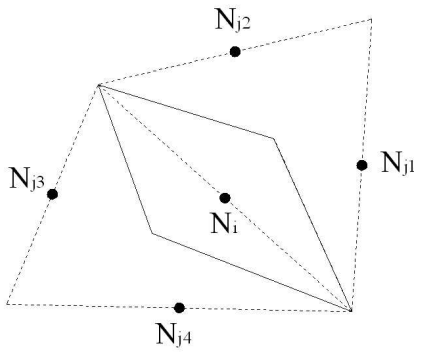

Figure 3.6: Nodes which contribute to the evaluation of the spacial derivatives at node N_i.

3.5.7 Discretisation of the bed slope source term

Traditionally, a centred scheme is generally used to discretise the source terms, as they do not present the stability problems which appear in the convective flux. However, after studying the discretisation of the bed slope source term, Bermúdez and Vázquez [10] showed the importance of using an upwind discretisation of that term in order to avoid non-physical oscillations in the solution. They showed that, in order to obtain the exact solution for hydrostatic flow, given by $q_x = q_y = 0$ and $z_s = h + z_b = cte$, it is necessary to discretise in a coherent manner the terms $gh\dfrac{\partial h}{\partial x}$ and $gh\dfrac{\partial z_b}{\partial x}$. Therefore, if the former one is upwinded with the convective flux, the latter one should also be upwinded. The upwind discretisation of the source terms has also been studied by other researchers [101, 23, 47].

In order to avoid an excessive number of subindices in the notation, in this section the bed slope term ($\mathbf{G_1}$ in Equation 3.46) will be addressed as $\mathbf{S}$.

Centred discretisation of the bed slope source term

If a centred discretisation is used, the bed slope source term is approximated at each node N_i as:

$$\mathbf{S}_i = \begin{pmatrix} 0 \\ -gh_i \left.\dfrac{\partial z_b}{\partial x}\right|_i \\ -gh_i \left.\dfrac{\partial z_b}{\partial y}\right|_i \end{pmatrix} \tag{3.78}$$

The gradient of the bed elevation at the cell nodes is computed as the mean value of the gradients in the two triangles to which the node belongs (Equation 3.77). The evaluation of the gradient in the triangular mesh is described in section 3.5.6. Other discretisations of the spatial gradients at the nodes may be used.

Upwind discretisation of the bed slope source term

One way in which the bed slope source term can be discretised in order to obtain the exact hydrostatic flow solution, is presented by Bermúdez and Vázquez in [10], and it is summarised below.

First, the integral of the source term over the cell C_i is divided in the sum of integrals over the sub-triangles T_{ij}, which have been defined in section 3.5.1 (Figure 3.3(a)). Each of the integrals over the sub-triangles is computed by means of a discrete source function $\boldsymbol{\psi}$, which gives the upwind character to the scheme. The discrete source function depends on the values of the variables at each side of the face, and on the normal vector to the face. The source term is then discretised as:

$$\mathbf{S}_i = \frac{1}{A_i}\int_{C_i} \mathbf{S}\, dA = \frac{1}{A_i}\sum_{j\in K_i}\int_{T_{ij}} \mathbf{S}\, dA \approx \frac{1}{A_i}\sum_{j\in K_i} A_{T_{ij}}\boldsymbol{\psi}_{ij}(\mathbf{w}_i, \mathbf{w}_j, \tilde{\mathbf{n}}_{ij}) \tag{3.79}$$

where $A_{T_{ij}} = \dfrac{d_{\perp,ij}|\mathbf{n}_{ij}|}{4}$ is the area of the sub-triangle T_{ij}, and $d_{\perp,ij}$ has been defined in section 3.5.1. Notice that $\boldsymbol{\psi}_{ij}$ depends on the unit normal vector $\tilde{\mathbf{n}}_{ij}$, while the numerical flux $\boldsymbol{\phi}_{ij}$ depends on $\mathbf{n}_{ij}$ (Equation 3.61), which includes the length of the face. The source functions $\boldsymbol{\psi}$ are evaluated in each sub-cell T_{ij} as:

$$\boldsymbol{\psi}_{ij}(\mathbf{w}_i, \mathbf{w}_j, \tilde{\mathbf{n}}_{ij}) = \left(\mathbf{I} - |\mathbf{Q}|_{ij}\mathbf{Q}_{ij}^{-1}\right)\tilde{\mathbf{S}}_{ij}^{BV} \tag{3.80}$$

where $\tilde{\mathbf{S}}_{ij}^{BV}$ is an approximation of the source term in the sub-cell T_{ij}, which depends on the variables $\mathbf{w}_i$ and $\mathbf{w}_j$. The matrices $|\mathbf{Q}|_{ij}$ and $\mathbf{Q}_{ij}^{-1}$ are evaluated at Roe's or van Leer's mean state $\tilde{\mathbf{w}}_{ij}$, i.e. $\mathbf{Q}_{ij}^{-1} = \mathbf{Q}^{-1}(\tilde{\mathbf{w}}_{ij})$ and $|\mathbf{Q}|_{ij} = |\mathbf{Q}|(\tilde{\mathbf{w}}_{ij})$. Notice that $|\mathbf{Q}|_{ij}\mathbf{Q}_{ij}^{-1} = \mathbf{X}_{ij}|\mathbf{D}|_{ij}\mathbf{D}_{ij}^{-1}\mathbf{X}_{ij}^{-1}$.

The expression proposed in [11] to compute $\tilde{\mathbf{S}}_{ij}^{BV}$ in order to obtain the exact hydrostatic solution is given by:

$$\tilde{\mathbf{S}}_{ij}^{BV} = -g\left(\frac{h_i + h_j}{2}\right)2\left(\frac{z_{b,j} - z_{b,i}}{d_{\perp,ij}}\right)\begin{pmatrix} 0 \\ \tilde{n}_{x,ij} \\ \tilde{n}_{y,ij}\end{pmatrix} \tag{3.81}$$

It will be shown later on in this section that with this definition of the bed slope the steady hydrostatic solution is computed exactly.

In the same line Fernández [47] shows the convenience of using an upwind discretisation of the source terms in order to improve the order of accuracy of the numerical scheme, and proposes a general way to upwind the source terms in 2D unstructured meshes, which is summarised here. The main idea is that the error introduced when upwinding the convection term should be balanced by a correction term in the discretisation of the source term. For the specific definition of the numerical flux given by Equation 3.61, the upwind source discretisation proposed in [47] reduces to:

$$\mathbf{S}_i = \mathbf{S}_i^C - \frac{1}{A_i}\sum_{j\in K_i}\frac{d_{\perp,ij}}{2}|\mathbf{n}_{ij}||\mathbf{Q}|_{ij}\mathbf{Q}_{ij}^{-1}\tilde{\mathbf{S}}_{ij}^{F} \tag{3.82}$$

where $\mathbf{S}_i$ is the upwind discretisation of the source term, $\mathbf{S}_i^C$ is a centred discretisation of the source term in the cell C_i, A_i is the area of the cell C_i, and $\tilde{\mathbf{S}}_{ij}^F$ is a centred approximation of the source term at the cell face. Notice the analogy between expression 3.82 and expression 3.25, which was presented in section 3.4 for the 1D case. In the case of the bed slope source term, and again for the specific definition of the numerical flux given by Equation 3.61, the proposed expressions in [47] for evaluating $\mathbf{S}_i^C$ and $\tilde{\mathbf{S}}_{ij}^F$ are:

$$\begin{aligned} \mathbf{S}_i^C &= -g\frac{1}{A_i}\sum_{j\in K_i}\frac{|\mathbf{n}_{ij}|}{2}\frac{h_i+h_j}{2}\left(z_{b,j}-z_{b,i}\right)\begin{pmatrix}0\\ \tilde{n}_{x,ij}\\ \tilde{n}_{y,ij}\end{pmatrix} \\ \tilde{\mathbf{S}}_{ij}^F &= -g\frac{h_i+h_j}{2}\frac{z_{b,j}-z_{b,i}}{d_{\perp,ij}}\begin{pmatrix}0\\ \tilde{n}_{x,ij}\\ \tilde{n}_{y,ij}\end{pmatrix} \end{aligned} \tag{3.83}$$

Even though the formulation is slightly different, the same discretisation of the bed slope source term is obtained with the scheme of Bermúdez and Vázquez (given by Equations 3.79, 3.80 and 3.81) and with the scheme of Fernández (given by Equations 3.82 and 3.83). This can be easily proved if we consider the following relations:

$$\frac{1}{A_i}\sum_{j\in K_i}A_{T_{ij}}\tilde{\mathbf{S}}_{ij}^{BV}=\mathbf{S}_i^C \qquad\qquad \tilde{\mathbf{S}}_{ij}^{BV}=2\tilde{\mathbf{S}}_{ij}^F \tag{3.84}$$

The definition of the source term $\tilde{\mathbf{S}}_{ij}$ given by Equations 3.81 and 3.83 differ by a factor 2, being the latter one more consistent with the definition of the bed slope derivative. For that reason the scheme 3.82 has been preferred in the numerical solver in order to upwind other source terms.

Upwind discretisation of the bed slope in hydrostatic flow conditions

In order to prove the convenience of upwinding the bed slope source term, the first order schemes of van Leer and Roe will be applied to hydrostatic flow conditions. In the hydrostatic assumption, the discrete equations reduce to:

$$\sum_{j\in K_i}\boldsymbol{\phi}_{ij}=\mathbf{S}_iA_i \tag{3.85}$$

Either Bermúdez and Vázquez or Fernández formulations may be used to discretise the bed slope term $\mathbf{S}_i$, leading to the same results. Nevertheless, Equations 3.82 and 3.83 will be used here in order to have a clear distinction between the centred and upwind contributions.

The numerical flux given by the schemes for the cell C_i is given by:

$$\boldsymbol{\phi}_{ij}=\frac{\mathbf{Z}_i+\mathbf{Z}_j}{2}-\frac{1}{2}\mathbf{X}_{ij}|\mathbf{D}|_{ij}\mathbf{X}_{ij}^{-1}(\mathbf{w}_j-\mathbf{w}_i) \tag{3.86}$$

where the subindices ij indicate either the Roe's or the van Leer's mean state, i.e. $\mathbf{X}_{ij} = \mathbf{X}(\tilde{\mathbf{w}}_{ij})$ and $|\mathbf{D}|_{ij} = |\mathbf{D}|(\tilde{\mathbf{w}}_{ij})$. Considering that $q_x = q_y = 0$ in all cells, the mean states of van Leer and Roe are reduced to:

$$\begin{array}{llll} \tilde{h}_{vl} = \dfrac{h_i + h_j}{2} & \tilde{c}_{vl} = \sqrt{g\dfrac{h_i + h_j}{2}} & \tilde{q}_{x,vl} = 0 & \tilde{q}_{y,vl} = 0 \\ \tilde{h}_{Roe} = \sqrt{h_i h_j} & \tilde{c}_{Roe} = \sqrt{g\dfrac{h_i + h_j}{2}} & \tilde{q}_{x,Roe} = 0 & \tilde{q}_{y,Roe} = 0 \end{array} \tag{3.87}$$

The values of the different vectors and matrices in Equation 3.86 are given by:

$$\mathbf{X}_{ij} = \begin{pmatrix} 0 & 1 & 1 \\ -\tilde{n}_{y,ij} & \tilde{c}_{ij}\tilde{n}_{x,ij} & -\tilde{c}_{ij}\tilde{n}_{x,ij} \\ \tilde{n}_{x,ij} & \tilde{c}_{ij}\tilde{n}_{y,ij} & -\tilde{c}_{ij}\tilde{n}_{y,ij} \end{pmatrix} \quad \mathbf{X}_{ij}^{-1} = \frac{1}{2\tilde{c}_{ij}} \begin{pmatrix} 0 & -2\tilde{c}_{ij}\tilde{n}_{y,ij} & 2\tilde{c}_{ij}\tilde{n}_{x,ij} \\ \tilde{c}_{ij} & \tilde{n}_{x,ij} & \tilde{n}_{y,ij} \\ \tilde{c}_{ij} & -\tilde{n}_{x,ij} & -\tilde{n}_{y,ij} \end{pmatrix} \tag{3.88}$$

$$\mathbf{D}_{ij} = \tilde{c}_{ij}|\mathbf{n}_{ij}| \begin{pmatrix} 0 & 0 & 0 \\ 0 & 1 & 0 \\ 0 & 0 & -1 \end{pmatrix} \quad |\mathbf{D}|_{ij} = \tilde{c}_{ij}|\mathbf{n}_{ij}| \begin{pmatrix} 0 & 0 & 0 \\ 0 & 1 & 0 \\ 0 & 0 & 1 \end{pmatrix} \quad \mathbf{D}_{ij}^{-1} = \frac{1}{\tilde{c}_{ij}|\mathbf{n}_{ij}|} \begin{pmatrix} 0 & 0 & 0 \\ 0 & 1 & 0 \\ 0 & 0 & -1 \end{pmatrix}$$

$$\mathbf{Z}_i = |\mathbf{n}_{ij}| \begin{pmatrix} 0 \\ g\dfrac{h_i^2}{2}\tilde{n}_{x,ij} \\ g\dfrac{h_i^2}{2}\tilde{n}_{y,ij} \end{pmatrix} \qquad \mathbf{w}_i = \begin{pmatrix} h_i \\ 0 \\ 0 \end{pmatrix}$$

Notice that, since $\tilde{c}_{vl} = \tilde{c}_{Roe} = \tilde{c}_{ij}$, expressions 3.88 are independent of the scheme used. Introducing expressions 3.88 into Equation 3.86 gives, after some mathematical manipulation, the total flux for the cell C_i as:

$$\sum_{j\in K_i} \boldsymbol{\phi}_{ij} = \sum_{j\in K_i} \frac{|\mathbf{n}_{ij}|}{2} g \frac{h_i^2 + h_j^2}{2} \begin{pmatrix} 0 \\ \tilde{n}_{x,ij} \\ \tilde{n}_{y,ij} \end{pmatrix} - \sum_{j\in K_i} \frac{|\mathbf{n}_{ij}|}{2} \tilde{c}_{ij}(h_j - h_i) \begin{pmatrix} 1 \\ 0 \\ 0 \end{pmatrix} \tag{3.89}$$

where the first addend accounts for the centred contribution and the second addend for the upwind contribution.

The discretisation of the bed slope term is obtained introducing expressions 3.88 into Equations 3.82 and 3.83, which yields:

$$\mathbf{S}_i A_i = \sum_{j\in K_i} -\frac{|\mathbf{n}_{ij}|}{2} g \frac{h_i + h_j}{2} (z_{b,j} - z_{b,i}) \begin{pmatrix} 0 \\ \tilde{n}_{x,ij} \\ \tilde{n}_{y,ij} \end{pmatrix} + \sum_{j\in K_i} \frac{|\mathbf{n}_{ij}|}{2} \tilde{c}_{ij}(z_{b,j} - z_{b,i}) \begin{pmatrix} 1 \\ 0 \\ 0 \end{pmatrix} \tag{3.90}$$

where the first addend accounts for the centred contribution and the second addend for the upwind

contribution.

Considering that in hydrostatic flow the water surface elevation is constant ($z_{b,i}+h_i = z_{b,j}+h_j$), it is straightforward to show that the upwind contribution in the convective flux (second addend in Equation 3.89) and in the source term (second addend in Equation 3.90) are equal. The balance of the centred contributions follows directly considering that for any closed volume the following property (Equation 3.91) applies for both the x and the y component of the normal vector:

$$\sum_{j \in K_i} h_i^2 \tilde{n}_{x,ij} |\mathbf{n}_{ij}| = h_i^2 \sum_{j \in K_i} n_{x,ij} = 0 \tag{3.91}$$

Second order upwind discretisation of the bed slope source term

If the second order extension of the van Leer's or Roe's schemes is used, the exact balance between the numerical flux and the bed slope source term is broken, even if a second order extrapolation is used to evaluate the bed elevation at the cell faces. This is because the extrapolated value of h_i is different at each cell face, and therefore,

$$\sum_{j \in K_i} h_{Ij} \tilde{n}_{x,ij} |\mathbf{n}_{ij}| \neq 0 \tag{3.92}$$

where h_{Ij} is the extrapolated value of the flux from the node N_i to the cell face L_{ij}. For this reason, the centred contributions in the flux term discretisation (Equation 3.89) and in the source term discretisation (Equation 3.90) do not balance any more. There is actually a deficit in the source term given by:

$$\mathbf{R}_i = \sum_{j \in K_i} -g \frac{|\mathbf{n}_{ij}|}{2} h_{Ij}^2 \begin{pmatrix} 0 \\ \tilde{n}_{x,ij} \\ \tilde{n}_{y,ij} \end{pmatrix} \tag{3.93}$$

and the following relation applies:

$$\sum_{j \in K_i} \boldsymbol{\phi}_{ij} = \mathbf{S}_i A_i + \mathbf{R}_i \tag{3.94}$$

We have found that a simple and efficient solution to this problem is to use a first order approximation for the water depth ($h_{Ij} = h_i$), and a second order approximation for the unit discharges. In this case the deficit $\mathbf{R}_i$ is zero:

$$\mathbf{R}_i = \sum_{j \in K_i} -g \frac{|\mathbf{n}_{ij}|}{2} h_i^2 \begin{pmatrix} 0 \\ \tilde{n}_{x,ij} \\ \tilde{n}_{y,ij} \end{pmatrix} = \begin{pmatrix} 0 \\ 0 \\ 0 \end{pmatrix} \tag{3.95}$$

and the exact balance between flux and source is recovered. This approach leads to an hybrid

scheme that is able to compute the hydrostatic flow solution exactly, and at the same time it does not introduce an excessive numerical diffusion which may interfere with the real turbulent diffusion.

Hubbard and García-Navarro [62] proposed a high order correction of the source term in order to obtain a fully second order scheme which gives an exact balance between convective flux and bed slope in the hydrostatic case. Following the ideas of Hubbard and García-Navarro, when using a second order scheme Equation 3.93 can be replaced by the more general relation:

$$\mathbf{R}_i = -\sum_{j\in K_i} [\mathbf{F}_{x,Ij} n_{x,ij} + \mathbf{F}_{y,Ij} n_{y,ij}] = -\sum_{j\in K_i} [(\mathbf{F}_{x,Ij} - \mathbf{F}_{x,i}) n_{x,ij} + (\mathbf{F}_{y,Ij} - \mathbf{F}_{y,i}) n_{y,ij}] \quad (3.96)$$

Equation 3.96 is actually a discretisation of the flux gradient between the node N_i and the face L_{ij}. Hence, it can be rewritten as:

$$\mathbf{R}_i = -\sum_{j\in K_i} \left(\frac{\partial \mathbf{F}_x}{\partial x} + \frac{\partial \mathbf{F}_y}{\partial y} \right)_{iI} |\mathbf{n}_{ij}| \frac{d_{\perp,ij}}{2} = -\sum_{j\in K_i} \mathbf{S}_{iI} |\mathbf{n}_{ij}| \frac{d_{\perp,ij}}{2} \quad (3.97)$$

where it has been considered that we want to maintain a balance between the convective flux and the bed slope source term in the hydrostatic case. The vector $\mathbf{S}_{iI}$ in Equation 3.97 accounts for a discretisation of the bed slope term between the node N_i and the face L_{ij}. Having this in mind, and considering Equation 3.94, the new discretisation of the source term is given by:

$$\begin{aligned} \mathbf{S}_i^* &= \mathbf{S}_i + \frac{1}{A_i}\mathbf{R}_i = \mathbf{S}_i - \frac{1}{A_i}\sum_{j\in K_i} \mathbf{S}_{iI} |\mathbf{n}_{ij}| \frac{d_{\perp,ij}}{2} \quad (3.98) \\ &= \mathbf{S}_i - \frac{1}{A_i}\sum_{j\in K_i} \left[-\frac{|\mathbf{n}_{ij}|}{2} g \frac{h_i + h_{Ij}}{2} 2(z_{b,Ij} - z_{b,i}) \right] \begin{pmatrix} 0 \\ \tilde{n}_{x,ij} \\ \tilde{n}_{y,ij} \end{pmatrix} \end{aligned}$$

where $\mathbf{S}_i^*$ is the new discretisation of the source term. In Equation 3.98, the upper-case subindices refer to extrapolated variables at the cell faces, and the lower-case subindices refer to node values. It is straightforward to show that the source term $\mathbf{S}_i^*$ balances exactly the convective flux in the hydrostatic case.

Most of the applications in this thesis have been computed with the hybrid first/second order scheme (first order for the water depth and second order for the unit discharges). Some of them have also been computed with the fully second order scheme proposed by Hubbard and García-Navarro. No significant differences have been found in the results given by both schemes, maybe because the water depth gradients were not large enough.

3.5.8 Discretisation of the viscous diffusive flux

As well as the bed slope, the diffusive flux source term may be discretised with a centred or with an upwind scheme.

Centred discretisation of the viscous diffusive flux

The viscous diffusive flux in the x-momentum equation is expressed as:

$$\frac{\partial}{\partial x}\left(\nu h \frac{\partial U_x}{\partial x}\right) + \frac{\partial}{\partial y}\left(\nu h \frac{\partial U_x}{\partial y}\right) \tag{3.99}$$

being ν the kinematic viscosity. Integrating Equation 3.99 over the cell C_i, and applying the Gauss theorem gives:

$$\int_{C_i} \frac{\partial}{\partial x}\left(\nu h \frac{\partial U_x}{\partial x}\right) + \frac{\partial}{\partial y}\left(\nu h \frac{\partial U_x}{\partial y}\right) dA \approx \sum_{j \in K_i} \nu_{ij} h_{ij} \left(\frac{\partial U_x}{\partial x}\tilde{n}_x + \frac{\partial U_x}{\partial y}\tilde{n}_y\right)_{ij} |\mathbf{n}_{ij}| \tag{3.100}$$

where the integral over the cell boundary has been split into the sum of integrals over each face L_{ij}. With this formulation the scheme remains conservative, since the diffusive flux is computed at the cell faces, assuring that the flux which exits any cell through one face is the same flux which enters the adjacent cell through the same face. Equation 3.100 is evaluated at all the cell faces.

The eddy viscosity, water depth, and velocity gradient at each cell face are computed as the average of their values at the nodes of the adjacent cells:

$$\nu_{ij} = \frac{\nu_i + \nu_j}{2} \qquad h_{ij} = \frac{h_i + h_j}{2} \qquad (\nabla U_x)_{ij} = \frac{(\nabla U_x)_i + (\nabla U_x)_j}{2} \tag{3.101}$$

The approach presented in section 3.5.6 is used in order to evaluate the velocity gradient at the cell nodes.

Upwind discretisation of the viscous diffusive flux

Equation 3.82 has been used to upwind the viscous term. The centred part is computed from Equations 3.100 and 3.101. In order to compute the upwind part, the laplacian of the velocity must be approximated at the cell faces. In order to do so, a 1D approach in the normal direction to the cell face is used, in the same way as it has been done when upwinding the convective flux and the bed slope source terms. In such a way, the laplacian of the velocity U_x at the cell face L_{ij} is approximated as:

$$\left.\frac{\partial^2 U_x}{\partial x^2}\right|_{ij} + \left.\frac{\partial^2 U_x}{\partial y^2}\right|_{ij} \approx \frac{1}{d_{\perp,ij}}\left(\left.\frac{\partial U_x}{\partial x}\right|_j - \left.\frac{\partial U_x}{\partial x}\right|_i\right)\tilde{n}_{x,ij} + \frac{1}{d_{\perp,ij}}\left(\left.\frac{\partial U_x}{\partial y}\right|_j - \left.\frac{\partial U_x}{\partial y}\right|_i\right)\tilde{n}_{y,ij} \tag{3.102}$$

where $d_{\perp,ij}$ is the distance between the nodes N_i and N_j measured in the normal direction to the cell face. The laplacian of the U_y velocity is evaluated in a similar way.

Semi-implicit diffusion

As it has been argued in section 3.4, when the viscosity is too large, it is convenient to implicit the main diagonal of the diffusion source term in order to relax the stability condition over the time step. In order to do so, following the ideas of Davidson [32], the total diffusive flux (D_{tot}) is decomposed in two parts: an orthogonal diffusion ($D_\perp$) and a non-orthogonal diffusion ($D_\parallel$):

$$D_{tot} = D_\perp + D_\parallel \tag{3.103}$$

In order to do so, the gradient of the velocity at the cell face L_{ij} (Equation 3.100) is computed applying the Gauss theorem to the volume A_{ij}, which is defined by the shaded area in Figure 3.7. The two sides of the volume A_{ij} which pass through the nodes N_i and N_j, are defined by the same normal vector as the cell face L_{ij}, i.e. $\mathbf{n}_{ij}$. The other two sides of the volume are parallel to the line which joins the nodes N_i and N_j, and are defined by the normal vector $\boldsymbol{\alpha}_{ij}$ ($|\boldsymbol{\alpha}_{ij}| = d_{ij}$). The area of the volume is given by $A_{ij} = |\mathbf{n}_{ij}| d_{\perp,ij}$.

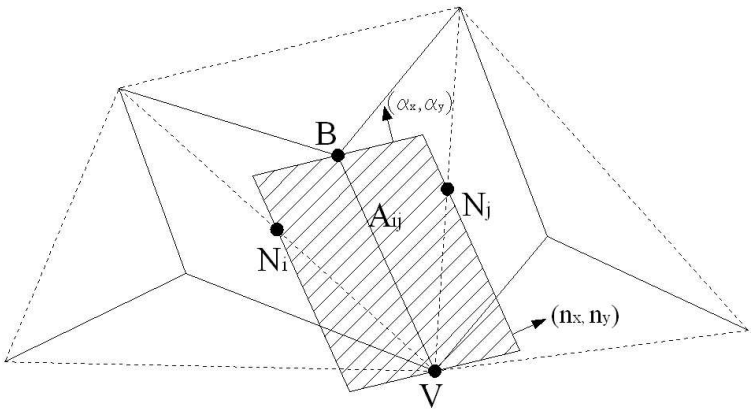

Figure 3.7: Evaluation of the diffusion term.

The derivatives of the velocity U_x at the cell face L_{ij} are evaluated as:

$$\begin{aligned}
\left.\frac{\partial U_x}{\partial x}\right|_{ij} &\approx \frac{1}{A_{ij}} \int_{A_{ij}} \frac{\partial U_x}{\partial x}\, dA = \frac{1}{A_{ij}} \int_L U_x \tilde{n}_x\, dL \\
&\approx \frac{1}{A_{ij}} \left(U_{x,j} n_{x,ij} + U_{x,B} \alpha_{x,ij} - U_{x,i} n_{x,ij} - U_{x,V} \alpha_{x,ij}\right) \\
\left.\frac{\partial U_x}{\partial y}\right|_{ij} &\approx \frac{1}{A_{ij}} \int_{A_{ij}} \frac{\partial U_x}{\partial y}\, dA = \frac{1}{A_{ij}} \int_L U_x \tilde{n}_y\, dL \\
&\approx \frac{1}{A_{ij}} \left(U_{x,j} n_{y,ij} + U_{x,B} \alpha_{y,ij} - U_{x,i} n_{y,ij} - U_{x,V} \alpha_{y,ij}\right)
\end{aligned} \tag{3.104}$$

Introducing the expressions 3.104 in Equation 3.100, and considering that $A_{ij} = |\mathbf{n}_{ij}| d_{\perp,ij}$, the following expression is obtained for the discrete diffusive flux at the cell C_i:

$$\sum_{j \in K_i} \nu_{ij} h_{ij} \left(\frac{\partial U_x}{\partial x} \tilde{n}_x + \frac{\partial U_x}{\partial y} \tilde{n}_y \right)_{ij} |\mathbf{n}_{ij}| \approx \underbrace{\sum_{j \in K_i} \nu_{ij} h_{ij} \frac{|\mathbf{n}_{ij}|}{d_{\perp,ij}} \left(U_{x,j} - U_{x,i} \right)}_{D_\perp \equiv \text{orthogonal}} + \underbrace{\sum_{j \in K_i} \nu_{ij} h_{ij} \frac{d_{ij}}{d_{\perp,ij}} \left(U_{x,B} - U_{x,V} \right) \left(\tilde{\alpha}_{x,ij} \tilde{n}_{x,ij} + \tilde{\alpha}_{y,ij} \tilde{n}_{y,ij} \right)}_{D_\parallel \equiv \text{non-orthogonal}} \tag{3.105}$$

The non-orthogonal part (second addend in Equation 3.105) is treated explicitly with the rest of source terms, while the orthogonal part (first addend in Equation 3.105) is split as:

$$D_\perp = \nu_{ij} h_{ij} \frac{|\mathbf{n}_{ij}|}{d_{\perp,ij}} (U_{x,j} - U_{x,i}) = \Gamma_{D_\perp} U_{x,j} - \frac{\Gamma_{D_\perp}}{h_i} q_{x,i} \tag{3.106}$$

where $\Gamma_{D_\perp} = \dfrac{\nu_{ij} h_{ij} |\mathbf{n}_{ij}|}{d_{\perp,ij}}$ is the orthogonal diffusion coefficient. It should be noticed that in orthogonal meshes, the vectors $\mathbf{n}_{ij}$ and $\boldsymbol{\alpha}_{ij}$ are perpendicular, and therefore, the non-orthogonal diffusion in Equation 3.105 vanishes ($D_\parallel = 0$). In Equation 3.106 all the variables are evaluated at time t^n except the unit discharge $q_{x,i}$, which is evaluated at time t^{n+1}. In this way no additional computational cost is introduced, since there is no need to solve any system of equations.

3.5.9 Discretisation of the Reynolds stresses

Depending on the turbulence model used, the Reynolds stresses are computed in different ways. In the eddy viscosity models the Reynolds stresses are computed with the Boussinesq approximation, and the form of the turbulent stress term is similar to that one of the viscous diffusion term, just replacing the kinematic viscosity by the eddy viscosity, which for the x-momentum equation reads:

$$\frac{\partial}{\partial x} \left(\nu_t h \frac{\partial U_x}{\partial x} \right) + \frac{\partial}{\partial y} \left(\nu_t h \frac{\partial U_x}{\partial y} \right) \tag{3.107}$$

This is the case of the mixing length model and the $k - \varepsilon$ model. In those cases it is used the same scheme as for the viscous diffusion term (section 3.5.8).

If the depth averaged algebraic stress model is used, the Reynolds stresses are computed with algebraic expressions, and it is not necessary to compute any derivative at the cell faces. In that case, the integral over the cell C_i of the turbulent stresses is computed as:

$$\int_{C_i} \frac{\partial \overline{u'^2}}{\partial x} + \frac{\partial \overline{u'v'}}{\partial y} \, dA = \int_{L_i} \overline{u'^2} \tilde{n}_{x,ij} + \overline{u'v'} \tilde{n}_{y,ij} \, dL \approx \sum_{j \in K_i} \overline{u'^2}_{ij} n_{x,ij} + \overline{u'v'}_{ij} n_{y,ij} \tag{3.108}$$

with an analogous expression for the y-momentum equation. Notice that the symbols $<>$ accounting for depth averaged values have been omitted for the sake of clarity in the notation. The value of any Reynolds stress at the cell face is computed as the average of the values at each adjacent node:

$$\overline{u'^2}_{ij} = \frac{\overline{u'^2}_i + \overline{u'^2}_j}{2} \tag{3.109}$$

The value of the Reynolds stresses at the cell nodes is obtained directly from the algebraic expressions presented in section 2.5. All the derivatives at the cell nodes are computed with the scheme presented in section 3.5.6. A centred discretisation scheme has always been used in order to evaluate the turbulent terms with the algebraic stress model.

3.5.10 Discretisation of the bed friction source term

Centred discretisation of the bed friction term

In order to improve the stability of the numerical scheme when the bed friction coefficient is large, both an explicit and a semi-implicit discretisation scheme for the bed friction source term ($\mathbf{G_2}$) have been implemented in the numerical solver.

In the explicit scheme the friction term is evaluated at each cell node at the time t^n. Any of the formulations which have been presented in section **??** may be used to compute the bed friction coefficient c_f:

$$\mathbf{G}^e_{\mathbf{2},i} = -\frac{c_f}{h_i^2}\begin{pmatrix} 0 \\ |\mathbf{q}|_i q_{x,i} \\ |\mathbf{q}|_i q_{y,i} \end{pmatrix} \tag{3.110}$$

where all the variables are evaluated at time t^n. The semi-implicit discretisation evaluates the friction term as:

$$\mathbf{G}^{si}_{\mathbf{2},i} = -\frac{c_f}{h_i^2}\begin{pmatrix} 0 \\ |\mathbf{q}|^n_i q^{n+1}_{x,i} \\ |\mathbf{q}|^n_i q^{n+1}_{y,i} \end{pmatrix} \tag{3.111}$$

The semi-implicit discretisation has not any additional computational cost, since it is linear in $q^{n+1}_{x,i}$ and in $q^{n+1}_{y,i}$. The conservative variable $q^{n+1}_{x,i}$ at the new time step is computed as:

$$q^{n+1}_{x,i} = \left(q^n_{x,i} + \Delta t \left(G^n_{1,i}(2) + G^n_{3,i}(2) - C^n_i(2)\right)\right) \frac{1}{1 + c_f \dfrac{|\mathbf{q}|_i}{h_i^2}\Delta t} \tag{3.112}$$

with an analogous expression for $q^{n+1}_{y,i}$. The terms $G^n_{1,i}(2)$ and $G^n_{3,i}(2)$ account for any explicit discretisation of the bed slope and turbulent diffusion source terms in the x-momentum equation. The term $C^n_i(2)$ accounts for any explicit discretisation of the convective flux in the x-momentum

equation.

Upwind discretisation of the bed friction term

The same upwind discretisation scheme which has been used for the bed slope and viscous source terms has been implemented in order to upwind the bed friction term. It should only be remarked that the centred part in Equation 3.82 may be computed with the explicit or semi-implicit schemes presented above, while an explicit scheme is always used for the upwind part.

3.6 Discretisation of the depth averaged $k-\varepsilon$ model

3.6.1 The depth averaged $k-\varepsilon$ model in conservative form

The depth averaged $k-\varepsilon$ model solves two transport equations, one for the depth averaged turbulent kinetic energy k, and another for the depth averaged dissipation rate ε. The equations of the model have been presented in chapter 2, and are repeated here in conservative and vectorial form:

$$\frac{\partial \mathbf{\Phi}}{\partial t}+\frac{\partial \mathbf{F_{\Phi,x}}}{\partial x}+\frac{\partial \mathbf{F_{\Phi,y}}}{\partial y}=\sum_{\mathrm{m}=1}^{4}\mathbf{H_m} \tag{3.113}$$

where the turbulent conservative variables $\mathbf{\Phi}$, and their physical fluxes $\mathbf{F_{\Phi,x}}$ and $\mathbf{F_{\Phi,y}}$, are given by:

$$\mathbf{\Phi}=\begin{pmatrix} hk \\ h\varepsilon \end{pmatrix} \qquad \mathbf{F_{\Phi,x}}=\begin{pmatrix} hkU_x \\ h\varepsilon U_x \end{pmatrix}=U_x\mathbf{\Phi} \qquad \mathbf{F_{\Phi,y}}=\begin{pmatrix} hkU_y \\ h\varepsilon U_y \end{pmatrix}=U_y\mathbf{\Phi} \tag{3.114}$$

The source terms $\mathbf{H_m}$ ($\mathrm{m}=1,4$), account respectively for the viscous and turbulent diffusion ($\mathbf{H_1}$), the production due to horizontal velocity gradients ($\mathbf{H_2}$), the production due to bed friction ($\mathbf{H_3}$), and the dissipation rate ($\mathbf{H_4}$):

$$\begin{aligned}
\mathbf{H_1}&=\begin{pmatrix} \dfrac{\partial}{\partial x_j}\left((\nu+\dfrac{\nu_t}{\sigma_k})h\dfrac{\partial k}{\partial x_j}\right) \\ \dfrac{\partial}{\partial x_j}\left((\nu+\dfrac{\nu_t}{\sigma_\varepsilon})h\dfrac{\partial \varepsilon}{\partial x_j}\right) \end{pmatrix} \qquad \mathbf{H_2}=\begin{pmatrix} \min\left(2\nu_t S_{ij}S_{ij}h, 10\varepsilon h\right) \\ c_{1\varepsilon}\dfrac{\varepsilon}{k}2\nu_t S_{ij}S_{ij}h \end{pmatrix} \\
\mathbf{H_3}&=\begin{pmatrix} \min(c_k u_f^3, 10\varepsilon h) \\ c_\varepsilon \dfrac{u_f^4}{h} \end{pmatrix} \qquad \mathbf{H_4}=\begin{pmatrix} -\varepsilon h \\ -c_{2\varepsilon}\dfrac{\varepsilon^2}{k}h \end{pmatrix}
\end{aligned} \tag{3.115}$$

with:

$$\nu_t=\min\left(c_\mu\frac{k^2}{\varepsilon},\frac{k}{3}\left(\frac{2}{S_{ij}S_{ij}}\right)^{1/2}\right)$$

where S_{ij} is the horizontal mean strain-rate tensor computed from the depth averaged velocity (Equation 2.65), and u_f is the bed friction velocity. The constants and coefficients of the model can be found in section 2.4.5 for the three versions implemented in the code (Rastogi and Rodi, Babarutsi and Chu, Booij). In the model of Babarutsi and Chu the vertical production source term is zero (${\mathbf{H_3}}^{BC} = 0$) and the source term $\mathbf{H_4}$ is replaced by:

$$
{\mathbf{H_4}}^{BC} = \begin{pmatrix} -\varepsilon h - F'h \\ -c_{2\varepsilon}\dfrac{\varepsilon^2}{k}h - hc_{1\varepsilon}\dfrac{\varepsilon'}{k'}(1-c_{3\varepsilon})F' \end{pmatrix} \tag{3.116}
$$

where the superindex BC refers to Babarutsi and Chu.

The transport equations for k and ε are coupled via the source terms $\mathbf{H_m}$. However, in contrast with the shallow water equations, there is no explicit coupling via the convective flux. Therefore, both equations will be discretised independently. In this case the normal flux $\mathbf{Z_\Phi} = \mathbf{F_{\Phi,x}}n_x + \mathbf{F_{\Phi,x}}n_y$ is an homogeneous function which can be decomposed as:

$$
\mathbf{Z_\Phi} = \frac{\partial \mathbf{Z_\Phi}}{\partial \mathbf{\Phi}}\mathbf{\Phi} = (U_x n_x + U_y n_y)\begin{pmatrix} 1 & 0 \\ 0 & 1 \end{pmatrix}\begin{pmatrix} hk \\ h\varepsilon \end{pmatrix} = (U_x n_x + U_y n_y)\mathbf{\Phi} \tag{3.117}
$$

The upwind direction for both equations is the same, and it is given directly by the depth averaged velocity field:

$$
\begin{aligned} \mathbf{Z_\Phi} &= \lambda \mathbf{\Phi} \\ \lambda &= U_x n_x + U_y n_y \end{aligned} \tag{3.118}
$$

The same considerations about the time and spatial discretisation schemes that have been exposed for the shallow water equations apply for the $k-\varepsilon$ model. The stability condition over the time step applied to the $k-\varepsilon$ equations gives (assuming a semi-implicit discretisation of the diffusive flux):

$$
\Delta t_i = \text{CFL}\frac{d_i}{|\mathbf{U}|_i} \qquad\qquad \text{CFL} \leq 1 \tag{3.119}
$$

where $d_i = \dfrac{A_i}{P_i}$ is the ratio between the area A_i and the perimeter P_i of each cell, and $|\mathbf{U}|_i$ is the module of the velocity vector. Condition 3.119 is less restrictive than the condition over the time step for the shallow water equations (Equation 3.55). For this reason the time step at each iteration is taken from condition 3.55, and it is used for both the shallow water and the $k-\varepsilon$ models. Nevertheless, it should be taken into account that the stability condition is obtained from the linear convection-diffusion equation without source terms. The source terms may influence the stability of the numerical scheme, specially considering that they are strongly dependent on the conservative variables as well as on their derivatives. The coupling between the flow and the

turbulence model is an additional source of instability. Therefore, the maximum CFL value in order to obtain stability may vary depending on the flow conditions. In the practical applications studied in this thesis the CFL values were usually in the range $0.7 - 1.3$.

3.6.2 Discretisation of the convective and diffusive fluxes

First order upwind scheme

Both the $k-\varepsilon$ model and the shallow water equations are hyperbolic systems of conservation laws with source terms. However, the fact that the two eigenvalues of the $k-\varepsilon$ equations are equal, makes the numerical scheme simpler, since the upwind direction depends only on the normal velocity to the cell face.

In order to discretise the convective flux at the cell faces, Equation 3.118 will be used. The convecting part, which is given by the normal velocity to the face (λ), is treated centred, while the convected part, which is given by the conservative turbulent variables ($\mathbf{\Phi}$), is upwinded. Hence, at the cell face L_{ij}, the numerical flux ($\mathbf{Z}^*_{\mathbf{\Phi},ij}$) is computed as:

$$\mathbf{Z}^*_{\mathbf{\Phi},ij} = \begin{cases} \lambda_{ij}\mathbf{\Phi}_i & \text{if} \quad \lambda_{ij} > 0 \\ \lambda_{ij}\mathbf{\Phi}_j & \text{if} \quad \lambda_{ij} \leq 0 \end{cases} \tag{3.120}$$

which can also be written as:

$$\mathbf{Z}^*_{\mathbf{\Phi},ij} = \underbrace{\lambda_{ij}\mathbf{\Phi}_{ij}}_{centred} - \underbrace{\frac{1}{2}|\lambda_{ij}|\left(\mathbf{\Phi}_j - \mathbf{\Phi}_i\right)}_{upwind} \tag{3.121}$$

where $\mathbf{Z}^*_{\mathbf{\Phi},ij}$ is the numerical flux. The subindex ij accounts for a centred discretisation at the cell face ($\mathbf{\Phi}_{ij} = \dfrac{\mathbf{\Phi}_i + \mathbf{\Phi}_j}{2}$, $\lambda_{ij} = \dfrac{\lambda_i + \lambda_j}{2}$). The scheme is first order accurate in space. All the source terms are discretised with a centred scheme.

As it has been done in the momentum equations, the diffusive flux ($\mathbf{H_1}$) is split in two parts: an orthogonal contribution ($\mathbf{H}_{\mathbf{1}\perp}$) and a non-orthogonal contribution ($\mathbf{H}_{\mathbf{1}\parallel}$):

$$\mathbf{H_1} = \mathbf{H}_{\mathbf{1}\perp} + \mathbf{H}_{\mathbf{1}\parallel} \tag{3.122}$$

Both contributions are computed in an analogous way as it was explained in section 3.5.8 for the momentum equations. In this way, using Equation 3.121, the following discrete equation is obtained for the node N_i:

$$\left(\frac{\partial \mathbf{\Phi}}{\partial t}\right)_i A_i + \sum_{j \in K_i} \left[\lambda_{ij}\frac{\mathbf{\Phi}_i + \mathbf{\Phi}_j}{2} - \frac{1}{2}\left|\lambda_{ij}\right|\left(\mathbf{\Phi}_j - \mathbf{\Phi}_i\right)\right] = \sum_{j \in K_i} \left[\Gamma_{D_\perp,ij}\left(\mathbf{\Phi}_j - \mathbf{\Phi}_i\right)\right] + \mathbf{H}_i A_i \tag{3.123}$$

where $\Gamma_{D_\perp,ij} = \dfrac{\nu_{e,ij}|\mathbf{n}_{ij}|}{d_{\perp,ij}}$ is the orthogonal diffusion coefficient (where ν_e is the effective viscosity), and A_i is the area of the cell C_i. The vector $\mathbf{H}_i$ accounts for all the source terms, including the non-orthogonal diffusion (but obviously excluding the orthogonal diffusion), evaluated in the cell C_i:

$$\mathbf{H}_i = \mathbf{H}_{\mathbf{1}\parallel,i} + \sum_{\mathrm{m}=2}^{4} \mathbf{H}_{\mathbf{m},i} \tag{3.124}$$

Rearranging terms in Equation 3.123 yields:

$$\left(\frac{\partial \mathbf{\Phi}}{\partial t}\right)_i A_i + \sum_{j\in K_i}\left[\lambda_{ij}\frac{\mathbf{\Phi}_i+\mathbf{\Phi}_j}{2} - \left(\frac{1}{2}|\lambda_{ij}| + \Gamma_{D_\perp,ij}\right)(\mathbf{\Phi}_j - \mathbf{\Phi}_i)\right] = \mathbf{H}_i A_i \tag{3.125}$$

It is very clear in Equation 3.125 that the upwind part of the convective flux is equivalent to an orthogonal diffusion term with a diffusion coefficient given by $\dfrac{1}{2}|\lambda_{ij}|$. Using an explicit discretisation in time, Equation 3.125 can be written in standard form as:

$$\mathbf{\Phi}_i^{n+1} = \left(1 - \frac{\Delta t}{A_i}a_i^n\right)\mathbf{\Phi}_i^n + \frac{\Delta t}{A_i}\sum_{j\in K_i} a_{ij}^n \mathbf{\Phi}_j^n + \Delta t \mathbf{H}_i^n \tag{3.126}$$

with the coefficients:

$$a_i = \sum_{j\in K_i}\left(\frac{\lambda_{ij}+|\lambda_{ij}|}{2} + \Gamma_{D_\perp,ij}\right) \qquad a_{ij} = \frac{-\lambda_{ij}+|\lambda_{ij}|}{2} + \Gamma_{D_\perp,ij} \tag{3.127}$$

Considering that $\Gamma_{D_\perp,ij}$ is always positive, it is straightforward to show that the artificial diffusion coefficient ($\frac{1}{2}|\lambda_{ij}|$) ensures that all the coefficients a_i and a_{ij} in Equation 3.126 are positive. Therefore, the scheme is stable for:

$$\Delta t < \frac{A_i}{a_i^n} \tag{3.128}$$

This condition is relaxed if the viscous diagonal is treated implicitly, in which case the value of a_i^n diminishes. If both the convective and the diffusive fluxes are treated implicitly, the stability condition over Δt disappears.

Hybrid scheme

When the diffusive flux is of the same order or larger than the convective flux, a second order centred scheme can be used to discretise the convective flux without stability problems. The hybrid central/upwind scheme [102] uses central differencing when diffusion predominates (leading to a second order scheme), and upwind differencing when convection predominates (returning to a first order scheme).

The upwind character of the first order scheme is given by the term $|\lambda_{ij}|$, which ensures that

all the coefficients in Equation 3.126 remain positive. In the hybrid scheme the term $|\lambda_{ij}|$ is used as a minimum diffusion coefficient in order to obtain stability. With this in mind, the coefficients a_i and a_{ij} in the hybrid scheme are given by:

$$a_i = \sum_{j \in K_i} \left[\frac{\lambda_{ij}}{2} + \max\left(\frac{|\lambda_{ij}|}{2}, \Gamma_{D_\perp, ij} \right) \right] \qquad a_{ij} = -\frac{\lambda_{ij}}{2} + \max\left(\frac{|\lambda_{ij}|}{2}, \Gamma_{D_\perp, ij} \right) \tag{3.129}$$

The term $|\lambda_{ij}|$ is only used when the real diffusion is not large enough to give stability, i.e. when the Peclet number is larger than 2 ($Pe = \dfrac{\lambda_{ij}}{\Gamma_{D_\perp, ij}} > 2$). An alternative way to write the coefficients a_i and a_{ij}, which shows clearly that all the coefficients are positive, is:

$$a_i = \sum_{j \in K_i} \max\left(0, \lambda_{ij}, \frac{\lambda_{ij}}{2} + \Gamma_{D_\perp, ij} \right) \qquad a_{ij} = \max\left(0, -\lambda_{ij}, -\frac{\lambda_{ij}}{2} + \Gamma_{D_\perp, ij} \right) \tag{3.130}$$

The hybrid scheme cannot be considered as second order accurate, since usually the Peclet number is larger than 2, and therefore, the coefficients given by Equation 3.130 return the first order upwind scheme (Equation 3.127). For this reason the hybrid scheme is only marginally better than the first order scheme.

Extension to second order

The extension of the first order upwind scheme to second order is obtained in the same way as in the shallow water equations (section 3.5). The conservative variables are extrapolated from the cell nodes to the cell faces with a MUSCL approach, using the two triangles associated to each cell face (Figure 3.4):

$$\begin{aligned} \mathbf{\Phi}_{Ij} &= \mathbf{\Phi}_i + \frac{1}{2}\mathbf{\Delta\Phi}_i^* \\ \mathbf{\Phi}_{iJ} &= \mathbf{\Phi}_j + \frac{1}{2}\mathbf{\Delta\Phi}_j^* \end{aligned} \tag{3.131}$$

with:

$$\mathbf{\Delta\Phi}_i^* = \begin{cases} \max\left[0,\, \min\left(\beta \nabla\mathbf{\Phi}_i \mathbf{r}_{ij},\, \mathbf{\Delta\Phi}_{ij} \right),\, \min\left(\nabla\mathbf{\Phi}_i \mathbf{r}_{ij},\, \beta\mathbf{\Delta\Phi}_{ij} \right) \right] & \text{if} \quad \mathbf{\Delta\Phi}_{ij} > 0 \\ \min\left[0,\, \max\left(\beta \nabla\mathbf{\Phi}_i \mathbf{r}_{ij},\, \mathbf{\Delta\Phi}_{ij} \right),\, \max\left(\nabla\mathbf{\Phi}_i \mathbf{r}_{ij},\, \beta\mathbf{\Delta\Phi}_{ij} \right) \right] & \text{if} \quad \mathbf{\Delta\Phi}_{ij} < 0 \end{cases}$$

with $\mathbf{\Delta\Phi}_{ij} = \mathbf{\Phi}_j - \mathbf{\Phi}_i$. In Equation 3.131, $\mathbf{\Phi}_{Ij}$ and $\mathbf{\Phi}_{iJ}$ are the extrapolated values on each side of the cell face L_{ij}, and $\mathbf{\Delta\Phi}_i^*$ and $\mathbf{\Delta\Phi}_j^*$ are the limited slopes. The value $\beta = 1$ gives the Minmod limiter, while the value $\beta = 2$ reproduces the Superbee limiter [134]. The extrapolated face values given by Equation 3.131 are used directly in Equation 3.126.

3.6.3 Discretisation of the source terms

All the source terms are discretised at the cell nodes using a centred scheme. Following the ideas of Davidson [32] all the negative source terms are included in the main diagonal of the system of equations in order to reinforce the stability of the scheme, and to help the turbulent variables to remain positive during the numerical computation. In order to do that, the source term is linearised as:

$$\mathbf{H} = \mathbf{H}_N^n \mathbf{\Phi}^{n+1} + \mathbf{H}_P^n \tag{3.132}$$

All the negative source terms are included in $\mathbf{H}_N^n$. The source terms in the $k-\varepsilon$ model are given by Equation 3.115. The production source terms $\mathbf{H}_2$ and $\mathbf{H}_3$ are always positive, and therefore are included explicitly in $\mathbf{H}_P^n$. The dissipation source term $\mathbf{H}_4$ is always negative, so it is included in $\mathbf{H}_N^n$ as:

$$\mathbf{H}_4 = \begin{pmatrix} -\varepsilon h \\ -c_{2\varepsilon}\dfrac{\varepsilon^2}{k}h \end{pmatrix} = \begin{pmatrix} -\dfrac{\varepsilon}{k} \\ -c_{2\varepsilon}\dfrac{\varepsilon}{k} \end{pmatrix}^n \begin{pmatrix} kh \\ \varepsilon h \end{pmatrix}^{n+1} \tag{3.133}$$

Finally, the diffusion term $\mathbf{H}_1$ may be positive or negative, and thus, it is included in $\mathbf{H}_P^n$ or $\mathbf{H}_N^n$ depending on its sign. With this considerations in mind, the terms $\mathbf{H}_N^n$ and $\mathbf{H}_P^n$ in Equation 3.132 are given by:

$$\begin{aligned} \mathbf{H}_N^n &= \min\left(\frac{\mathbf{H_1}}{\mathbf{\Phi}}, 0\right)^n + \begin{pmatrix} -\dfrac{\varepsilon}{k} \\ -c_{2\varepsilon}\dfrac{\varepsilon}{k} \end{pmatrix}^n \\ \mathbf{H}_P^n &= \max\left(\mathbf{H_1}, 0\right)^n + \mathbf{H_2}^n + \mathbf{H_3}^n \end{aligned} \tag{3.134}$$

and Equation 3.126 is replaced by:

$$\mathbf{\Phi}_i^{n+1}\left(1 - \mathbf{H}_{N,i}^n\right) = \left(1 - \frac{\Delta t}{A_i}a_i^n\right)\mathbf{\Phi}_i^n + \frac{\Delta t}{A_i}\sum_{j\in K_i} a_{ij}^n \mathbf{\Phi}_j^n + \Delta t \mathbf{H}_{P,i}^n \tag{3.135}$$

with the coefficients a_i and a_{ij} given by Equation 3.127.

3.7 Implementation of the depth averaged ASM

The depth averaged algebraic stress model proposed in section 2.5 needs to solve first the $k-\varepsilon$ equations in order to compute the turbulent kinetic energy, the dissipation and the eddy viscosity. The $k-\varepsilon$ equations are solved as explained in section 3.6, with the only difference that the turbulent kinetic energy production term P_k is computed directly from its exact expression using the

Reynolds stresses:

$$P_k = -\overline{u_i' u_j'} \frac{\partial U_i}{\partial x_j} = -\overline{u'^2} \frac{\partial U}{\partial x} - \overline{u'v'} \left(\frac{\partial U}{\partial y} + \frac{\partial V}{\partial x} \right) - \overline{v'^2} \frac{\partial V}{\partial y} \tag{3.136}$$

Once the $k - \varepsilon$ model is solved, the values of the turbulent kinetic energy, dissipation and eddy viscosity are directly plugged into the algebraic expressions given by Equation 2.105, in order to compute the Reynolds stresses at each cell node.

3.8 Implementation of the wall boundary condition

Depending on the mesh size, three different ways of implementing the wall boundary conditions have been explained in section 1.4, namely: the no-slip condition, wall functions and the slip condition.

3.8.1 No-slip condition

The no-slip condition is used either when the near wall mesh size is very fine ($y^+ \approx 1$) or when the flow is laminar. All the variables, except the water depth, are fixed at the wall boundary nodes:

$$q_{x,w} = q_{y,w} = 0 \qquad k_w = 0 \qquad \varepsilon_w = \nu \frac{\partial^2 k}{\partial y^2} \tag{3.137}$$

$$\overline{u'^2}_w = \overline{u'v'}_w = \overline{v'^2}_w = 0$$

where y is the normal direction to the wall. In turbulent flows this implementation requires a very fine mesh near the walls, with the first inner node at approximately $y^+ \approx 1$. It requires also to use low-Reynolds versions of the standard turbulence models, with near wall correction terms. This kind of approach has not been used in the practical applications in this thesis. This is because the extent of the computational domains, and the flow conditions, would require meshes with a number of nodes too large for the available computer power.

3.8.2 Wall functions

The second way of implementing the wall boundary condition is using wall functions. The main differences with the no-slip condition are: (1) the turbulent variables are fixed at the first inner nodes (log-law nodes in Figure 3.3(b)) and not at the boundary nodes; (2) it is the wall friction, and not the tangential velocity, that is imposed at the boundary nodes. The wall boundary conditions

are implemented as:

$$q_{y,w} = 0 \qquad \tau_w = \rho u_*^2 \qquad k_1 = \frac{u_*^2}{\sqrt{c_\mu}} \qquad \varepsilon_1 = \frac{u_*^3}{\kappa y} \tag{3.138}$$

$$\overline{u'^2}_1 = 3.63 u_*^2 \qquad \overline{u'v'}_1 = -u_*^2 \qquad \overline{v'^2}_1 = 0.825 u_*^2$$

where the subindex 1 refers to the values at the first inner node (log-law nodes), τ_w is the shear stress at the wall, which is imposed directly as a source term at the boundary faces, and u_* is the wall friction velocity, which is computed from the logarithmic law, using the mesh independent wall functions approach of Menter [90] (see section 1.4).

3.8.3 Slip condition

The slip condition is only used when the near wall mesh is very coarse, and therefore, the first inner node lies outside the logarithmic layer. It is difficult to fix a value where the boundary condition should change from logarithmic law to slip condition, and this is left to the user criterion. It should be noticed that the usual agreed limits for the validity of the logarithmic law are $11 < y^+ < 50 - 100$.

The slip condition sets to zero the normal velocity in the boundary wall nodes. The tangential velocity, as well as the water depth, are left free. The shear stress at the wall is neglected, as well as the diffusion of the turbulent quantities through the wall.

$$q_{y,w} = 0 \qquad \tau_w = 0 \qquad \left.\frac{\partial k}{\partial y}\right|_w = 0 \qquad \left.\frac{\partial \varepsilon}{\partial y}\right|_w = 0 \tag{3.139}$$

$$\left.\frac{\partial \overline{u'^2}}{\partial y}\right|_w = 0 \qquad \left.\frac{\partial \overline{u'v'}}{\partial y}\right|_w = 0 \qquad \left.\frac{\partial \overline{v'^2}}{\partial y}\right|_w = 0$$

where y is the normal direction to the wall.

3.9 Wet-dry fronts. The wet-dry condition

Many of the practical applications in which the shallow water equations are used include regions of the spatial domain that may be dry or wet due to changes in the water surface elevation. In those situations it appears a moving boundary, defined by a wet-dry front, which needs to be treated adequately in order to obtain accurate and stable results. Typical problems with wet-dry fronts include flood simulation, unsteady river flow, propagation of tidal waves in estuaries, and estimation of long wave runup in coastal regions, among others.

Several approaches exist in order to model the movement of the wet-dry front. Some models use a computational mesh that moves with the boundary, as for example the finite element models of Akanbi and Katopodes [1] and Stockstill et al. [129]. This approach is computationally very expensive, since the mesh must be regenerated each time the boundary moves, and may require the addition of new nodes in order to avoid an excessive deformation of the numerical cells.

A more common approach to the problem is to consider a fixed mesh, and to allow the control volumes to wet and dry. This approach is used by many researchers in finite volume models [19, 40, 49] as well as in finite element models [71, 131], and it has been the one adopted in the numerical solver.

A wet-dry tolerance parameter (ε_{wd}) is defined, so if the water depth in a cell is lower than ε_{wd}, the cell is considered to be dry. In the same way, if the mean water depth at the face L_{ij} is lower than ε_{wd}, the face is considered to be dry and it does not participate in the calculation. The water depth is never forced to zero, in order to keep the mass conservation property of the scheme. The wet-dry tolerance parameter helps to avoid negative water depths which might cause instabilities in the solution. The lowest value of ε_{wd} is desired in order to obtain accurate solutions. However, an excessively low value of ε_{wd} promotes the numerical instabilities and obliges to use a very small CFL, specially when dealing with a very irregular bathimetry.

The wet-dry tolerance parameter is also used in the turbulence models. In the dry cells ($h_i \leq \varepsilon_{wd}$) the eddy viscosity is set to zero and, in the case of the ASM and $k-\varepsilon$ models, the turbulent energy and dissipation are fixed to a residual value (ε_k and ε_{eps}), which is several orders of magnitude smaller than the minimum values expected in the flow. At the same time the production terms due to vertical and horizontal shear are set to zero ($P_{kv} = P_k = P_{\varepsilon v} = P_\varepsilon = 0$). The diffusion and convection terms are fixed to zero in the dry faces. When a cell is wet ($h_i > \varepsilon_{wd}$) but the water depth is very small, the vertical production term P_{kv} might become very large. In those situations, the production limiter given by Equation 2.89 helps to control the maximum value of P_{kv}, giving more stable results. Actually, the fact of limiting the vertical production allows using smaller values of the wet-dry tolerance parameter without producing instabilities in the $k-\varepsilon$ model.

The fix mesh approach needs a suitable wet-dry condition at the fluid interface which assures conservation of mass and momentum, and at the same time not diffusive and free of spurious

oscillations. If a well-balanced condition is not used, the dry cells may get artificially wet and non-physical movements of the free surface may appear under hydrostatic conditions, specially in the presence of large bed slopes. As it is detailed by Brufau in [17], this movement is a consequence of the difference between the computed water depth and bed elevation gradients. The ideas of Brufau et al. [19] with a slight modification in the reflection condition will be used here in order to deal with the wet-dry front.

In order to deal with the wet-dry front, a piecewise constant distribution of the bed elevation will be assumed (Figure 3.8). This is the usual finite volume approach, used when computing the convective flux with a first order upwind scheme. When used with a correct numerical scheme, this approach is able to capture discontinuities in the solution without diffusing them, which is a very valuable feature when dealing with large bed slopes or discontinuities in the bed elevation, i.e. vertical walls.

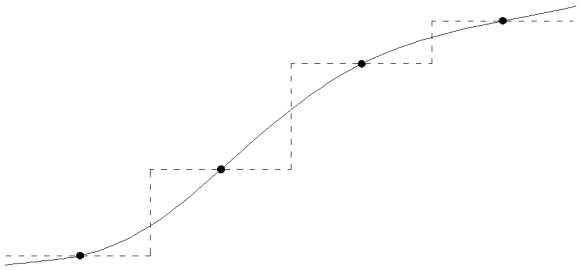

Figure 3.8: Discretisation of the bed elevation.

Assuming a constant bed elevation in each cell, there are two conditions which need to be imposed at the wet-dry fronts: (1) redefinition of the bed elevation; (2) reflection condition.

The aim of redefining the bed elevation is to obtain an exact balance at the wet-dry front between the bed slope and the hydrostatic pressure terms for hydrostatic flow. If the bed slope is not redefined, spurious waves are generated at the front, which may be stronger or weaker depending on the slope gradient and on the flow conditions. If the wet-dry front occurs between the cells C_i and C_j, the increment in the bed elevation at the front ($\Delta z_{b,ij}$) is defined as:

$$\Delta z_{b,ij} = \begin{cases} h_i - h_j & \text{if} \quad h_j \leq \varepsilon_{wd} \quad \text{and} \quad h_i < z_{b,j} - z_{b,i} \\ z_{b,j} - z_{b,i} & \text{otherwise} \end{cases} \tag{3.140}$$

where it has been assumed without loss of generality that the cell C_i is always the wet one. The modified bed slope is given by $\Delta z_{b,ij}$, h is the water depth, z_b is the bed elevation, and ε_{wd} is the wet-dry tolerance parameter. Note that only the first condition in 3.140 modifies the real bed elevation.

The treatment of the wet-dry fronts given by Equation 3.140 gives the exact hydrostatic flow so-

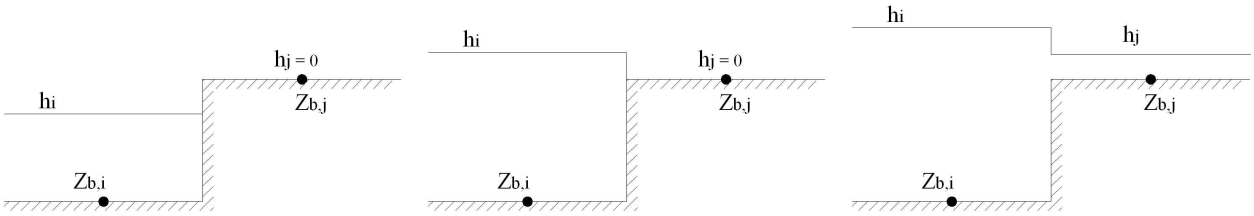

(a) Bed redefinition $\Delta z_{b,ij} = h_i$. Reflection condition $q_{ij} = 0$

(b) No redefinition. No reflection condition

(c) No redefinition. No reflection condition

Figure 3.9: Wet-dry front.

lution for any bed elevation without diffusing the front. In order to prove that, the first order scheme of van Leer will be applied to hydrostatic flow with the bed slope defined by Equation 3.140. The numerical flux and source terms computed by the van Leer's scheme with an upwind treatment of the source terms were obtained in section 3.5.7, and are given by Equations 3.89 and 3.90. The necessary condition in order to show that the numerical flux balances exactly the source term, is given by $z_{b,i} + h_i = z_{b,j} + h_j$, which is a constant free surface elevation condition. This is always fulfilled in hydrostatic wet domains. However, in a wet-dry front like that one shown in Figure 3.9(a) this condition does not apply unless the bed slope is modified as it is defined in Equation 3.140, in which case the exact balance in the momentum equation is obtained. In other case the water would climb through the front in order to balance the equations, diffusing in such a way the wet-dry front.

In a general case the velocity on the left wet cell is different from zero ($q_i \neq 0$). In this situation the reflection condition fixes the normal unit discharge at the wet-dry front ($q_{n,ij}$) to zero when computing the numerical flux, which actually is the kinetic condition at any wall or surface.

$$q_{n,ij} = q_{x,ij}\tilde{n}_{x,ij} + q_{y,ij}\tilde{n}_{y,ij} = 0 \tag{3.141}$$

where the subindex ij refers to the interface values. Condition 3.141 only applies when $h_i < z_{b,j} - z_{b,i}$ (Figure 3.9(a)). The fact of setting the normal unit discharge to zero at the interface is justified by the assumption of a constant bed elevation in each cell with discontinuities at the cell faces, which is similar to have a set of small vertical walls (Figure 3.8). In this way the wet-dry front is only allowed to advance when the water depth in the wet cell is larger than the bed step between cells ($h_i > z_{b,j} - z_{b,i}$, Figure 3.9(b)). It should be noticed that the unit discharge is not set to zero in the left cell, but only at the face L_{ij} when computing the numerical flux at the wet-dry front.

Condition 3.141 also assures that the convective transport of k and ε is zero at wet-dry fronts with $h_i < z_{b,j} - z_{b,i}$ (Figure 3.9(a)). In these cases the diffusive flux of k and ε over the face L_{ij} is also set to zero.

Chapter 4

Code validation

4.1 Introduction

In chapter 3, a numerical solver for the depth averaged shallow water equations has been presented and discussed. In this chapter the solver is applied to simple flow conditions in order to verify its correct behaviour. The evaluation of the convective flux with the first order van Leer's and Roe's schemes, as well as the upwind discretisation of the bed slope source term, have been taken from previous works of Vázquez-Cendón [143]. A detailed description of the performance of those schemes can be found in [10, 143, 144]. Here we will focus on the diffusion term as well as in the turbulence models. The performance of the second order extension of van Leer's and Roe's schemes, and the treatment of wet-dry fronts are also checked. Three simple channel flow conditions will be used in this chapter:

- Uniform channel flow.
  It is the flow taking place in the centre region of an infinitely wide rectilinear channel. The flow is homogeneous in the transverse direction, and thus, it can be modelled using either the 2D or the 1D shallow water equations.

- Laminar channel flow.
  It is the flow in a finite width channel when the Reynolds number is small enough, and turbulence has not yet developed.

- Turbulent channel flow.
  It is the flow in a finite width channel when the Reynolds number is large, and turbulence is fully developed.

It should be noticed that a turbulence model cannot predict whether the flow is laminar or turbulent. Therefore, when the flow is laminar the eddy viscosity must be set to zero.

4.2 Some hydrostatic flow computations

The hydrostatic flow condition is given by:

$$q_x = 0 \qquad q_y = 0 \qquad z_b + h = \text{cte} \tag{4.1}$$

Despite the simplicity of the flow conditions, if a correct discretisation of the bed slope source term is not used the solution may show spurious waves, as it has been pointed out in previous works by Bermúdez and Vázquez [10] and Brufau [17] among others. In hydrostatic conditions, the momentum equations reduce to a balance between the hydrostatic pressure gradient and the bed slope term (gravity force):

$$\frac{\partial h}{\partial x} = -\frac{\partial z_b}{\partial x} \qquad \frac{\partial h}{\partial y} = -\frac{\partial z_b}{\partial y} \tag{4.2}$$

From Equation 4.2 it is obvious that if the hydrostatic pressure gradient, which is included in the convective flux term, is discretised with an upwind scheme, it is also necessary to upwind the bed slope gradient in order to have a correct balance of momentum. In other case an error is introduced in the equations. In general, for small bed slopes the error is not large, but it can be important for steep bed gradients, as it will be shown in the following examples.

4.2.1 Example 1: steep bed slope

The hydrostatic flow in a rectilinear channel (Figure 4.1) with discontinuities in the bed elevation will be computed. The bed shape is given by:

$$z_b = \begin{cases} 0 & \text{if} \quad 0 \leq x < 2 \\ -1 & \text{if} \quad 2 \leq x < 4 \\ 1 & \text{if} \quad 4 \leq x < 6 \\ -1 & \text{if} \quad 6 \leq x < 8 \\ 0 & \text{if} \quad 8 \leq x \leq 10 \end{cases} \tag{4.3}$$

This bed shape can be found in many practical situations with submerged walls or ditches. The computations have been done in a 2D rectilinear channel with a relatively coarse mesh. Figure 4.1 shows the triangular mesh from which the control volumes are generated in the way it has been explained in section 3.5.1.

The hydrostatic solution is a constant free surface level, given by the water depth imposed at the right boundary. Table 4.1 summarises the 5 different discretisation schemes which have been applied to compute the hydrostatic solution. The results presented in this section apply to

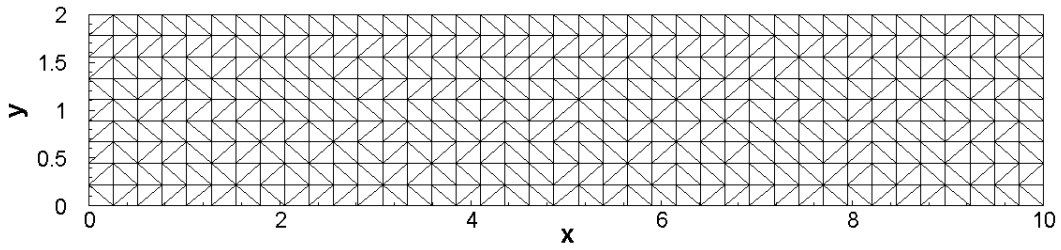

Figure 4.1: Triangulation of the numerical domain in a rectilinear channel.

both, van Leer's and Roe's schemes. Scheme A is the usual first order upwind scheme with a centred discretisation of the source term. As it was proved in chapter 3, this scheme generates non-physical oscillations of the free surface (Figure 4.2(a)). The oscillations are even larger for the unit discharge (Figure 4.2(b)). The exact solution is obtained with Scheme B, which uses a first order upwind discretisation of the bed slope. However, when the second order extension of the upwind schemes is used to discretise the convective flux, spurious waves appear again, even if the source term is also upwinded with a second order scheme (Scheme C). The exact solution is recovered again with Scheme D, where the second order extension is only used to compute the unit discharges, while keeping the first order upwind approximation for the water depth and the bed slope. Scheme D is first order in h and z_b, and second order in q_x and q_y. In order to obtain a fully second order scheme free of spurious oscillations, Scheme E uses the second order upwind discretisation for all the variables, including the source term, but with a second order correction of the bed slope source term, as it has been explained in section 3.5.7.

	Convective Flux	Bed slope	Exact hydrostatic solution?
Scheme A	Upwind order 1	Centred	No
Scheme B	Upwind order 1	Upwind order 1	Yes
Scheme C	Upwind order 2	Upwind order 2	No
Scheme D	Upwind order 122	Upwind order 1	Yes
Scheme E	Upwind order 2	Upwind order 2 mod	Yes

Table 4.1: Discretisation schemes for computing hydrostatic flow.

Most of the practical applications in this thesis have been computed with Scheme D. Although a comprehensive and systematic comparison between the schemes D and E has not been done, both of them have been used in some practical applications, obtaining similar results. Nevertheless, in problems with large water depth gradients, Scheme E is expected to be more accurate, but also more unstable. Scheme B introduces too much numerical diffusion, which produces too flattened velocity profiles. Scheme C has proved to work well if there are not steep gradients or discontinuities in the bed elevation.

The same hydrostatic solution has been computed on a smooth bed with a slope of 25%, in order to chech how the bed shape affects the results. In this case the spurious oscillations appearing in

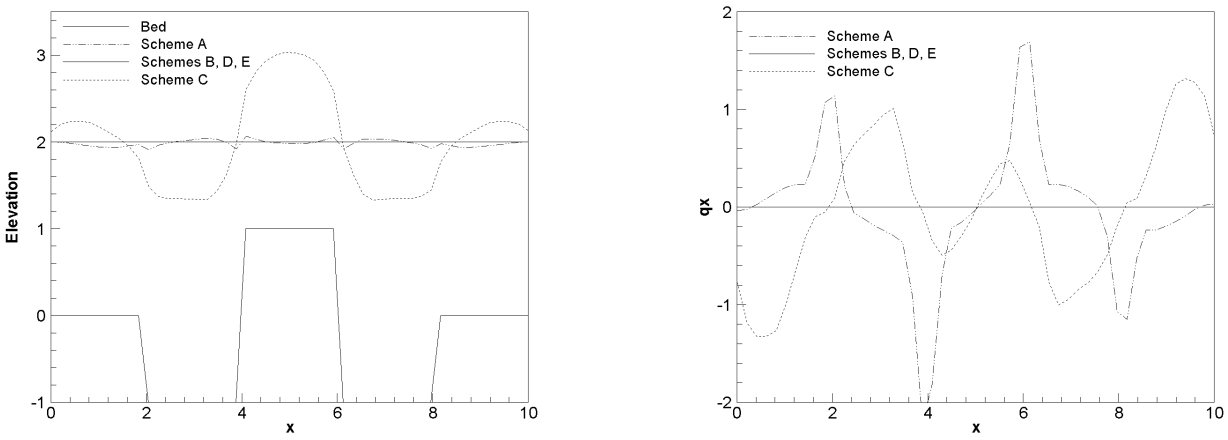

(a) Water surface elevation (b) Unit discharge q_x

Figure 4.2: Hydrostatic flow with steep bed gradient.

the free water surface are negligible, and cannot even be distinguish in Figure 4.3(a), although they exist. This is because the bed is much smoother. However, the oscillations in the unit discharge are still considerable (Figure 4.3(b)).

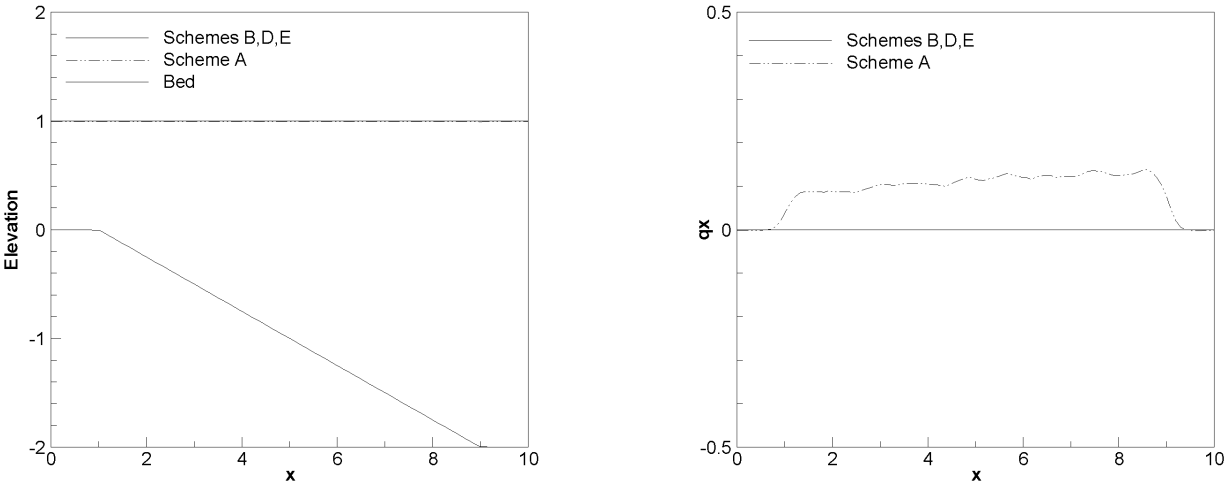

(a) Water surface elevation (b) Unit discharge q_x

Figure 4.3: Hydrostatic flow with smooth bed gradient.

Many practical situations in hydraulic engineering are defined by a smooth bed slope, specially in river and coastal engineering. In those cases the non-physical oscillations in the water level will be small and mixed up with real waves. On the other hand, in the presence of steep bed gradients or discontinuities in the bed elevation, the velocity oscillations may be larger and also more difficult to identify.

4.2.2 Example 2: steady wet-dry front

If the free surface level in example 1 is lowered to $0.5m$, the central part of the channel becomes dry, and a wet-dry front appears in the domain. If Roe's or van Leer's schemes are directly applied at the wet-dry front, the numerical method generates artificial movements of the free surface, even if the bed slope term is upwinded. Figure 4.4 shows the water surface elevation and unit discharge computed with and without the wet-dry treatment presented in section 3.9. Only the 3 schemes which give the exact solution in example 1 have been considered here (Schemes B, D, E). The solution given by the first order van Leer's scheme applied directly with no wet-dry front treatment is also shown.

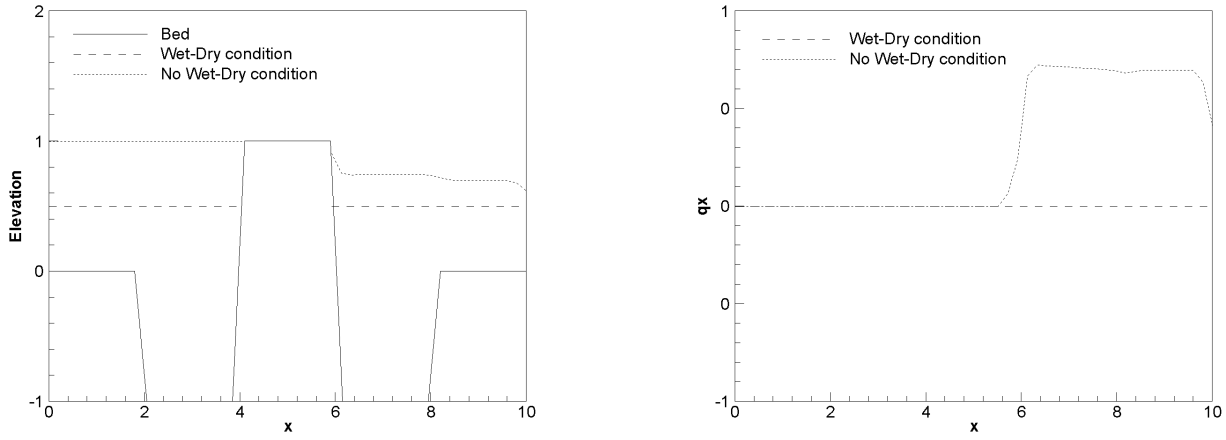

(a) Water surface elevation

(b) Unit discharge q_x

Figure 4.4: Hydrostatic flow with wet-dry front.

All the schemes compute the exact solution when the wet-dry condition is used. When no special treatment of the wet-dry front is done, the dry cells drag the water from the adjacent wet cells, raising up the water level and originating a water wave. Since at the left boundary the water depth is not fixed as boundary condition the water level is free to rise. This permits the wave originated at the wet-dry front to propagate completely until the left boundary. On the other hand, since the water depth is fixed at the right boundary, a water level gradient appears in that region.

4.3 Upwind discretisation of a mass source term in 1D channel flow

4.3.1 The 1D shallow water equations for a rectilinear channel

The 1D shallow water equations for a rectilinear channel can be obtained in a similar way as the 2D equations (section 2.3). Integrating the 3D shallow water equations over the channel cross section, and neglecting the dispersion terms which arise due to non-uniformities in the velocity and water depth, the 1D shallow water equations are obtained as [51]:

$$\frac{\partial A}{\partial t} + \frac{\partial Q}{\partial x} = S_1 \tag{4.4}$$

$$\frac{\partial Q}{\partial t} + \frac{\partial}{\partial x}\left(\frac{Q^2}{A}\right) + gA\frac{\partial \xi}{\partial x} = S_2$$

where $A(x,t)$ is the wet cross section, $Q(x,t)$ is the total water discharge, and S_1 and S_2 account for the source terms. If a rectangular section of constant width is assumed, Equation 4.4 can be simplified as:

$$\frac{\partial \mathbf{w}(x,t)}{\partial t} + \frac{\partial \mathbf{F}(w)}{\partial x} = \sum_k \mathbf{G_k}(x,w) \tag{4.5}$$

$$\mathbf{w} = \begin{pmatrix} h \\ q \end{pmatrix} \qquad \mathbf{F} = \begin{pmatrix} q \\ \frac{q^2}{h} + \frac{gh^2}{2} \end{pmatrix}$$

where the conservative variables are the water depth $h(x,t)$ and the discharge per unit width $q(x,t) = hu_x$. The vectors $\mathbf{G_k}$ account for the source terms. In this section the bed friction and diffusion terms will be neglected, in order to focus only on the discretisation of a mass/sink source term. Therefore, only the following two sources will be considered:

$$\mathbf{G_1} = \begin{pmatrix} 0 \\ -gh\frac{\partial z_b}{\partial x} \end{pmatrix} \qquad \mathbf{G_2} = \begin{pmatrix} m \\ 0 \end{pmatrix}$$

where the mass source $m(x)$ (mass per unit surface) can be defined by any function. The eigenvalues λ of the Jacobian matrix of the system of Equations 4.5 are given by:

$$\lambda_1 = \frac{q}{h} + c \qquad \lambda_2 = \frac{q}{h} - c \tag{4.6}$$

where $c = \sqrt{gh}$ is the wave celerity.

4.3.2 A steady state solution

In order to analyse the mass source term, a steady state solution will be used. Following the ideas of Vázquez-Cendón [144], a constant depth solution is proposed, and the bed shape is calculated in order to accomplish with this solution. After integration of the mass conservation equation, the unit discharge is obtained as:

$$q(x) = q(x_0) + \int_{x_0}^{x} m(x)\, dx \tag{4.7}$$

Since a solution with constant water depth is sought, the momentum conservation equation can be simplified as:

$$\frac{1}{h}\frac{\partial q^2}{\partial x} = -gh\frac{\partial z}{\partial x} \tag{4.8}$$

Integration of Equation 4.8 yields the following expression for the bed elevation:

$$z(x) - z(x_0) = -\frac{1}{gh^2}\left(q^2(x) - q^2(x_0)\right) \tag{4.9}$$

where the unit discharge $q(x)$ is given by Equation 4.7.

4.3.3 Numerical results

The convenience of upwinding the mass source term has been analysed by Cea et al. in [21], showing that, if the mass source term is upwinded, the steady solution given by Equation 4.9 is computed exactly. On the other hand, if a centred discretisation of the mass term is used, an error of first order in Δx is introduced in the solution. In the following numerical examples the bed friction has been neglected, and the effective viscosity has been set to zero.

Considering that for the steady solution proposed the water depth is constant in space, when adding a mass source to the flow, the speed will increase in the longitudinal direction, and so will do the Froude number. Depending on the boundary conditions and on the mass source, the flow may be always subcritical, always supercritical, or there might be a change from subcritical to supercritical flow inside the domain. These three situations were tested using the source terms and boundary conditions shown in Table 4.2.

Test case	mass	q_0	h_0	q_L	h_L	Fr_0	Fr_L
1	$m = 10x$	5.0	—	—	5.0	0.143	0.714
2	$m = x$	5.0	0.5	—	—	4.52	6.32
3	$m = 2x$	1.0	—	—	—	0.319	1.60

Table 4.2: Mass source terms and boundary conditions tested.

In the first test case the flow is always subcritical. The flow discharge is imposed upstream and the water depth is imposed downstream. In the second case the flow is supercritical, and thus, the

discharge and the water depth are fixed upstream. Finally, in the third case there is a change from subcritical to supercritical flow. In this case only the discharge is fixed upstream, and nothing is imposed downstream.

Figure 4.5(a) shows the results for the test case 1. A mesh with 20 inner nodes was used at first. When using the upwind discretisation of the source term the unit discharge is computed exactly, while a negligible error occurs in the water depth due to the implementation of the boundary condition. If a centred discretisation of the mass is used, a large error in the water depth appears, while the unit discharge is still quite accurate.

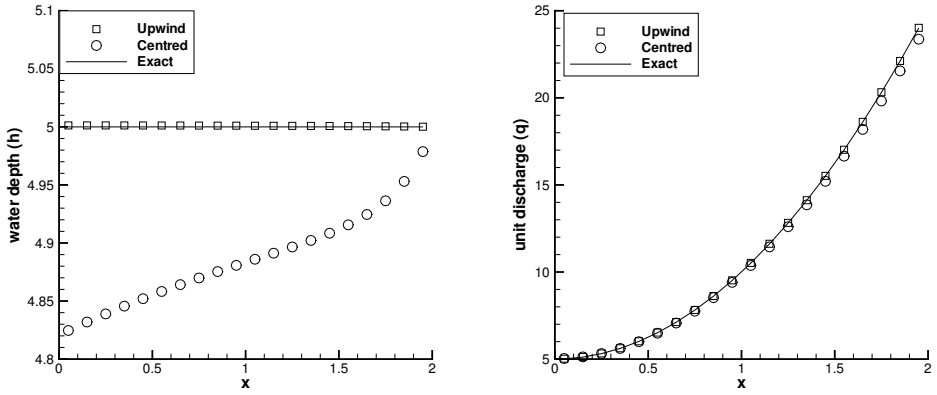

(a) 20 inner nodes.

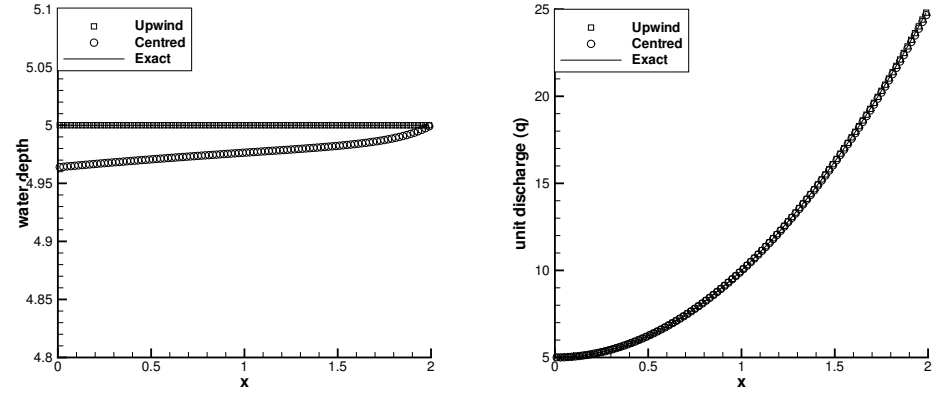

(b) 100 inner nodes.

Figure 4.5: Mass source term. Test case 1.

In order to see the influence of the mesh size in the solution, a more refined mesh with 100 inner nodes was used. With the refined mesh the error diminishes (Figure 4.5(b)), but still the results obtained with the centred discretisation in the refined mesh (100 nodes) are worse than those obtained with the upwind discretisation in the coarse mesh (20 nodes). Similar results have been obtained for test case 2 (see Figure 4.6) and test case 3.

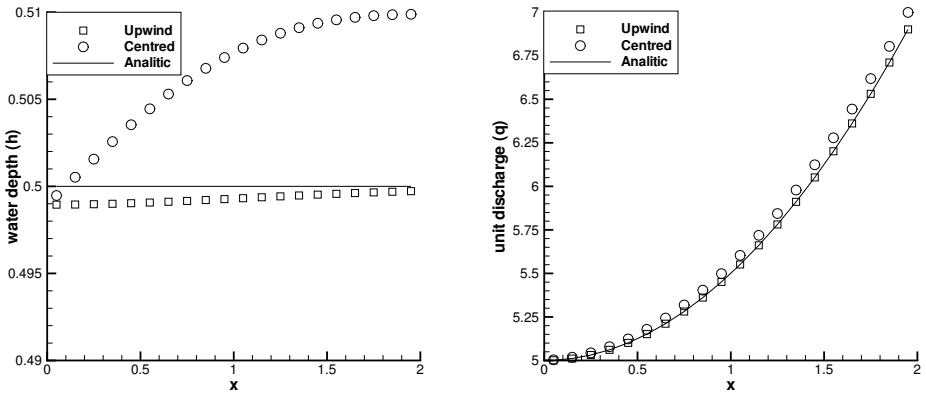

Figure 4.6: Mass source term. Test case 2. 20 inner nodes.

4.4 Viscous diffusion term in laminar channel flow

4.4.1 Fully developed laminar channel flow

The fully developed laminar flow in a rectilinear channel with constant bed slope will be used to test the discretisation of the viscous diffusion source term. In order to avoid the influence of other terms, the bed friction will be neglected. Since the flow is laminar, the no-slip condition has been used at the boundary walls.

The fully developed channel flow solution is, by definition, homogeneous in the longitudinal direction, i.e.:

$$\frac{\partial U}{\partial x} = \frac{\partial V}{\partial x} = \frac{\partial h}{\partial x} = 0 \tag{4.10}$$

Under this assumption, the transverse velocity V is obtained from the continuity equation as:

$$\frac{\partial hV}{\partial y} = 0 \qquad \rightarrow \qquad hV = 0 \qquad \rightarrow \qquad V = 0 \tag{4.11}$$

where it has been considered that the transverse velocity is zero at the walls, and that the water depth is not zero. Using the homogeneous conditions 4.10 and 4.11, the x and y momentum equations are simplified as:

$$0 = -g\frac{\partial z_b}{\partial x} + \nu\frac{\partial^2 U}{\partial y^2} \qquad\qquad \frac{\partial h}{\partial y} = 0 \tag{4.12}$$

Equation 4.12 is a balance between the bed slope term (gravity force) and the viscous shear stress. The solution of Equation 4.12 with no-slip wall boundary conditions is given by the parabolic profile:

$$U(y) = \frac{g}{\nu}\frac{\partial z_b}{\partial x}\left(\frac{y^2}{2} - Ly\right) \tag{4.13}$$

where the channel width is equal to $2L$. The maximum velocity, which occurs at the centre line (U_{cl}), is equal to:

$$U_{cl} = -\frac{gL^2}{2\nu}\frac{\partial z_b}{\partial x} \tag{4.14}$$

The total discharge is obtained after integration of the mean velocity over the transverse direction, as:

$$Q = h\int_0^{2L} U(y)\,dy = \frac{4}{3}hLU_{cl} \tag{4.15}$$

4.4.2 Numerical results

The velocity profile given by the exact solution (Equation 4.13) depends on the kinematic viscosity ν, on the bed slope ($\frac{\partial z_b}{\partial x}$), and on the channel width ($2L$). The following non-dimensional values have been used in the numerical computations:

$$\nu = 0.1 \qquad \frac{\partial z_b}{\partial x} = -\frac{1}{g} \qquad L = 1 \qquad h = 15 \tag{4.16}$$

With these values the exact solution is given by:

$$U = 5(2y - y^2) \qquad Q = 100 \tag{4.17}$$

The flow is subcritical, with a maximum Froude number of $Fr_{max} = 0.41$ at the centre-line. The Reynolds number based on the channel width and on the centre line velocity is $Re = \frac{2LU_{cl}}{\nu} = 100$. The numerical computations have been done in a rectilinear channel. A uniform velocity profile is imposed at the inlet boundary, and the wall boundary layer is allowed to develop as the viscous stresses propagate from the wall into the fluid, until the velocity profile is fully developed. The water depth is imposed at the outlet boundary. Assuming that the viscous stresses propagate from the wall into the fluid in a similar way as they do in a Blasius laminar boundary layer, the propagation depth δ can be approximated as:

$$\delta \approx \sqrt{4\nu t} \approx \sqrt{\frac{4\nu x}{U_{cl}}} \tag{4.18}$$

which, using the flow parameters given by 4.16, yields:

$$\delta \approx \sqrt{0.08x} \tag{4.19}$$

According to Equation 4.19, the flow should be fully developed at approximately $x_{fd} \approx 12$.

The triangular mesh size used in the computations is similar to that one shown in Figure 4.1, but the mesh size of the triangles in this case is $\Delta x = 0.2, \Delta y = 0.1$, and the length of the domain

is 20 (based on the former approximation of x_{fd}).

When comparing the numerical and exact solutions we should look not only at the velocity profile at the end of the channel, but also at the water depth gradient, which should be zero once the flow is fully developed. A non-zero water depth gradient has the effect of an additional source in the momentum equations, which is not present in the original equations.

The first and second order upwind schemes of Roe and van Leer have been used in the numerical computations. An upwind discretisation scheme has always been used for the bed slope term. The diffusion term has been discretised with an upwind as well as a centred scheme, without finding any significant difference in the results. The second order extension of the upwind schemes improves the results in a significant way (Figure 4.7). The accuracy of the results obtained with the hybrid first/second order scheme (order 122 in Figure 4.7), and the fully second order scheme (order 2) is similar.

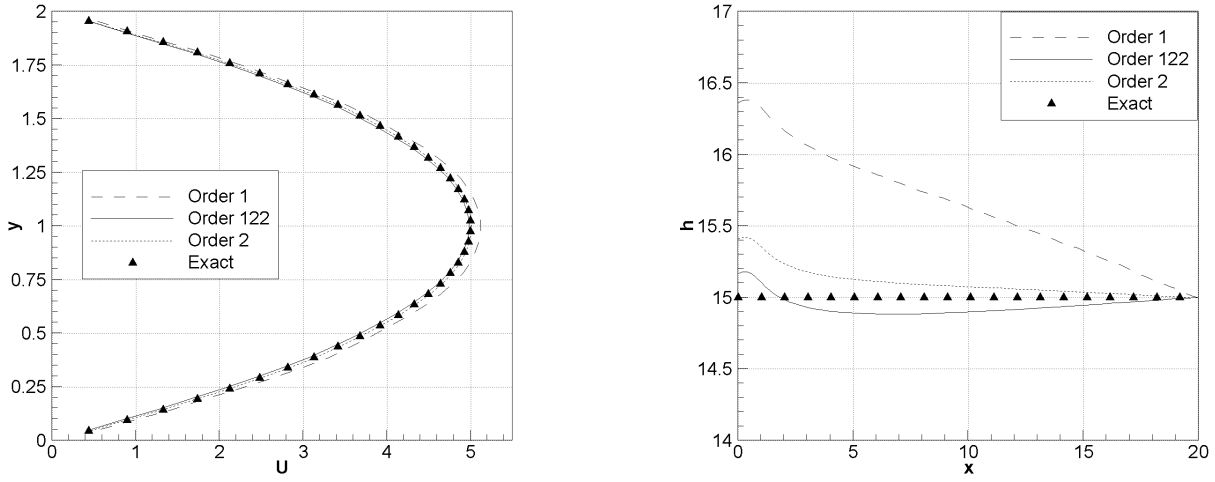

(a) Velocity profile U at $x = 19$.

(b) Water depth h

Figure 4.7: Laminar channel flow. Velocity profile and water depth.

Near the entrance of the channel the wall friction is rather large, because a uniform velocity profile is imposed as upstream boundary condition, which creates a high velocity gradient near the wall. As the boundary layer develops, the wall friction diminishes until it reaches an equilibrium value which corresponds to fully developed flow. The higher friction near the entrance is balanced by an increment in the water depth gradient, as it can be observed in Figure 4.7(b). When the flow is fully developed the water depth gradient should be zero. It should be noticed that with the first order scheme a significant water depth gradient remains in the fully developed region, which is due to the lack of accuracy of the scheme. All the schemes compute rather well the velocity profile at the end of the channel (Figure 4.7(a)). However, for the same velocity profile, the first order scheme produces larger shear stresses. This is because the numerical diffusion of the scheme is larger, and it is the reason why a non-zero water depth gradient is created in order to balance the

additional shear produced by the scheme.

Figure 4.8 shows the evolution of the velocity profile at different cross sections, as well as the evolution of the centre-line velocity. Between $x = 10$ and $x = 15$ the flow reaches the fully developed state, which agrees fairly well with the approximation of x_{fd} based on the Blasius boundary layer.

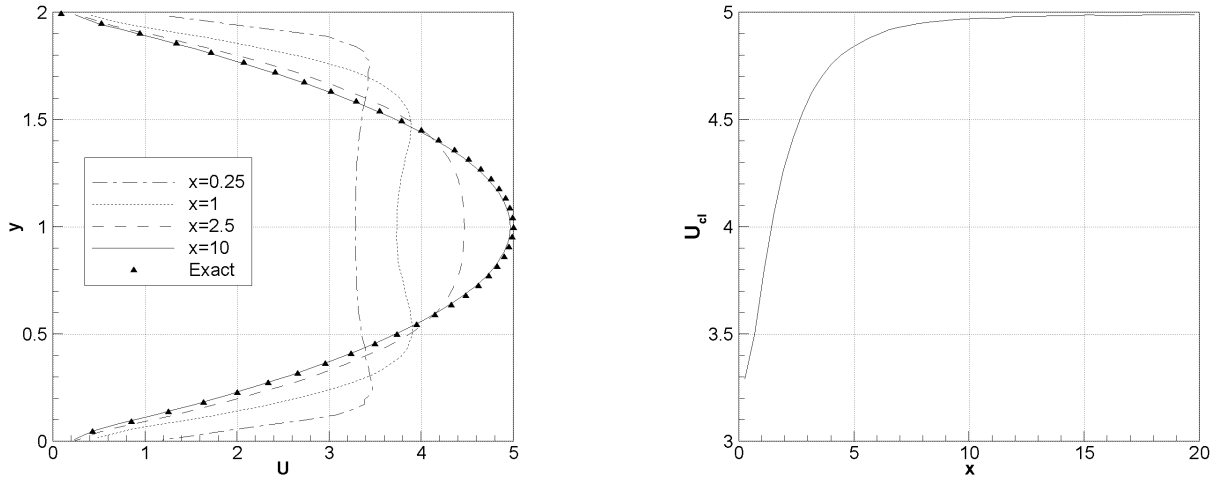

(a) Velocity profile U

(b) Velocity at the centre line U_{cl}

Figure 4.8: Laminar channel flow. Evolution of the velocity profile. Second order scheme

4.5 Turbulent channel flow

In the previous section the numerical discretisation of the diffusion term has been verified for laminar channel flow. In this section the turbulence models presented in chapter 2 will be tested for turbulent channel flow. Since no analytical solution exists for this situation, some LES and DNS results for fully developed 2D incompressible channel flow will be used for comparison [94].

4.5.1 Fully developed turbulent channel flow

Under the fully developed flow hypothesis in a constant slope rectilinear channel, neglecting the bed friction, the momentum equations for turbulent flow reduce to:

$$0 = -g\frac{\partial z_b}{\partial x} + \frac{\partial}{\partial y}\left((\nu + \nu_t)\frac{\partial U}{\partial y}\right) \qquad V = 0 \qquad h = \text{cte} \tag{4.20}$$

where the Boussinesq assumption has been used to model the Reynolds stresses. If the ASM is used, the turbulent diffusion term in Equation 4.20 should be replaced by:

$$\frac{\partial}{\partial y}\left(\nu_t \frac{\partial U}{\partial y}\right) \qquad \rightarrow \qquad -\frac{\partial \overline{u'v'}}{\partial y} \tag{4.21}$$

Equation 4.20 is equivalent to the x-momentum equation for 2D incompressible flow in a fully developed channel boundary layer, with the pressure gradient given by $\frac{\partial P}{\partial x} = \rho g \frac{\partial z_b}{\partial x}$. Hence, the numerical results will be compared with fully developed boundary layer LES and DNS calculations in a rectilinear channel [94]. The integration of the x-momentum equation (Equation 4.20) over the channel width ($2L$) gives the relation between the wall shear stress and the bed slope:

$$0 = -g\frac{\partial z_b}{\partial x} 2L + \left(\left.\frac{\tau_w}{\rho}\right|_{y=2L} - \left.\frac{\tau_w}{\rho}\right|_{y=0} \right) \tag{4.22}$$

Considering the symmetry between the upper and lower walls ($\tau_w(y = 2L) = -\tau_w(y = 0)$), the wall friction velocity is given by:

$$\left.\frac{\tau_w}{\rho}\right|_{y=0} = u_*^2 = -gL\frac{\partial z_b}{\partial x} \tag{4.23}$$

Equation 4.23 can be introduced in the x-momentum Equation 4.20 to give:

$$0 = \frac{u_*^2}{L} + \frac{\partial}{\partial y}\left((\nu + \nu_t)\frac{\partial U}{\partial y}\right) \tag{4.24}$$

The non-dimensional variables will be defined as:

$$\tilde{U} = \frac{U}{u_*} \qquad \tilde{\nu}_t = \frac{\nu_t}{u_* L} \qquad \tilde{y} = \frac{y}{L} \tag{4.25}$$

Using the dimensional relations 4.25 in Equation 4.24 yields:

$$0 = 1 + \frac{1}{R_*}\frac{\partial^2 \tilde{U}}{\partial \tilde{y}^2} + \frac{\partial}{\partial \tilde{y}}\left(\tilde{\nu}_t \frac{\partial \tilde{U}}{\partial \tilde{y}}\right) \tag{4.26}$$

where $R_* = \frac{L u_*}{\nu}$ is a Reynolds number based on the wall friction velocity. The non-dimensional momentum equation depends only on the parameter R_*. The dependence of the original shallow water equations on the Froude number has been eliminated by assuming a constant water depth.

4.5.2 A boundary layer code for fully developed turbulent channel flow

The numerical computations have been done with the 2D shallow water equations solver described in chapter 3, as well as with a 1D boundary layer code for fully developed turbulent channel flow which solves directly Equation 4.20 coupled with a turbulence model.

The boundary layer code has been used with several turbulence models: a mixing length model with damping function, a low-Reynolds-number $k-\varepsilon$ model by Rahman et al. [112], and a standard Reynolds Stress Turbulence Model (RSTM). Wall functions were used as boundary condition with the mixing length and the RSTM, while the low-Reynolds $k-\varepsilon$ model was integrated down to the wall using the no-slip condition. Since the boundary layer code solves a diffusion equation, it is not necessary to use an upwind scheme. Instead a second order centred finite volume scheme was used.

The 2D shallow water code has been used with the mixing length model, the standard 2D $k-\varepsilon$ model and the 2D algebraic stress model. In all the cases a wall function approach was used at the wall.

The results given by a boundary layer code are difficult to improve with Navier-Stokes models [126]. The 1D boundary layer code is expected to perform better than the 2D shallow water code for several reasons: (1) it solves the exact diffusion equation, and therefore, no error is introduced in the discretisation of the convective flux, which is exactly zero; (2) the numerical mesh is exactly aligned with the velocity gradient, avoiding discretisation errors due to the non-orthogonality of the cell faces and the flux in unstructured meshes; (3) it is much easier to obtain a higher order of accuracy in the spatial discretisation; (4) the numerical scheme is more stable.

The same number of nodes in the transverse direction have been used in the boundary layer and shallow water computations. Only half part of the channel has been modelled with the 1D boundary layer code, applying a symmetry boundary condition at the centre line. The symmetry boundary condition sets to zero all the derivatives in the transverse direction at the centre line of the channel, except for the Reynolds stress $\overline{u'v'}$, which is fixed to zero:

$$\left.\frac{\partial U}{\partial y}\right|_{cl} = 0 \qquad \left.\frac{\partial \varepsilon}{\partial y}\right|_{cl} = 0 \qquad \left.\frac{\partial k}{\partial y}\right|_{cl} = 0 \qquad (4.27)$$
$$\left.\frac{\partial \overline{u'^2}}{\partial y}\right|_{cl} = 0 \qquad \left.\frac{\partial \overline{v'^2}}{\partial y}\right|_{cl} = 0 \qquad \left.\overline{u'v'}\right|_{cl} = 0$$

where the subindex cl refers to the centre line of the channel.

4.5.3 Numerical results

The numerical results will be compared with LES data obtained for a Reynolds number of $R_* = 2000$, and DNS data for a Reynolds number of $R_* = 395$. For these flow conditions the mean

velocity over a cross section is around $20u_*$, which gives a Reynolds number based on the mean velocity equal to $R_U \approx 40000$ for $R_* = 2000$, and $R_U \approx 8000$ for $R_* = 395$.

The numerical computations have been done with the following non-dimensional parameters:

$$L = 1 \qquad u_* = 1 \qquad \nu = \frac{1}{R_*} \tag{4.28}$$

According to Equation 4.23, the bed slope is fixed to a constant value of:

$$\frac{\partial z_b}{\partial x} = -\frac{u_*^2}{gL} = -\frac{1}{g} \tag{4.29}$$

The governing Equation 4.20 does not depend on the water depth, since its value is constant in fully developed conditions. In the numerical calculations the water depth is given by the boundary conditions. Depending on its value the flow may be subcritical or supercritical. Several water depths were used in the computations in order to verify its possible influence on the results. No significant differences were found in the solution.

The value of the velocity imposed as upstream boundary condition has been obtained from integration of the LES/DNS velocity profiles as:

$$U_{in} = \frac{Q}{2L} = \frac{h}{2L}\int_0^{2L} U(y)\, dy \tag{4.30}$$

where $U(y)$ is the velocity profile given by the LES/DNS calculations.

Numerical mesh

A uniform velocity profile has been used as upstream boundary condition, in order to allow the turbulent boundary layer to develop along the channel. This is a rather slow process, and therefore, the channel must be long enough. Usually it is assumed that, depending on the geometry, it takes between 100 and 200 diameters to achieve a fully developed turbulent channel flow profile. Based on this approximation, a computational domain with a length of $200L$ has been used in the numerical simulations. The triangular mesh size is $\Delta x \approx 1.5, \Delta y \approx 0.05$. The distance from the first inner node to the wall is approximately $y^+ \approx 50$.

Computations with the mixing length turbulence model

In order to reduce the shallow water mixing length model to the correspondent 2D model, the bed friction has been neglected, and the water depth has been assumed to be large enough so that the turbulent length scale is given by the wall distance rather than being given by the water depth. Under these assumptions, in a fully developed boundary layer the mixing length model

(Equation 2.69) reduces to:

$$\nu_t = l_s^2 \frac{\partial U}{\partial y} \qquad l_s = \kappa y \tag{4.31}$$

The simplicity of the model does not allow it to account properly for the development of the boundary layer, since it assumes that turbulence is in an equilibrium state. The mixing length model, as formulated in Equation 4.31, gives rather poor results because it predicts too large values for the eddy viscosity, which flattens too much the velocity profile. This problem is generally solved by using damping and limiting functions [34], which limit the value of the turbulent length scale l_s. In order to show the improvement obtained in the numerical results, the following definition of the turbulent length scale has been used:

$$l_s = \min\left(\kappa y, 0.09L\right) \tag{4.32}$$

It should be noted that the value of 0.09 is specific for plane channel flow [148], and it is not a general value. In addition, in shallow water flows the turbulent length scale is usually given by the water depth rather than by the wall distance. For this reason this kind of limits can only be used in very specific flow configurations. Nevertheless, it will be used in this chapter in order to verify the numerical code. Figure 4.9(a) shows the comparison between the velocity profile obtained with the mixing length model, with and without damping function. Both the first and second order upwind schemes have been used in order to show the need of using a second order discretisation to obtain accurate results. It should be noticed in Figure 4.9(b) that, when using the damping given by Equation 4.32, the eddy viscosity is reduced almost by a factor 3. Still, the first order upwind scheme with damping gives a more flattened velocity profile than the second order upwind scheme without damping. This means that the numerical diffusion given by the first order scheme is larger than the real turbulent diffusion.

The wall distance of the first inner node is $y^+ \approx 53$, which lies inside the logarithmic region. It is interesting to show the longitudinal profile of the water depth, as well as the evolution of the wall friction velocity over the length of the channel (Figure 4.10). As it has been noticed in section 4.4 for laminar channel flow, when using the first order upwind scheme, an almost constant water depth gradient appears along the channel (Figure 4.10(a)), which is not physically correct. This water depth gradient introduces an additional source term in the x-momentum equation, which is balanced by an increase in the wall friction, as it is shown in the longitudinal profile of the wall friction velocity (Figure 4.10(b)). Better results are obtained with the second order upwind scheme, which gives a more accurate wall friction velocity.

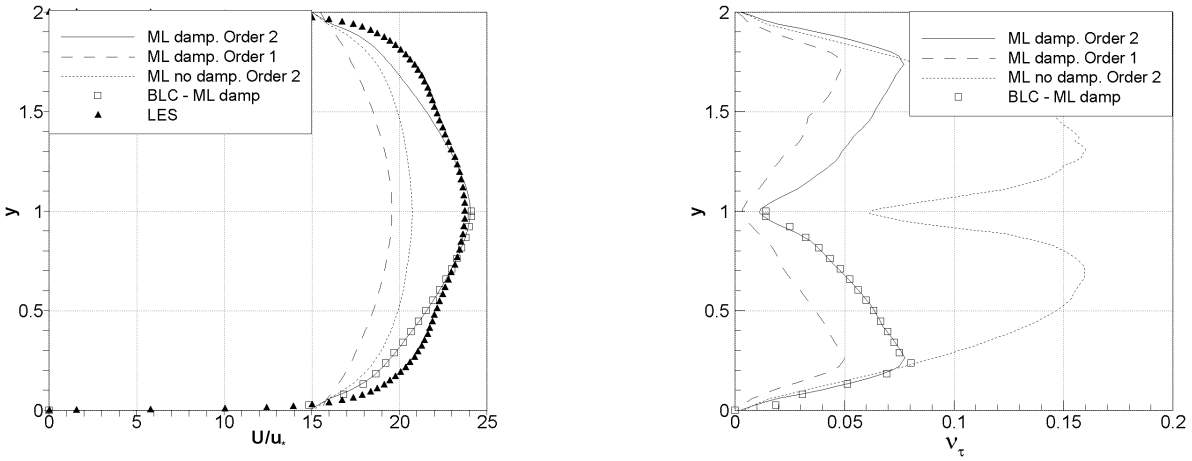

(a) Velocity profile $\frac{U}{u_*}$.

(b) Eddy viscosity ν_t.

Figure 4.9: Turbulent channel flow. Velocity and eddy viscosity profile. Mixing length model with and without damping. $R_* = 2000$. 2D-SWE and boundary layer code (BLC).

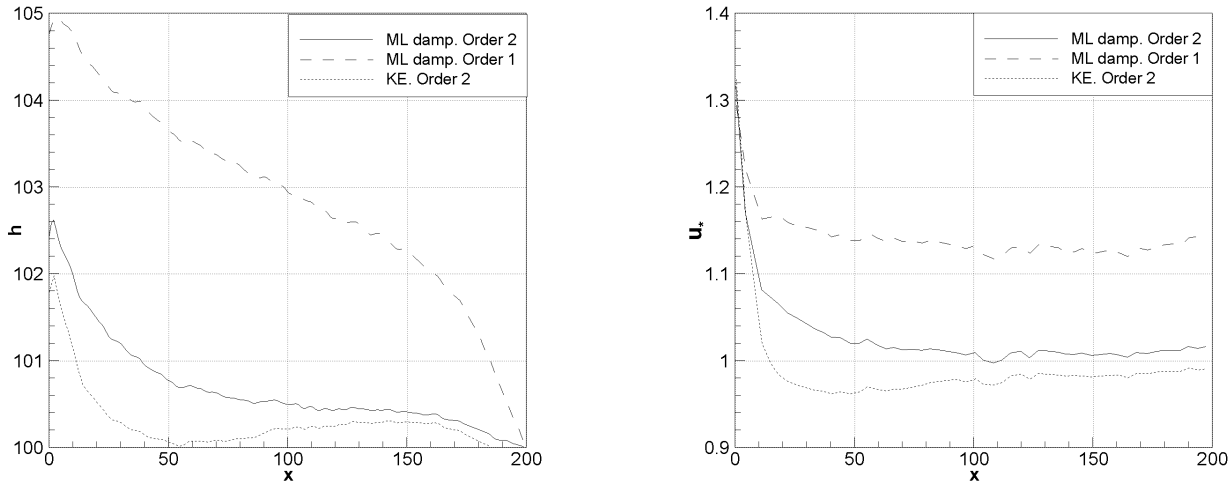

(a) Water depth h.

(b) Wall friction velocity u_*.

Figure 4.10: Turbulent channel flow. Longitudinal profiles. Mixing length model with damping, and $k - \varepsilon$ model. $R_* = 2000$.

Computations with the $k - \varepsilon$ turbulence model

When using the mixing length model to compute the turbulent channel flow, a specific damping function is needed in order to obtain accurate results. With the $k-\varepsilon$ model good results are obtained without using any damping function. Always under the assumptions given by Equation 4.10, the

transport equations of the $k-\varepsilon$ model can be simplified as:

$$
\begin{aligned}
0 &= \frac{\partial}{\partial y}\left((\nu+\frac{\nu_t}{\sigma_k})\frac{\partial k}{\partial y}\right)+\nu_t\left(\frac{\partial U}{\partial y}\right)^2-\varepsilon \\
0 &= \frac{\partial}{\partial y}\left((\nu+\frac{\nu_t}{\sigma_\varepsilon})\frac{\partial \varepsilon}{\partial y}\right)+c_{1\varepsilon}\frac{\varepsilon}{k}\nu_t\left(\frac{\partial U}{\partial y}\right)^2-c_{2\varepsilon}\frac{\varepsilon^2}{k}
\end{aligned}
\tag{4.33}
$$

$$
\nu_t = c_\mu \frac{k^2}{\varepsilon}
$$

Equations 4.33 are a balance between production, dissipation and diffusion of turbulence. The turbulent kinetic energy is generated near the wall, where the largest velocity gradients occur. From the walls, it diffuses to the centre of the channel.

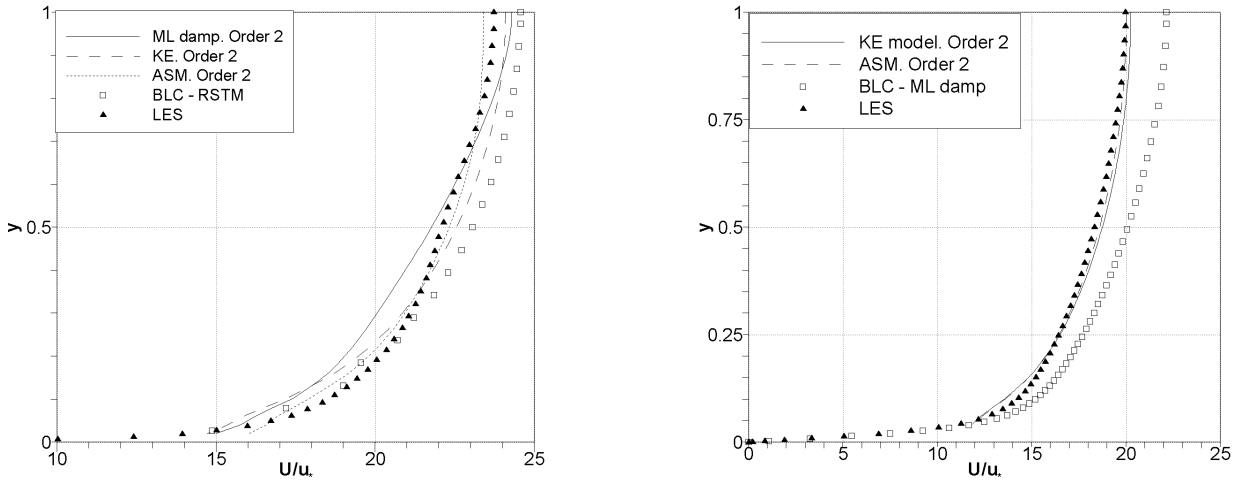

(a) $R_* = 2000$. (b) $R_* = 395$.

Figure 4.11: Turbulent channel flow. Velocity profiles with several turbulence models. 2D-SWE and boundary layer code (BLC).

The second order upwind scheme has been used in all the computations. The velocity results can be considered satisfactory (Figure 4.11), with a degree of accuracy similar to the boundary layer code with the standard RSTM. Concerning the turbulent variables, the $k-\varepsilon$ model gives acceptable results (Figure 4.12). However, the prediction of the Reynolds stresses is, as it could be expected, not accurate. Even the 1D boundary layer results show a considerable disagreement with the LES values.

Computations with the ASM

The depth averaged algebraic stress model for shallow water flows proposed in chapter 2 reduces to the 2D-ASM when the bed friction coefficient vanishes. The ASM can be considered as an extension of the $k-\varepsilon$ model. It is not computationally more expensive, since it is not necessary

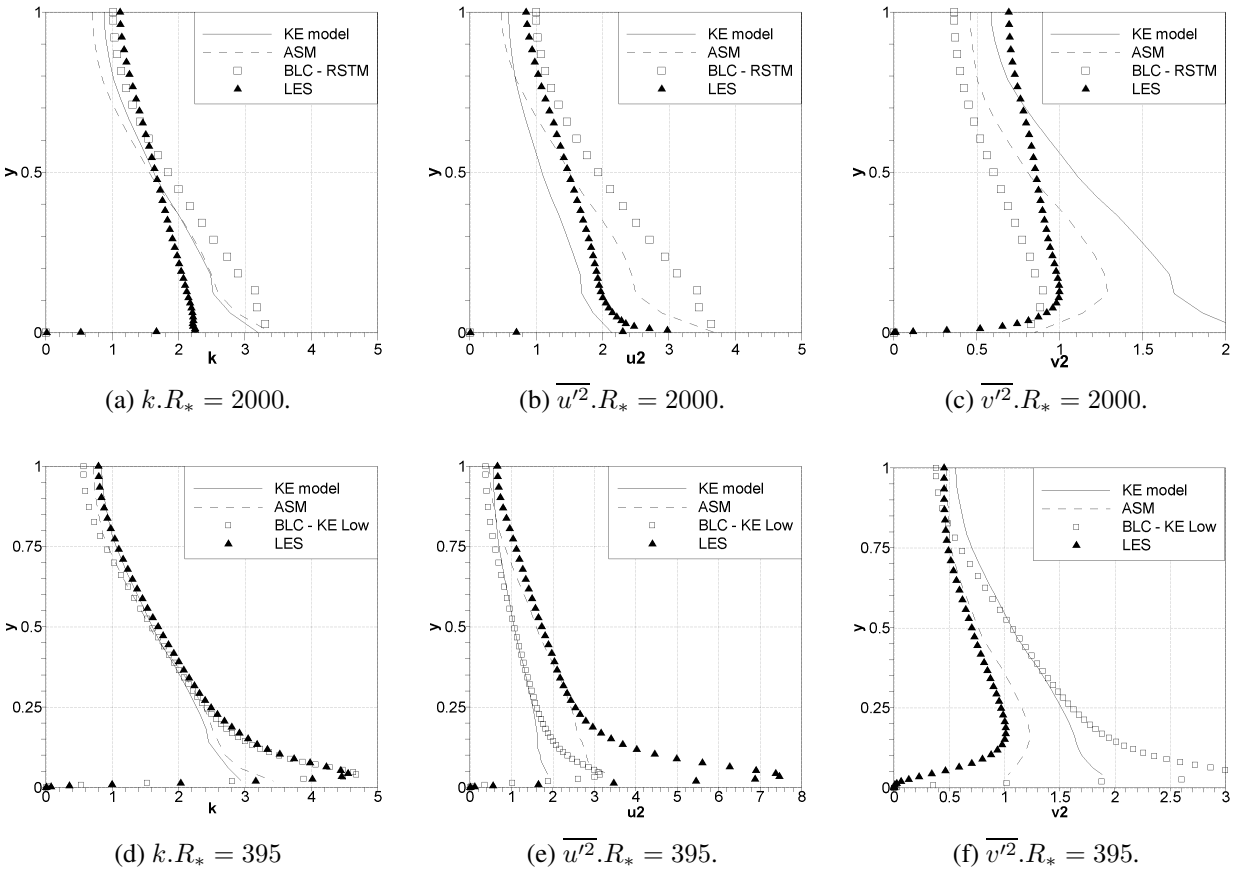

(a) $k.R_* = 2000$. (b) $\overline{u'^2}.R_* = 2000$. (c) $\overline{v'^2}.R_* = 2000$.

(d) $k.R_* = 395$ (e) $\overline{u'^2}.R_* = 395$. (f) $\overline{v'^2}.R_* = 395$.

Figure 4.12: Turbulent channel flow. Turbulent variables with ASM and $k - \varepsilon$ models. 2D-SWE and boundary layer code (BLC).

to solve any additional differential equation, but it is expected to be more unstable than the $k - \varepsilon$ model.

The mean velocity profile obtained with the ASM is similar to that one obtained with the $k - \varepsilon$ model (Figure 4.11). Similar results are also obtained for the turbulent kinetic energy (Figure 4.12(a,d)). Some differences appear in the Reynolds stresses, which are slightly more accurate with the ASM (Figure 4.12(b,c,e,f)). This is due to the assumption of isotropic eddy viscosity used in the $k - \varepsilon$ model. The ASM gives a higher degree of anisotropy between the turbulent stresses.

Part III

The Applications

Chapter 5

Shallow waves generated by bed and boundary movements

5.1 Introduction

Natural hazards such as tsunamis, avalanches or hill slope sliding in reservoirs have been studied with great interest in the last decades. One of the first researchers to carry out laboratory studies of gravity waves generated by the movement of submerged bodies was Wiegel in the fifties [146]. He performed one-dimensional experiments in a rectilinear flume and studied the properties of the waves generated (period, maximum wave height, ...) relating them with the characteristics of the generation movement (shape and dimensions of the submerged body, velocity, ...). These experiments have been carried out after Wiegel by other researchers [145, 58]. Not only the generation process, but also the runup of long waves on sloping surfaces have been studied experimentally in order to estimate the overtopping rate on coastal structures [36].

In the last years many numerical models have been developed in order to simulate the propagation and runup of long waves on the coast line [71, 70, 83, 82, 60, 61, 41]. The main advantage of using numerical models in the design of coastal structures is that they can be easily and rapidly applied to different geometries and wave conditions. After studying the overtopping rate of random waves on sloping seawalls, Dodd [40] concluded that solving the shallow water equations gives much better estimations than using empirical formulae. On the other hand, experimental tests are absolutely necessary in order to validate and define the limitations of the numerical models.

Some numerical models solve the 2D Navier-Stokes equations on a vertical plane in order to simulate solitary waves in a 1D flume [41, 82]. However, due to computer power requirements, these models are still not commonly used in 3D practical computations. For this reason, numerical models which solve the depth averaged shallow water equations with an adequate treatment of the coastline, where a wet-dry transition occurs, are much more common. Several studies have

been made in order to assess the performance of depth averaged models in long wave simulations [61, 60, 83, 71]. The accuracy of the results depends on the degree to which the shallow water approximations are fulfilled. Nevertheless, rather satisfactory results have been obtained even in situations where the shallow water hypotheses were expected to give poor results [60, 61].

In this chapter the 1D depth averaged shallow water equations are used to model the generation, propagation and reflection of shallow waves generated by bed and boundary movements. Experimental tests in a 1D flume have been done in order to compare with the numerical results. The wave generation in the experiments was achieved by the movement of a paddle with several slopes. An overtopping vertical wall was used as the reflection condition.

5.2 Experimental tests

5.2.1 Experimental procedure

The experimental tests were carried out in a $60cm$ wide by $15m$ long flume at the CITEEC's (Centro de Innovación Tecnolóxica en Edificación e Enxeñería Civil, University of A Coruña, Spain) hydraulics laboratory. The experimental results have been used to analyse the wave generation as well as the runup and reflection on the vertical overtopping wall.

The waves were generated by the horizontal movement of a slanted paddle, which was located at the beginning of the channel (Figure 5.1). The maximum paddle displacement was $0.59m$, and the maximum speed $0.59m/s$. The paddle moves forward at constant speed, and stays still after the forward movement has finished. The initial paddle acceleration, until it reaches a constant speed, as well as the final paddle deceleration, are fast enough to avoid considering them in the simulation. Thus, for modelling purposes it can be assumed that the paddle moves with constant velocity during the whole motion. Once generated, the wave propagates until it reaches a vertical wall of $36cm$ height. Depending on the initial water depth, on the paddle slope, and on the paddle speed, the wall may be overtopped or not by the wave. The water depth was measured at 5 locations (Table 5.1 and Figure 5.1) with conductivity-based depth probes (DHI Wave Gauge Type 202). The sampling rate of the gauges was set to $100Hz$. All the wave gauges were calibrated before each experimental test. The measurement error of the wave gauges is 0.7%. In order to verify the uncertainty in the measurements of the free surface elevation, every test was made twice, and no significant differences were observed in the experimental data (the difference in the free surface elevation was always smaller than 1%, i.e. the same order of magnitude as the wave gauge precision).

Four different water depths were used in the experiments: $15cm, 20cm, 25cm$ and $30cm$. For each water depth, three different paddle slopes were used ($45^o, 60^o$ and 90^o) combined with two different paddle movements, which will be addressed as slow movement and fast movement hereafter (Table 5.2). The origin of coordinates is defined as the point where the paddle intersects the

bottom of the flume once the generation movement has finished. In the tests in which the paddle slope is 45^o and 60^o, the wave gauge S1 was placed at the origin of coordinates. In the tests in which the paddle is vertical (90^o), the gauge S1 was attached to the paddle.

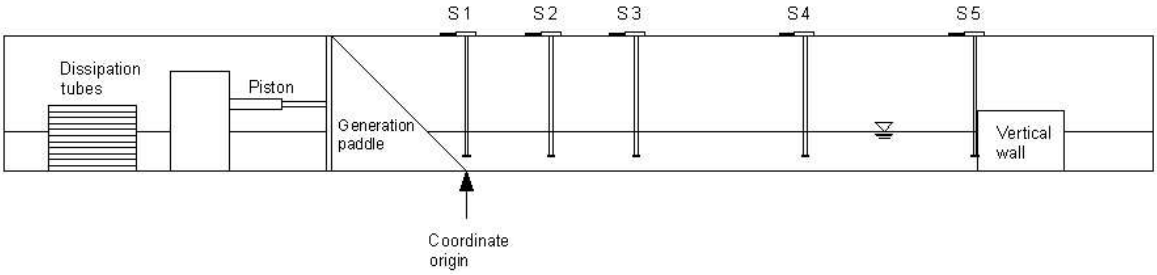

Figure 5.1: Wave generation and runup on a vertical wall. Experimental configuration.

	S1	S2	S3	S4	S5	Vertical wall
45^o and 60^o paddles	$0.00m$	$0.50m$	$1.00m$	$2.00m$	$3.00m$	$3.01m$
90^o paddle	Generation paddle	$0.50m$	$1.00m$	$2.00m$	$3.00m$	$3.01m$

Table 5.1: Position of the wave gauges in the experimental tests (see Figure 5.1).

	Slow movement	Fast movement
Amplitude	$0.58m$	$0.29m$
Velocity	$0.29m/s$	$0.58m/s$

Table 5.2: Movement of the generation paddle.

5.2.2 Characteristics of the waves generated

The height and period of the waves generated by both the slow and the fast paddle movements are defined in Table 5.3, Table 5.4 and Figure 5.2. The shallow water theory has been used to evaluate an approximated wave celerity C_{sw} as:

$$C_{sw} = \sqrt{g\left(d + \frac{H_{max,1} + H_{max,4}}{2}\right)} \tag{5.1}$$

where g is the gravity acceleration, d is the initial water depth, and $H_{max,1}$ and $H_{max,4}$ are the wave heights measured at the gauges $S1$ and $S4$. The experimental wave celerity C_{exp} is computed from the data registered by the wave gauges $S1$ and $S4$ as:

$$C_{exp} = \frac{x_4 - x_1}{t_4 - t_1} \tag{5.2}$$

where x_1 and x_4 are the position of the wave gauges S1 and S4, and t_1 and t_4 are the times at which the maximum water level is registered at the gauges S1 and S4. The characteristic wave length L

is defined as $L = C_{sw}T$, where C_{sw} is the wave celerity given by Equation 5.1, and T is the wave period, as defined in Figure 5.2. With these values, the ratio between the vertical and horizontal length scales can be evaluated as $\frac{d}{L}$. It should be noticed that the shallow water approximation assumes a separation of the horizontal and vertical scales, i.e. a ratio $\frac{d}{L}$ much smaller than 1.

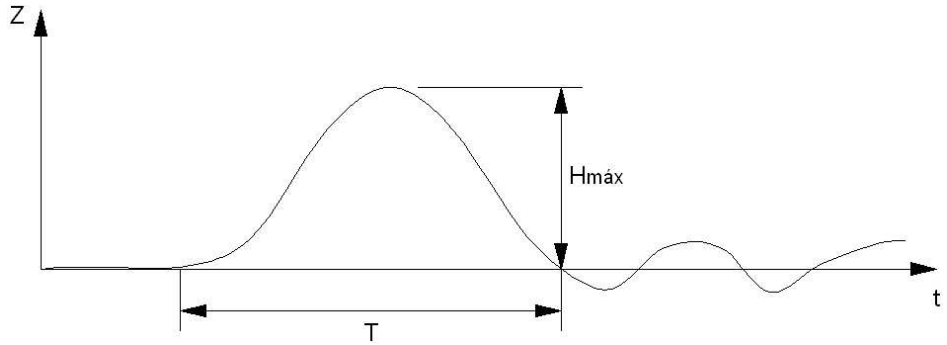

Figure 5.2: Wave height and period.

The ratio between the non-linear and dispersive effects is given by the Ursell number, which is defined as:

$$Ur = \frac{gH_{max}T^2}{2d^2} \tag{5.3}$$

The Ursell number is widely used in order to establish the dispersive character of waves. The smaller the Ursell number is, the more important the dispersive effects are, and the sooner they will appear. Dispersive waves are mainly deep waves, which travel with a velocity which depends on the wave period. Deep water waves are not affected by the bed surface, and the velocity profile is not uniform over the water depth. Hence, the role of the dispersion terms, which are neglected in the depth averaged model (see section 2.3.4 and Equation 2.28), in the momentum equations is important. On the other hand, shallow waves (which are non-dispersive) are strongly influenced by the bed surface, travelling with a velocity which depends only on the water depth. The velocity profile is rather uniform in the vertical direction, and the dispersion terms are much less important than in the deep waves. Since the depth averaged model does not account for the dispersive effects, and it assumes a separation between the vertical and horizontal length scales, the accuracy of the numerical results is expected to deteriorate as the Ursell number diminishes and the ratio $\frac{d}{L}$ increases.

The paddle speed in the fast movement is $0.58m/s$, with an amplitude of $0.29m$. Table 5.3 shows the properties of the waves generated by the fast movement. The paddle speed in the slow movement is $0.29m/s$, with an amplitude of $0.58m$. The properties of the waves generated by the slow movement are shown in Table 5.4. The Ursell number is much higher in the slow movement than in the fast movement. This is because the length of the slow movement ($2s$) is larger than the length of the fast movement ($0.5s$), and therefore, the wave period of the former one is larger.

The less the water depth is, the larger the Ursell number is. In all the tests the Ursell number

Paddle slope	$d(m)$	$T(s)$	$L(m)$	$H_{max}(m)$	$\frac{d}{L}$	Ur	$C_{exp}(m/s)$	$C_{sw}(m/s)$	$\frac{C_{sw}}{C_{exp}}$
45^o	0.15	0.74	1.15	0.095	0.13	11.3	1.54	1.55	1.01
45^o	0.20	0.82	1.41	0.102	0.14	8.4	1.65	1.71	1.03
45^o	0.25	0.89	1.66	0.107	0.15	6.6	1.71	1.85	1.08
45^o	0.30	0.97	1.95	0.113	0.15	5.8	1.77	1.99	1.12
60^o	0.15	0.59	0.93	0.105	0.16	8.0	1.60	1.58	0.99
60^o	0.20	0.65	1.15	0.119	0.17	6.2	1.67	1.74	1.05
60^o	0.25	0.72	1.38	0.127	0.18	5.2	1.74	1.89	1.09
60^o	0.30	0.74	1.53	0.135	0.20	4.0	1.83	2.03	1.10
90^o	0.15	0.59	0.97	0.123	0.15	9.3	1.61	1.57	0.98
90^o	0.20	0.59	1.08	0.140	0.18	6.0	1.69	1.79	1.05
90^o	0.25	0.60	1.20	0.159	0.21	4.5	1.72	1.95	1.13
90^o	0.30	0.56	1.20	0.172	0.25	2.9	1.80	2.09	1.16

Table 5.3: Properties of the waves generated by the fast movement.

is larger than 1, and therefore, the non-linear effects are expected to dominate over the dispersive effects in the wave propagation. Nonetheless, in some of the tests the Ursell number is close to 1, and thus, the importance of the dispersive effects increases. The ratio $\frac{d}{L}$ is of the order 0.1, which might be considered the upper limit for shallow water waves theory. The wave height is quite large, reaching values of 50% the water depth in some cases. Hence, the non-linear effects are important in the wave propagation. Due to the dispersive character of the waves, which is not considered in Equation 5.1, the experimental wave celerity C_{exp} is somewhat smaller than the approximated celerity C_{sw}. As the Ursell number diminishes the dispersive effects become more important in the propagation process, and the difference between C_{sw} and C_{exp} increases.

Paddle slope	$d(m)$	$T(s)$	$L(m)$	$H_{max}(m)$	$\frac{d}{L}$	Ur	$C_{exp}(m/s)$	$C_{sw}(m/s)$	$\frac{C_{sw}}{C_{exp}}$
45^o	0.15	2.32	3.25	0.050	0.04	58.6	1.36	1.41	1.04
45^o	0.20	2.39	3.77	0.054	0.05	37.8	1.50	1.59	1.06
45^o	0.25	2.47	4.31	0.060	0.06	28.7	1.67	1.75	1.05
45^o	0.30	2.52	4.76	0.064	0.06	22.1	1.74	1.90	1.09
60^o	0.15	2.20	3.10	0.053	0.05	55.9	1.35	1.42	1.05
60^o	0.20	2.23	3.55	0.058	0.06	35.3	1.49	1.59	1.07
60^o	0.25	2.27	3.99	0.065	0.06	26.3	1.63	1.76	1.08
60^o	0.30	2.30	4.37	0.068	0.07	19.6	1.69	1.90	1.12
90^o	0.15	2.14	3.01	0.052	0.05	51.9	1.39	1.42	1.02
90^o	0.20	2.14	3.41	0.059	0.06	33.1	1.49	1.60	1.08
90^o	0.25	2.14	3.77	0.067	0.07	24.1	1.60	1.77	1.11
90^o	0.30	2.14	4.09	0.073	0.08	18.2	1.72	1.91	1.11

Table 5.4: Properties of the waves generated by the slow movement.

5.3 Numerical results and experimental validation

5.3.1 Model equations

The experimental tests have been modelled with the 1D depth averaged shallow water equations. The Manning's formula has been used to compute the bed friction, assuming a Manning's coefficient of $0.015 s/m^{1/3}$. Nonetheless, the bed friction has very little influence on the numerical results, which are very insensitive to the Manning's number.

The turbulence level is very small in all the experiments, since there is not any important source of turbulent energy. In the numerical simulations made in this chapter it has been considered that the turbulent diffusion is not significant. This is the usual approach made when modelling the propagation of long shallow waves with the depth averaged shallow water equations [15, 19, 61, 40]. Hence, the equations solved are given by:

$$\frac{\partial h}{\partial t} + \frac{\partial q}{\partial x} = 0 \tag{5.4}$$

$$\frac{\partial q}{\partial t} + \frac{\partial}{\partial x}\left(\frac{q^2}{h} + \frac{gh^2}{2}\right) = -gh\frac{\partial z_b}{\partial x} - gh\frac{n^2 q^2}{h^{10/3}}$$

5.3.2 Wave generation

Two different forces appear when generating a wave by the movement of a paddle: the friction between the paddle and the water, and a pressure force perpendicular to the paddle. The friction between the paddle and the water produces a shear stress in the same direction as the bed slope. The magnitude of the shear stress depends directly on the relative velocity between the paddle and the water, on the paddle rugosity, and on the water depth.

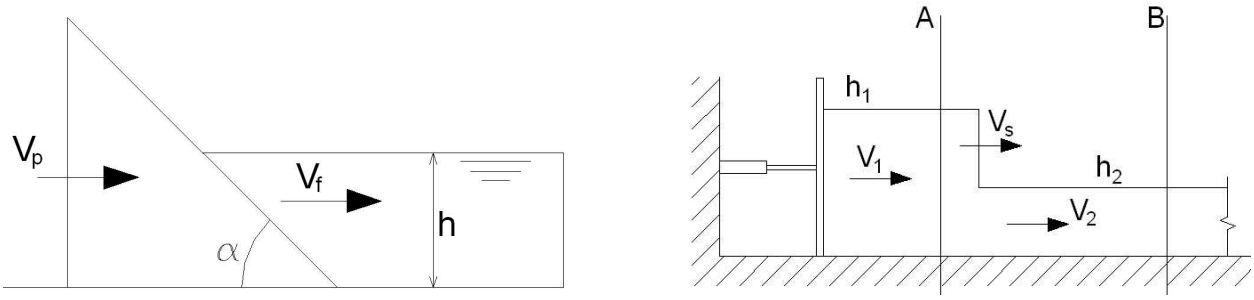

(a) Slanted paddle.

(b) Vertical paddle.

Figure 5.3: Wave generation by the paddle movement.

The horizontal projection of the shear stress produced by the paddle movement can be expressed as:

$$\tau_{p,h} = c_f \left[(V_p - V_f)\cos\alpha\right]^2 \cos\alpha \tag{5.5}$$

where $\tau_{p,h}$ is the horizontal projection of the shear stress produced by the paddle movement, α is the angle defining the paddle slope, V_p is the paddle velocity, V_f is the horizontal velocity of the water, and c_f is the bed friction coefficient. The bed stress given by Equation 5.5 is equivalent to the force produced by a bed slope given by:

$$\frac{n^2(V_p - V_f)^2 \cos^2 \alpha}{h^{4/3}} \cos \alpha \tag{5.6}$$

where the Manning's formula has been used to evaluate the bed friction coefficient. The Manning's coefficient of the flume is approximately $0.015 s/m^{1/3}$, the maximum velocity of the paddle in the experiments is $0.58 m/s$, the minimum paddle angle is 45^o, and the minimum water depth is $0.15 m$. With these values the largest bed friction is obtained, which, according to Equation 5.6, is equivalent to a bed slope of $1.79\,10^{-4}$ (0.01^o). This value is negligible in the wave generation process, and therefore, it will not be considered in the numerical simulations.

The numerical scheme used to simulate the wave generation depends on the paddle slope. With the 45^o and 60^o paddles (Figure 5.3(a)) a bed movement is used to generate the wave. In this way it is not necessary to impose any special moving boundary condition. Instead, the wet-dry condition participates directly in the generation process. When simulating the wave generation by a vertical paddle (90^o) this technique is no longer valid, because it produces instabilities and numerical oscillations due to the discontinuity in the bed elevation. Numerical instabilities due to the large bed slope also appear with the 60^o slope if a coarse mesh is used. In order to avoid numerical instabilities it has been necessary to use a $2cm$ grid with the 60^o slope, instead of the $4cm$ grid used with the 45^o slope.

When the generation paddle is vertical (90^o) there is always a point where a discontinuity in the bed elevation occurs, and therefore, it is necessary to use a moving boundary condition. In order to do so, the effect produced by the horizontal movement of a vertical wall has been considered to be physically equivalent to an imposed horizontal unit discharge (Figure 5.4). During the generation process the boundary moves with the paddle. Meanwhile the paddle moves inside the cell C_i (Figure 5.4), the unit discharge is imposed at the boundary $X_{i+1/2}$ as:

$$q_c^{n+1} = \frac{X_w^{n+1} - X_w^n}{t^{n+1} - t^n} h_A \tag{5.7}$$

where q_c^{n+1} is the imposed flux at the boundary $X_{i+1/2}$, X_w^n is the position of the paddle at the time step t^n, and h_A is equal to the water depth in the cell C_i when the paddle gets into it. The value of h_A in Equation 5.7 is kept constant meanwhile the paddle is inside the cell C_i. When the paddle moves into the next cell (C_{i+1}), the new value h_A is taken equal to h_{i+1} at that precise time step. With this scheme the volume of water introduced in the domain meanwhile the paddle is moving inside the cell C_i, is equal to the volume of water in that cell when the paddle gets into

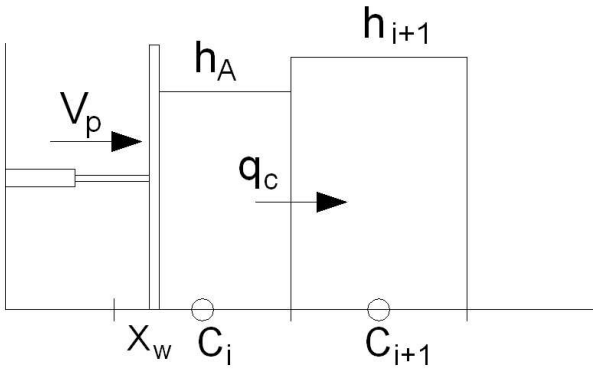

Figure 5.4: Boundary condition for the wave generation by a vertical paddle.

it, achieving in this way the conservation of mass. This formulation is only valid when simulating moving boundaries which are not overtopped by the generated wave.

A rough approximation of the wave generated by the movement of a vertical wall with constant velocity can be obtained applying the conservation of mass and momentum to the control volume AB in Figure 5.3(b), which yields:

$$h_1 V_1 - h_2 V_2 = (h_1 - h_2) V_s \tag{5.8}$$

$$\frac{1}{2} g h_1^2 + h_1 V_1^2 - \frac{1}{2} g h_2^2 - h_2 V_2^2 = (h_1 V_1 - h_2 V_2) V_s$$

The subindices 1 and 2 in Figure 5.3(b) and in Equation 5.8 refer respectively to variables at the left and right sides of the wave front. The only unknown variables in Equation 5.8 are the speed of the wave front V_s and the water depth h_1. The velocity V_1 is assumed to be equal to the paddle velocity, V_2 is zero (the water is still before the experiment starts), and h_2 is the initial water depth.

A grid size of $4cm$ was used in the tests with the 45^o and 90^o paddles, while the grid size was reduced to $2cm$ in the simulations with the 60^o paddle for the reasons exposed above. As it is shown in Figures 5.5(a,b,c), during the slow paddle movement the water surface oscillates around an equilibrium level. These oscillations, which are mainly produced by vertical accelerations, are larger as the paddle slope increases. The numerical model is not able to resolve them because the vertical accelerations are neglected in the shallow water approximation. However, the numerical scheme predicts fairly well the equilibrium water depth (Table 5.5 and Figure 5.5). The wave height approximation given by Equation 5.8 ($H_{5.8}$ in Table 5.5) also agrees well with the experimental data.

It should be noticed from Figure 5.5 and Table 5.5 that the dependence of the wave height predicted by the model on the paddle slope is low. The wave height depends mainly on the initial water depth and on the paddle speed. It should also be remarked that in Figures 5.5(a) and 5.5(b) the wave was generated by a bed movement, while in Figure 5.5(c) it was generated by the moving boundary condition (Equation 5.7). The wave height predicted by both mechanisms is the same.

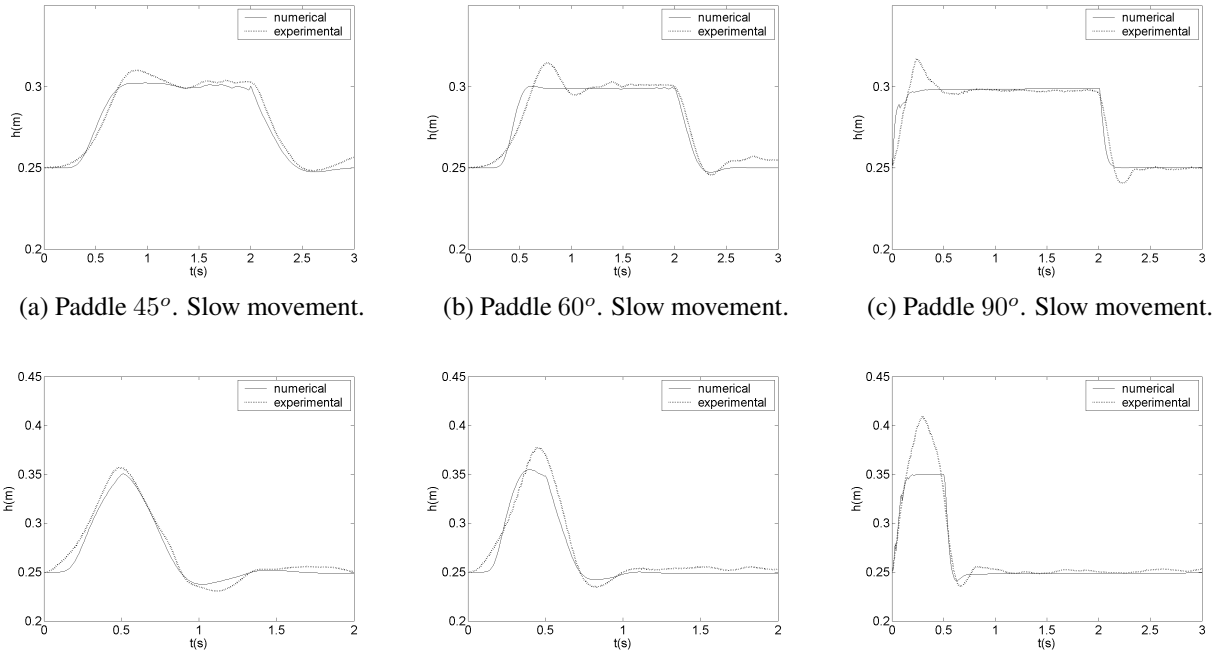

(a) Paddle 45^o. Slow movement. (b) Paddle 60^o. Slow movement. (c) Paddle 90^o. Slow movement.

(d) Paddle 45^o. Fast movement. (e) Paddle 60^o. Fast movement. (f) Paddle 90^o. Fast movement.

Figure 5.5: Wave generation. Experimental and numerical results at gauge S1. d=$0.25m$.

Paddle slope	$d(m)$	$H_{exp}(m)$	$H_{num}(m)$	$H_{5.8}(m)$
45^o	0.15	0.0395	0.0390	-
45^o	0.20	0.0456	0.0440	-
45^o	0.25	0.0520	0.0500	-
45^o	0.30	0.0562	0.0520	-
60^o	0.15	0.0385	0.0390	-
60^o	0.20	0.0442	0.0440	-
60^o	0.25	0.0501	0.0500	-
60^o	0.30	0.0535	0.0540	-
90^o	0.15	0.0385	0.0390	0.0378
90^o	0.20	0.0420	0.0430	0.0434
90^o	0.25	0.0475	0.0490	0.0483
90^o	0.30	0.0520	0.0530	0.0527

Table 5.5: Equilibrium wave height. Slow movement.

The length of the fast movement is not large enough to achieve an equilibrium wave height. Nonetheless, it seems from Figure 5.5(f) that the equilibrium water depth given by the model is approximately $0.35m$. The effects of vertical accelerations are much larger in this case. For this reason the maximum wave height produced by the vertical paddle with the fast movement is underpredicted by the numerical model.

5.3.3 Wave propagation and runup

Figures 5.6 and 5.7 show the numerical and experimental results over $10s$ of simulation for several tests. During this time the wave is generated, reflected in the vertical wall, and reflected again in the generation paddle. The vertical wall is modelled by a discontinuity in the bed elevation, which allows to account easily for the overtopping waves. For this reason, the wet-dry treatment plays a very important role in the reflection of the wave.

The experimental water surface elevation oscillates around the numerical predictions (Figures 5.6 and 5.7). Nonetheless, the model predicts fairly well the mean water surface level, specially considering that errors below 20% are inside the admissible limits in the simulation of solitary waves [72].

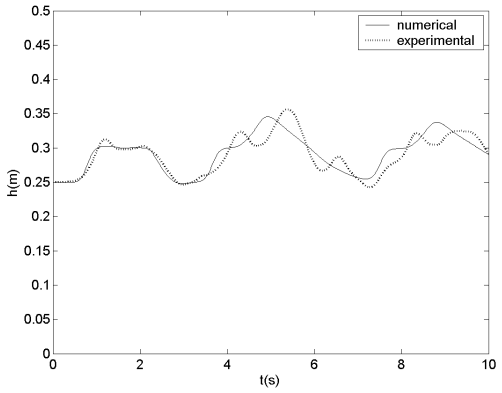

(a) Paddle 45^o. d=$0.25m$. Gauge S1.

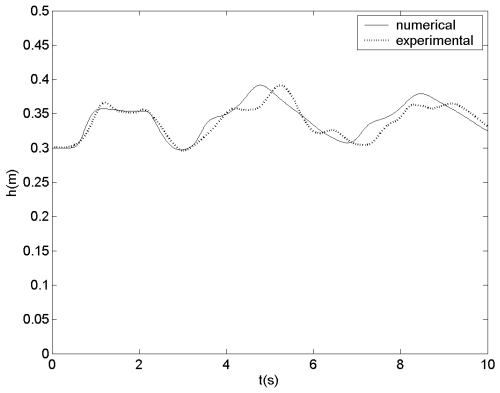

(b) Paddle 45^o. d=$0.30m$. Gauge S3.

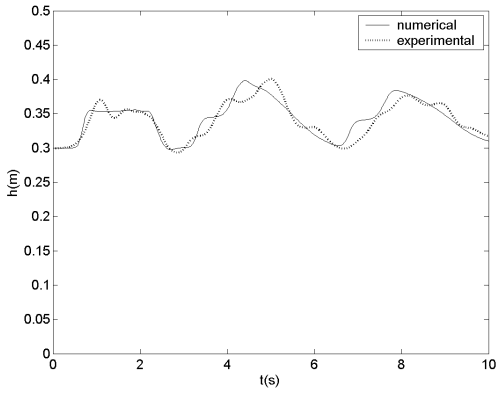

(c) Paddle 60^o. d=$0.30m$. Gauge S2.

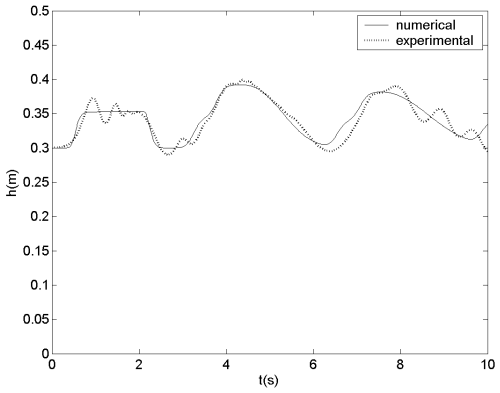

(d) Paddle 90^o. d=$0.30m$. Gauge S2.

Figure 5.6: Experimental and numerical results in the slow movement.

In order to verify that there is not a trend in the numerical results, an error is defined considering the total area between the experimental and numerical curves as:

$$\text{error} = \sum_{i=1}^{n} \frac{(h_i^{exp} - h_i^{num})\Delta t}{t_{max} H_{max}} \tag{5.9}$$

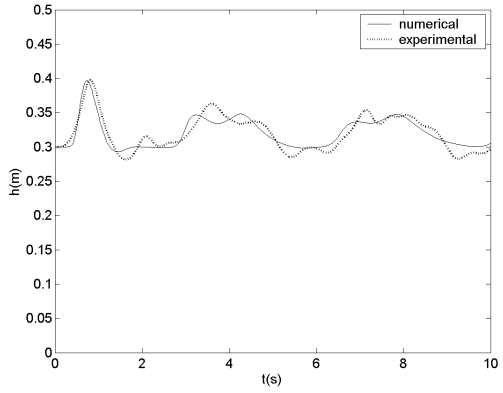

(a) Paddle 45^o. d=$0.30m$. Gauge S2.

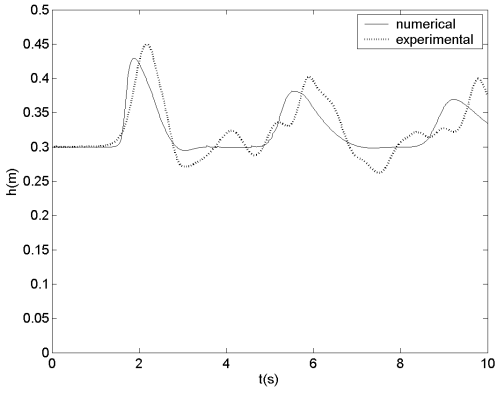

(b) Paddle 45^o. d=$0.30m$. Gauge S5.

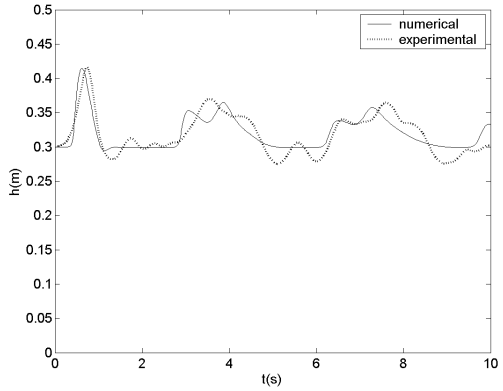

(c) Paddle 60^o. d=$0.30m$. Gauge S2.

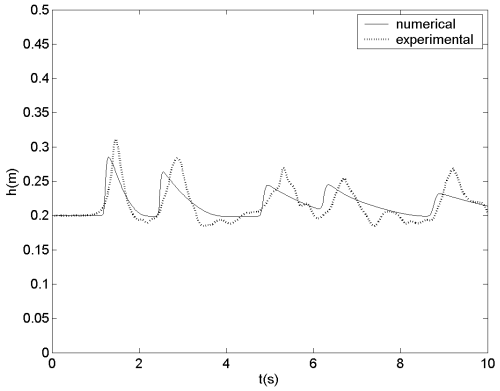

(d) Paddle 90^o. d=$0.20m$. Gauge S4.

Figure 5.7: Experimental and numerical results in the fast movement.

where n is the number of experimental samples, h_i^{exp} is the experimental water depth, h_i^{num} is the numerical water depth, Δt is the time step between two consecutive samples, t_{max} is the total time of simulation ($10s$), and H_{max} is the initial wave height as defined in Figure 5.2.

The error given by Equation 5.9 does not increase monotonically in time, as it is shown in Figures 5.8 and 5.9 for several tests. This is because a depth averaged model is able to compute the time evolution of the mean free surface level, but not the high frequency oscillations which are mainly produced by vertical accelerations and are subject to dispersion effects (Figure 5.6). Tables 5.6 and 5.7 show the error at each wave gauge after $10s$ of simulation, which is in most cases smaller than 5%, and only in 5 cases out of 120 exceeds 10%.

Figure 5.10 shows the water surface elevation computed by the model in the whole flume at several time steps, revealing a satisfactory global agreement with the experimental results. It should be noticed how the wave overtops the wall without originating any spurious oscillation (Figures 5.10(a,b,d)), and how it is reflected without any numerical diffusion of the water front from the wet to the dry cells (Figure 5.10(c)).

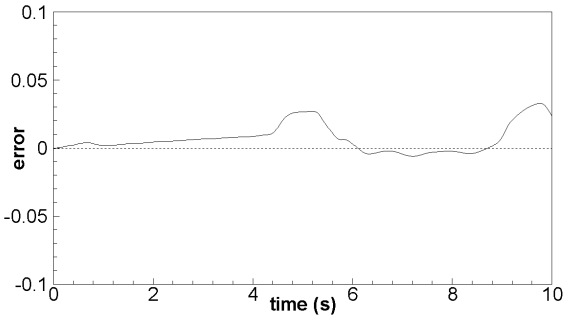

(a) Paddle 45^o. d=$0.20m$. Gauge S1.

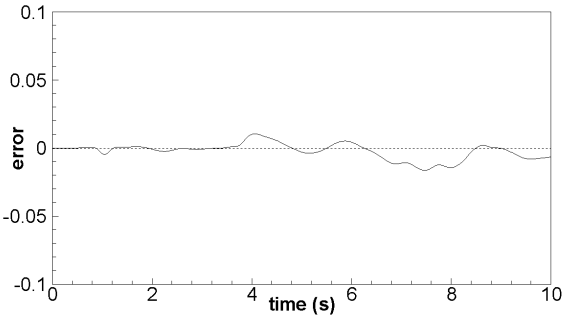

(b) Paddle 45^o. d=$0.20m$. Gauge S5.

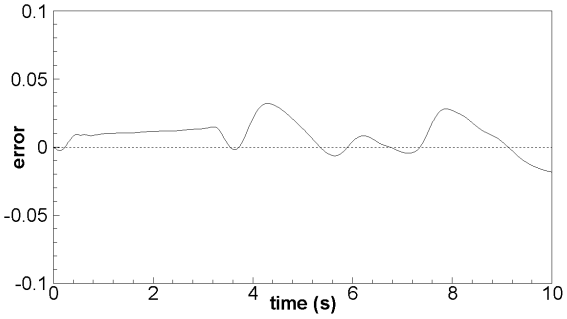

(c) Paddle 60^o. d=$0.30m$. Gauge S1.

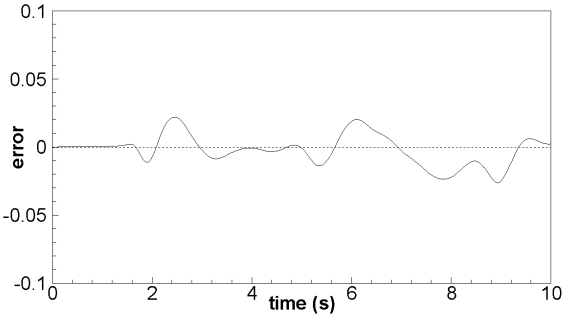

(d) Paddle 60^o. d=$0.30m$. Gauge S2.

Figure 5.8: Error vs. time, as defined in Equation 5.9, in the fast movement.

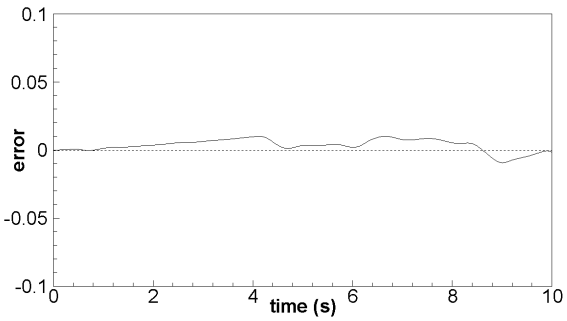

(a) Paddle 45^o. d=$0.20m$. Gauge S1.

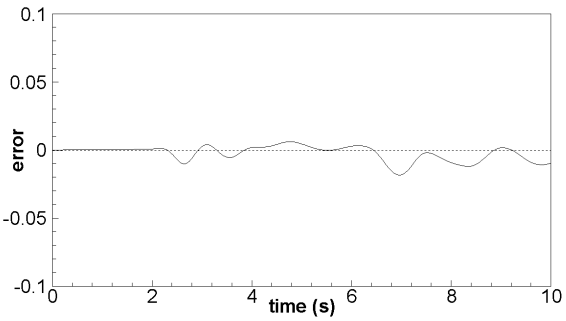

(b) Paddle 45^o. d=$0.20m$. Gauge S5.

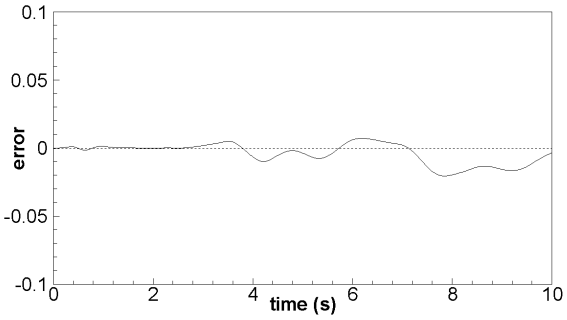

(c) Paddle 60^o. d=$0.30m$. Gauge S1.

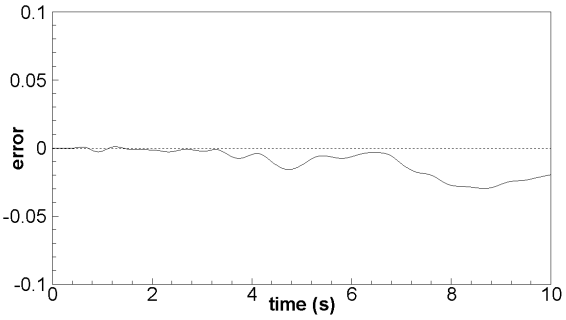

(d) Paddle 60^o. d=$0.30m$. Gauge S2.

Figure 5.9: Error vs. time, as defined in Equation 5.9, in the slow movement.

Paddle slope	$d(m)$	Gauge S1	Gauge S2	Gauge S3	Gauge S4	Gauge S5
45^o	0.15	0.025	0.047	0.007	0.027	0.005
45^o	0.20	0.011	0.001	0.015	0.021	0.007
45^o	0.25	0.121	0.018	0.031	0.027	0.022
45^o	0.30	0.141	0.005	0.021	0.055	0.006
60^o	0.15	0.051	0.042	0.030	0.012	0.023
60^o	0.20	0.077	0.060	0.050	0.059	0.069
60^o	0.25	0.037	0.004	0.021	0.024	0.002
60^o	0.30	0.024	0.010	0.037	0.025	0.001
90^o	0.15	0.012	0.005	0.003	0.001	0.005
90^o	0.20	0.005	0.023	0.021	0.014	0.002
90^o	0.25	0.011	0.024	0.025	0.019	0.001
90^o	0.30	0.016	0.030	0.034	0.023	0.002

Table 5.6: Error (see Equation 5.9) in the fast movement at $t = 10s$.

Paddle slope	$d(m)$	Gauge S1	Gauge S2	Gauge S3	Gauge S4	Gauge S5
45^o	0.15	0.020	0.017	0.052	0.035	0.032
45^o	0.20	0.003	0.035	0.070	0.041	0.018
45^o	0.25	0.044	0.034	0.078	0.091	0.058
45^o	0.30	0.025	0.125	0.086	0.180	0.091
60^o	0.15	0.189	0.053	0.077	0.064	0.047
60^o	0.20	0.210	0.010	0.034	0.045	0.017
60^o	0.25	0.020	0.028	0.058	0.059	0.079
60^o	0.30	0.005	0.029	0.074	0.097	0.072
90^o	0.15	0.036	0.016	0.018	0.018	0.015
90^o	0.20	0.025	0.021	0.013	0.042	0.020
90^o	0.25	0.018	0.013	0.040	0.037	0.016
90^o	0.30	0.023	0.019	0.041	0.062	0.041

Table 5.7: Error (see Equation 5.9) in the slow movement at $t = 10s$.

5.4 Concluding remarks

The treatment of the wet-dry fronts presented in section 3.9 has been used in this chapter to model the reflection and overtopping of long waves on a vertical wall, as well as the wave generation by the movement of a paddle.

In order to simulate the generation of a wave by the movement of a slanted surface, two different schemes have been proposed depending on the slope of the surface. When the wave is generated by a vertical wall, a moving boundary condition for this particular case is used. The generation of waves by a slanted surface is achieved by a bed movement, using the wet-dry condition. The performance of both schemes is satisfactory. The differences observed between the experimental and the numerical results are mainly due to the existence of important vertical accelerations, specially near the vertical walls, which invalidate the hydrostatic pressure hypothesis made in the shallow water models. The numerical model is able to predict the mean movement

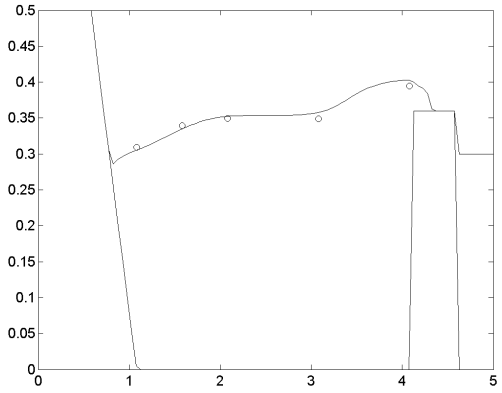

(a) Paddle 45^o. d=$0.30m$.

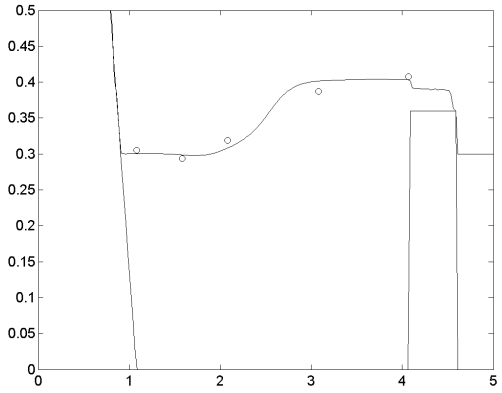

(b) Paddle 60^o. d=$0.30m$.

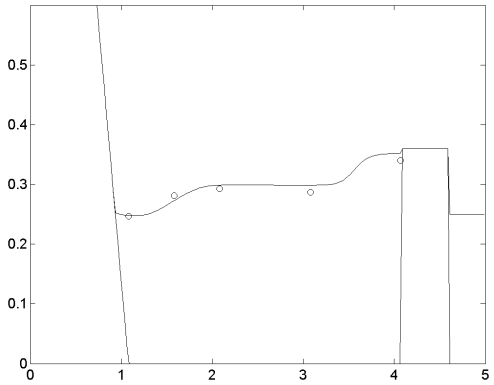

(c) Paddle 60^o. d=$0.25m$.

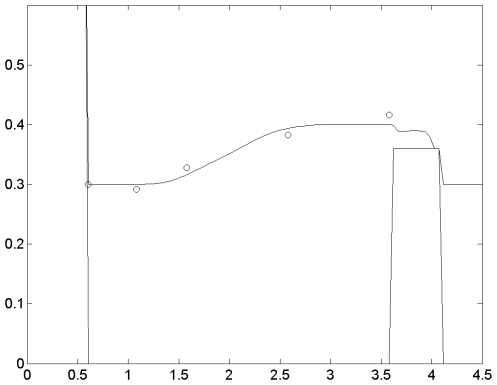

(d) Paddle 90^o. d=$0.30m$.

Figure 5.10: Water surface elevation at several time steps in the slow movement. t=$2.5s$. Continuous line: numerical predictions. Circles: experimental results.

of the free surface, but it fails to simulate the oscillations around this mean level. This should be considered when analysing the numerical results given by the shallow water equations, because the model underpredicts the maximum runup on very steep walls, which is an important parameter in the design of dams, bridges or similar civil structures.

Chapter 6

Tidal flow in the Crouch estuary

6.1 Introduction

The hydrodynamic modelling of estuaries is of great importance in order to understand, predict and control the physical processes taking place in coastal regions. Not only an adequate representation of the mean velocity and water depth fields is desired, but also a good estimation of the turbulent kinetic energy, which plays a crucial role in the transport and mixing processes of pollutants and heat. Kawanisi [69] studied the shallow flow in a tidal estuary and pointed out the importance of the turbulence structure in the transport processes. Turbulence has also a great influence on the bed load sediment transport in rivers. The intermittent and streaky pattern in the sediment motion is apparently caused by the turbulent bursting processes near the bed wall. Sumer et al. [130] found that for a constant mean bed shear stress, the sediment motion depends on the near-bed turbulence, with a very strong correlation. For increments of just 20% in the turbulent kinetic energy, the sediment transport can increase up to 600%.

In this chapter the tidal flow in the Crouch estuary (Essex, England) is computed with the depth averaged shallow water equations for a time period of 5 days. The Crouch estuary is characterised by a rather thin and long shape, with a longitudinal extension of around $25Km$, and a width of approximately $1Km$ at the mouth (Figure 6.1). The mouth of the estuary is located in the North Sea, approximately $15Km$ north of the River Thames. $5Km$ upstream from the mouth the estuary bifurcates into the River Crouch, which extends 20 additional kilometres upstream from the bifurcation, and the River Roach, which extends around $10Km$. The estuary has extensive flooding and recession areas in the lateral margins, which wet and dry with each tidal cycle and need to be modelled with a suitable wet-dry condition. In the south part of the estuary there are two large internal islands defined by vertical walls which keep them always dry. In the upper part of the estuary, between the coordinates $x = 588000m$ and $x = 591500m$ (UK Ordnance Survey Coordinates), there is a large island (Bridgemarsh island) which dries out at low tide and completely floods at high tide.

The external fresh water contribution to the flow in the whole estuary is scarce and negligible when compared to the tidal flow [150]. Hence, the flow in the estuary is completely driven by the tidal waves at the mouth entrance. The tidal range at the mouth varies between $3m$ (neap tide) and $5m$ (spring tide), with maximum velocities of approximately $1.5m/s$. The bed of the estuary in the sub-tidal and inter-tidal channels is formed by muddy sediments. The estuary has also several marsh regions, usually in areas which are above the mean spring high water level.

The large spatial domain through which the estuary extends, as well as the fact of being driven by tidal cycles, makes it necessary to solve an unsteady problem over a large temporal and spatial domain. Since the fresh water contribution in the estuary flow is scarce, the gradients of salinity are negligible [150] and do not need to be taken into account in the numerical modelling. Hence, using a one-layer depth averaged shallow water model is a very reasonable option.

Three depth averaged RANS turbulence models, the mixing length model (ML), the $k - \varepsilon$ model of Rastogi and Rodi, and the depth averaged algebraic stress model proposed in section 2.5 (ASM), have been used in the simulations. Some computations without any turbulence modelling, neglecting the diffusion forces, have also been done.

The numerical results are compared with the experimental mean current speed and water depth at several locations in the estuary. The location of the observation points is defined in Table 6.1 and shown in Figure 6.1. All the experimental data was obtained by the Coastal and Estuarine Research Unit (CERU) at the University College of London (UCL).

Point	Location	X(m)	Y(m)	River
P1	Holliwell	600420	195250	Crouch
P2	Creeksea	592780	195860	Crouch
P3	Fambridge	585960	196330	Crouch
P4	Wallasea	598750	194150	Roach
P5	Paglesham	596180	192450	Roach

Table 6.1: Location of the experimental data points in the Crouch estuary.

The current speed was measured with self recording impeller-type sensors (Valeport type 104 and Valeport type 105). At all the experimental points the mean current speed and the water depth were measured at intervals of 15 minutes. Near the mouth of the estuary (Holliwell) the current direction was also recorded, and it turned out to be essentially bi-directional. The current speed probes were located at a fixed height above the bed ($3m$ in the Crouch and $2m$ in the Roach). The velocity profile is assumed to be rather uniform over the water depth. Hence, in order to compare with the numerical results, the experimental speed is considered to be representative of its depth averaged value.

6.2 Numerical model

The numerical model covers the whole estuary, including all the marsh regions which are only flooded in spring tides, with around 48995 control volumes. The total size of the numerical domain is approximately $27.65Km^2$. Several cross sections of the bed elevation were obtained from a nautical chart, and extruded along the main channels in order to obtain the bathimetry for the numerical model (Figure 6.1). More detailed bathimetry was used in Bridgemarsh island, where the LIDAR data provided by the UK Environmental Agency was used. The bed elevation varies between $z_b \approx -15m$ in the deepest areas of the main channels, and $z_b \approx 3m$ in the highest marsh regions. The transverse bed slope in the lateral margins of the main channels is quite steep. Some parts of the boundary are defined by vertical walls which are never overtopped, and thus, do not need to be included in the simulation.

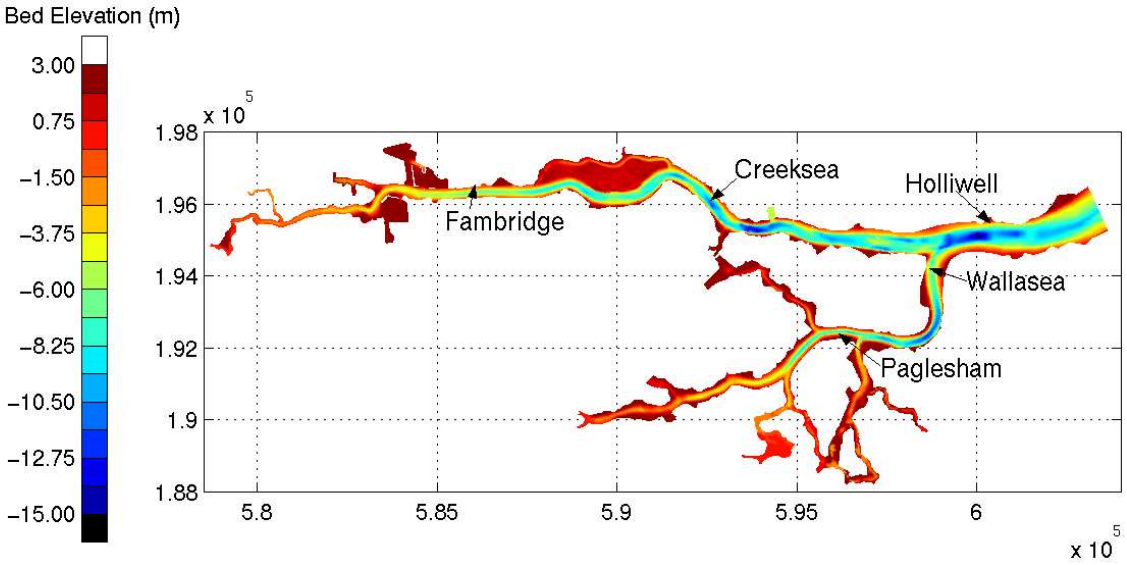

Figure 6.1: Bathimetry of the Crouch estuary $z_b(m)$. Relative to the mean sea level at the mouth.

6.2.1 Numerical mesh

The numerical mesh is more refined in the sub-tidal and inter-tidal channels, while the size of the control volumes increases in the most upstream regions of the estuary, which are only flooded occasionally. Table 6.2 shows the characteristics of both the finite volume mesh and the associated triangular mesh (see section 3.5.1 for details about how the finite volume mesh is built from the associated triangular mesh). The size of the control volumes in the main channel is about $330m^2$. The largest control volumes are located upstream in the River Roach, with a size of approximately $1300m^2$. The average size of the control volumes is $570m^2$. Some details of the numerical mesh in several regions of the estuary are shown in Figures 6.2 and 6.3.

	Triangular mesh		Finite volume mesh	
	vertex	elements	volumes	faces
Mesh Crouch	17258	31733	48995	95199

Table 6.2: Characteristics of the numerical mesh for the Crouch estuary.

Bridgemarsh island (Figure 6.2) has a surface of approximately $2Km^2$ which floods and dries with each tidal cycle. The bed elevation in the island is rather flat, which makes the drying process slow, since there is not a large slope to help the drainage. At the same time the topography is quite irregular, with several big holes and bumps. During the ebb tide, the water may remain trapped in these holes, creating spread patches of still water all over the island. It should also be noticed how, in a very short distance, the bed elevation goes from $z_b \approx 3m$ in the island, down to $z_b \approx -9m$ in the main channel. Due to the large extent of the whole estuary, this strong step in the bathimetry had to be resolved in the numerical mesh with only 3 or 4 elements, although a more refined mesh would be desirable. This problem about mesh resolution, which was also present in other regions (specially in the most upper parts of the estuary), may produce in the numerical solution some high velocity spots. These high velocity spots have only a local influence on the solution, and do not affect the numerical results in other parts of the estuary. Nevertheless, if the numerical scheme is not robust and stable, they may lead to convergence and stability problems.

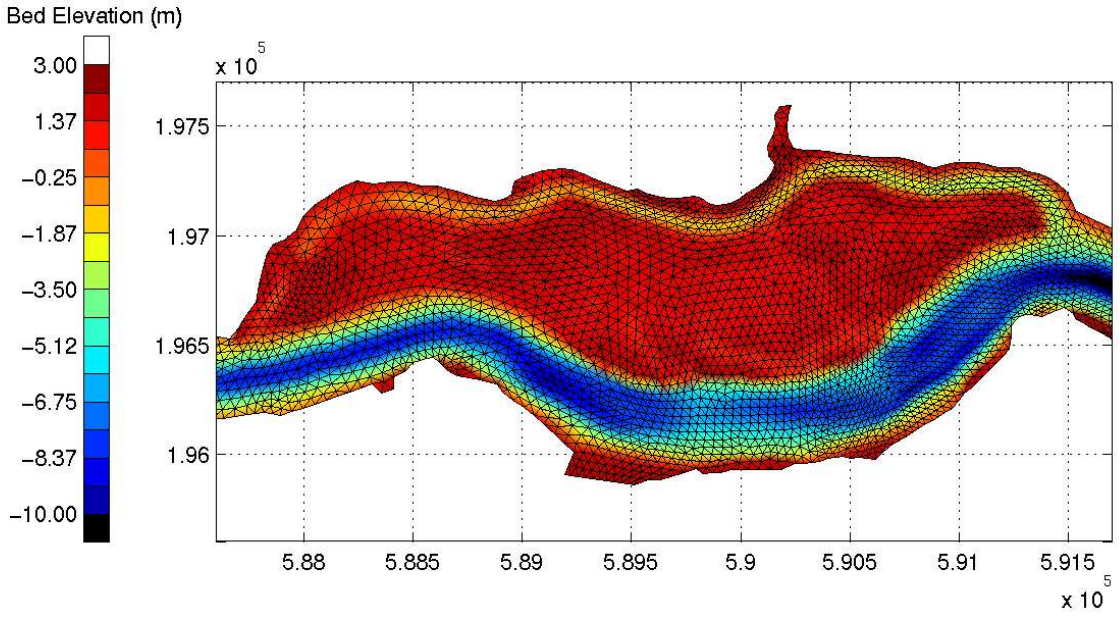

Figure 6.2: Detail of the numerical mesh in Bridgemarsh island.

Figure 6.3 shows the triangular mesh in the Roach river. The mesh is more refined in the main channel. The size of the control volumes gets considerably coarser in the upper regions. This is because we are only interested in the bulk effect that these areas have in the main channel flow, and not in resolving the flow patterns in them. It should be noticed that the geometry of these regions is quite complex, and therefore, a very refined mesh and a very detailed bathimetry would

be required in order to resolve the flow patterns in them with a reasonable degree of accuracy.

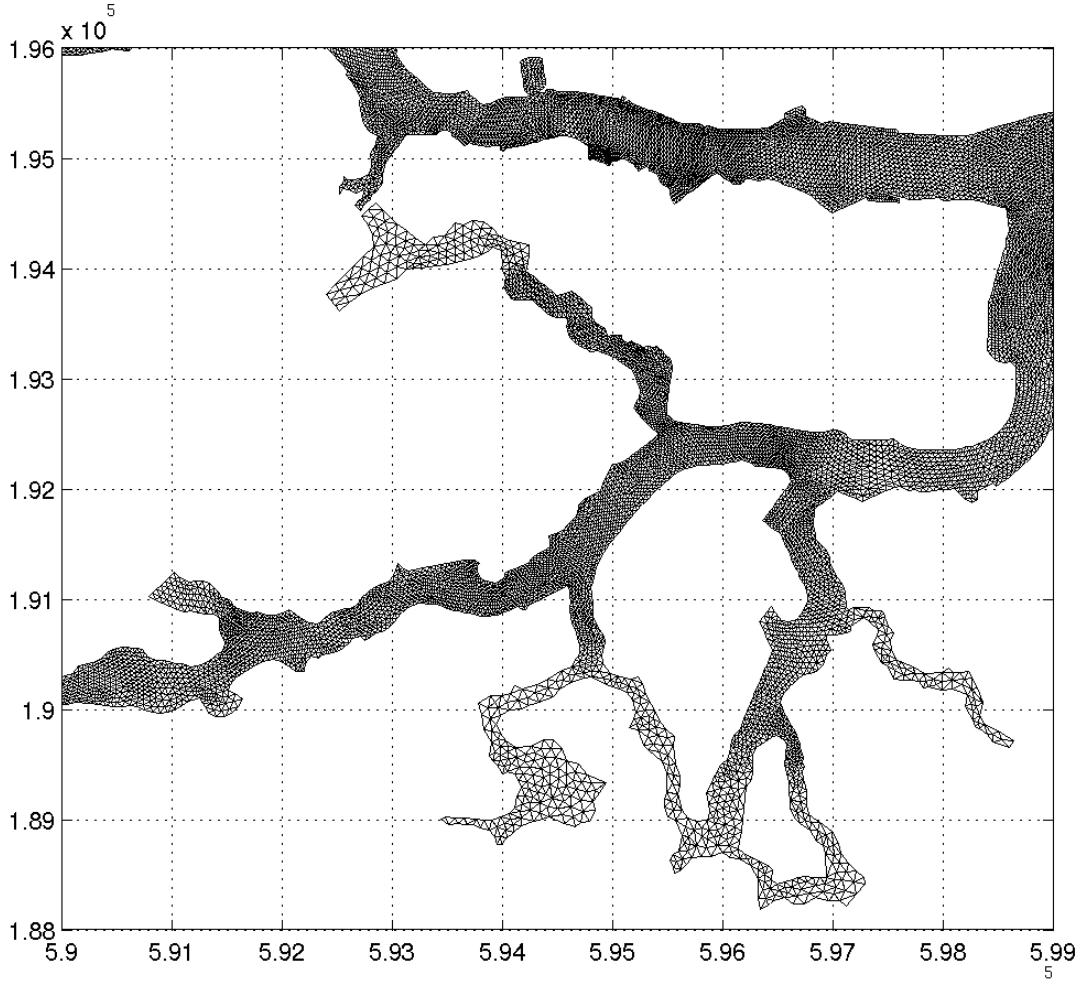

Figure 6.3: Detail of the numerical mesh in the river Roach.

6.2.2 Boundary conditions

The freshwater apportions in the whole estuary are very scarce and can be neglected in the simulations. The flow is completely driven by the water surface elevation at the mouth, which is the only open boundary condition to be imposed. The rest of the boundaries are treated as walls. Due to the extension of the spatial domain ($27.85Km^2$), the mesh size near the walls is relatively coarse, which precludes the use of wall functions as the wall boundary treatment. Instead, a slip condition has been used. Nevertheless, most of the time during the simulation the wall boundaries are dry, and therefore, they do not participate in the solution. On the other hand, the role of the wet-dry front, which defines the fluid extension, becomes more important.

The water surface elevation at the mouth open boundary is assumed to be constant all along the boundary. Its level is directly obtained from a tidal gauge which was located near the northern

shoreline. Water surface elevation samples were taken at constant intervals of 15 minutes (Figure 6.4). The flow at the mouth is always subcritical. Hence, only the water depth is imposed during the ebb tide (subcritical outlet). During the flood tide the inlet flow is forced to be perpendicular to the boundary, as an additional condition to the water depth (subcritical inlet). Some regions of the mouth boundary may become dry or wet depending on the water surface level. Obviously, the minimum imposed water depth is zero (dry open boundary). However, special care must be taken at the boundary line, because it may be the case that the imposed water depth is too small, and the flow becomes supercritical. This is likely to occur when the flow enters the domain if the bed slope at the boundary is large, as it is the case in the present model. This case is avoided by limiting the maximum Froude number at the inlet boundary to 0.95, assuring in this way that the flow is always subcritical. In order to do so, the normal unit discharge at the inlet boundary is limited as:

$$q_{n,in} \leq 0.95\sqrt{gh_{in}^3} \tag{6.1}$$

where $q_{n,in}$ is the normal unit discharge at the inlet, and h_{in} is the water depth at the inlet, which is imposed from the wave gauge experimental data. Condition 6.1 only needs to be applied in very few boundary cells, and at very few time steps during the simulation.

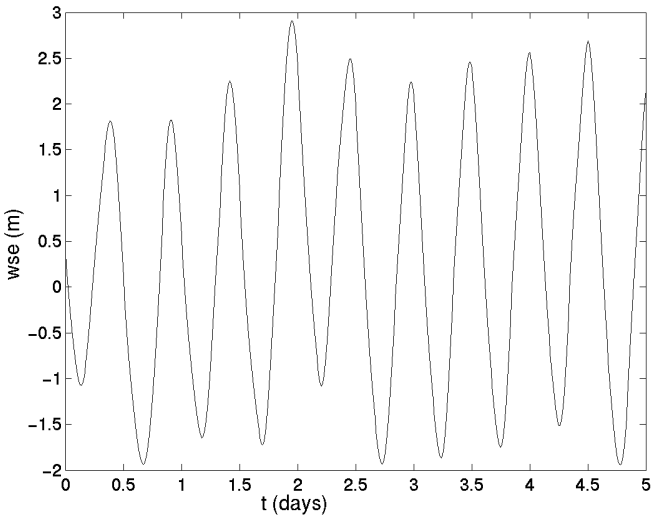

Figure 6.4: Measured water surface elevation at the mouth of the Crouch estuary. Relative to the mean sea level.

6.2.3 Wet-dry fronts

A correct modelling of the wet-dry fronts is of great importance in the Crouch estuary. The bathimetry of the estuary, with several flat marsh areas, and the rather large tidal range ($5m$ in spring tide), produce a large inter-tidal region. During the 5 days of simulation, the maximum dry area at low tide is about $11Km^2$, while at the highest spring tide the dry area is only $0.25Km^2$.

Considering that the total extension of the numerical domain is $27.65Km^2$, there is up to a 40% of the surface of the estuary which floods and dries periodically. Hence, an inappropriate numerical treatment of the flooding and drying processes will lead to erroneous results.

In order to check the sensibility of the numerical solution to the wet-dry tolerance parameter ε_{wd} (see section 3.9), three different values were tried in the computations. The smallest value of ε_{wd} is desired from an accuracy point of view. But too small values of ε_{wd} promote the numerical instabilities, specially in domains with a very irregular bathimetry and a relatively coarse mesh, leading to very small time steps. After doing the sensibility analysis for several values of the wet-dry tolerance parameter ($\varepsilon_{wd} = 10^{-2}m, 10^{-3}m, 10^{-4}m$), it was found that no differences appear in the numerical results for values of ε_{wd} smaller than $10^{-3}m$ (Figure 6.5), which was the value chosen for the definitive simulations. It should be noticed in Figures 6.5 and 6.6 the differences in the results when the parameter ε_{wd} is diminished from $10^{-2}m$ to $10^{-3}m$, specially in the depth averaged velocity, but also in the water depth in the shallowest regions of the estuary. This shows the importance of doing a sensibility analysis of the solution to the wet-dry tolerance parameter. A priori, a value of $\varepsilon_{wd} = 10^{-2}m$ might seem small enough, specially considering the spatial dimensions of the problem, but it turns out after the sensibility analysis that a smaller value is desirable. These results apply only for the specific wet-dry treatment used in this work, and may vary for other schemes.

6.2.4 Influence of the bed friction on the numerical solution

All the inter-tidal and sub-tidal regions of the estuary are formed by muddy sediments, which are assumed to have a Manning's coefficient of approximately $n \approx 0.02m/s^{1/3}$. There are also several marsh areas in the estuary, specially in Bridgemarsh island, in the upper part of the estuary and in the side margins of the main channels. These areas are usually higher than the mean high water level at spring tide. The Manning's coefficient in the marsh regions ($z_b > 1.5m$) is estimated to be around $n \approx 0.05m/s^{1/3}$.

In order to check the sensibility of the model to the bed friction coefficient, several computations have been made with different bed friction coefficients. The following Manning's numbers have been considered: (1) a constant value of $n = 0.015m/s^{1/3}$ in the whole estuary; (2) a constant value of $n = 0.020m/s^{1/3}$ in the whole estuary; (3) a constant value of $n = 0.025m/s^{1/3}$ in the whole estuary; (4) $n = 0.020m/s^{1/3}$ in the sub-tidal and inter-tidal channels and $n = 0.050m/s^{1/3}$ in the marsh regions. The sensibility of the numerical solution to the Manning's number is low for both the water depth and the current speed (Figure 6.7).

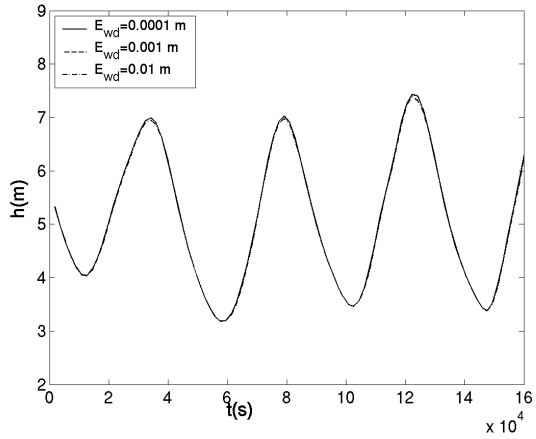

(a) Water depth $h(m)$. Wallasea.

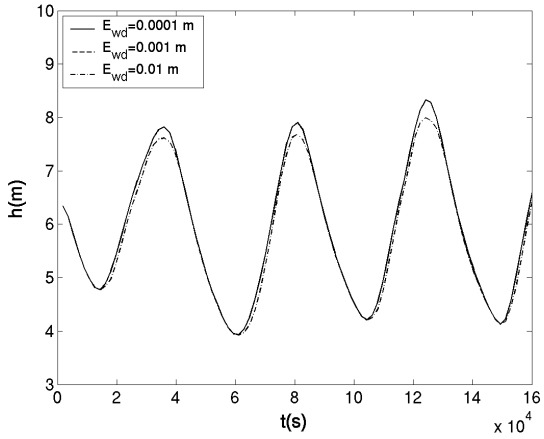

(b) Water depth $h(m)$. Fambridge.

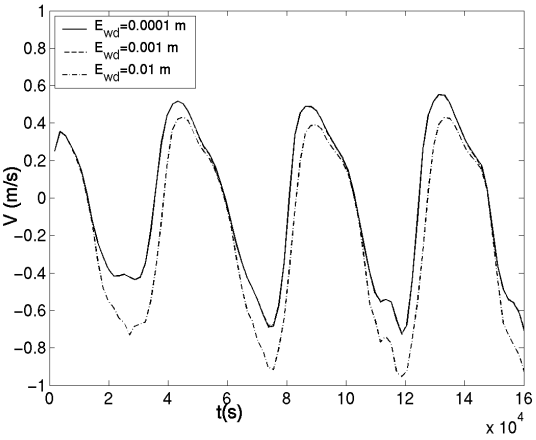

(c) Current speed (m/s). Wallasea.

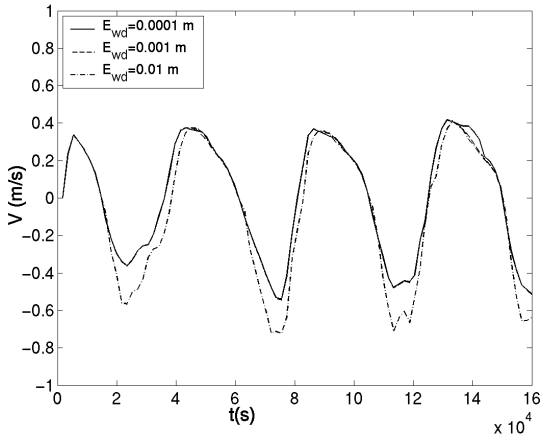

(d) Current speed (m/s). Fambridge.

Figure 6.5: Dependence of the numerical solution on the wet-dry tolerance parameter (ε_{wd}). Water depth $h(m)$ and current speed (m/s) at several locations in the Crouch estuary. The differences between the results obtained with $\varepsilon_{wd} = 0.001m$ and with $\varepsilon_{wd} = 0.0001m$ cannot even be appreciated in the plots.

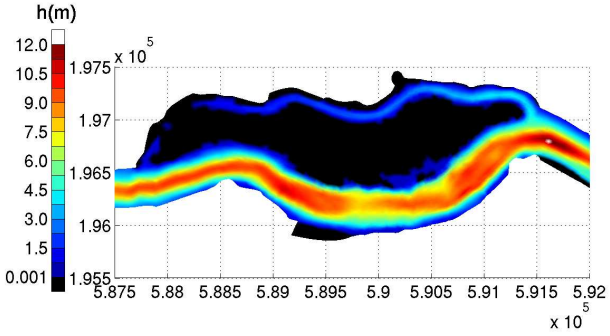

(a) Water depth $h(m)$. $\varepsilon_{wd} = 0.01m$.

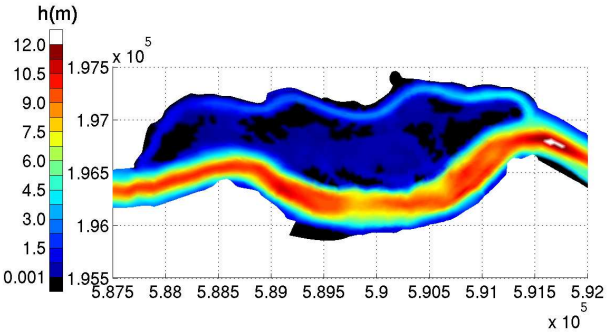

(b) Water depth $h(m)$. $\varepsilon_{wd} = 0.001m$.

Figure 6.6: Dependence of the water depth $h(m)$ at Bridgemarsh island on the wet-dry tolerance parameter (ε_{wd}). $t = 22h$. Flood tide. Dry regions are shown in black.

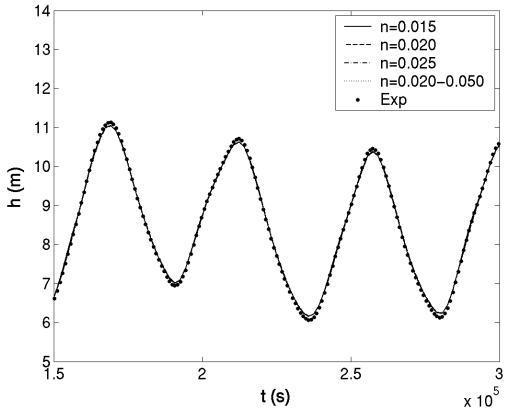

(a) Water depth $h(m)$. Holliwell.

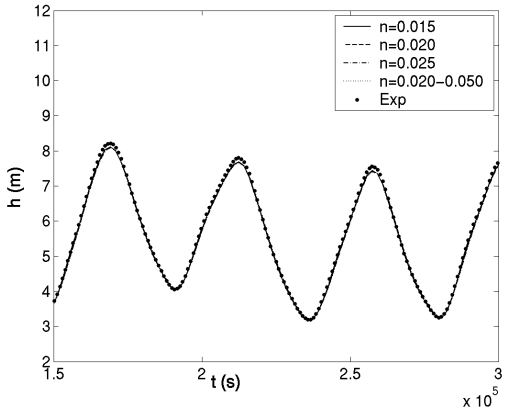

(b) Water depth $h(m)$. Wallasea.

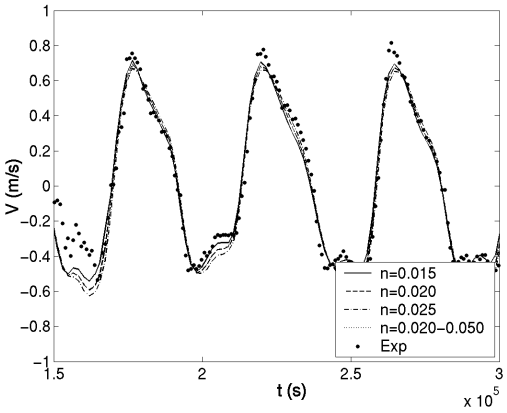

(c) Current speed (m/s). Holliwell.

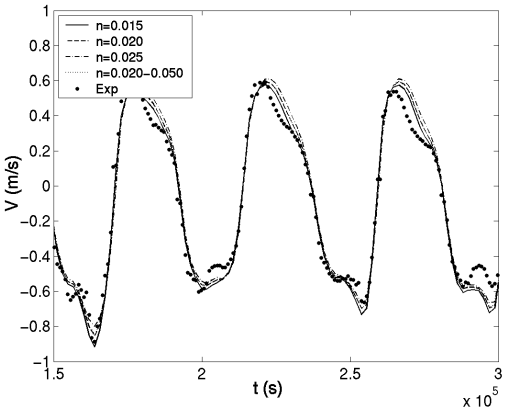

(d) Current speed (m/s). Wallasea.

Figure 6.7: Dependence of the numerical solution on the bed friction coefficient. Water depth $h(m)$ and current speed (m/s) at several locations in the Crouch estuary.

6.3 Numerical results and experimental validation

All the computations have been made with the hybrid first/second order scheme (see section 3.5.7), which uses a second order extrapolation on the cell faces for the unit discharges and a first order approximation for the water depth. The scheme is therefore, second order in q_x, q_y and first order in h. Both van Leer's and Roe's schemes have been used without finding any difference in the numerical results.

6.3.1 Water depth and current speed

The flow in the Crouch estuary can be described as a very long shallow wave (tidal wave) propagating in a narrow channel with irregular bathimetry. Assuming a mean depth in the main channel of the estuary of the order of $d \approx 10m$, a rough estimation of the wave celerity is given by $c_w = \sqrt{gd} \approx 10m/s$. Considering that the tidal period is approximately $T_w \approx 12h$, the wave length of

such a wave propagating in a $10m$ depth channel would be around $L_w = c_w T_w \approx 430Km$. This gives a ratio between the vertical and horizontal length scales of $\frac{d}{L_w} \approx 2.10^{-5}$, which is very small, specially when compared with the ratios obtained in chapter 5 (Tables 5.3 and 5.4). At the same time the Ursell number, which is a ratio between the non-linear and the dispersive effects (see section 5.2.2), can be approximated as $Ur = \frac{gH_{max}T_w^2}{2d^2} \approx 10000$, which is a very high value. Therefore, this is a very shallow non-dispersive wave which should be adequately modelled by the 2D shallow water equations.

From the numerical results obtained with the different turbulence models (ML, $k-\varepsilon$ and ASM), it has been observed that the velocity and water depth fields are very insensitive to the turbulence model used. Further, even when the turbulent diffusion is neglected by forcing the eddy viscosity to zero, the mean flow results are very similar to those obtained with the turbulence models. This is because the turbulence level in the estuary is rather low. Turbulence is mainly produced in the main channel due to bed shear stress. Hence, a rough estimation of the eddy viscosity can be done with the parabolic eddy viscosity model (section 2.4.3) as:

$$\nu_t^{par} \approx \frac{1}{6}\kappa u_f h \approx 0.1h\frac{\sqrt{g}n|\mathbf{U}|}{h^{1/6}} \approx 0.06m^2/s \tag{6.2}$$

where it has been assumed a water depth of $10m$, a Manning's number of $0.02m/s^{1/3}$, and a depth averaged velocity of $1.5m/s$. With the estimation given by Equation 6.2, and assuming a length scale of $1000m$ (which is approximately the width of the estuary at the mouth), a turbulent horizontal Reynolds number can be defined as $Re_t = \frac{UL}{\nu_t} \approx 21000$. This is a rather large value, which means that the turbulent diffusion forces are small when compared to the convective forces (in the fishway flow (chapter 8), where turbulence plays an important role in the mean flow field, the turbulent Reynolds number is three orders of magnitude smaller). The small magnitude of the diffusive forces in the momentum equations diminishes the influence of the turbulence model on the mean velocity field. At the same time, since the three turbulence models give a similar estimation of the eddy viscosity produced by bed friction, the eddy viscosity field obtained with all the models is very similar (Figure 6.8). The ASM and $k-\varepsilon$ models give slightly larger eddy viscosity values than the ML model, but the differences are not significant. It should be noticed that the estimation of ν_t given by Equation 6.2 agrees fairly well with the numerical results (Figure 6.8), which confirms that turbulence is mainly produced by bed friction. An eddy viscosity of the same order of magnitude was obtained by Kawanisi in a shallow tidal estuary [69]. Velocity and water depth fields independent of the turbulence model were also obtained by Babarutsi et al. [5] when modelling shallow recirculating flows dominated by bed friction, by Davies et al. [35] when computing the tidal flow in the Irish Sea, and by Lloyd and Stansby [84] when modelling the flow around conical islands.

Assuming an approximated wave celerity of $10m/s$, it takes around $40min$ for the tidal wave

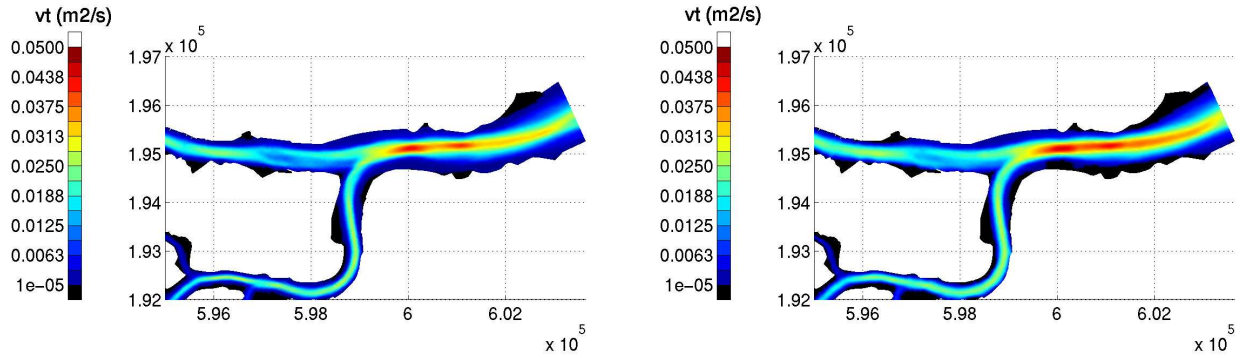

(a) $\nu_t(m^2/s)$. ML model.

(b) $\nu_t(m^2/s)$. $k-\varepsilon$ model.

Figure 6.8: Eddy viscosity field $\nu_t(m^2/s)$ at the mouth of the Crouch estuary. $t = 50h$. Ebb tide. ML and $k-\varepsilon$ models. Dry regions are shown in black.

to propagate from the mouth to the upper part of the estuary. For a tidal range of $5m$ this produces a maximum difference in the water surface level over the whole estuary of approximately $0.5m$, as it is shown in Figure 6.9.

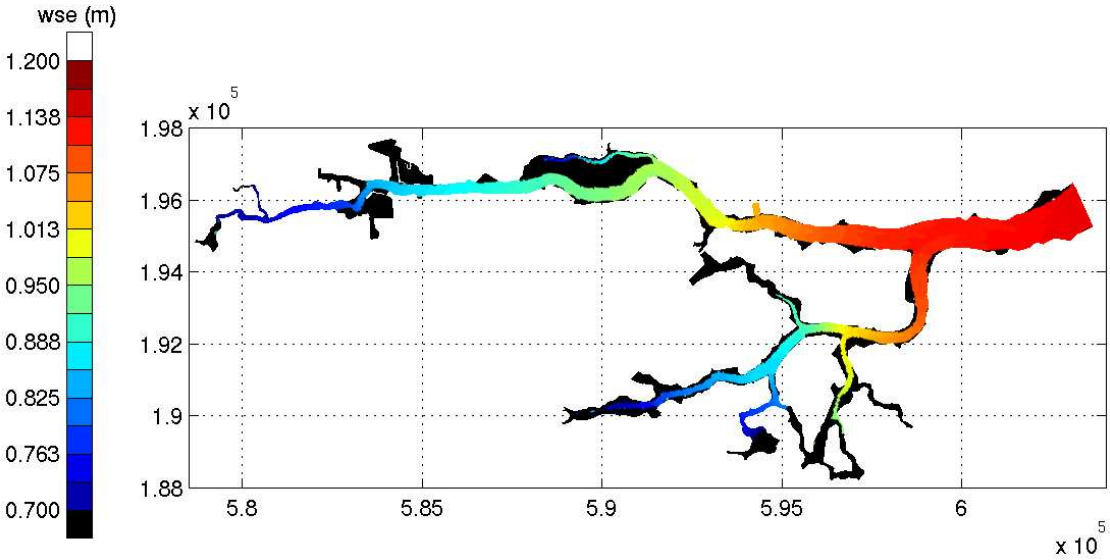

Figure 6.9: Water surface elevation in the Crouch estuary. $t = 7.5h$. Flood tide. Dry regions are shown in black.

The highest velocities given by the model occur near the mouth (Figure 6.10), with values around $1.5m/s$. High velocities are also predicted by the model at the entrance of the Roach river and near Bridgemarsh island, which are regions where the tidal channel narrows and gets shallow (Figure 6.1). Some high velocity spots appear in the upper part of the estuary. As it has been said, this velocity peaks are due to the lack of resolution in the bathimetry and to the coarse numerical mesh used in the upper part of the estuary, which cause large bed slopes at some specific points of the numerical model. Nevertheless, they are scarce and do not have any influence on the global solution. It should be remembered that we are not interested in resolving the flow patterns in these

parts of the estuary, and they are included in the model just in order to account for their bulk effect on the global flow.

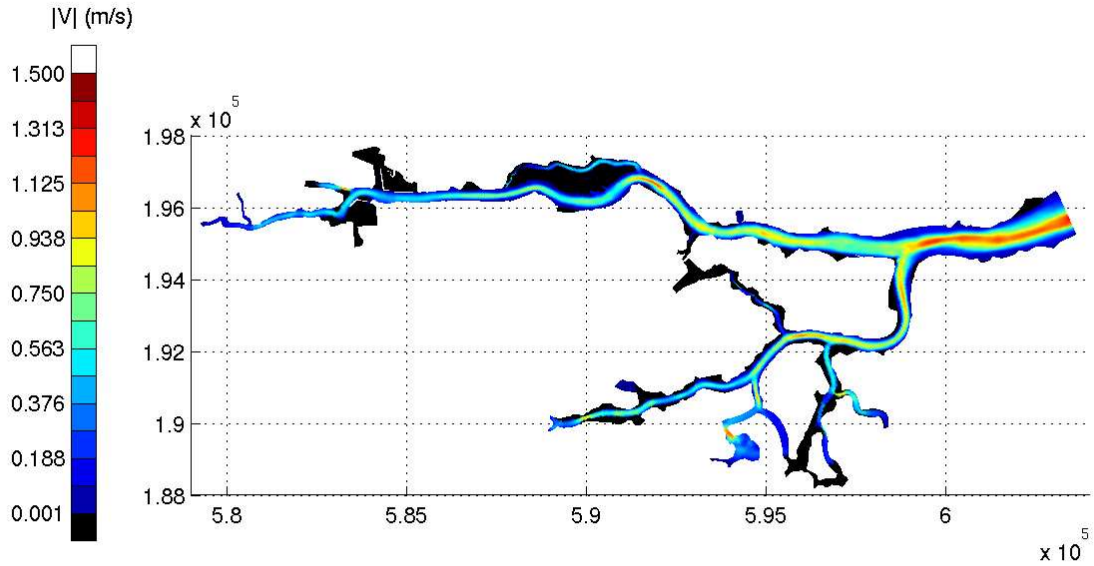

Figure 6.10: Depth averaged velocity field $|\mathbf{U}|(m/s)$ in the Crouch estuary. $t = 45h$. Flood tide. Dry regions are shown in black.

The flooding and drying of Bridgemarsh island is shown in Figures 6.11 and 6.12. Although no experimental measurements are available inside the island, it is known from visual observations that it floods completely. The numerical results show a good behaviour, without any spurious oscillations. As it has been pointed out previously, due to the irregular bathimetry, there are several isolated holes were the water gets trapped without possibility of drainage.

Figures 6.13 and 6.14 show the comparison between the experimental and numerical results. As it has been argued, the numerical water depth and velocity are independent of the turbulence model used. In general the water depth is rather well predicted by the model (Figure 6.13) except at Fambridge, where the maximum water depth is slightly underpredicted. The agreement on the depth averaged velocity varies between the different experimental stations (Figure 6.14). Both the ebbing and flooding flow at Wallasea are very well predicted. The agreement at Holliwell and Fambridge is also rather satisfactory, although the maximum ebbing velocity is slightly underpredicted by the model. The results at Paglesham and Creeksea are poorer, being the maximum flooding and ebbing velocities overpredicted by the model. It is clear from Figures 6.10 and 6.1 that the velocity field in the whole estuary is very dependent on the bed elevation, being the velocity higher in the deepest regions of the estuary. It is also clear from Figures 6.7 and 6.14 that the numerical solution is almost independent of the Manning's number and of the turbulence model. Hence, the disagreements between the numerical and the experimental results are probably due to errors in the local bathimetry. Another possible reason for the experimental-numerical disagreements is the presence of local flow patterns which would need a more refined numerical model to be resolved.

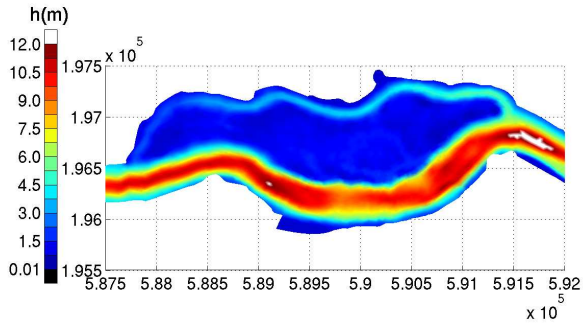

(a) Water depth $h(m)$. $t = 48h$.

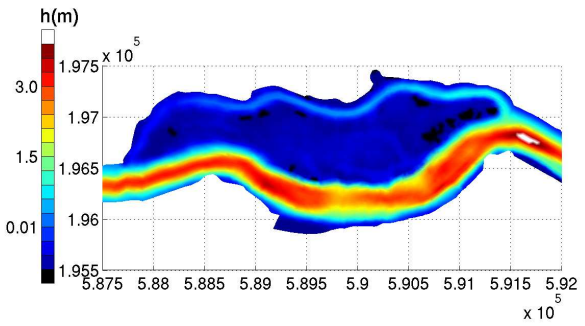

(b) Water depth. $h(m)$. $t = 49h$.

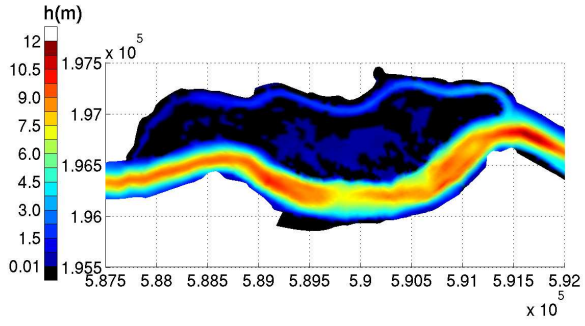

(c) Water depth. $h(m)$. $t = 50h$.

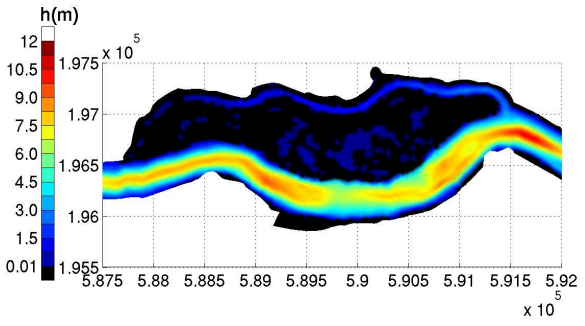

(d) Water depth. $h(m)$. $t = 51h$.

Figure 6.11: Water depth field $h(m)$ at Bridgemarsh island during an ebb tide. Dry regions are shown in black.

6.3.2 Turbulence field

The largest values of turbulent kinetic energy appear at the mouth of the estuary (Figure 6.15), where the highest velocities occur. There is also a high turbulent energy region at the entrance of the Roach river. However, even in those regions of the estuary, the turbulent kinetic energy is not excessively high, taking values around $0.015 m^2/s^2$. This gives a maximum turbulence intensity in the estuary of approximately $T_k = \dfrac{\sqrt{k}}{|\mathbf{U}|} \approx 0.08$, which is a relatively low value.

Both the ASM and $k-\varepsilon$ models give very similar turbulent energy fields (Figure 6.16). This is because turbulence is mainly produced by bed friction, and both models account in a similar way for this process.

Although there are not experimental measurements of the turbulent variables, the time evolution of the turbulent kinetic energy predicted by the model at several locations in the estuary is shown in Figure 6.17. The differences between the ASM and $k-\varepsilon$ models are so small that they cannot be appreciated in the plots. From the numerical results it should be noticed the asymmetry on the turbulence level at Holliwell and Wallasea during the flood and ebb tides, specially at Wallasea, where the turbulent energy is three times larger in the flood tide than in the ebb tide. It should be remarked that this strong asymmetry does not appear in the depth averaged velocity (Figure 6.14). In other locations, like Paglesham, similar values of turbulent energy are predicted

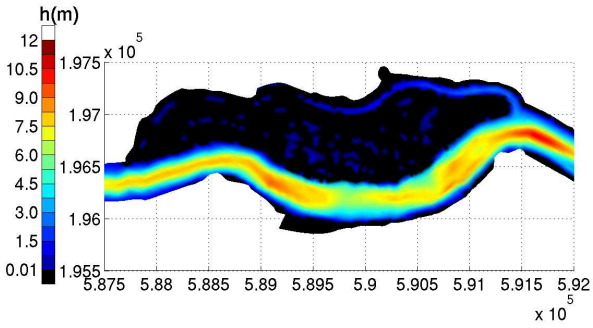

(a) Water depth $h(m)$. $t = 31.5h$.

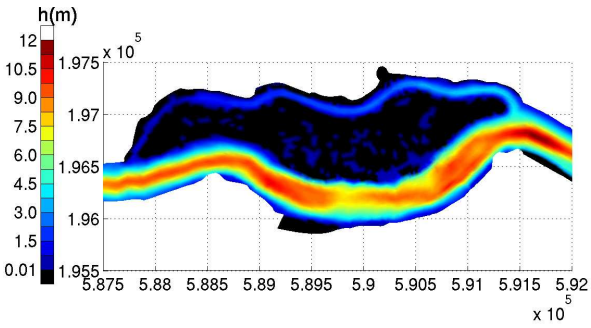

(b) Water depth $h(m)$. $t = 33h$.

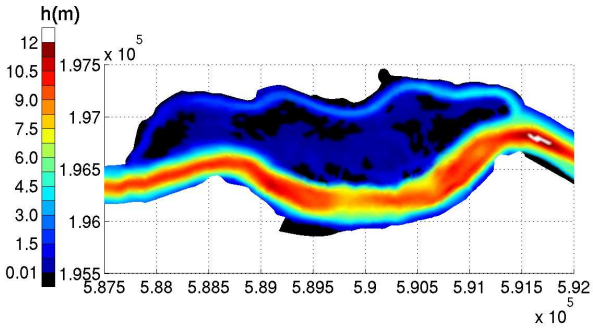

(c) Water depth $h(m)$. $t = 33.5h$.

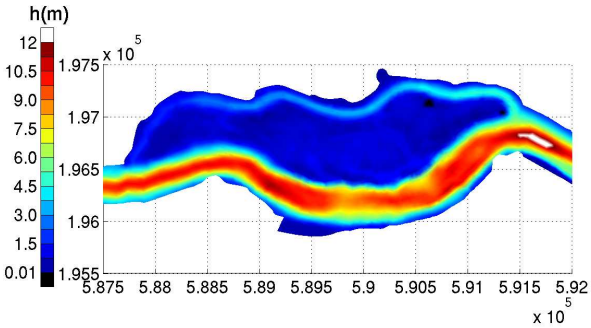

(d) Water depth $h(m)$. $t = 34.5h$.

Figure 6.12: Water depth field $h(m)$ at Bridgemarsh island during a flood tide. Dry regions are shown in black.

during the flood and ebb tides. In any case, since the main production of turbulence is due to bed friction, the turbulence level is expected to be rather dependent on the bed friction coefficient. Turbulence experimental measurements would be required in order to calibrate and validate the turbulence models.

The Reynolds stresses given by the ASM and $k - \varepsilon$ models show some differences in the maximum values (specially in $\overline{v'^2}$ and $\overline{u'v'}$), but still a very similar spatial distribution and time evolution are obtained with both models (Figures 6.18 and 6.19).

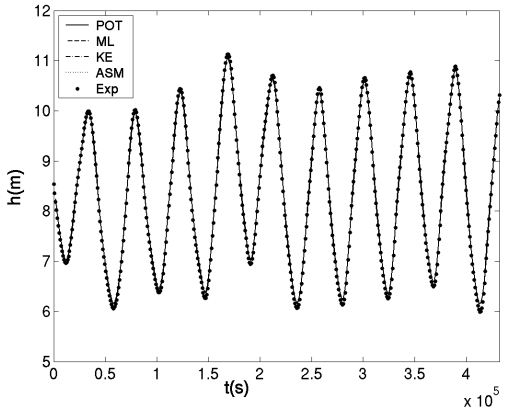

(a) Water depth $h(m)$. Holliwell.

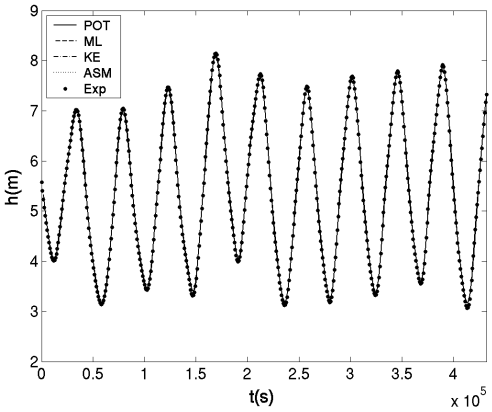

(b) Water depth $h(m)$. Wallasea.

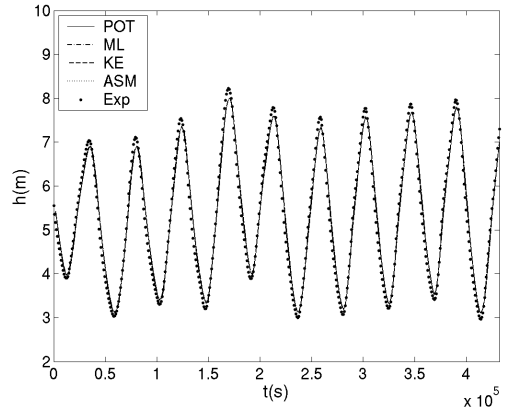

(c) Water depth $h(m)$. Paglesham.

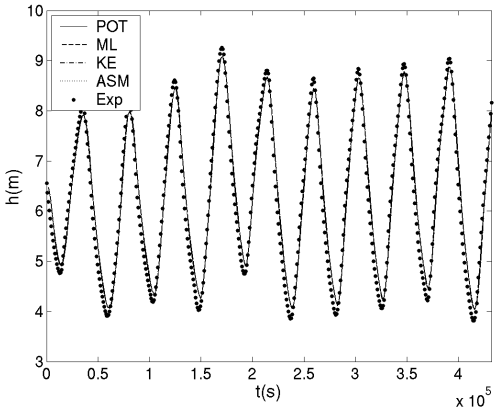

(d) Water depth $h(m)$. Fambridge.

Figure 6.13: Water depth $h(m)$ at several locations in the Crouch estuary. 5 day time series. Several turbulence models (ML, $k-\varepsilon$, ASM) and zero eddy viscosity (POT).

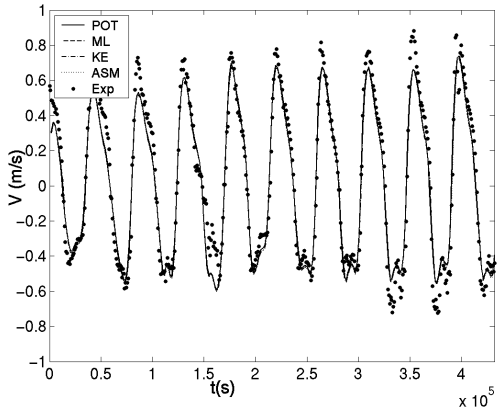

(a) Current speed $V(m/s)$. Holliwell.

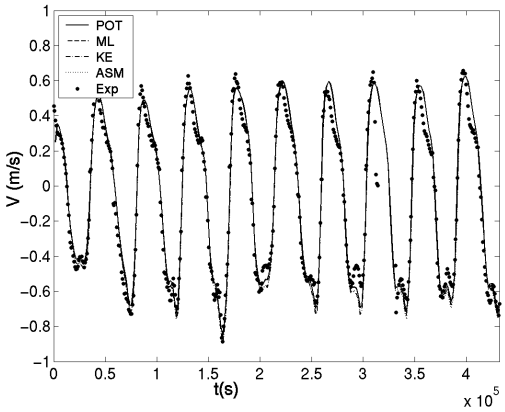

(b) Current speed $V(m/s)$. Wallasea.

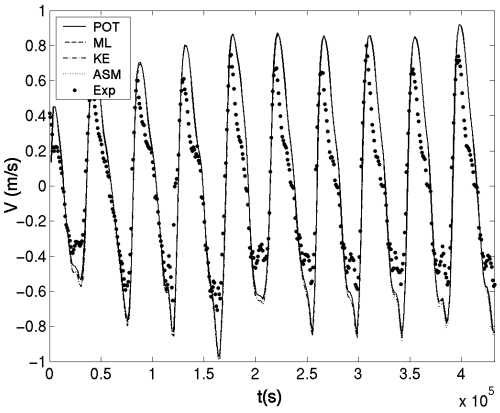

(c) Current speed (m/s). Paglesham.

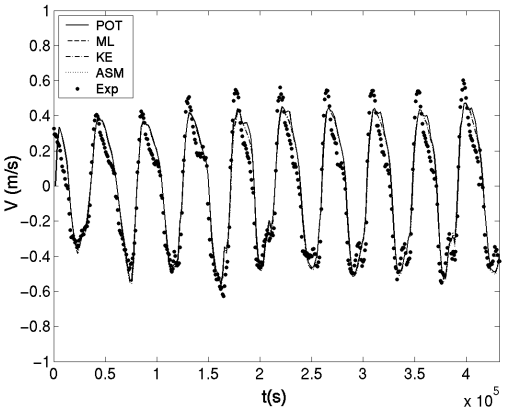

(d) Current speed (m/s). Fambridge.

Figure 6.14: Depth averaged current speed (m/s) at several locations in the Crouch estuary. 5 day time series. Several turbulence models (ML, $k-\varepsilon$, ASM) and zero eddy viscosity (POT).

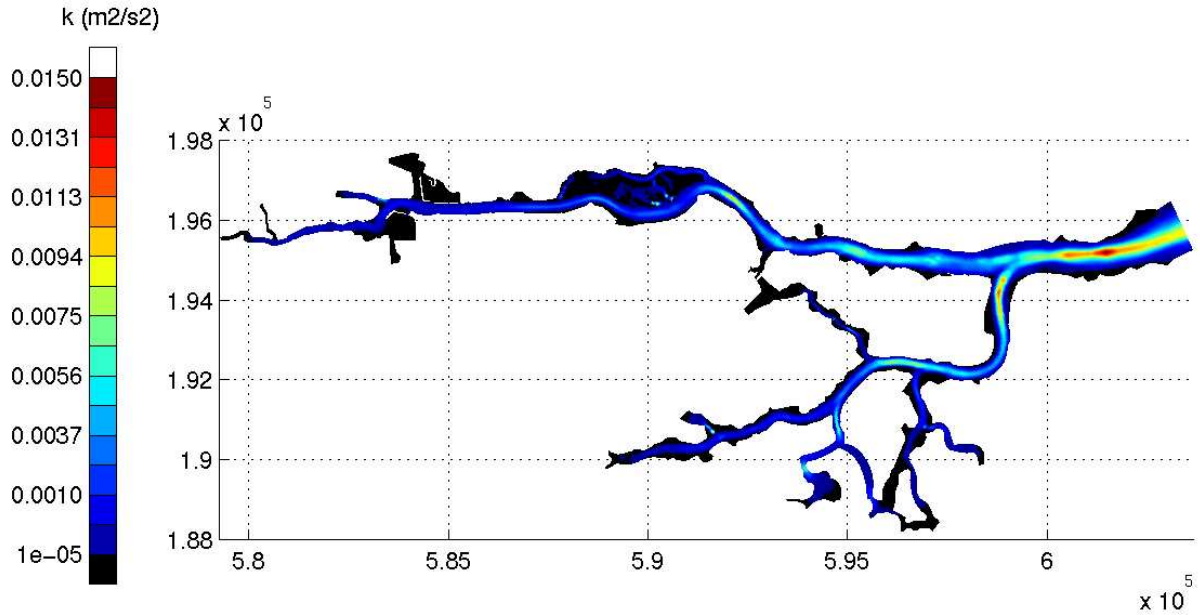

Figure 6.15: Turbulent kinetic energy field $k(m^2/s^2)$ in the Crouch estuary. $t = 36.5h$. Ebb tide. $k - \varepsilon$ model.

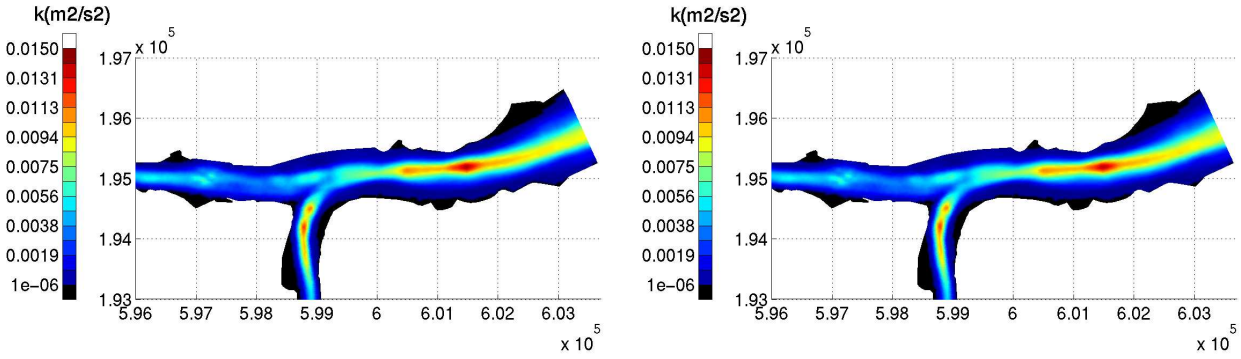

(a) Turbulent energy $k(m^2/s^2)$. $k - \varepsilon$ model.

(b) Turbulent energy $k(m^2/s^2)$. ASM.

Figure 6.16: Turbulent kinetic energy field $k(m^2/s^2)$ at the mouth of the Crouch estuary. $t = 37h$. Ebb tide. ASM and $k - \varepsilon$ models.

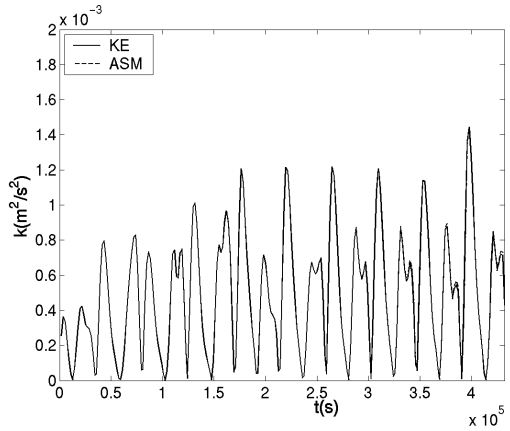

(a) Turbulent energy $k(m^2/s^2)$. Holliwell.

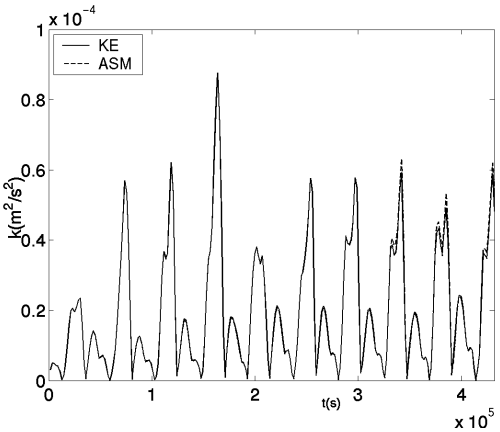

(b) Turbulent energy $k(m^2/s^2)$. Wallasea.

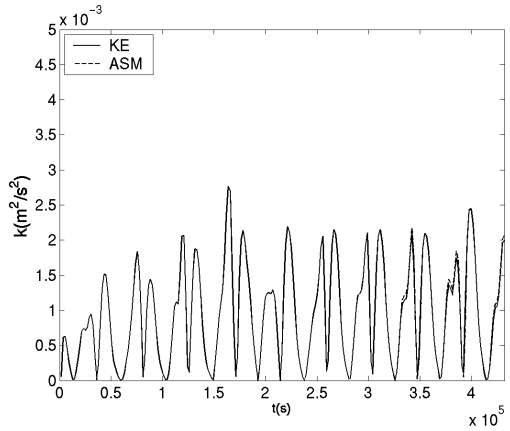

(c) Turbulent energy $k(m^2/s^2)$. Paglesham.

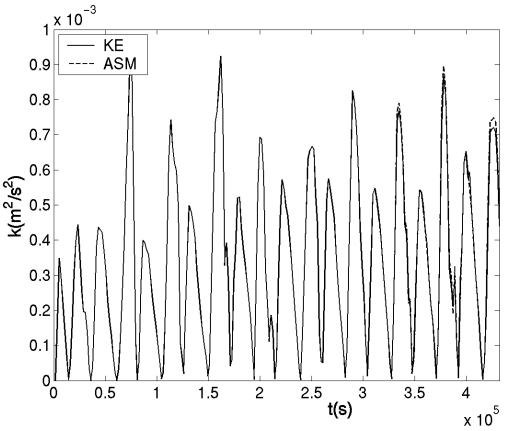

(d) Turbulent energy $k(m^2/s^2)$. Fambridge.

Figure 6.17: Turbulent kinetic energy $k(m^2/s^2)$ at several locations in the Crouch estuary. 5 day time series. ASM and $k-\varepsilon$ models.

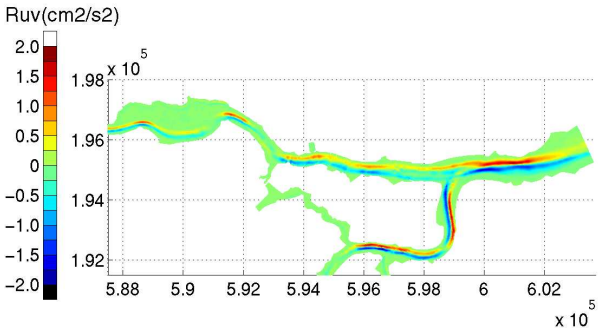

(a) $\overline{u'v'}$. $k-\varepsilon$ model.

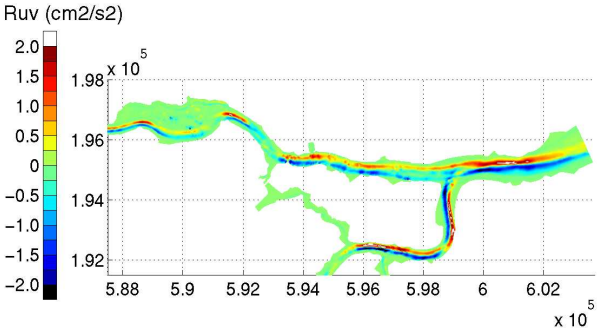

(b) $\overline{u'v'}$. ASM.

Figure 6.18: $\overline{u'v'}$ field. $t = 50h$. Ebb tide. ASM and $k-\varepsilon$ models.

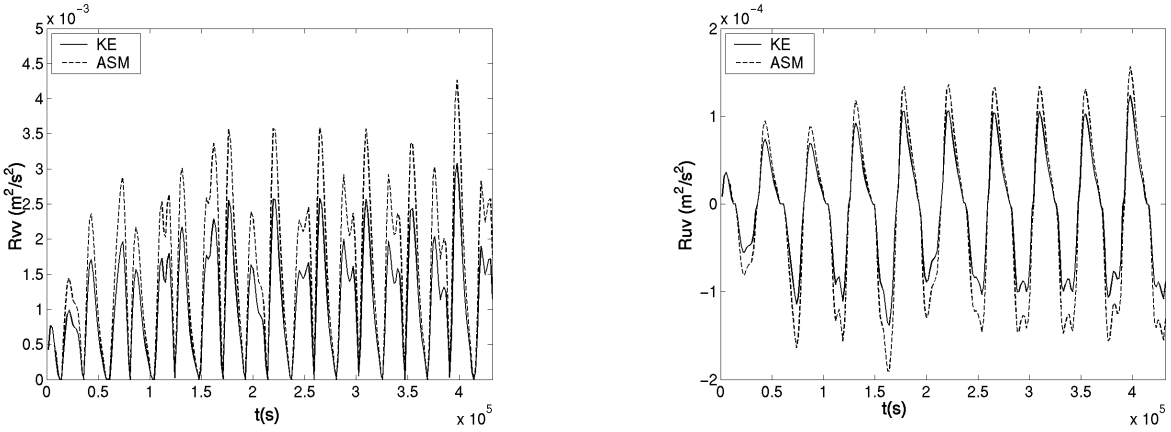

(a) $\overline{v'^2}$. Holliwell. (b) $\overline{u'v'}$. Holliwell.

Figure 6.19: Reynolds stresses $\overline{v'^2}$ and $\overline{u'v'}$ at Holliwell. 5 day time series. ASM and $k - \varepsilon$ models.

Chapter 7

Open channel flow around a 90^{o} bend

7.1 Introduction

In this chapter the free surface flow in an open channel with a 90^{o} bend is computed and compared with the experimental velocity data obtained by Bonillo [13]. Three depth averaged turbulence models have been used in the numerical computations: the mixing length model (ML), the $k-\varepsilon$ model of Rastogi and Rodi, and the depth averaged algebraic stress model presented in section 2.5 (ASM). Four different grids, with different mesh size near the wall, have been used in the simulations. The influence of the bed friction is also examined, comparing the results obtained for different Manning numbers.

7.2 Experimental tests

7.2.1 Experimental setup

The experimental tests were carried out by Bonillo [13] at the hydraulic laboratory of the CITEEC (Centro de Innovación Tecnolóxica en Edificación e Enxeñería Civil, University of A Coruña, Spain). A brief description of the experimental procedure is done in this section. A detailed description of the experimental setup can be found in [13].

The experiments were performed in a concrete rectangular channel with two rectilinear sections joined by a 90^{o} bend (Figure 7.1). The first section is $0.86m$ wide with a flat bed. At the end of the first section, just before the bend, there is a small step with a change in the bed elevation of $\Delta z_b = -0.013m$. The second section is $0.72m$ wide with a flat bed.

The three-dimensional velocity was measured with an Acoustic Doppler Velocimeter (Sontek ADV). The control volume of the ADV is a $6mm$ height cylinder with a diameter of $4mm$ ($75mm^3$), which is located $5cm$ away from the ADV in order to avoid interferences with the flow (Figure 7.2). The experimental velocity was measured at 1029 spatial points, distributed in

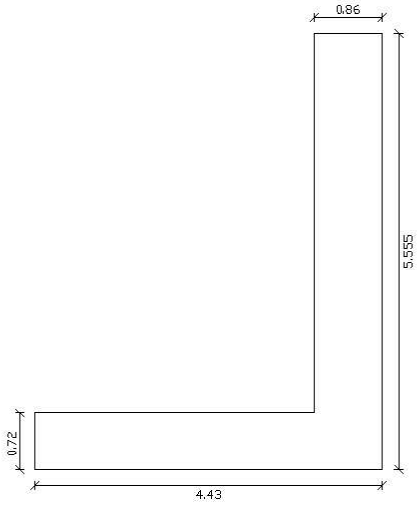

Figure 7.1: Spatial domain in the 90^o bend.

(a) MicroADV. (b) Sampling volume.

Figure 7.2: MicroADV and sampling volume.

a horizontal plane located at approximately the mid-point between the bed and the free surface (Figure 7.3(a)). At each data point 40 instantaneous samples were registered.

The total water discharge in the experiments was $29.5l/s$. At the end of the channel the water depth was fixed to $0.180m$. With this boundary conditions the mean velocity at the beginning of the channel was $0.20m/s$, and the water depth $0.173m$. The horizontal Reynolds number based on the channel width, and the Froude number based on the water depth at the entrance of the channel are given by:

$$Re = \frac{|\mathbf{U}|L}{\nu} = 1.7\,10^5 \qquad\qquad Fr = \frac{|\mathbf{U}|}{\sqrt{gh}} = 0.153 \tag{7.1}$$

where $|\overline{\mathbf{u}}|$ is the module of the experimental mean velocity. The turbulence intensity in the main section of the channel is around $T_k = \dfrac{\sqrt{k}}{|\overline{\mathbf{u}}|} \approx 0.05$, where k is the turbulent kinetic energy. The

variability of the mean velocity estimated from the experimental data ($\varepsilon_{\overline{u}_N}$) is equal to:

$$\varepsilon_{\overline{u}_N} = \sqrt{\frac{\sigma^2_{\overline{u}_N}}{\overline{u}^2}} = \frac{1}{\sqrt{N}}\frac{\sigma_u}{\overline{u}} \approx \frac{1}{\sqrt{N}}\sqrt{\frac{2}{3}}T_k \approx 0.007 \tag{7.2}$$

where N is the number of independent instantaneous samples ($N = 40$), $\overline{u}_N$ is the estimation of the mean velocity obtained with the N independent samples, $\sigma^2_{\overline{u}_N}$ is the variance of the estimated mean velocity, and σ^2_u is the variance of the instantaneous velocity. In the inner and outer corner of the bend, due to the strong velocity gradients the turbulence intensity increases considerably, achieving values of nearly 100%, which corresponds to a variability of the experimental mean velocity of approximately 15%. This values should be taken into account when comparing the numerical and experimental results.

7.2.2 Experimental results

The experimental data points, as well as the horizontal and vertical experimental velocity fields are shown in Figure 7.3. In the first section of the channel the velocity is quite uniform, with only some perturbations at the upstream entrance, and the vertical velocity is almost zero. A small recirculation bubble appears in the inner corner of the bend. At the same time, a vertical eddy which expands over almost the entire channel width is generated in the bend due to the change in the direction of the flow. This secondary flow can be clearly identified in the vertical velocity field near the bend (Figure 7.3(d)). The vertical eddy may produce some non-homogeneities in the vertical profile of the horizontal velocity. For this reason, in this region the dispersion terms due to non-uniformities in the vertical direction (see section 2.3), which are neglected in the depth averaged model, may introduce some modelling errors in the momentum conservation equations. The influence of these errors in the numerical simulations can only be checked by the agreement between the experimental and the numerical results. The effect of the bend is present in the flow until the end of the second section of the channel, although the secondary flow has almost disappeared at $1.5m$ downstream the bend.

Figure 7.4 shows the experimental turbulent kinetic energy field, as well as the normal Reynolds stresses. The vertical Reynolds stress ($\overline{w'^2}$) is always smaller than the horizontal ones. There is an important production of turbulence in the inner corner of the bend due to horizontal velocity gradients (Figure 7.4(d)). The turbulence level in the first section of the channel, which is mainly given by the bed friction production, is rather low, specially compared with the turbulence level in the bend region. There is also some production of turbulence in the outer corner of the bend due to the stagnation conditions. However, the production in that area is much lower than in the recirculation bubble, and it has little influence on the downstream flow.

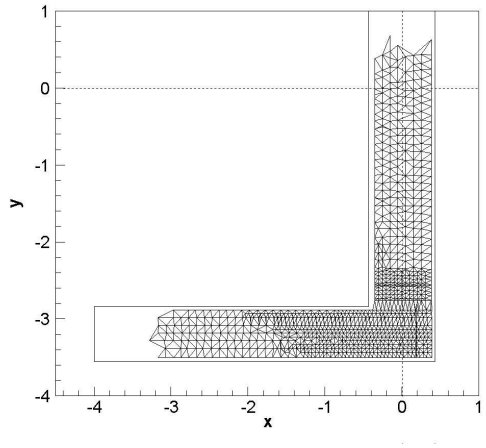

(a) Experimental data points.

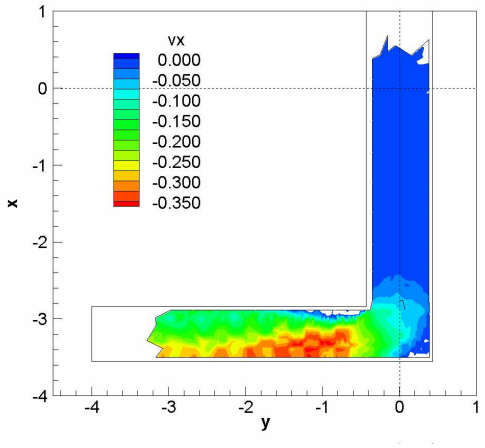

(b) $V_x(m/s)$.

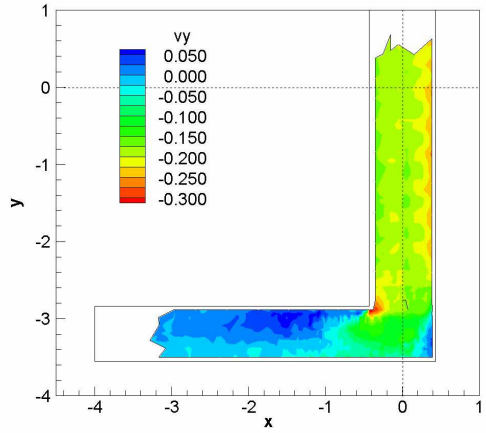

(c) $V_y(m/s)$.

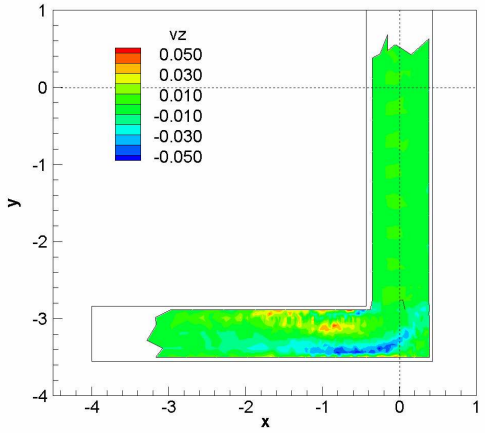

(d) $V_z(m/s)$.

Figure 7.3: Experimental velocity field in the 90^o bend.

7.3 Numerical model

Considering the flow configuration and the experimental results, it seems reasonable to use a depth averaged model to compute the free surface flow in the bend. The most challenging point of the numerical simulation is the correct prediction of the separated region which appears in the inner corner of the bend. It is well known that RANS models usually fail to give accurate predictions of strong separated flows over 3D geometries. However, in this case the 2D forcing produced by the shallowness of the flow is expected to reduce the 3D features of the flow field, helping to improve the accuracy of the results.

Three depth averaged turbulence models have been used: the mixing length model (ML), the $k - \varepsilon$ model of Rastogi and Rodi, and the depth averaged algebraic stress model presented in section 2.5 (ASM). All the models have been used with the original constants, without any modification or previous calibration.

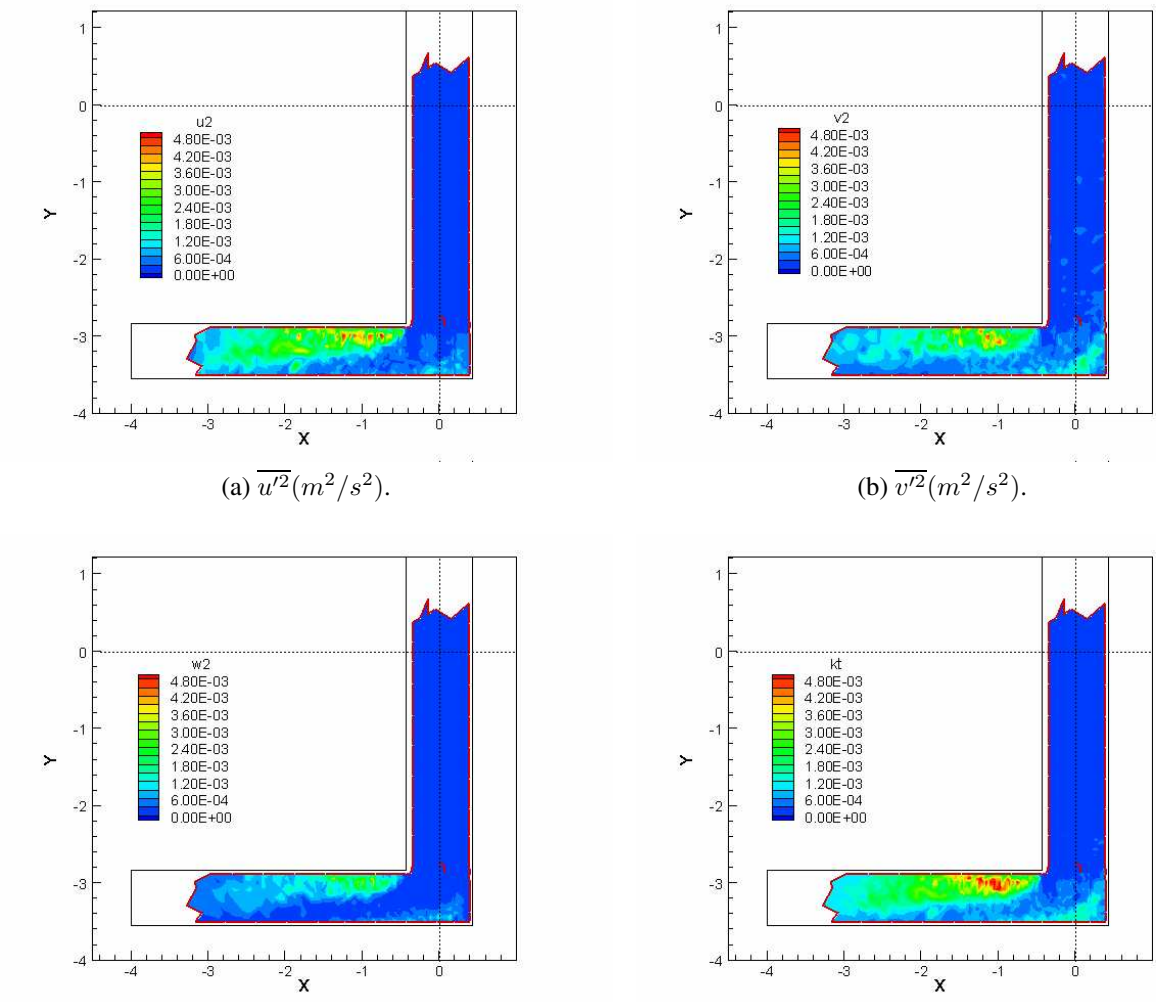

(a) $\overline{u'^2}(m^2/s^2)$.

(b) $\overline{v'^2}(m^2/s^2)$.

(c) $\overline{w'^2}(m^2/s^2)$.

(d) $k(m^2/s^2)$.

Figure 7.4: Experimental normal turbulent stresses fields in the 90^o bend.

7.3.1 Influence of the numerical scheme on the solution

As it has been discussed in the validation of the solver (chapter 4), it is very important to use an accurate numerical scheme with a low numerical diffusion. Otherwise the solution may be too diffusive, and the velocity profiles too flattened. In order to check the influence of the numerical scheme on the solution, three different numerical schemes have been used: the first order van Leer's scheme, its second order extension, and the second order extension of Roe's scheme. The results shown in Figures 7.5 and 7.6 have been obtained without using any turbulence model. Furthermore, the effective viscosity was set to zero, and therefore, all the diffusion comes from the numerical scheme.

The first order scheme is too diffusive, and thus, it is not able to generate a recirculation region downstream the bend (Figure 7.5(a)). On the other hand, the second order scheme, with a much lower numerical diffusion, produces a large recirculation bubble (Figure 7.5(b)). The less diffusive

the numerical scheme is, the larger the recirculation bubble is. Eventually, if a scheme with no numerical diffusion at all was used (which would be actually a centred scheme), the bubble, and the scheme, would become unstable. The differences between Roe's and van Leer's schemes are negligible (Figure 7.6). Since the water surface elevation and the bed are almost flat, the hybrid first/second order and the fully second order schemes (see section 3.5 for a detailed description of the schemes) produce exactly the same results (order 2 in Figure 7.6). All the results presented in this chapter have been obtained with the second order extension of the van Leer's scheme.

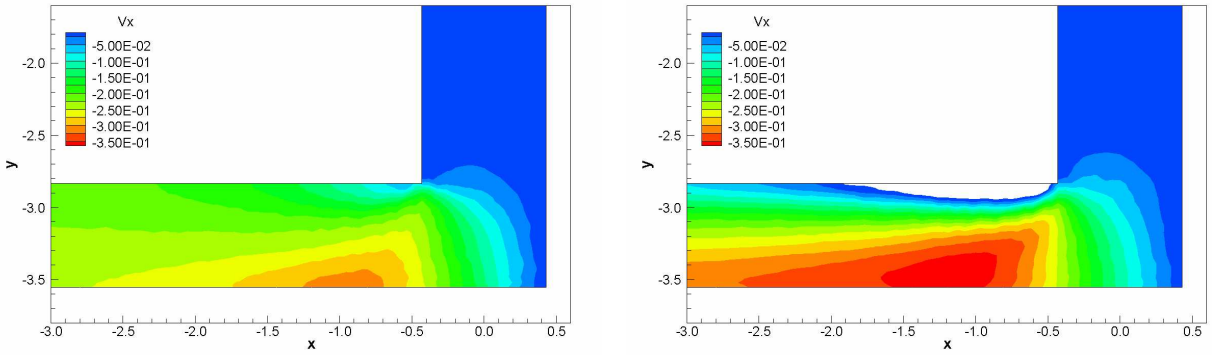

(a) First order van Leer's scheme.

(b) Second order van Leer's scheme.

Figure 7.5: Influence of the numerical scheme on the velocity field. Longitudinal velocity $V_x(m/s)$ field.

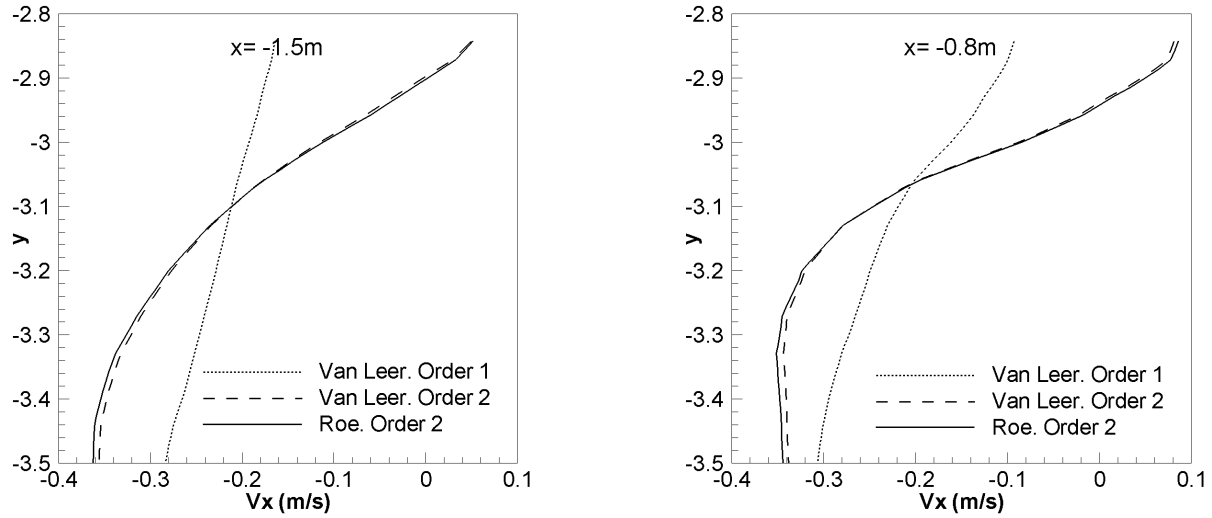

(a) Cross section x=$-1.5m$.

(b) Cross section x=$-0.8m$.

Figure 7.6: Influence of the numerical scheme on the velocity field. Cross sections of the longitudinal velocity $V_x(m/s)$ downstream the bend.

7.3.2 Mesh convergence

Four different meshes have been used in the computations. The spatial domain covered by the meshes is shown in Figure 7.1. The finite volume mesh is generated from a triangular mesh by the procedure presented in section 3.5.1. Figure 7.7 shows the near bend region of the four triangular meshes which have been used to build the respective finite volume meshes. The characteristics of both the triangular and the finite volume grids are shown in Table 7.1. The main difference between them is the mesh size near the wall and in the separated region. A refined grid is needed in this area in order to resolve the recirculation bubble, and to avoid an excessive numerical diffusion which may interfere with the turbulent diffusion. Notice that in Table 7.1 the most important parameter in order to characterise the mesh resolution is the distance from the first inner node to the wall in the bubble region (Δy_{wall}). On the other hand, the computational cost is proportional to the number of faces in the finite volume mesh, since all the main loops in the numerical solver are done over volume faces. Therefore, the computational cost of mesh M4 is around 4 times higher than the cost of mesh M1, while the resolution in the bubble region is almost 8 times higher. The grid size in the recirculation region differs approximately by a factor 2 between each mesh.

	Triangular mesh		Finite volume mesh		
	vertex	elements	volumes	faces	Δy_{wall}
M1	738	1296	2033	3888	0.031 m
M2	1697	3124	4820	9372	0.018 m
M3	2495	4712	7206	14136	0.008 m
M4	3003	5700	8702	17100	0.004 m

Table 7.1: Characteristics of the computational grids for the 90^o bend. Δy_{wall}: distance from the first inner node to the wall in the recirculation region.

The mesh convergence has been analysed according to the separation length and the velocity profiles in the recirculation region, since it is there where the largest differences between the four meshes appear. Table 7.2 shows the recirculation length computed with several meshes and turbulence models. Unfortunately, the bubble length cannot be determined from the experimental results due to the minimum distance required between the ADV and the wall of the channel. Nevertheless, the bubble width can be determined from the experimental data, showing a very good agreement with the numerical results given by the three turbulence models (Table 7.3).

	ML	$k-\varepsilon$	ASM
M1	0.38 m	0.43 m	0.35 m
M2	1.12 m	1.05 m	1.12 m
M3	1.46 m	1.10 m	1.09 m
M4	1.71 m	1.15 m	1.15 m

Table 7.2: Recirculation length computed with several meshes and turbulence models.

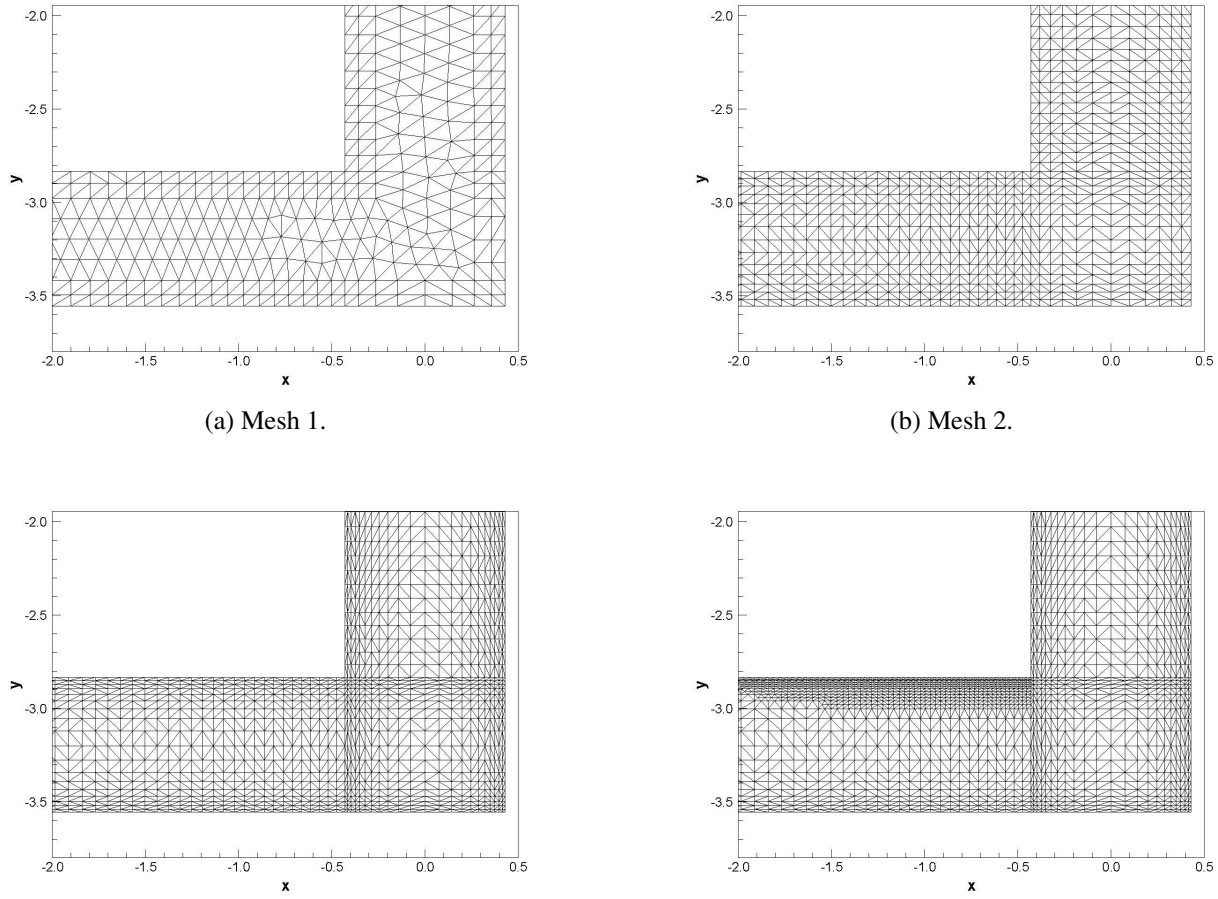

(a) Mesh 1.

(b) Mesh 2.

(c) Mesh 3.

(d) Mesh 4.

Figure 7.7: Numerical meshes in the near bend region.

	Exp.	ML	$k-\varepsilon$	ASM
M4	0.13 m	0.12 m	0.11 m	0.12 m

Table 7.3: Recirculation width computed with mesh M4.

The results obtained with the mesh M1 are rather independent of the turbulence model used. This is because the grid is too coarse (Figure 7.7), and the numerical diffusion dominates over the turbulent diffusion. With this mesh (M1), the near wall mesh size (y^+) grows quickly, reaching values larger than 100 at $0.8m$ downstream the bend ($x = -1.23m$ in Figure 7.8(b)). Notice also in Figure 7.8(a) how with the mesh M4 the lower limit in y^+ (see section 1.4) acts from $x = -1.4m$ to $x = -1.8m$.

The wall friction velocity (u_*) obtained with the different turbulence models and grids is shown in Figure 7.9. The ASM and $k-\varepsilon$ models give similar results. The stagnation point ($u_* = 0$) defining the limit of the recirculation bubble is very similar for grids M2, M3 and M4. However, the maximum friction velocity does not reach convergence until grid M3. The results are quite insensitive to further mesh refinement. No significant differences appear between grids M3 and M4

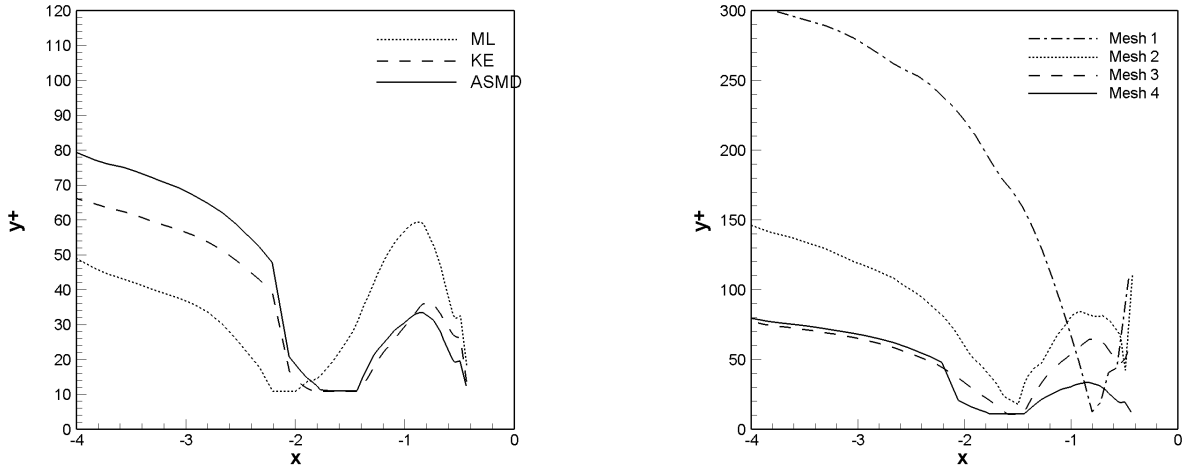

(a) Mesh 4. Several turbulence models.

(b) ASM. Several meshes.

Figure 7.8: $y^+ = \dfrac{yu_*}{\nu}$ in the recirculation wall in the 90^o bend.

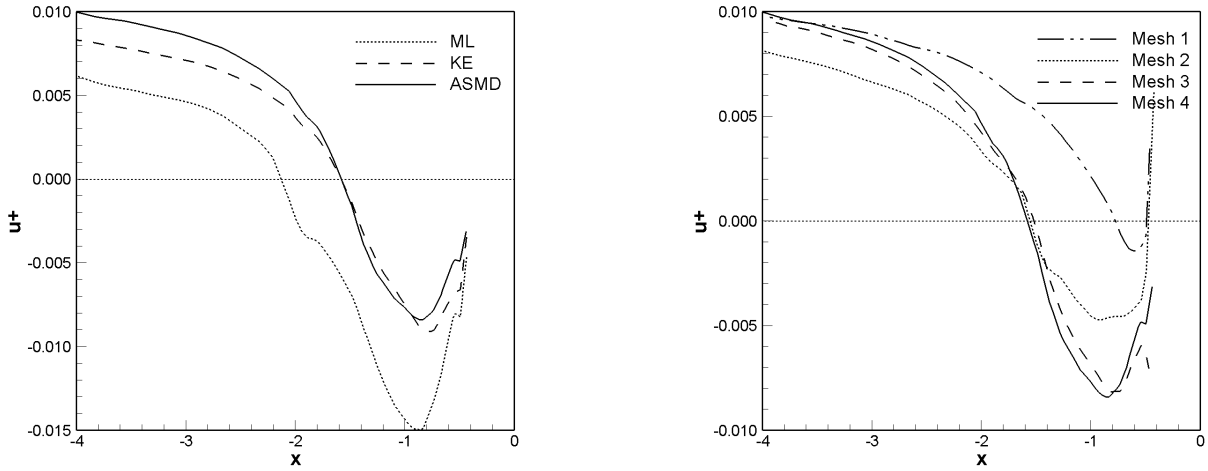

(a) Mesh 4.

(b) ASM.

Figure 7.9: Wall friction velocity $u_*(m/s)$ in the recirculation wall in the 90^o bend.

(Figures 7.9(b) and 7.10(b,c)). On the other hand, the ML model is more sensitive to mesh refinement, appearing still some differences between the velocity profiles obtained with the grids M3 and M4 (Figure 7.10(a)).

7.3.3 Influence of the bed friction on the numerical solution

Several Manning's numbers have been used in the computations in order to analyse the effect of the bed friction on the numerical solution. It has turned out that, in the range of expected values for the Manning's coefficient in the experimental concrete channel, the bed friction has very little influence on the mean flow field (Figure 7.11). On the other hand, it does have influence on the

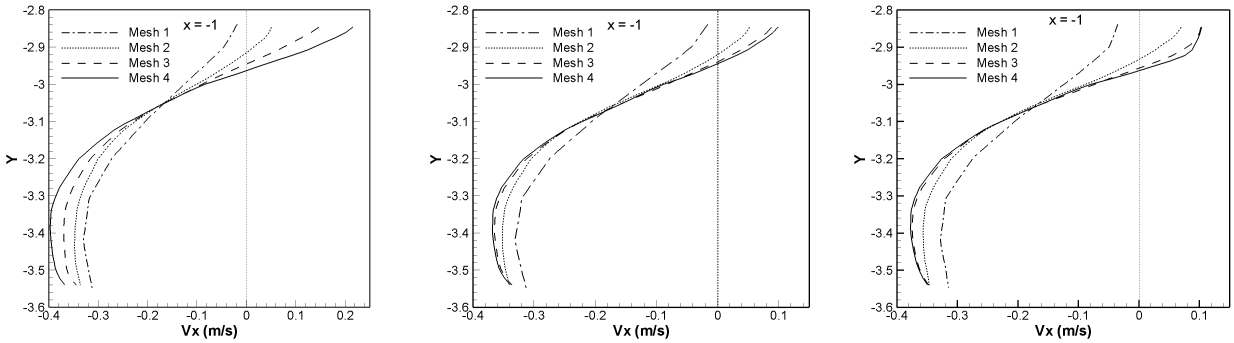

(a) ML model. (b) $k-\varepsilon$ model. (c) ASM.

Figure 7.10: Mesh convergence in the 90^o bend. Velocity profile $V_x(m/s)$ at $x = -1m$.

turbulence level in the first section of the channel, where turbulence is mainly produced by vertical shear. Nevertheless, near the bend the production of turbulence due to horizontal shear is more important than the production due to vertical shear, and therefore, the effect of the bed friction in the recirculation bubble is minor (Figure 7.12(a)).

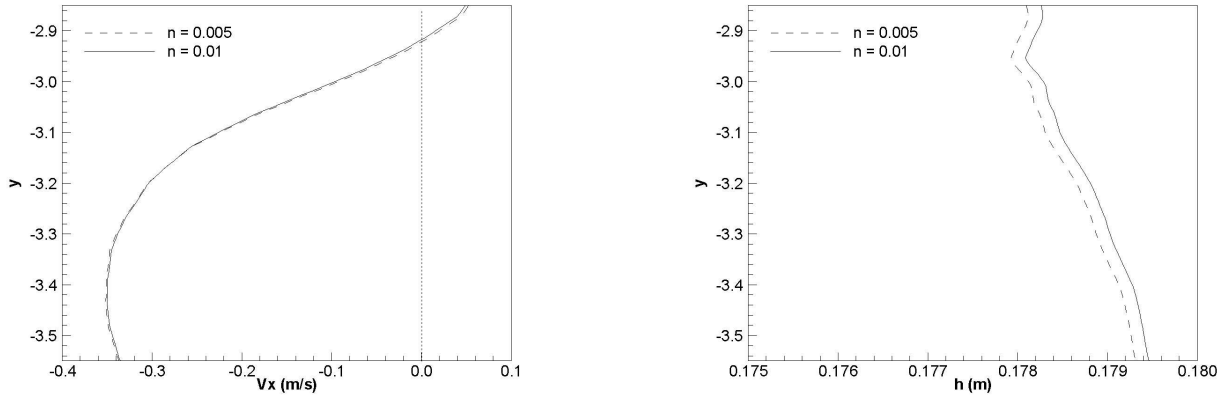

(a) Longitudinal velocity $V_x(m/s)$. (b) Water depth $h(m)$.

Figure 7.11: Dependence of the mean flow at $x = -1m$ on the bed friction.

Figure 7.12 shows the turbulent kinetic energy predictions obtained with two different Manning's numbers. It is clearly shown the high turbulent energy reached in the recirculation region, which is mainly produced by horizontal shear strain, and independent of the bed friction. Outside the recirculation bubble turbulence is mainly produced by bed friction, and thus, some differences appear in the turbulent kinetic energy when the Manning's number is increased. However, these differences do not affect the mean flow field, as it is shown in Figure 7.11. From the agreement between experimental and numerical results in the first section of the channel, a Manning's coefficient of $n = 0.005 s/m^{1/3}$ was chosen for the definitive computations. It should be noticed that this value is rather small compared to the Manning's coefficients which are often used in the simulation of open channel flow. This is probably because many simulations do not include the

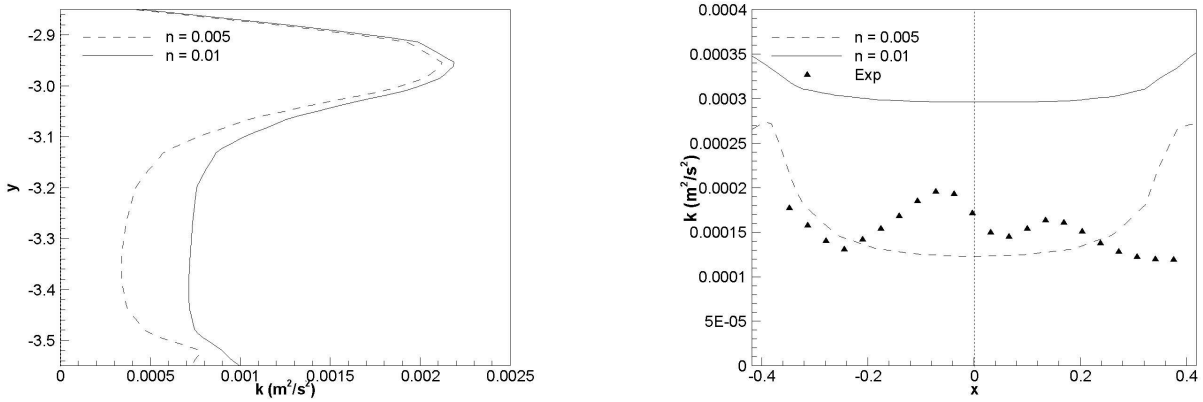

(a) Section $x = -1m$.

(b) Section $y = 0m$.

Figure 7.12: Dependence of the turbulent kinetic energy field $k(m^2/s^2)$ on the bed friction.

turbulent diffusion effects, and therefore, an increased Manning's coefficient is used in order to account partially for the dissipation effects of turbulence.

7.4 Numerical results and experimental validation

The comparison between the numerical results and the experimental data will be made in the recirculation region, since the first section of the channel does not present any interesting flow features. The following facts should be taken into consideration when comparing the numerical and experimental results: (1) the numerical velocity is the depth averaged velocity, while the experimental velocity is the horizontal velocity at approximately the mid-point between the bed of the channel and the free surface ($z_{exp} \approx \frac{h}{2}$); (2) the experimental values plotted in the cross sections have been obtained by interpolation of the actual measurements, which were made in the experimental mesh shown in Figure 7.3(a); (3) according to the turbulence level and the number of instantaneous samples which have been used to compute the statistical estimators of the mean variables, the variability of the experimental mean velocity in the recirculation region is about 10%.

It should be noticed that in uniform channel flow the velocity profile is quite homogeneous in the vertical direction, and the velocity at z_{exp} is approximately equal to the depth averaged velocity. However, near the bend the vertical eddy generated in the flow tends to destroy the homogeneity in the vertical direction. This has two main effects. First, the differences between the depth averaged velocity and the experimental velocity measured at z_{exp} may increase, depending on the actual vertical profile. Second, a modelling error is introduced in the depth averaged equations, which neglect the dispersion terms due to the non-homogeneity of the vertical profiles (section 2.3).

Despite these 3D flow features appearing in the near bend region, the overall agreement between the experimental and the numerical fields is very satisfactory, as it is shown in Figure 7.14. The ML model overpredicts the recirculation region (white colour in Figure 7.14). This is because

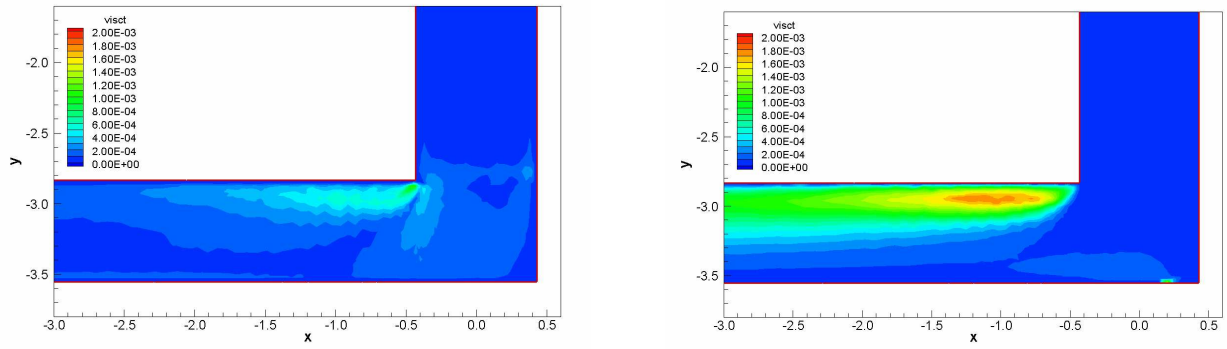

(a) ML model.

(b) $k-\varepsilon$ model.

Figure 7.13: Eddy viscosity field $\nu_t(m^2/s)$ in the 90^o bend. ML and $k-\varepsilon$ models.

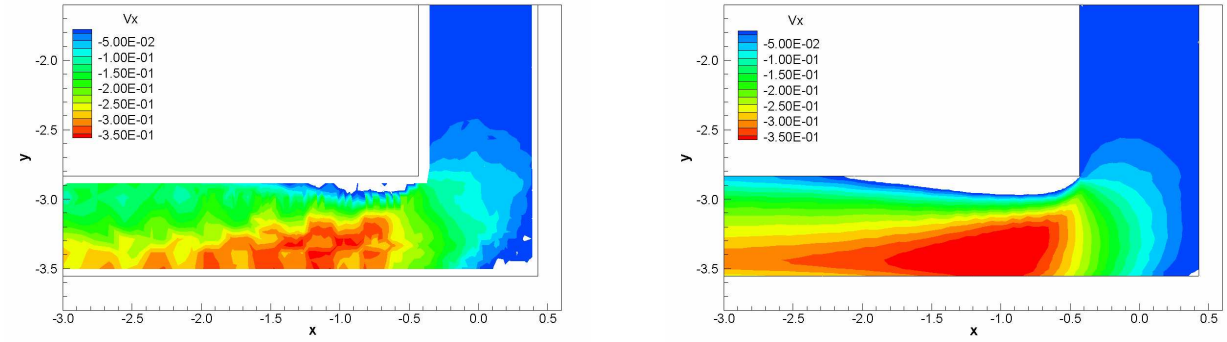

(a) Experimental.

(b) ML model.

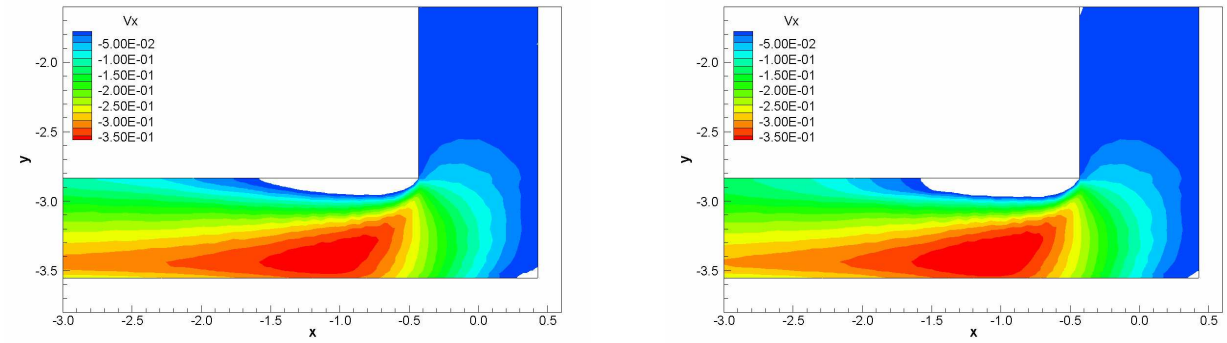

(c) $k-\varepsilon$ model.

(d) ASM.

Figure 7.14: Velocity field $V_x(m/s)$ in the 90^o bend. Several turbulence models and experimental results. White colour accounts for positive V_x.

the model does not account for transport processes, and therefore, all the eddy viscosity generated in the inner corner of the bend is not convected, neither diffused, downstream the bend, as it is in the ASM and $k-\varepsilon$ models (Figure 7.13). The size of the recirculation bubble computed with the ASM and $k-\varepsilon$ models shows a better agreement with the experimental one, although it is still somewhat larger.

The turbulent energy field predicted by the solver agrees rather well with the experimental one

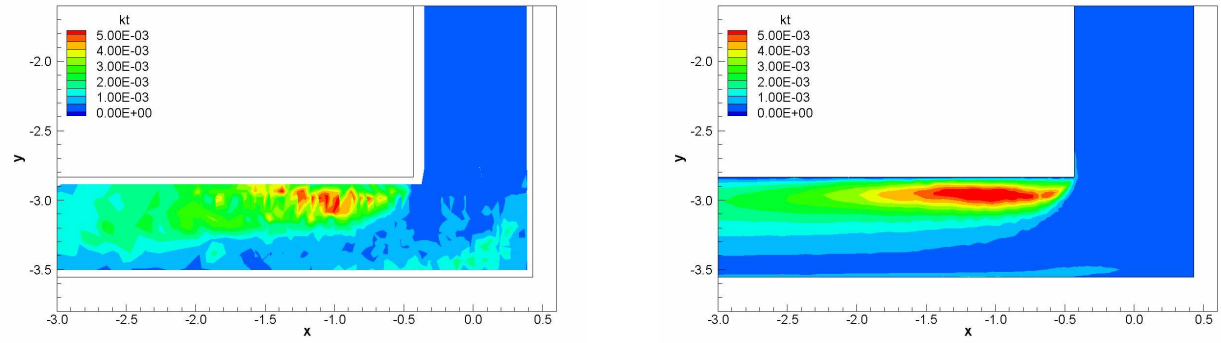

(a) Experimental. (b) ASM.

Figure 7.15: Turbulent kinetic energy field $k(m^2/s^2)$ in the 90^o bend. ASM and experimental results.

(Figure 7.15). The production of turbulence in the inner corner, as well as the convection and diffusion downstream are well predicted. The diffusion of turbulent kinetic energy is somewhat larger in the experimental results than in the numerical prediction, probably due to the convection and mixing produced by the vertical eddies which are not considered in the model.

The agreement between the experimental and numerical fields of the normal Reynolds stresses is rather satisfactory for both the ASM and the $k-\varepsilon$ models (Figure 7.16). The lateral diffusion of $\overline{u'^2}$ downstream the bend is slightly better predicted by the ASM, but still smaller than the experimental one. As it has been said, this difference is probably due to the lateral dispersion introduced by the vertical eddy. The maximum level of $\overline{u'^2}$ is well given by both models, while the maximum value of $\overline{v'^2}$ is slightly overpredicted by the $k-\varepsilon$ model.

A more detailed comparison of the experimental and numerical fields is done in cross sections downstream the bend. Considering the variability of the experimental data, the agreement in the velocity is very satisfactory (Figure 7.17). From the cross section at $x=-1.5m$ (Figure 7.17(a)), it seems that the length of the recirculation bubble is overestimated by all the models, specially by the ML model, which is the one which predicts the largest recirculation region. The cross sections at $x=-0.8m$ and $x=-1.3m$ show a small bump in the experimental velocity profile near the outer wall, which seems to propagate towards the wall. This bump occurs in the region of maximum vertical velocity, which means that it is probably generated by the secondary flow originated in the bend region. It should be remarked again that, since the experimental velocity has been measured at mid-water depth, it may not be representative of the depth averaged velocity at points with non-uniform vertical profiles.

Regarding the performance of the turbulence models, the differences between the computed velocity fields, which appear mainly in the recirculation bubble, are really small compared with the scatter in the experimental data. The ML model gives a slighter poorer prediction of the bubble length, but its degree of accuracy is rather satisfactory, specially considering the simplicity of the model. The ASM and $k-\varepsilon$ models give very similar results. Larger differences appear in the

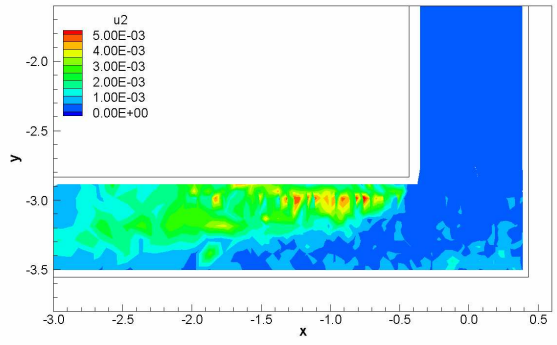

(a) Experimental $\overline{u'^2}(m^2/s^2)$ field.

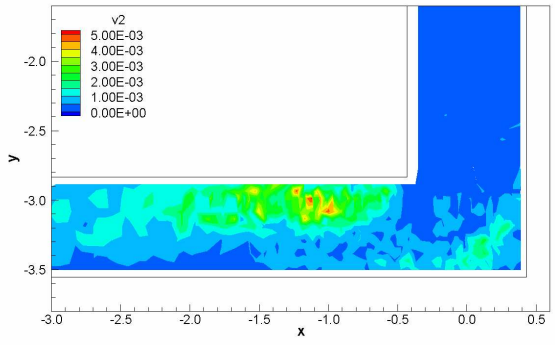

(b) Experimental $\overline{v'^2}(m^2/s^2)$ field.

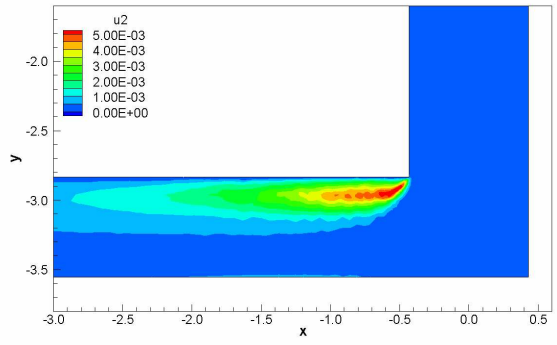

(c) $k-\varepsilon$ model. $\overline{u'^2}(m^2/s^2)$ field.

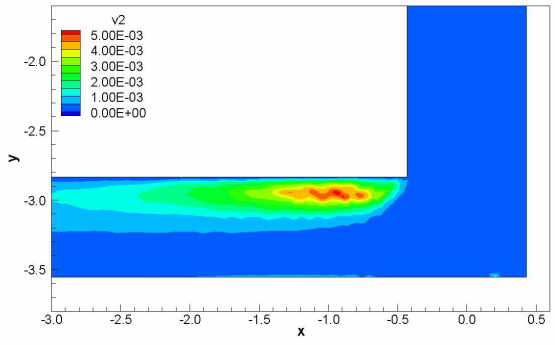

(d) $k-\varepsilon$ model. $\overline{v'^2}(m^2/s^2)$ field.

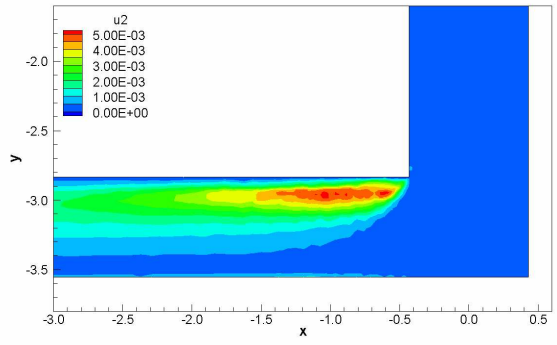

(e) ASM model. $\overline{u'^2}(m^2/s^2)$ field.

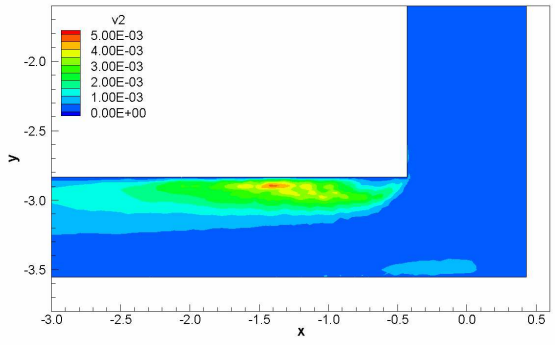

(f) ASM model. $\overline{v'^2}(m^2/s^2)$ field.

Figure 7.16: Reynolds stresses fields in the 90^o bend. ASM and $k-\varepsilon$ models, and experimental results.

turbulence intensity near the bend (cross section $x = -0.8m$), where the maximum turbulent kinetic energy is better predicted by the ASM model than by the $k-\varepsilon$ model (Figure 7.18(c)). However, the differences between models smear out really fast downstream, and no difference at all can be observed at the cross section $x = -1.3m$ (Figure 7.18(b)). Although both models slightly over-predict the turbulence intensity inside the bubble, the overall agreement and downstream evolution is very satisfactory.

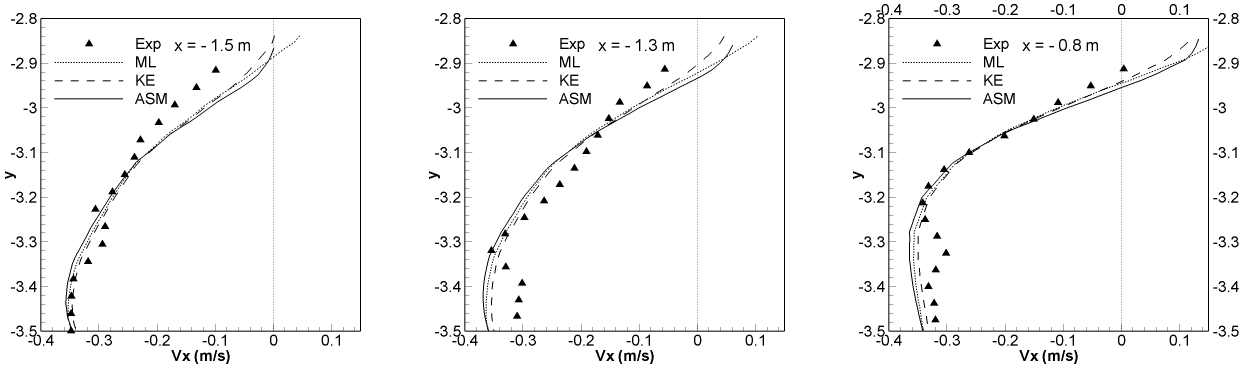

(a) Section $x = -1.5m$. (b) Section $x = -1.3m$. (c) Section $x = -0.8m$.

Figure 7.17: Longitudinal velocity $V_x(m/s)$ at several cross sections in the 90^o bend.

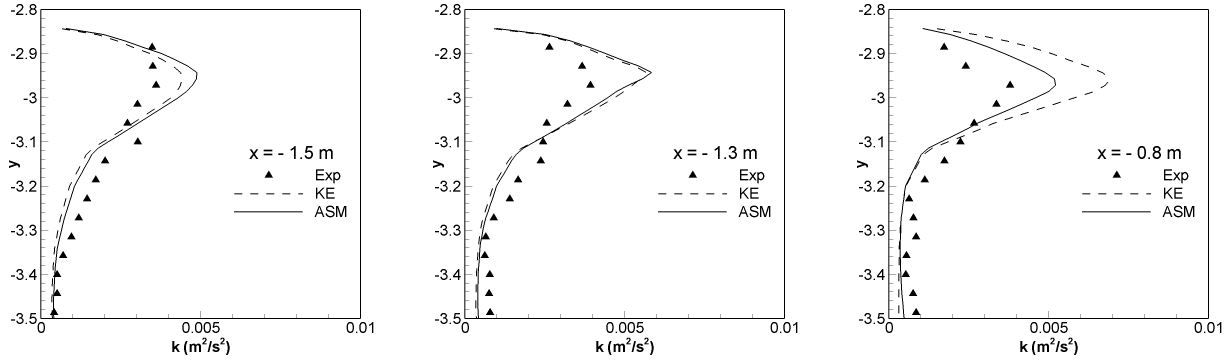

(a) Section $x = -1.5m$. (b) Section $x = -1.3m$. (c) Section $x = -0.8m$.

Figure 7.18: Turbulent kinetic energy $k(m^2/s^2)$ at several cross sections in the 90^o bend.

Chapter 8

Turbulent flow in a vertical slot fishway

8.1 Introduction

Fishways are hydraulic structures which allow the upstream migration of fishes through engineering constructions and natural obstructions in rivers. A vertical slot fishway is a channel divided into several pools separated by slots. Migrating fishes are supposed to swim upstream by the fishway in order to overcome any obstruction in the river. The vertical slot fishways work effectively for a wide range of discharges and water levels [30], because the flow pattern is relatively insensitive to variations on the discharge.

The flow pattern in the pools, which is determined by the pool geometry and boundary conditions, has a great importance in order to guide the fish through the fishway. Not only do the velocity field and the water depth in the pool affect the swimming costs of fishes, but also the turbulence level has proved to increment it considerably [46, 30, 110]. An excessive turbulence level can preclude the passage of fishes through the pools [110]. Clay [30] suggests that when designing a fishway it is necessary to locate the areas of high turbulence and to assess how they can influence the fish behaviour. Enders et al. [46] consider that in order to estimate correctly the swimming costs of fish in turbulent flows, it is necessary to consider explicitly both the mean velocity and the turbulent kinetic energy fields.

The flow field in several designs of vertical slot fishways was studied experimentally by Rajaratnam et al. [114, 113], Puertas et al. [111], Pena [105] and Pena et al. [106]. Those studies show that the mean velocity field in vertical slot fishways is almost two-dimensional, being the vertical velocity much lower than the horizontal one. At the same time the flow pattern is rather uniform over the vertical direction. Therefore, using a depth averaged shallow water model is justified. Nevertheless, the quality of the numerical results cannot be assessed a priori, since the shallow water approximations are not fulfilled in some regions of the pools, specially near the vertical slot.

The experimental results of Pena [105], obtained for several discharges and water depths, will be used in this chapter in order to test the numerical model in such kind of flows. The principal

aim is to assess the possibility of using a depth averaged shallow water model in order to compute the flow in vertical slot fishways. The turbulent characteristics of the velocity field will also be studied in this chapter, in order to understand more deeply the flow field. Under the experimental conditions used by Pena, the flow is highly turbulent and non-isotropic. The experimental velocity and turbulent kinetic energy fields are compared with the numerical results given by the shallow water model.

8.2 Experimental setup

All the experimental measurements were carried out at the CITEEC (Centro de Innovación Tecnolóxica en Edificación e Enxeñería Civil, University of A Coruña, Spain) by Pena [105]. The fishway scale model was built in a $12m$ long channel, with a $1m$ width square cross section (Figure 8.1).

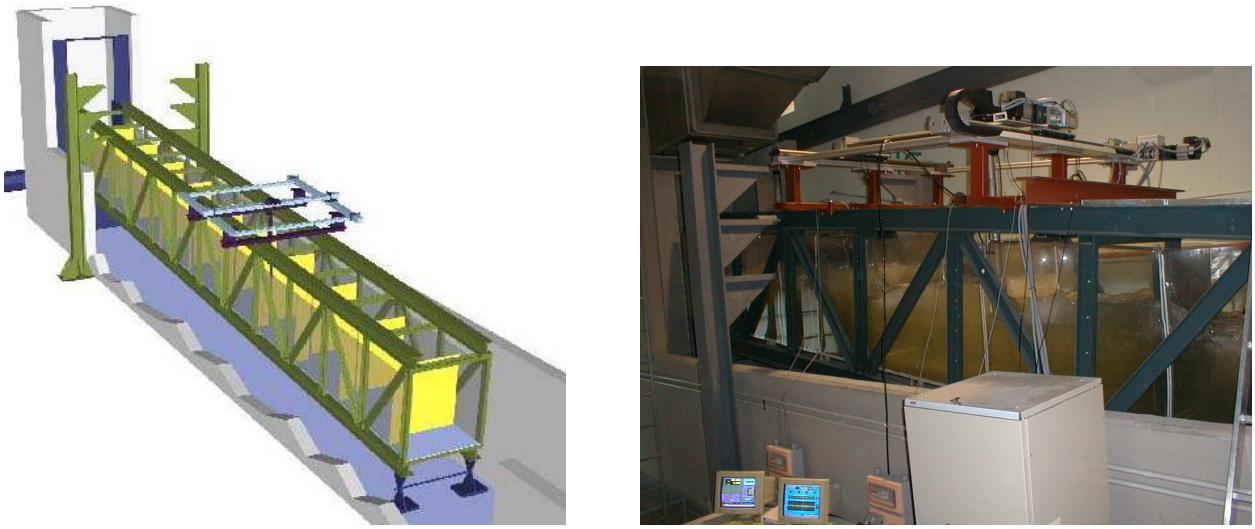

(a) 3D view. (b) Lateral view.

Figure 8.1: Experimental fishway model.

The channel was divided into nine active pools (Figure 8.2(a)). The water discharge was fixed as inlet boundary condition. At the lower end of the flume, a tailgate causing overflow was used to fix the water depth. Two different pool designs were tested, which will be addressed as T1 and T2 (Figures 8.2(b) and 8.2(c)). The pool design T2 was used in the first 4 pools, the fifth was a transition pool, and the last 4 pools had a T1 design. The experimental measurements were registered in pools number 3 and 7.

A conceptual state of uniform flow, as defined by Rajaratnam et al. [113], was used in the experiments, so that the mean water depth at the middle cross section was the same in all the pools. This was achieved, for any fixed discharge, by controlling the downstream boundary condition. In

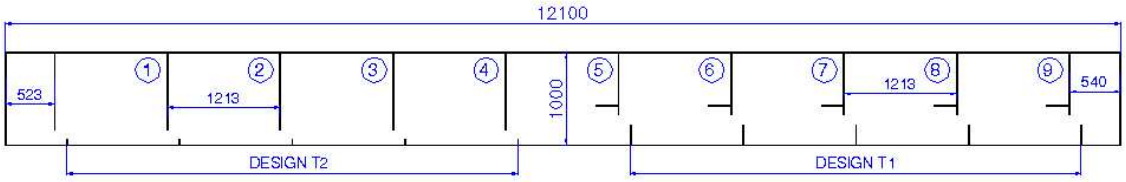

(a) Fishway model.

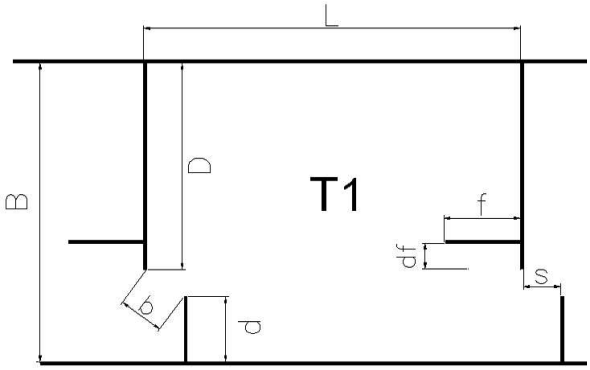

(b) Pool design T1.

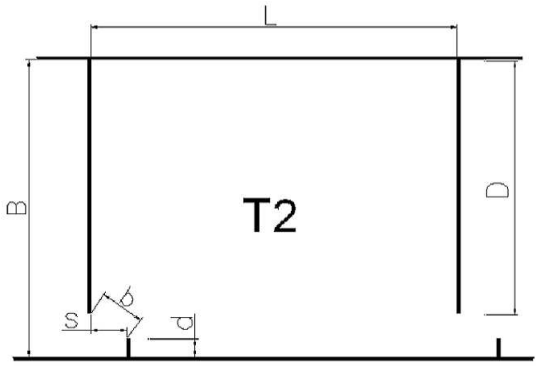

(c) Pool design T2.

Figure 8.2: Fishway pool designs. Dimensions in Table 8.1.

	L	B	D	d	b	s	f	df
T1	1213	1000	683	218	163	129	243	86
T2	1213	1000	839	61	165	131	-	-

Table 8.1: Fishway pool dimensions in mm (see Figure 8.2).

all the results presented in this chapter the bed slope of the flume was 10%, which is in the range of the most frequently used slopes in this kind of structures [30, 76].

The 3D velocity field was measured with a MicroAcoustic Doppler Velocimeter (ADV). The sampling volume of the ADV is a $6mm$ length cylinder with a diameter of $4mm$ (sample volume of $0.08cm^3$). The control volume is located $5cm$ away from the probe in order to reduce flow interference (Figure 7.2). The maximum sampling rate of the ADV used in the experiments is $50Hz$. The water depth in the pools was measured with a conductivity-based depth probe, DHI Wave Gauge Type 202. The x - axis in the experiments is defined in the longitudinal direction of the fishway. The y - axis is defined in the transverse direction, being the xy - plane parallel to the bottom of the fishway (Figure 8.4).

The three mean velocity components ($\overline{u}$, $\overline{v}$, $\overline{w}$) were registered at several points on planes parallel to the flume bed. The number of measurement planes depends on the water depth in the pool, which is given by the water discharge, the distance between planes being usually $10cm$. The location of the measurement points on each plane is shown in Figure 8.3 for the pool design T1. A similar density of data points was used for the design T2. The experimental sampling rate was set to $15Hz$, and the sampling time was 15 seconds (225 instantaneous measurements at each point).

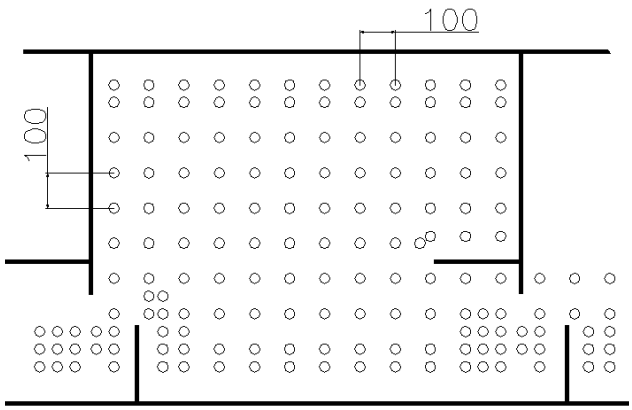

Figure 8.3: Experimental data points in design T1. Horizontal view.

In order to compute the power spectra more detailed data was obtained at some points. For this purpose 5 representative points were chosen in the pool design T1, and 4 points in the pool design T2, since the flow pattern is simpler in the latter one. The location of the data points is defined in Figure 8.4 and in Table 8.2.

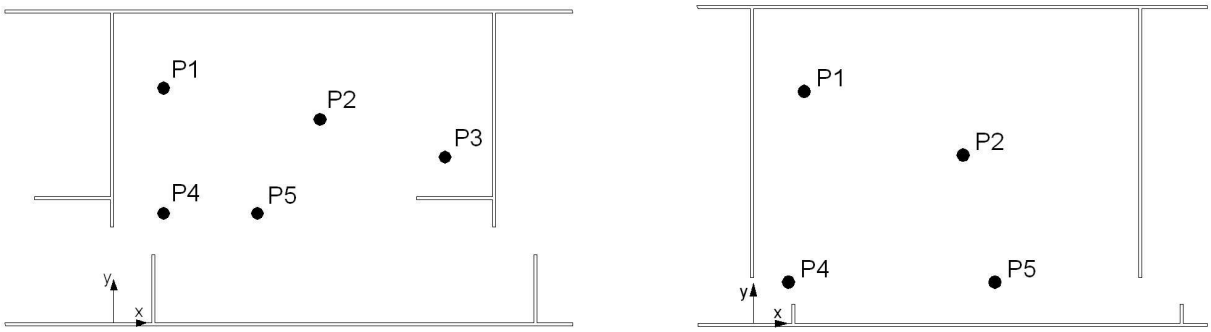

(a) Design T1. (b) Design T2.

Figure 8.4: Data points for computing the power spectra. Coordinates in Table 8.2.

Region	Corner	Central eddy	Baffle	Slot region	Main flux
Data point	P1	P2	P3	P4	P5
T1	(16,76)	(66,66)	(106, 54)	(16,36)	(46,36)
T2	(16,74)	(66,54)	—	(11,14)	(76,14)

Table 8.2: Data points for computing the power spectra. Coordinates in cm, relative to the reference system shown in Figure 8.4.

The upper left corner of the pool (point P1) is a very quiet region, with small velocities and a low turbulence level. Point P2 is located in the middle of the pool. The velocity here is generally small, and, depending on the flow conditions, it can be the centre point of a large eddy. The longitudinal baffle region (point P3) is an area with quite strong flow curvature. The highest velocity and turbulent kinetic energy occur near the slot (point P4). The flow is accelerated just before going through the slot and decelerated afterwards, producing a high amount of turbulence.

At this point there is also some entrance of air in the flow, which generates even more turbulence and makes the flow more complex. Finally, point P5 is located in the main flow stream across the pool, where the velocity is quite large.

The fluctuating velocity frequency spectrum (power spectrum) allows us to know how the turbulent kinetic energy is distributed over different frequencies. It permits us also to check the isotropy of the Reynolds stresses in both the large and the small turbulent scales. In order to be able to compute the largest frequency range of the spectrum, the sampling rate was set to $50Hz$ (the maximum achieved with the ADV used in the experiments), although higher frequencies would be helpful, as will be shown in the results. Around 50000 samples were obtained at each point, over a time of 15 minutes.

8.3 Statistical analysis of the velocity field

8.3.1 Turbulent scales

In flows where the Reynolds number is large enough and turbulence is in a local equilibrium state, it can be assumed a separation of the small (dissipative) and the large (energetic) fluctuating scales. The turbulent kinetic energy is mainly contained in the large scales, and it is transported through the inertial subrange to the small scales, where the dissipation of turbulent energy into internal energy occurs. In this situation the energy flux from the energetic to the dissipative scales is approximately equal to the dissipation rate. This picture of the energy spectrum is originally due to Kolmogorov [73]. Due to the link between the large and the small scales, the order of magnitude of the dissipation, which occurs mainly in the smallest scales of motion, can be estimated from the large velocity and length turbulent scales as:

$$\varepsilon \sim \frac{u_s^3}{L_s} \tag{8.1}$$

where ε is the dissipation rate of turbulent energy, u_s is the fluctuating velocity scale, and L_s is the turbulent integral length scale. The fluctuating velocity scale u_s is defined as the root mean square of the fluctuating velocity. The most commonly used turbulent length scales are defined by the normal Reynolds stresses as:

$$L_{ii} = \frac{1}{\overline{u_i'^2}} \int_V R_{ii}(\mathbf{x}, t; \mathbf{x} + \mathbf{r}, t)\, \mathbf{dr} \tag{8.2}$$

where L_{ii} ($i = 1, 3$) is the integral length scale for each spatial direction, and R_{ii} is the spatial correlation function, which is defined by:

$$R_{ii}(\mathbf{x}, t; \mathbf{x} + \mathbf{r}, t) = \overline{u_i'(\mathbf{x}, t) u_i'(\mathbf{x} + \mathbf{r}, t)} \tag{8.3}$$

In a practical case the volume integral in Equation 8.2 extends to the flow boundaries. In order to compute R_{ii} in a stationary flow, a large number of simultaneous spatial data points are necessary. In our case a rough estimation of L_s will be made from the water depth, which is the largest size that a 3D turbulent eddy may have in the fishway.

The fluctuating velocity scale varies widely over the pool, reaching its highest values near the slot. In that region it can be roughly estimated from the experimental data as $u_s \approx 0.5 m/s$. Assuming a length scale of approximately $L_s \approx 0.5 m$ gives an estimated dissipation rate of:

$$\varepsilon \approx 0.25\, m^2/s^3 \tag{8.4}$$

The Kolmogorov's spatial (η_k) and time (τ_k) micro-scales, which are the smallest significant scales of motion in the flow, are defined as:

$$\eta_k = \left(\frac{\nu^3}{\varepsilon}\right)^{1/4} \qquad\qquad \tau_k = \left(\frac{\nu}{\varepsilon}\right)^{1/2} \tag{8.5}$$

Considering that the kinematic viscosity of water is approximately $10^{-6} m^2/s$, and using the estimation of the dissipation rate given by Equation 8.4, the estimated Kolmogorov micro-scales are:

$$\eta_k \approx 5 \times 10^{-2}\, mm \qquad\qquad \tau_k \approx 1\, msec \tag{8.6}$$

The sampling frequency needed in order to resolve this time scale is $2000 Hz$. Although this is only a rough approximation, the sampling frequency of the ADV ($50 Hz$) is much lower. Therefore, in the near slot region, where the turbulent kinetic energy is highest, it will not be possible to resolve the smallest time scales in the flow, as it will be shown in the plots of the frequency spectra. Furthermore, the spatial micro-scale is much smaller than the sampling volume of the ADV, which is a cylinder of $6mm$ length. In other regions of the pool the turbulence level is much lower ($u_s \approx 0.1 m/s$), and the time micro-scale is approximately $0.03 s$, which can be resolved with a sampling frequency of $60 Hz$. These estimations show that the size of the turbulent scales which can be resolved with the ADV depends strongly on the specific spatial point considered, as it will be shown in the power spectra plots.

8.3.2 Errors due to the finite size of the control volume

As it has just been shown, in some regions of the flow the Kolmogorov micro-scale is two orders of magnitude smaller than the length of the ADV's control volume. This is an important limitation when trying to compute the smallest scales in the wave-number spectra. However, when interested only in the mean velocity and turbulent kinetic energy this restriction is not so important. The 1D Taylor expansion of the real mean velocity ($\overline{u}$) over the measuring point is given by:

$$\overline{u}(x) = \overline{u}(x_0) + \left.\frac{\partial \overline{u}}{\partial x}\right|_{x_0} (x - x_0) + \left.\frac{\partial^2 \overline{u}}{\partial x^2}\right|_{x_0} \frac{(x - x_0)^2}{2} + \theta(\Delta x^3) \tag{8.7}$$

where x_0 is the measuring point. The measured mean velocity is proportional to the average value of the real mean velocity within the control volume. Averaging Equation 8.7 over the sampling volume yields:

$$\overline{u}_m \approx \overline{u}(x_0) + \left.\frac{\partial^2 \overline{u}}{\partial x^2}\right|_{x_0} \frac{d^2}{24} + \theta(d^4) \tag{8.8}$$

where $\overline{u}_m$ is the measured mean velocity, and d is the size of the control volume. The relative error in the measured velocity is given by:

$$\frac{\overline{u}_m - \overline{u}(x_0)}{\overline{u}(x_0)} \approx \frac{1}{\overline{u}(x_0)} \left.\frac{\partial^2 \overline{u}}{\partial x^2}\right|_{x_0} \frac{d^2}{24} + \theta(d^4) \tag{8.9}$$

Considering that the ADV's control volume size is $6mm$, the relative error in the measured instantaneous velocity given by Equation 8.9 is negligible compared with the variability of the estimator due to its random nature.

8.3.3 Errors in the turbulence measurements due to Doppler noise

The Doppler noise is a source of error when measuring turbulence with any Doppler-based backscatter system [87]. The relative importance of this error depends on the fluid characteristics as well as on the flow conditions (velocity, presence of particles in the flow, bubbles, ...). The errors introduced when measuring the turbulence field with an ADV were studied by Lohrmann [87], concluding that the turbulent energy given by the ADV is larger than the real turbulent energy in the flow, and that the spectrum of the horizontal velocity components is biased high for frequencies above $5Hz$ (meaning by horizontal components those ones perpendicular to the ADV's longitudinal axis). Nonetheless, he noticed that the errors in the turbulent energy can be neglected in high energy flows.

Nikora [96] also studied the ADV measurements of turbulence under several flow conditions, obtaining the following conclusions: (1) the ADV noise is Gaussian white, which corresponds to an horizontal line in the power spectrum; (2) the noise in the two horizontal components (which

are perpendicular to the ADV's longitudinal axis) is up to 30 times larger than the noise in the vertical component (which is parallel to the ADV's axis), and that is due to the sensor geometry; (3) there is a great increase of noise in the presence of bubbles (up to 5 times in the experiments by Nikora); (4) the noise level depends on the flow velocity.

The findings of Lohrmann and Nikora are of great interest, specially those ones regarding the non-isotropic distribution of the noise between the three velocity components, and the increase of noise due to the presence of bubbles in the flow. Considering the air entrance which occurs near the vertical slot in the fishway, it should be expected a high level of noise in that region. On the other hand, the high energy of the flow near the slot reduces the relative importance of this noise in the measured Reynolds stresses and turbulent kinetic energy. Nevertheless, it should still be considered when looking at the high frequency range of the power spectra.

Regarding the non-isotropic distribution of the noise, it is important the remark made by Nikora about the fact that this effect is due to the sensor geometry. Since in the experimental measurements the longitudinal axis of the ADV was positioned in the transverse direction of the fishway (y - direction), it should be expected a lower level of noise in this component than in the other two.

The noise level is difficult to estimate, specially considering its dependence on the flow properties. However, its presence can sometimes be detected by a tendency of the power spectra to be horizontal in the high frequency range (since the ADV noise distribution is Gaussian white, the noise spectrum is an horizontal line through all the spectral range, which establishes a minimum value in the measured spectra).

8.3.4 Time integral scale

When sampling at a fixed spatial point in a steady turbulent flow, a stochastic set of data is obtained. In stationary random ergodic processes, as turbulent flow, the ensemble average can be estimated from a finite set of data as a time average. In this way, the mean velocity is estimated for each spatial component as:

$$\overline{u}_T = \frac{1}{T}\int_0^T u(t)\,dt \approx \frac{1}{N}\sum_{i=1}^{N} u_i \tag{8.10}$$

where $u(t)$ is the instantaneous velocity, $\overline{u}_T$ is the estimator of the mean velocity, and N is the number of statistically independent realisations. If the sampling rate is too high, two consecutive samples may not be statistically independent, in which case they do not contribute to the convergence of the statistical estimator. The time interval between two statistically independent samples depends on the time integral scale (T_{int}), which is defined as:

$$T_{int} = \int_0^\infty \rho(\tau)\,d\tau \qquad\qquad \rho(\tau) = \frac{\overline{u'(t)u'(t+\tau)}}{\overline{u'^2}} \tag{8.11}$$

where u' is any component of the fluctuating velocity, and ρ is the auto-correlation coefficient. From Equation 8.11, a time integral scale can be defined for each spatial direction. The mean estimator given by Equation 8.10 is unbiased, being its variability given by:

$$\varepsilon^2_{\overline{u}_T} = \frac{\sigma^2_{\overline{u}_T}}{\overline{u}^2} = \frac{2T_{int}}{T}\frac{\sigma^2_u}{\overline{u}^2} \tag{8.12}$$

where $\varepsilon_{\overline{u}_T}$ is the variability of the mean estimator $\overline{u}_T$, $\sigma^2_{\overline{u}_T}$ is the variance of $\overline{u}_T$, and σ^2_u is the variance of the instantaneous velocity. According to Equation 8.12, only the samples detached by a time interval larger than $2T_{int}$ contribute to the convergence of the mean, and therefore, can be considered to be statistically independent.

The time integral scale and auto-correlation curve give also information about the size of the coherent structures which are present in the flow. A correlation curve that goes quickly to zero is indicative of very weak correlated turbulence and chaotic fluctuations. In such a case the time integral scale takes very low values. On the other hand, a correlation curve that remains above zero for some time before falling down reveals the presence of large coherent structures in the flow. In that case the large fluctuations are not completely chaotic but organised in a coherent motion. Although this analysis is rather qualitative, it helps to characterise the turbulence properties in the different regions of the pool with just one point data sets. A more exhaustive characterisation of the turbulent structures in the fishway flow would need very accurate instantaneous measurements in a refined spatial mesh.

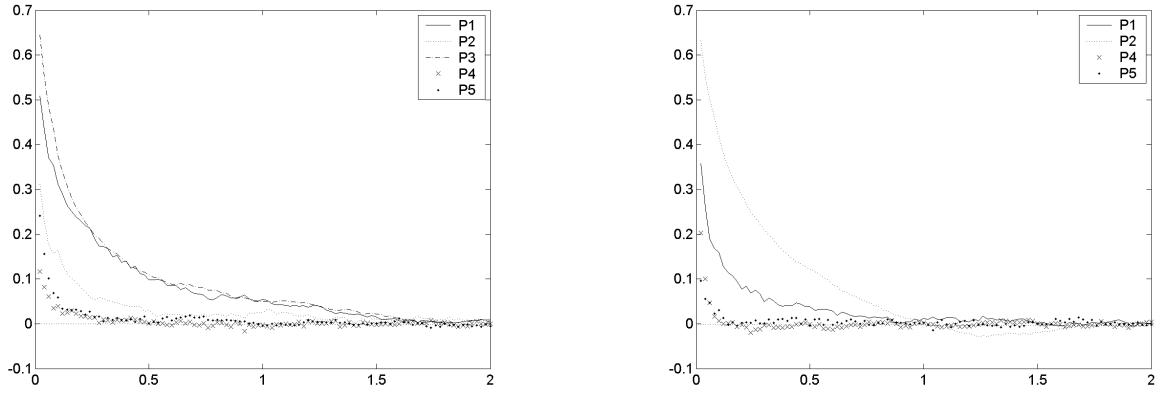

(a) Design T1.

(b) Design T2.

Figure 8.5: Auto-correlation curves for the fluctuating velocity. Q=$105l/s$. z=$5cm$.

The time integral scale in the fishway is highly dependent on the local flow conditions, varying widely within the different regions of the pool (Tables 8.3 and 8.4). It should be noticed that the time integral scale takes always much lower values in the vertical component ($T_{int,w}$) than in the horizontal components ($T_{int,u}, T_{int,v}$), which means that the turbulence is much less correlated in the vertical direction than in the horizontal directions. This should be contrasted with the fact that,

as it will be shown later on in this section, the vertical Reynolds stress $\overline{w'^2}$ is much more energetic than the horizontal stress $\overline{v'^2}$.

	P1	P2	P3	P4	P5
$T_{int,u}$	0.380 - 1.900	0.046 - 0.290	0.270 - 1.050	0.012 - 0.085	0.026 - 0.110
$T_{int,v}$	0.330 - 1.200	0.110 - 0.270	0.190 - 0.360	0.047 - 0.110	0.044 - 0.089
$T_{int,w}$	0.110 - 0.220	0.022 - 0.067	0.034 - 0.190	0.012 - 0.024	0.019 - 0.028

Table 8.3: Time integral scales (sec). Minimum and maximum values for several discharges and heights above the bottom. Design T1.

	P1	P2	P4	P5
$T_{int,u}$	0.150 - 0.930	0.350 - 0.750	0.003 - 0.018	0.016 - 0.031
$T_{int,v}$	0.360 - 0.630	0.280 - 0.520	0.005 - 0.018	0.005 - 0.024
$T_{int,w}$	0.060 - 0.220	0.160 - 0.340	0.005 - 0.022	0.007 - 0.021

Table 8.4: Time integral scales (sec). Minimum and maximum values for several discharges and heights above the bottom. Design T2.

8.3.5 Water depth field

In all the experiments, for a given discharge, the mean water depth at the middle cross section was the same in all the pools of the fishway model. This was achieved by controlling the water depth at the downstream boundary. Under these flow conditions the water surface elevation is almost constant in each pool, and the water depth gradient is similar to the bed slope, except in the near slot region, where there is a strong gradient in the water depth (Figure 8.6). The minimum water depth occurs just downstream the inlet slot, due to the vertical acceleration of the flow in this region.

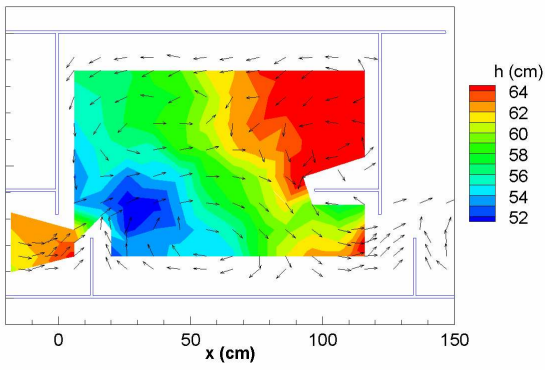

(a) Design T1. Q=105l/s.

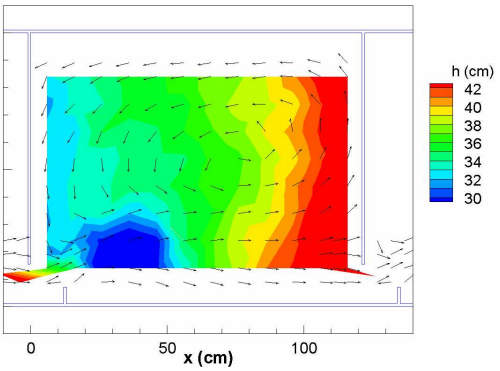

(b) Design T2. Q=65l/s.

Figure 8.6: Experimental water depth field $h(cm)$. Designs T1 and T2.

8.3.6 Mean velocity field

The mean velocity field in both pool designs is almost two-dimensional. The vertical velocity is very small compared to the horizontal velocity (Figures 8.7 and 8.8). The flow in the pools can be roughly described as a confined jet between two slots. In the pool design T1 the jet is strongly curved, creating two large recirculation areas, one on each side of the jet (Figure 8.7). On the other hand, the curvature of the jet in the design T2 is much smaller, being the upper recirculation region much larger than the lower one (Figure 8.8).

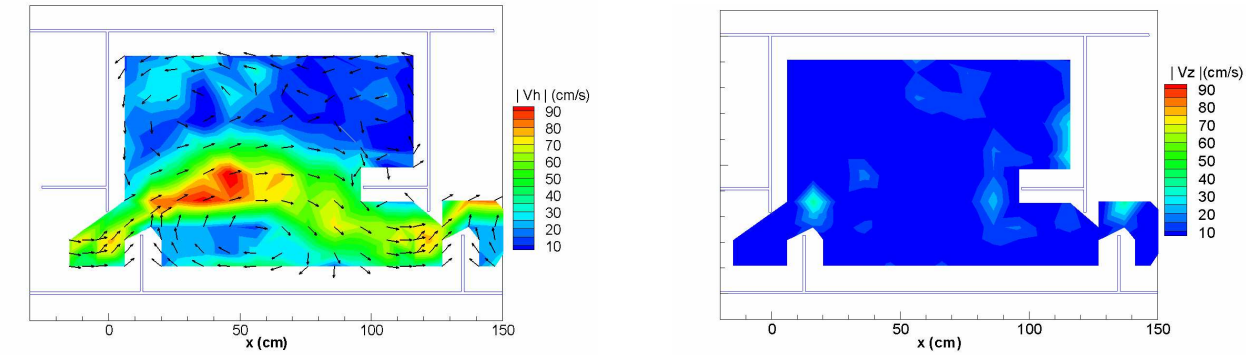

(a) Horizontal velocity $|V_h|(cm/s)$. (b) Vertical velocity $|V_z|(cm/s)$.

Figure 8.7: Experimental horizontal and vertical velocity fields. Design T1. Q=$105l/s$. z=$25cm$.

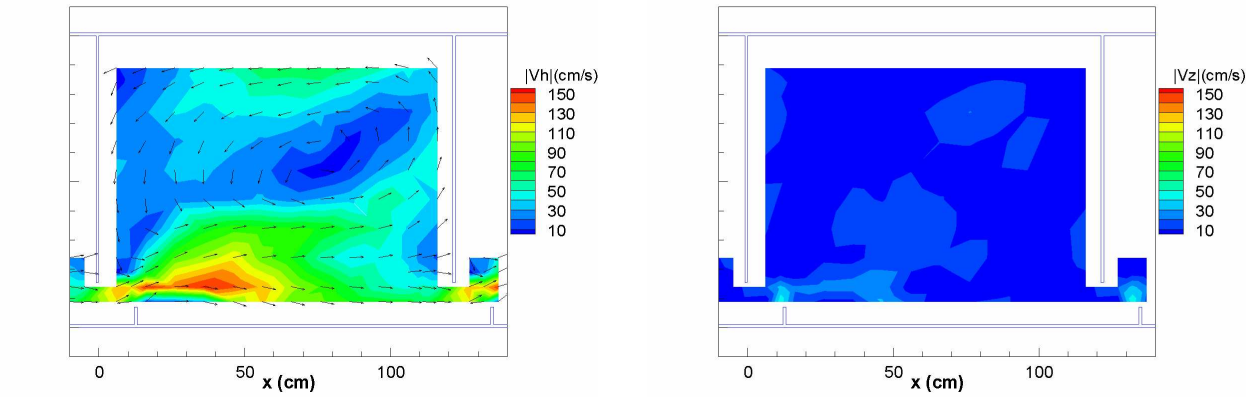

(a) Horizontal velocity $|V_h|(cm/s)$. (b) Vertical velocity $|V_z|(cm/s)$.

Figure 8.8: Experimental horizontal and vertical velocity fields. Design T2. Q=$65l/s$. z=$20cm$.

The horizontal velocity field is almost independent of the height above the bottom of the pool (Figure 8.9). The vertical profile of the velocity is rather uniform, except near the free surface due to the air-water interface influence, and near the bottom of the pool due to the bed surface influence.

Since the velocity field is rather homogeneous in the vertical direction, it is reasonable to work with a depth averaged velocity, as it is done in the shallow water models. In addition, the

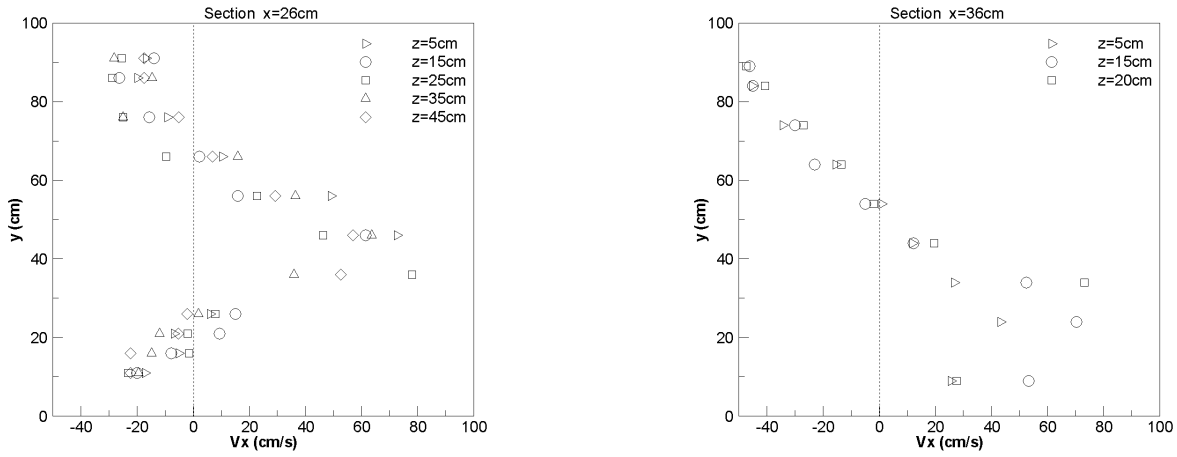

(a) Design T1. Q=$105l/s$. x=$26cm$.

(b) Design T2. Q=$65l/s$. x=$36cm$.

Figure 8.9: Experimental cross sections of the longitudinal velocity $V_x(cm/s)$ at several heights above the bottom.

fact that the vertical velocity and acceleration are small, enhances the quasi-hydrostatic pressure distribution, which is the main shallow water approximation (see section 2.3). These features apply to the whole range of discharges used in the experiments.

8.3.7 Turbulent kinetic energy field

The turbulence intensity ($T_k = \dfrac{\sqrt{k}}{|\overline{\mathbf{u}}|}$, where $|\overline{\mathbf{u}}|$ is the module of the mean velocity) is very high in all the pool, specially near the inlet slot, where it reaches values larger than 100%. Turbulence is mainly generated in the slot region, where the largest velocity gradients occur, and it is strongly convected downstream following the confined jet which crosses the pool. Since the mean velocity field is strongly two-dimensional, it could be expected that the turbulence field was 2D too, which would mean that the longitudinal and transverse Reynolds stresses were larger than the vertical one ($\overline{u'^2} \approx \overline{v'^2} >> \overline{w'^2}$). However, this is not the case. Furthermore, the transverse Reynolds stress $\overline{v'^2}$ is always the less energetic one. This is because the two main sources of turbulence as the flow passes through the slot are the mean velocity gradients and the entrance of air in the flow. Although the mean velocity field is quasi-2D, the strong curvature of the flow, the recirculation eddies, and the stagnation regions appearing in the pool produce an anisotropic distribution of the turbulent energy amongst the two horizontal Reynolds stresses ($\overline{u'^2}$ and $\overline{v'^2}$). At the same time, the air bubbles and the local 3D features of the flow in the slot region contribute strongly to the production of the vertical turbulent stress $\overline{w'^2}$, which reaches large values all over the pool, specially near the slot (Figure 8.10). Since the longitudinal direction in the experiments is parallel to the fishway bed, the air bubbles contribute in a lower degree to the production of $\overline{u'^2}$. Once the turbulence is produced in any Reynolds stress, it is distributed amongst the others stresses via the

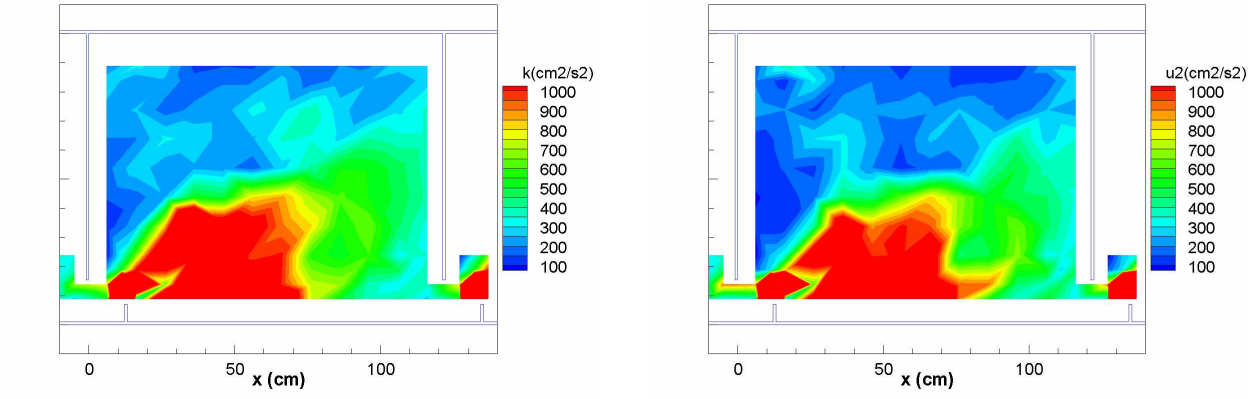

(a) $k(cm^2/s^2)$.

(b) $\overline{u'^2}(cm^2/s^2)$.

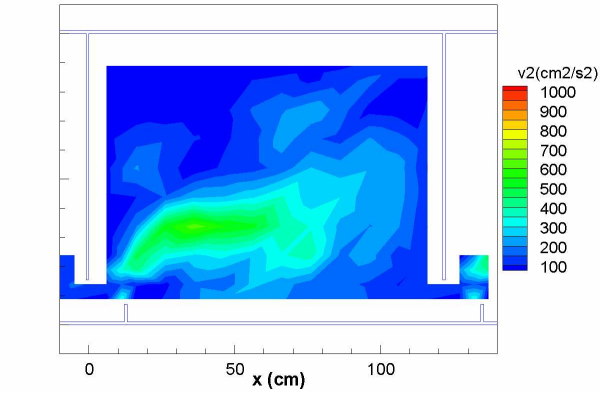

(c) $\overline{v'^2}(cm^2/s^2)$.

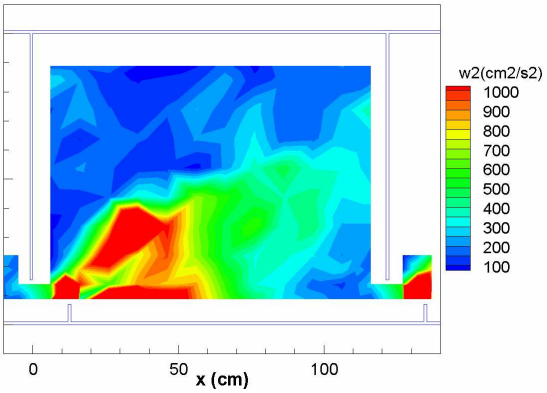

(d) $\overline{w'^2}(cm^2/s^2)$.

Figure 8.10: Experimental Reynolds stresses fields. Design T2. Q=$65l/s$. z=$20cm$.

pressure-strain term, in a process which depends on the particular flow conditions. It is important to remark that the effects of the air bubbles in the flow are not taken into account in the numerical model.

Figures 8.11(a-c) show the longitudinal evolution of the horizontal Reynolds stress $\overline{u'^2}$. At the cross section $x = 26cm$ (Figure 8.11(a)), extremely large values of $\overline{u'^2}$ are reached in the slot region, specially near the free water surface ($z = 15$ and $20cm$). Probably the air bubbles in the flow, which are present in a larger concentration near the free surface, contribute to this turbulence peak. Just $20cm$ downstream (Figure 8.11(b)) the peak value has diminished considerably, appearing mainly at $z = 20cm$. Further downstream, at $x = 86cm$ (Figure 8.11(c)), the Reynolds stresses are rather homogeneous in the vertical direction, and the peak value has almost disappeared. The behaviour of $\overline{u'^2}$ should be compared with the transverse Reynolds stress $\overline{v'^2}$ (Figures 8.11(d-f)). The peak in the slot region is not so strong in the $\overline{v'^2}$ profiles, the values are much lower all over the pool, and the profiles are more uniform over the vertical direction.

Figure 8.11 shows clearly that turbulence is strongly anisotropic all over the pool. In order to

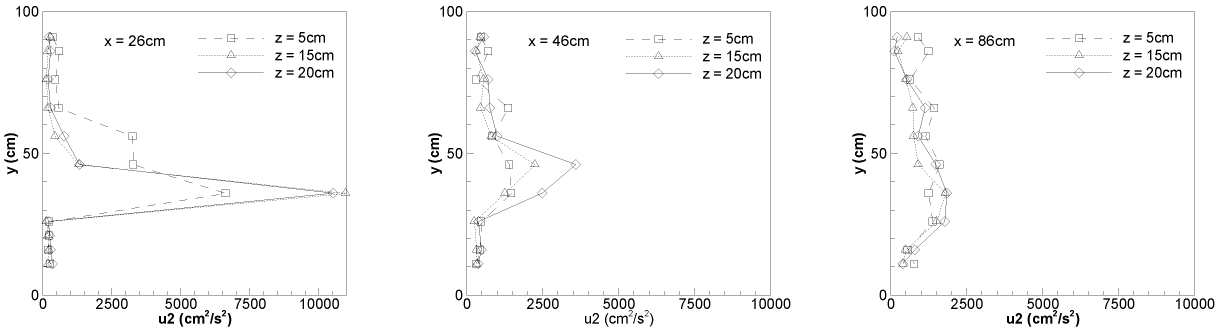

(a) $\overline{u'^2}(cm^2/s^2)$. x=26$cm$. (b) $\overline{u'^2}(cm^2/s^2)$. x=46$cm$. (c) $\overline{u'^2}(cm^2/s^2)$. x=86$cm$.

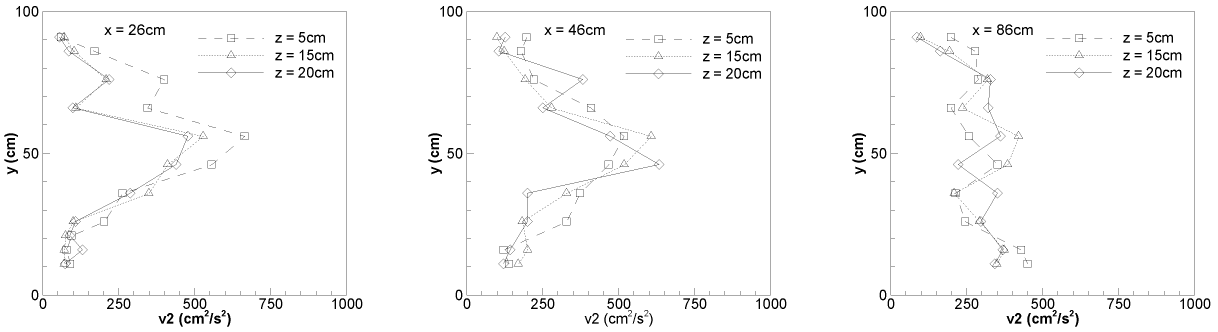

(d) $\overline{v'^2}(cm^2/s^2)$. x=26$cm$. (e) $\overline{v'^2}(cm^2/s^2)$. x=46$cm$. (f) $\overline{v'^2}(cm^2/s^2)$. x=86$cm$.

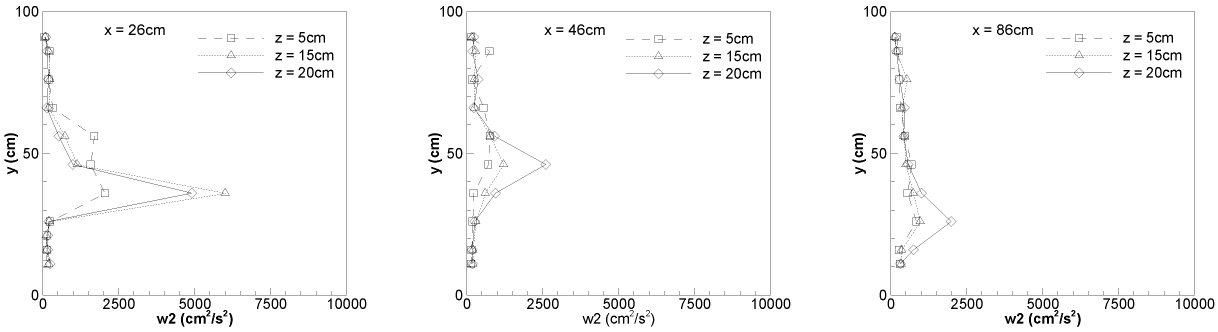

(g) $\overline{w'^2}(cm^2/s^2)$. x=26$cm$. (h) $\overline{w'^2}(cm^2/s^2)$. x=46$cm$. (i) $\overline{w'^2}(cm^2/s^2)$. x=86$cm$.

Figure 8.11: Experimental cross sections of the Reynolds stresses at several locations and heights. Design T1. Q=65l/s. Notice the different scales in the horizontal axes.

quantify the three-dimensional isotropy, an isotropy coefficient I_c has been defined as:

$$\begin{aligned} I_c &= 1 - \frac{(\overline{u'^2} - \overline{v'^2})^2 + (\overline{u'^2} - \overline{w'^2})^2 + (\overline{v'^2} - \overline{w'^2})^2}{8k^2} \\ &= \frac{3}{4}\frac{\overline{u'^2}\,\overline{v'^2} + \overline{u'^2}\,\overline{w'^2} + \overline{v'^2}\,\overline{w'^2}}{k^2} \end{aligned} \tag{8.13}$$

If the turbulence is completely isotropic in the three spatial directions, the isotropy coefficient equals one. The more anisotropic the turbulence is, the smaller the isotropy coefficient is. The

level of isotropy at any point depends mainly on its location in the pool. The variations of the isotropy level with the height above the bottom and with the total discharge are smaller than the variations between the different regions of the pool. Table 8.5 shows the range in which the isotropy coefficient I_c varies at the spatial points defined in Figure 8.4. In both pool designs the most isotropic region is the upper left corner of the pool (point P1), while it is in the slot region (point P4) and in the main jet stream (point P5) where turbulence is more anisotropic.

	Design T1					Design T2			
	P1	P2	P3	P4	P5	P1	P2	P4	P5
max	0.95	0.87	0.90	0.78	0.85	0.91	0.94	0.76	0.82
min	0.92	0.79	0.75	0.74	0.76	0.89	0.85	0.30	0.62
average	0.94	0.83	0.82	0.76	0.81	0.90	0.90	0.62	0.71

Table 8.5: Isotropy coefficient. Minimum, maximum and average values.

The strong anisotropy between the horizontal Reynolds stresses ($\overline{u'^2}$ and $\overline{v'^2}$) is a handicap to the performance of the linear eddy viscosity models, which assume an isotropic eddy viscosity. The large value of the vertical Reynolds stress $\overline{w'^2}$, which is not considered in the shallow water models, may affect the numerical results. Nonetheless, the relative importance of these flow features in the numerical simulations cannot be assessed a priori, and will be discussed later on, when the numerical results will be presented.

8.3.8 Spectral analysis

Several kinds of velocity spectra are often used in the experimental analysis of turbulent flows. In general flow conditions, only the frequency spectrum (also called power spectrum) can be computed from one point statistics. In homogeneous flows with a low turbulence intensity the Taylor's hypothesis can be used in order to obtain the one-dimensional wave-number spectrum from the frequency spectrum [31]. In homogeneous isotropic turbulence the energy spectrum can also be obtained from the frequency spectrum. On the other hand, in a highly non-homogeneous and non-isotropic flow like the one in the fishway, a Proper Orthogonal Decomposition in space should be done in order to decompose the flow field in different coherent structures or modes [53]. This kind of analysis, which needs simultaneous measurements at different points in the pool, is beyond the scope of this thesis. We will limit to the evaluation and analysis of the power spectra at the spatial points defined in Figure 8.4.

Since the flow is stationary, a Fourier decomposition in time of the fluctuating velocity has been made in order to compute the power spectra. Considering that the sampling rate is $50Hz$ at periodic time intervals, the spectra obtained will extend up to $25Hz$ [55]. The Fourier Transform

in time of the fluctuating velocity is defined as:

$$\hat{u}(f) = \int_{-\infty}^{\infty} u'(t) e^{-i2\pi ft}\, dt \tag{8.14}$$

where f is the angular frequency (Hz), $u'(t)$ is the fluctuating velocity, and $\hat{u}(f)$ is the Fourier Transform of $u'(t)$. The original velocity field can be reconstructed by the inverse Fourier Transform, which is given by:

$$u'(t) = \int_{-\infty}^{\infty} \hat{u}(f) e^{i2\pi ft}\, df \tag{8.15}$$

From the Fourier Transform of the fluctuating velocity, the power spectrum $S(f)$ is defined as:

$$S(f)\delta(f_i - f_j) = \overline{\hat{u}(f_i)\hat{u}^*(f_j)} \tag{8.16}$$

where $\delta(f_i - f_j)$ is the delta function, and $\hat{u}^*(f)$ is the complex conjugate of $\hat{u}(f)$. From the definition of $S(f)$ it can be shown that the power spectrum and the one-point time correlation function $B(\tau)$ form a Fourier pair, i.e:

$$S(f) = \int_{-\infty}^{\infty} B(\tau) e^{-i2\pi f\tau}\, d\tau \qquad\qquad B(\tau) = \int_{-\infty}^{\infty} S(f) e^{i2\pi f\tau}\, df \tag{8.17}$$

where $B(\tau)$ is the one-point time correlation function, which is given by:

$$B(\tau) = \overline{u(t)u(t+\tau)} \tag{8.18}$$

The time correlation function $B(\tau)$ has already been used in the definition of the time integral scale (Equation 8.11). It gives information about the life time of the coherent structures which are present in the flow.

Since any sampled velocity field is a finite set of data, estimators of the Fourier Transforms and power spectra are needed. The Fourier Transform of the fluctuating velocity can be estimated from a finite record length as:

$$\hat{u}_T(f) = \int_0^T u'(t) e^{-i2\pi ft}\, dt \approx \sum_{j=0}^{N-1} u'(j\Delta t) e^{-i2\pi fj\Delta t} \Delta t \tag{8.19}$$

where T is the measuring time, N is the total number of samples, Δt is the time step between consecutive samples, and $\hat{u}_T(f)$ is a finite estimator of $\hat{u}(f)$. The resolution of the estimated Fourier Transform is equal to $\Delta f = \dfrac{1}{T}$. For this reason the measuring time T should be large enough to avoid loss of resolution. The frequency spectrum can be estimated from the Fourier

Transform of the fluctuating velocity as:

$$S_T(f) = \frac{\hat{u}_T(f)\hat{u}_T^*(f)}{T} \tag{8.20}$$

The variance of the estimator $S_T(f)$ is given by:

$$\sigma^2_{S_T} = S^2(f) \tag{8.21}$$

which is independent of the record length T. From Equation 8.21, the variability of the estimator $S_T(f)$ is equal to 1, no matter how long the measuring time is. In order to diminish the variability, several spectra computed from non-overlapping samples must be averaged, and the new estimator is given by:

$$\overline{S}_T(f) = \overline{\frac{\hat{u}_T(f)\hat{u}_T^*(f)}{T}} \tag{8.22}$$

The variability of the estimator 8.22 decreases with the number of spectra used as:

$$\varepsilon_{\overline{S}_T} = \sqrt{\frac{\sigma^2_{\overline{S}_T}}{S^2}} = \sqrt{\frac{1}{N_b}\frac{\sigma^2_{S_T}}{S^2}} = \sqrt{\frac{1}{N_b}} \tag{8.23}$$

where N_b is the number of spectra (or non-overlapping blocks of data) used in the estimation. Hence, in order to obtain a variability of $\varepsilon_{\overline{S}_T} = 0.1$, 100 blocks are needed, while for a variability of $\varepsilon_{\overline{S}_T} = 0.01$, 10000 blocks should be used. It should be noticed that although the sampling time (T) does not have any influence on the variability of the estimator, it must be large enough to avoid loss of resolution. Figure 8.12 shows the effect that the variability of the estimator has on the computed power spectrum.

Using a finite record length to estimate the Fourier Transform of the velocity (Equation 8.19), is equivalent to filter the real signal in the physical space with a rectangular filter of length T. An alternative way to write Equation 8.19 is given by:

$$\hat{u}_T(f) = \int_{-\infty}^{\infty} \omega(t)u'(t)e^{-i2\pi ft}\,dt \tag{8.24}$$

where $\omega(t)$ is a filter function. The rectangular filter is given by:

$$\omega(t) = \begin{cases} 1 & \text{if} \quad t \in (0,T) \\ 0 & \text{otherwise} \end{cases} \tag{8.25}$$

which introduced in Equation 8.24 recovers Equation 8.19. Since the rectangular filter is discontinuous in the physical domain, it might produce secondary lobes and suppress some of the harmonics in the spectral space. For that reason other filters have been proposed, as for example the Hanning's

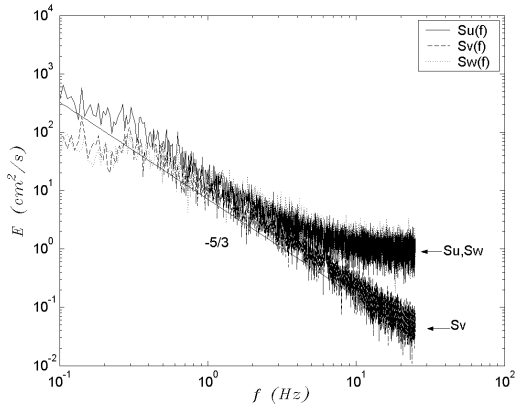

(a) 8 blocks. $\varepsilon_{\overline{S}_T} = 0.354$.

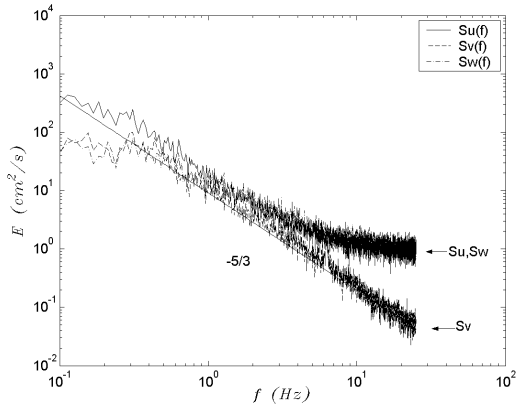

(b) 16 blocks. $\varepsilon_{\overline{S}_T} = 0.250$.

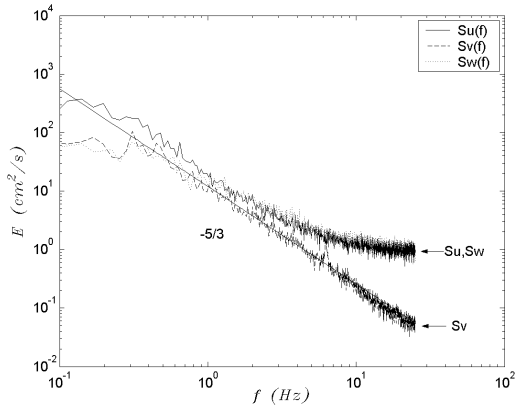

(c) 32 blocks. $\varepsilon_{\overline{S}_T} = 0.177$.

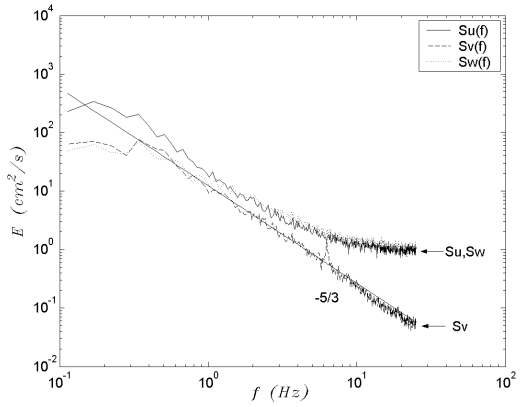

(d) 64 blocks. $\varepsilon_{\overline{S}_T} = 0.125$.

Figure 8.12: Effect of the number of blocks used to compute the power spectrum. Design T2. Point P2. Q=$105l/s$. z=$5cm$.

filter and the Gaussian filter, among others. The Hanning's filter function, for example, is given by:

$$\omega(t) = \frac{1}{2}\left[1 + \cos\left(\frac{2\pi(t - T/2)}{T}\right)\right] \tag{8.26}$$

In our case the filter used has little influence on the computed spectrum, as it is shown in Figure 8.13. All the spectra shown in this chapter have been computed with the rectangular filter.

Kolmogorov [73] established a very well known theory about the turbulence spectrum behaviour in incompressible large Reynolds number flows. According to Kolmogorov's theory, if turbulence is fully developed and the Reynolds number is large enough, the turbulence spectrum can be split into three different subranges, namely: the energetic, the inertial, and the dissipation subranges. The energetic subrange, which corresponds to the large turbulent scales, is where turbulence is produced by the Reynolds stresses acting against the mean velocity gradients. Large coherent turbulent structures, with low frequencies, may be contained in this region of the spectrum. In the dissipation subrange (smallest scales) the turbulent kinetic energy is dissipated into

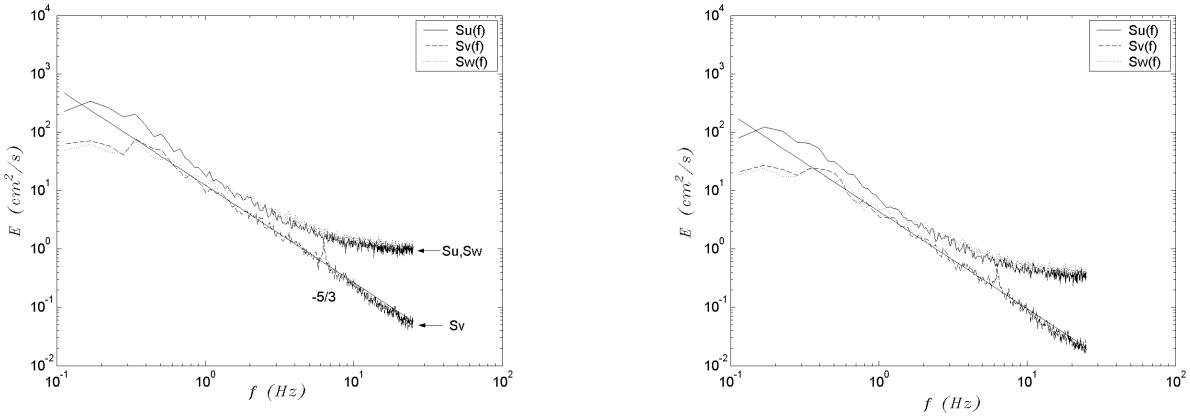

(a) Rectangular filter.

(b) Hanning's filter.

Figure 8.13: Effect of the filter used on the computed power spectrum. Design T2. Point P2. Q=$105l/s$. z=$5cm$.

internal energy due to viscous friction. Oscillations of high frequency and small wave length occur. The energetic and dissipation subranges are linked by the inertial subrange, which transports the energy from the large scales to the small scales in a process known as *cascade energy transfer*. These three spectral subranges appear distinctly only when the Reynolds number is large enough. As the Reynolds number decreases the inertial subrange tends to disappear, and the energetic and dissipation subranges merge together. From dimensional analysis it can be argued that the behaviour of the wave-number spectrum in the inertial subrange is given by:

$$E(\mathrm{k}) \sim \varepsilon^{2/3}\mathrm{k}^{-5/3} \tag{8.27}$$

where $E(\mathrm{k})$ is the wave-number energy spectrum, ε is the dissipation rate of turbulent energy, and k is the wave-number. In nearly homogeneous flows with a not very high turbulence level, the Taylor's approximation [31] can be used to transform the wave-number spectrum into the frequency spectrum as:

$$S(f) = \frac{C}{(2\pi)^{2/3}} U^{2/3}\varepsilon^{2/3} f^{-5/3} \tag{8.28}$$

where $S(f)$ is the frequency spectrum, U is the convective velocity, f is the angular frequency (Hz), and C is a proportionality constant. Kraichnan [74] proposed a value of $C = 0.5$ for fully developed turbulence. The $-5/3$ power law of the spectrum is usually associated with a fully developed 3D turbulent flow. Even though turbulence is always 3D, there are several studies about the behaviour of the energy spectra in 2D turbulence, understanding by 2D turbulence flows in which two of the normal Reynolds stresses are clearly larger than the third one. In those situations, 2D coherent structures appear distinctively in the flow. This may be the case of some shallow free surface flows, but it is not the case in the fishway flow, where, as it is shown by the experimental results, the vertical Reynolds stress is even larger than the transverse one. The turbulence in the

fishway is strongly 3D, even though the mean velocity field is quasi-2D.

In order to evaluate the power spectra, the experimental data has been split into 64 blocks, which gives a variability of the estimated spectra of $\varepsilon_{\overline{S}_T} = 0.125$. A rectangular filter window has always been used. The record time per block is approximately 15 seconds, which gives a frequency resolution of $0.067Hz$. Since the sampling rate is $50Hz$, the spectra obtained will extend up to $25Hz$, which is an important limitation, specially for the velocity components with a high turbulence level, where a large part of the spectrum might be missed. The size of the spectrum which is resolved is related to the turbulent kinetic energy. Assuming a constant length scale, the value of the Kolmogorov's micro-scale depends on the turbulent kinetic energy roughly as $\eta_k \sim k^{-3/4}$, which implies that in the regions with a higher turbulent energy, the resolved part of the spectrum is smaller. This limitation is clearly shown in Figures 8.14 and 8.15. All the inertial and dissipation subranges are missed from the spectra at point P4, which is situated in the most energetic region of the pool, just downstream the inlet slot. On the other hand, at points P1 and P2, which are situated in a more quiet region, the spectra show very clearly the $-5/3$ power law, specially on the transverse component $\overline{v'^2}$, which is the less energetic one.

Another important factor which should be considered when analysing the spectra is the high noise level which is present in the $\overline{u'^2}$ and $\overline{w'^2}$ components, due to the air bubbles present in the flow. As it has been argued in section 8.3.3, due to the ADV geometry the noise in these two components is likely to be larger than the noise in the transverse component. The ground noise level in $\overline{u'^2}$ and $\overline{w'^2}$ is clearly shown in the spectra at points P1 and P2 in both pool designs (Figures 8.14(a,b) and 8.15(a,b)). This might explain why the $-5/3$ power law does not appear so clearly in the $\overline{u'^2}$ and $\overline{w'^2}$ spectra as it does in the $\overline{v'^2}$ spectra.

The less energetic region in the pools is the upper left corner, which is represented by point P1. At that point the noise level deforms the dissipation subrange in the $\overline{u'^2}$ and $\overline{w'^2}$ spectra, establishing a ground value of approximately $8m^2/s$ for frequencies higher than $5Hz$. The $-5/3$ power law appears very clear in the $\overline{v'^2}$ spectra, which does not show any appreciable level of noise in the resolved part of the spectrum. The region between the longitudinal baffle and the upper right corner in the design T1 (point P3) is not shown in Figure 8.14, but its features are very similar to those of point P1. In the central eddy (point P2) and in the main jet stream region (point P5) there is a strong anisotropy in the large scales. These regions of the pool have a larger concentration of air bubbles, which establishes a ground noise level around $20-30cm^2/s$ in the $\overline{u'^2}$ and $\overline{w'^2}$ spectra. The slot region (point P4) is the most energetic, as well as the one which shows the strongest anisotropy in the Reynolds stresses. None of the spectra show the $-5/3$ power law, probably because all of them are abruptly cut at $25Hz$, missing the entire inertial range.

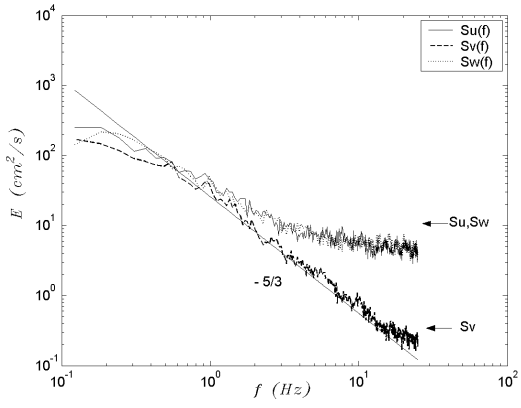

(a) Point P1. Q=$115l/s$. z=$45cm$.

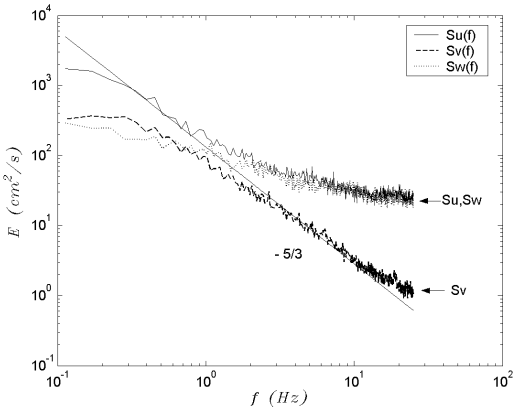

(b) Point P2. Q=$105l/s$. z=$5cm$.

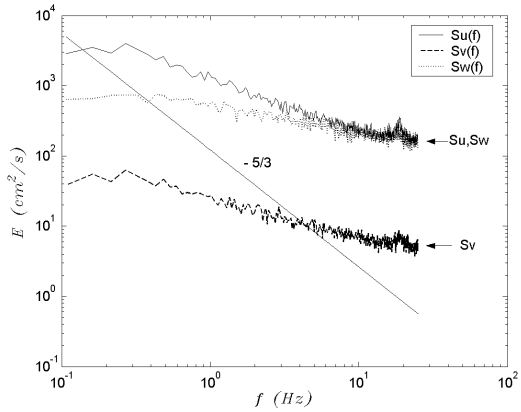

(c) Point P4. Q=$115l/s$. z=$5cm$.

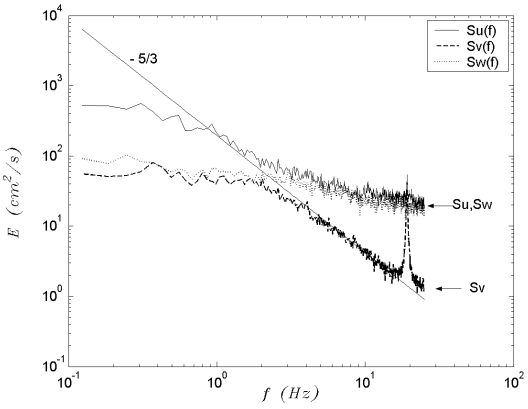

(d) Point P5. Q=$85l/s$. z=$5cm$.

Figure 8.14: Frequency spectra at several locations. Design T1.

8.4 Similarity analysis of the flow in a vertical slot fishway

Similarity solutions are a very interesting issue in the study of fluid flows, since they permit to characterise the flow field in a given geometry under a wide range of boundary conditions by a few non-dimensional parameters. Once the flow field is known in a specific geometry for a specific set of boundary conditions, similarity solutions permit to obtain the flow field in other situations with the same geometry shape, but different global dimensions and boundary conditions. In this section we sill seek approximate similarity solutions for the flow in the vertical slot fishway designs T1 and T2.

In section 2.3.6, the non-dimensional depth averaged shallow water equations have been obtained, which in a general case depend on three non-dimensional parameters: the Froude number, the horizontal Reynolds number (based on the horizontal length scale), and a non-dimensional bed friction parameter which accounts for the vertical shear stress. In a similar way, the 3D shallow water equations depend also on the Froude number, on the horizontal Reynolds number, and on the vertical Reynolds number (based on the water depth), which is the equivalent to the non-

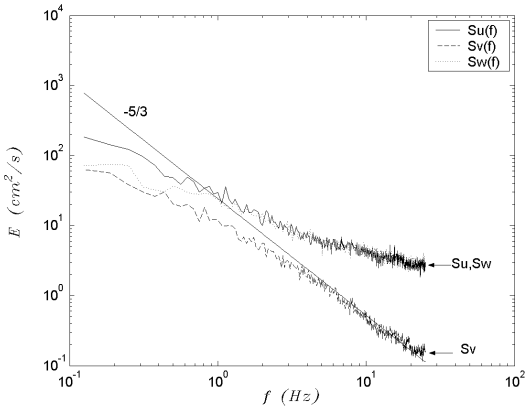

(a) Point P1. Q=$125l/s$. z=$25cm$.

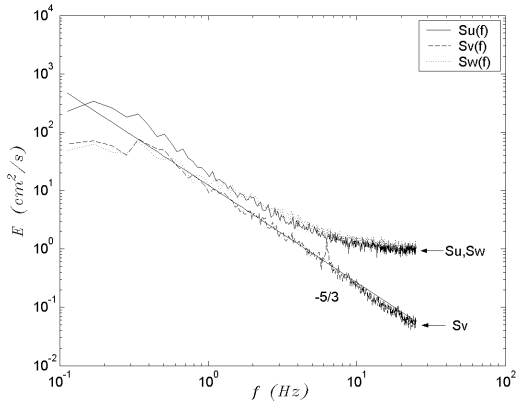

(b) Point P2. Q=$105l/s$. z=$5cm$.

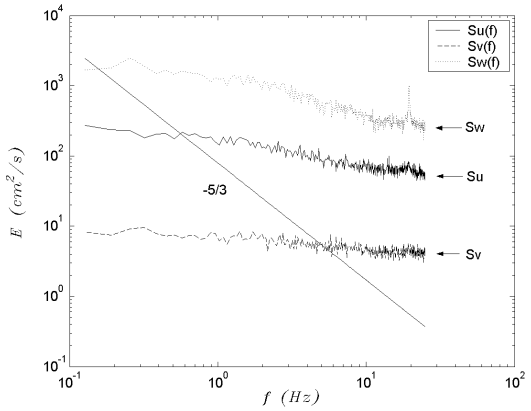

(c) Point P4. Q=$125l/s$. z=$25cm$.

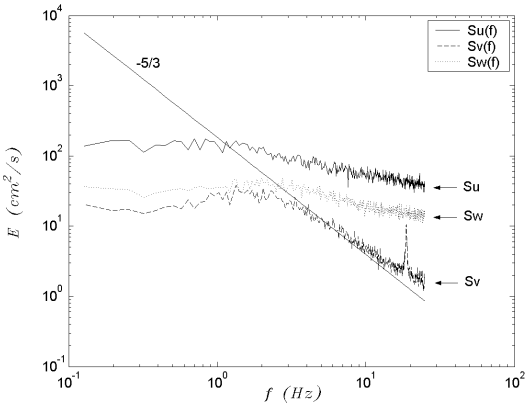

(d) Point P5. Q=$85l/s$. z=$5cm$.

Figure 8.15: Frequency spectra at several locations. Design T2.

dimensional friction in the depth averaged equations. In general 3D flow conditions, the vertical and horizontal Reynolds number dependence establishes the proportionality between the length scales in the three spatial directions. However, in some free surface flows the vertical shear stress has little influence on the mean flow, and therefore, similarity solutions may be obtained for different vertical Reynolds number (or non-dimensional bed friction, in the case of the depth averaged equations).

In the fishway designs studied in this chapter the strong horizontal velocity gradients have much more influence on the flow structure than the bed friction, which, due to the smooth flume surface, can be neglected in the momentum equations. Hence, the non-dimensional mean flow equations depend only on the Froude number and on the horizontal Reynolds number, and thus, in order to obtain full similarity solutions these two parameters should be kept constant. However, it has been found by Puertas et al. [111] that the velocity field in vertical slot fishways is almost independent of the water depth. This means that very similar solutions of the mean flow equations are obtained for different Froude numbers, defined as $Fr = \dfrac{|\mathbf{U}|}{\sqrt{gh}}$. This suggests that another parameter rather

than the total water depth may be used as vertical length scale in order to obtain quasi-similarity solutions.

An hydrostatic pressure distribution will be assumed, which justifies the use of the 3D shallow water equations to describe the flow field. Notice that this is only an assumption which must be confirmed by the experimental results. The total water depth will be decomposed as:

$$h(x,y) = H_o + H_s f_h(x,y) \tag{8.29}$$

where H_0 is a constant value, H_s is a water depth scale, and $f_h(x,y)$ is a water depth similarity function. All the other flow variables can be scaled as it has been done in section 1.1.3, i.e.:

$$\overline{u}(x,y,z) = u_s f_u(x,y,z) \quad \overline{v}(x,y,z) = v_s f_v(x,y,z) \quad \overline{w}(x,y,z) = w_s f_w(x,y,z) \tag{8.30}$$

$$z_b(x,y) = Z_s f_z(x,y) \qquad \overline{u_i' u_j'} = R_{ij,s} f_{u_i u_j}(x,y,z)$$

$$x = L_x x^* \qquad y = L_y y^* \qquad z = L_z z^*$$

where u_s, v_s, w_s are the velocity scales, Z_s is the bed elevation scale, and $R_{ij,s}$ are the Reynolds stresses scales. The length scales L_x, L_y, L_z are defined by the problem geometry. It should be noticed the difference between the vertical length scale L_z and the water depth scale H_s in Equations 8.29 and 8.30. A proper definition of L_z would be the maximum water depth in the pool $L_z = h_{max}$. In the case of the fishway, the bed elevation and horizontal length scales are linked by the bed slope θ_s, as:

$$\theta_s = \frac{Z_s}{L_x} \tag{8.31}$$

It is straightforward to show that using Equations 8.29 and 8.30 in the 3D shallow water equations yields the following similarity relations:

$$\frac{u_s}{L_x} \sim \frac{v_s}{L_y} \sim \frac{w_s}{L_z} \tag{8.32}$$

$$\frac{u_s^2}{L_x} \sim \frac{gH_s}{L_x} \sim \frac{gZ_s}{L_x} \sim \frac{\nu u_s}{L_x^2} \sim \frac{\nu u_s}{L_y^2} \sim \frac{\nu u_s}{L_z^2} \sim \frac{R_{uu,s}}{L_x} \sim \frac{R_{uv,s}}{L_y} \sim \frac{R_{uw,s}}{L_z}$$

According to the similarity relations given by Equation 8.32, the only terms in the momentum conservation equation which depend on the vertical length scale are the turbulent and viscous vertical shear stresses ($\frac{R_{uw,s}}{L_z}$, $\frac{\nu u_s}{L_z^2}$). The vertical homogeneity of the flow in the fishway may reduce the importance of the vertical shear stresses to a small layer near the bottom of the pool. For large water depths, the influence of this layer on the whole flow pattern is small, i.e. the bed friction effect on the mean flow is negligible. Nevertheless, only the experimental results may confirm this proposition. With this hypothesis, the dependence of the momentum equations on the total water

depth L_z is eliminated. Assuming also that the wall friction has little influence on the global flow pattern in the pools, i.e. the viscous diffusion is negligible in the momentum equations, the only scale relations which remain from Equation 8.32 are:

$$H_s \sim Z_s \qquad u_s \sim \sqrt{gZ_s} \qquad R_{uu,s} \sim u_s^2 \qquad R_{uu,s} \sim u_s v_s \tag{8.33}$$

It is important to notice that, according to the scale relations 8.33, it is the scale H_s, and not the total water depth, which is proportional to the bed elevation scale Z_s. Computing the water depth with Equation 8.29 in two different spatial points yields:

$$\begin{aligned} h(x_1, y_1) &= H_o + H_s f_h(x_1, y_1) \\ h(x_2, y_2) &= H_o + H_s f_h(x_2, y_2) \end{aligned} \tag{8.34}$$

From Equations 8.33 and 8.34, the relation between the water depth at any two points in the pool is given by:

$$h(x_2, y_2) = h(x_1, y_1) + Z_s \left(f_h(x_2, y_2) - f_h(x_1, y_1) \right) \tag{8.35}$$

The most straightforward conclusion from Equation 8.35 is that, for a given bed elevation ($Z_s = cte$), the relation between the water depth at any two points is a straight line with slope 1. This is in direct agreement with the results of Puertas et al. [111], who found the relation between several characteristic water depths in the fishway designs T1 and T2 (Table 8.6).

Design	h_{min}	h_b	h_{max}
T1	0.97h_m-0.38b	1.00h_m+0.29b	1.02h_m+0.61b
T2	0.92h_m-0.41b	0.99h_m+0.28b	1.03h_m+0.48b

Table 8.6: Experimental relationships between water depths in the fishway. Bed slope 10.054%. h_{min}: minimum water depth in the pool; h_{max}: maximum water depth in the pool; h_b: water depth at the slot; h_m: mean water depth in the middle section of the pool. (From Puertas et al. [111]).

The flow discharge through the slot can be approximated as:

$$Q \approx b \int_0^{h_b} u_b \, dz = b \int_0^{h_b} u_s f_u(x_b, y_b, z) \, dz = C b u_s h_b \tag{8.36}$$

where h_b is the water depth in the slot, u_b is the velocity in the slot, and C is a constant equal to the average value of f_u in the slot. Using relations 8.33 yields the following water discharge:

$$Q = C \sqrt{g b^2 L_x \theta_s} h_b \tag{8.37}$$

where $\theta_s = \dfrac{Z_s}{L_x}$ is the bed slope. The constant C depends only on the geometry of the pool. It is common to define a discharge scale Q_s which depends only on the geometry of the pool, and

not on the water depth. Considering that the slot width b is proportional to the length scale L_x, a logical choice for Q_s from Equation 8.37 is given by:

$$Q_s = \sqrt{gb^5\theta_s} \tag{8.38}$$

which, introduced into Equation 8.37 gives the linear relation:

$$\frac{Q}{Q_s} = C'\frac{h_b}{b} \tag{8.39}$$

The discharge scale given by Equation 8.38 has been used by Puertas et al. [111] and Rajaratnam et al. [114]. Kamula [68] uses a slightly different expression for the non-dimensional discharge, $Q_s = \sqrt{gb^2L_x^3\theta_s}$, which is also a logical choice from Equation 8.37, and leads also to a linear relation between the non-dimensional discharge and the water depth.

It is quite common to use the water depth in the middle of the fishway h_m instead of the water depth in the slot h_b in Equation 8.39. Using Equation 8.29 for the water depth, the expression for the non-dimensional discharge becomes:

$$\frac{Q}{Q_s} = C'\left(\frac{h_m}{b} + \frac{Z_s(f_h(x_b,y_b) - f_h(x_m,y_m))}{b}\right) \tag{8.40}$$

where h_m is the water depth in the middle of the fishway. Expression 8.40 is not valid for very small water depths ($h_m \rightarrow 0$), since in that case the vertical stress becomes important in the development of the flow patterns, and additional constraints over the total water depth appear from Equation 8.32. This means that a linear relation like Equation 8.39 cannot be applied for small water depths.

Equation 8.40 allows an offset given by $C'\dfrac{Z_s(f_h(x_b,y_b) - f_h(x_m,y_m))}{b}$ when adjusting the experimental data for large values of h_m. According to the relation between h_b and h_m given in Table 8.6, this offset is positive for both pool designs, and its value is very small compared to the main term $C'\dfrac{h_m}{b}$. Hence, Equation 8.40 can be simplified as:

$$\frac{Q}{Q_s} \approx C'\frac{h_m}{b} \tag{8.41}$$

The fact that the scalings derived in this section are in accordance with the experimental results supports the approximations of hydrostatic pressure distribution and minor importance of the vertical stresses, at least as a global characteristic of the flow pattern, and justifies the use of the shallow water equations when modelling the fishway flow.

8.5 Numerical model

Three depth averaged turbulence models have been used in the numerical simulations (mixing length, $k-\varepsilon$ of Rastogi and Rodi, and algebraic stress model) in order to determine the differences in the computed velocity and turbulence fields. All the simulations have been done with the original constants of the models, without any empirical calibration. Some hydraulic manuals present empirical eddy viscosities which depend on the flow conditions. This is a very aleatory parameter which can be modified in an artificial way in order to match the experimental results, but always with an a priori knowledge of the results which are being seek. Molls et al. [93] are able to compute the recirculation region behind a spur-dike using a constant eddy viscosity approach, choosing its value by trial and error in order to match the experimental results. The fact of choosing a specific constant eddy viscosity have so much influence on the results that it can lead to erroneous conclusions. For this reason no simulations at all have been done with this approach, not even to make any comparison with the results given by the turbulence models.

All the flow field plots shown in this section are referred to the system of reference used in Figure 8.16. All the cross section plots are referred to the system of reference defined in Figure 8.4. The only difference between both systems of reference is the origin of the x - axis. In the flow field plots the x - axis is globally defined for the whole fishway model, while in the cross section plots it is locally defined for the specific pool considered.

8.5.1 General comments on the validity of the modelling hypothesis

Before doing the analysis of the numerical simulations, the experimental results presented in section 8.3 will be used here in order to assess the validity of the modelling assumptions which are done in the depth averaged shallow water equations and in the turbulence models.

The small magnitude of the vertical velocity, as well as the homogeneity of the mean velocity and turbulent kinetic energy in the vertical direction (except in the near slot region), justify the possibility of using a depth averaged model to simulate the flow in the fishway. In addition, the similarity analysis presented in section 8.4 supports the hypothesis of quasi-hydrostatic pressure distribution. Nevertheless, some problems may appear near the slot, where the vertical velocity is relatively high due to the large water surface gradient. This produces a depression in the free surface elevation which may not be accurately resolved by a depth averaged model.

The hypothesis of fully developed turbulence, which is made in all the turbulence models used in this thesis, is clearly fulfilled all over the fishway. On the other hand, the anisotropy between the transverse and longitudinal Reynolds stresses is a drawback to the linear eddy viscosity models. The large value of the vertical Reynolds stress, which is of the same order of magnitude as the horizontal turbulent stresses, is also an inconvenience, since its possible effects on the mean flow are not considered in the depth averaged equations.

Considering the strong horizontal velocity gradients in the flow, it is clear that the turbulent energy is mainly produced by horizontal shear strain, and not by bed friction, and therefore, the bed friction coefficient does not play an important role in the turbulence field.

Although no direct check has been made, the Boussinesq hypothesis is expected to work reasonably well in the upper part of the pools (points P1 and P3 in Figure 8.4), where the turbulence is nearly isotropic, and a clear separation between energetic and dissipative scales appear in the spectra. On the other hand, the eddy viscosity assumption should not be expected to perform well near the slot neither in the main jet stream (points P4 and P5 in Figure 8.4), where the flow is strongly anisotropic.

8.5.2 Flow features

The structure of the flow in both pool designs can be described as a confined curved jet which crosses the pool from the inlet to the outlet slot. On each side of the jet a recirculation eddy appears. The size and strength of these eddies depend on the specific pool design. There are several impinging areas in the pool, which may cause the realizability constraints in the turbulence models to limit the eddy viscosity value (see sections 2.4.5 and 2.5.3).

From the experimental results it follows that for uniform flow conditions the velocity field in both pool designs is almost independent of the total discharge. On the other hand, the water depth is proportional to the flow discharge with an almost linear relation. Hence, the first feature we should expect from the numerical model is to reproduce this behaviour. In order to prove so, three different discharges covering almost the full range of experimental flow conditions have been used in the computations: $35l/s$, $65l/s$ and $105l/s$.

The numerical model should also predict correctly the size of the two recirculation regions which occur on both sides of the main jet. The upper eddy is generated by shear friction, resembling a cavity flow. The eddy is driven by turbulent shear stress, and therefore, its prediction is very dependent on the turbulence model used. The flow separates behind the inlet slot baffle and the so-called lower eddy appears. Going through the outlet slot the flow is forced to reattach. The correct identification of these eddies is of great importance from a practical point of view, since they have a big influence guiding the fish through the pool.

The maximum velocity, which occurs in the vertical slot region, is another important flow feature which should be correctly computed. It determines whether or not fishes are able to pass from one pool to another. If the slot velocity is too high the fish may not be able to swim against it.

A correct turbulence modelling is of great importance in the prediction of all the previously described flow features. An excessively large turbulence level will diffuse too much the velocity profiles, tending to eliminate the recirculation eddies. On the other hand, a too low level of

turbulent kinetic energy will sharpen the profiles too much, producing too large velocities. Nevertheless, the sensitivity of the mean velocity field to the level of turbulence in the pool is not as high as it could be expected, and therefore, good predictions of the mean flow field can be obtained even if the resolution of the turbulence field is not highly accurate. This is a usual characteristic of RANS turbulence models, which tend to predict better the mean flow field than the turbulent kinetic energy field.

It should be remarked the effect that the accuracy of the numerical scheme has on the results. An order one scheme produces to much numerical diffusion unless an extremely fine mesh is used. Therefore, the results with such a scheme are very dependent on the mesh size. This dependence is even larger if the turbulence level is low. For a certain mesh resolution, an order one scheme without turbulence modelling may give a rather accurate velocity field, just because the numerical diffusion for that particular mesh size is approximately equal to the real turbulent diffusion. Such results are completely erroneous from a physical as well as from a mathematical point of view. All the simulations presented in this chapter have been done with a second order scheme.

The only empirical parameter which shows up in the mean flow equations is the bed friction coefficient. It turns out that its influence on the mean velocity field is minimal, mainly because the walls of the experimental model are rather smooth, and the Reynolds number very high. For this reason, the turbulent stresses play a more important role in the flow field than the bed shear stress. The turbulence production due to bed friction is also low compared to the horizontal shear production. A sensibility analysis of the results to the bed friction coefficient has been done using the Manning's formula. No significant differences were found for values of the Manning's coefficient in the range $n = 0 - 0.03 s/m^{1/3}$, which cover widely the possible values in the experimental model.

8.5.3 Boundary conditions

For all the discharges studied the flow is subcritical at the open boundaries. At the inlet boundary the total water discharge was distributed over a uniform unit discharge profile perpendicular to the boundary, while the water depth was computed by the numerical scheme. Three discharges were used in the simulations: $35 l/s$, $65 l/s$ and $105 l/s$. At the outlet boundary the free surface elevation was fixed for each discharge in order to obtain approximately the same water depth at the middle section of all the pools. This is the same procedure by which the downstream boundary condition was fixed in the experimental model. It should be mentioned that the numerical velocity field is quite insensitive to small changes in the downstream boundary condition. The sensitivity of the water depth field is somewhat higher but still low.

When using the $k - \varepsilon$ and the algebraic stress models the turbulent kinetic energy and the dissipation must be imposed at the inlet boundary. The actual value of these two variables at the

boundary is difficult to estimate. A too high turbulence level is not desirable since it would take too much time to dissipate, and therefore, it would affect strongly the results in the downstream pools. It is more adequate to let the flow produce the real state of turbulence as it passes through the first pool. In all the simulations the turbulent variables were fixed at the inlet boundary to $k_{in} = 10^{-2} m^2/s^2$ and $\varepsilon_{in} = 10^{-2} m^2/s^3$, which gives an eddy viscosity of approximately $\nu_{t,in} \approx 10^{-3} m^2/s$.

Wall functions were used at the solid boundaries. Due to the different local flow conditions, the wall mesh size varies widely with the location inside the pool, but it was kept always below an upper limit of $y^+ < 100$.

8.5.4 Mesh convergence

In order to perform the numerical simulations, the whole experimental model (Figure 8.2) was split in 2 sections. Each section contains an inlet pool, three active pools with either a T2 design (first section) or a T1 design (second section), and an outlet pool (Figure 8.16). The first active pool has a transition role, allowing the turbulent kinetic energy and velocity fields to develop. The second pool has been used in order to compare the numerical and experimental flow fields. In all the cases it has been checked that there are no significant differences between the flow fields in the second and third pools (Figure 8.17). Hence, a uniform state of the flow in pools 2 and 3 can be assumed.

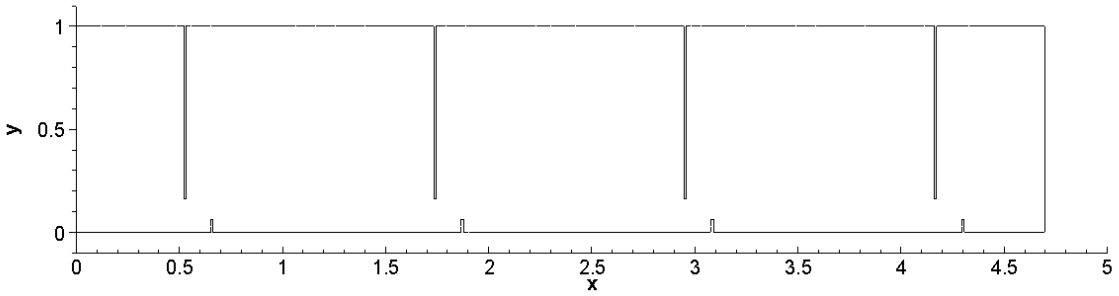

(a) Section 1. Design T2.

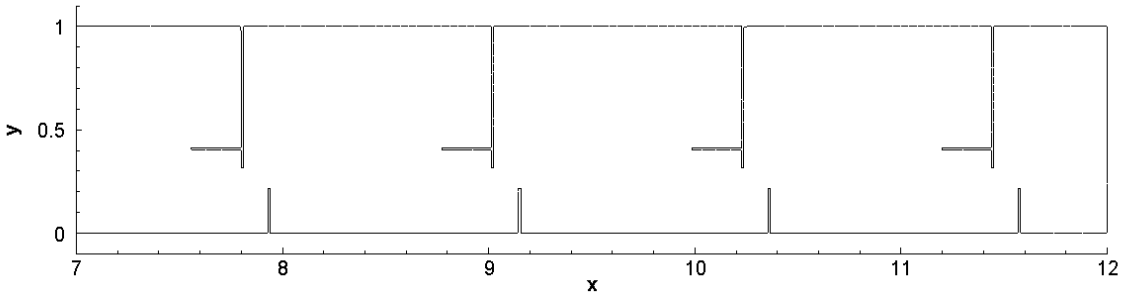

(b) Section 2. Design T1.

Figure 8.16: Numerical domain for the fishway. First and second sections.

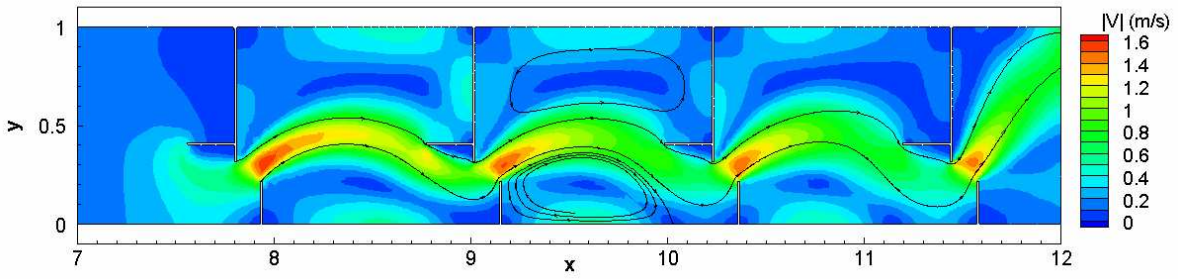

(a) Depth averaged speed (m/s). Design T1.

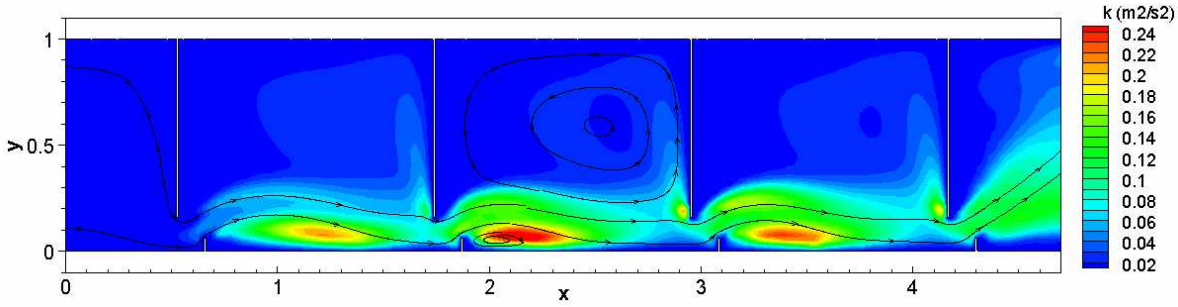

(b) Turbulent kinetic energy (m^2/s^2). Design T2.

Figure 8.17: Depth averaged speed and turbulent kinetic energy fields. Q=$65l/s$. $k-\varepsilon$ model.

In order to obtain a mesh independent solution, three meshes with different spatial resolution have been used for each pool design, which will be addressed as T1m0, T1m1, T1m2, for design T1, and T2m0, T2m1, T2m2, for design T2 (Tables 8.7 and 8.8). Figure 8.18 shows the resolution of the meshes T1m1 and T2m1, which are the ones chosen to perform the definitive computations. It should be remembered that the finite volume mesh is built from the triangular mesh by the procedure presented in section 3.5.1.

	Triangular mesh		Finite volume mesh	
	vertex	elements	volumes	faces
T1m0	1462	2545	4006	7635
T1m1	5610	10334	15943	31002
T1m2	8932	16926	25857	50778

Table 8.7: Characteristics of the numerical meshes for the pool design T1.

	Triangular mesh		Finite volume mesh	
	vertex	elements	volumes	faces
T2m0	3588	6692	10279	20076
T2m1	6182	11716	17897	35148
T2m2	8692	16610	25301	49830

Table 8.8: Characteristics of the numerical meshes for the pool design T2.

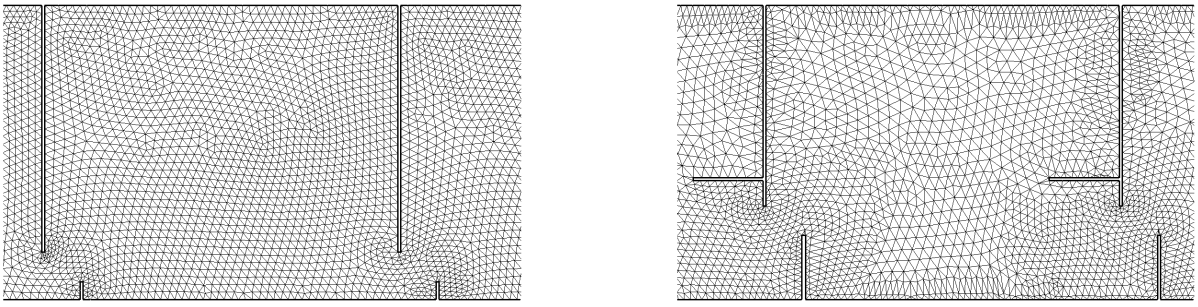

(a) Mesh T2m1. (b) Mesh T1m1.

Figure 8.18: Numerical meshes for the fishway. Designs T1 and T2.

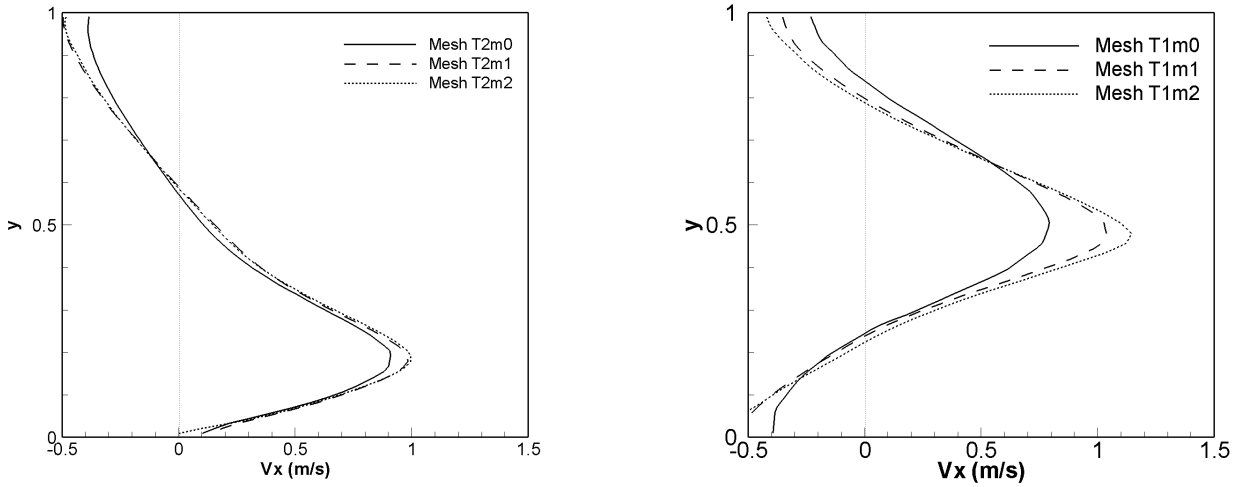

(a) Section 1. Design T2. ML model. (b) Section 2. Design T1. $k-\varepsilon$ model.

Figure 8.19: Mesh convergence. Longitudinal velocity $V_x(m/s)$ profile at the cross section $x = 0.4m$. Q=$65l/s$.

The mesh convergence analysis was done for the discharge of $65l/s$, with the mixing length and the $k-\varepsilon$ models. No significant differences were found in the results obtained with the intermediate (T1m1, T2m1) and the finest meshes (T1m2, T2m2), as it is shown in Figure 8.19. All the results presented in this chapter have been obtained with the meshes T1m1 and T2m1.

8.5.5 Influence of the numerical scheme on the solution

Figure 8.20 shows the velocity and water depth fields obtained with several numerical schemes on the mesh T1m1, for the discharge of $65l/s$, with the mixing length turbulence model. All the schemes use an upwind discretisation of the bed slope term. In the following plots, the hybrid first/second order scheme (see section 3.5.7), which uses a first order discretisation of the water depth and a second order discretisation of the unit discharges, is addressed as *order 122*. The fully second order scheme, which includes the high order correction of the upwind bed slope proposed

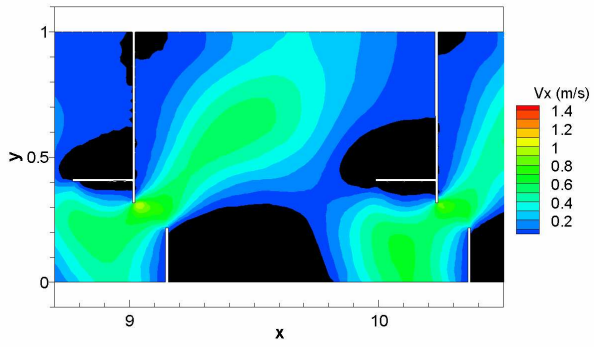

(a) $V_x(m/s)$. van Leer order 1.

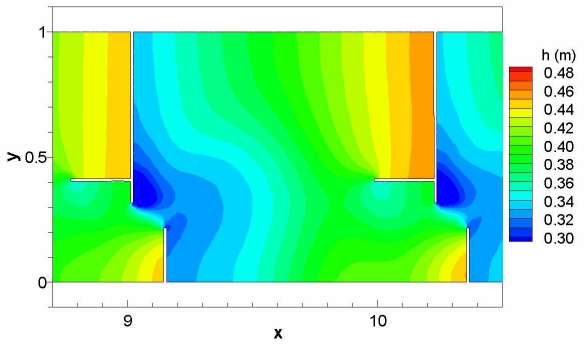

(b) $h(m)$. van Leer order 1.

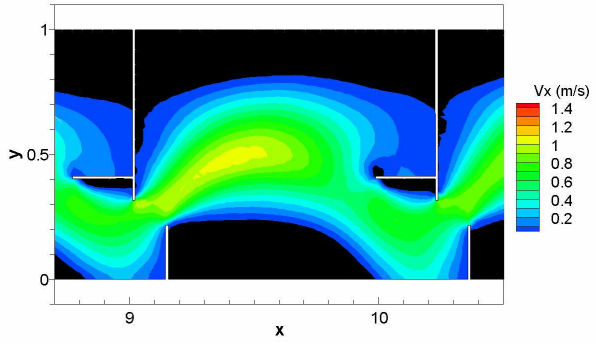

(c) $V_x(m/s)$. van Leer order 122.

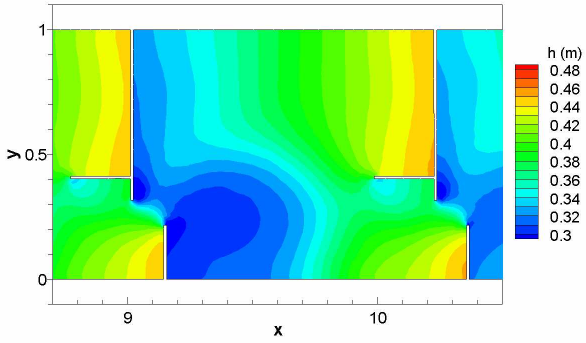

(d) $h(m)$. van Leer order 122.

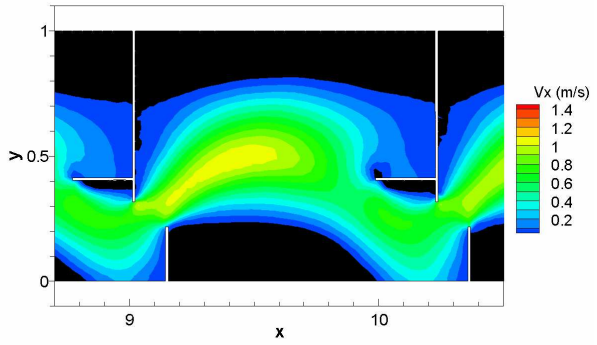

(e) $V_x(m/s)$. Roe order 2.

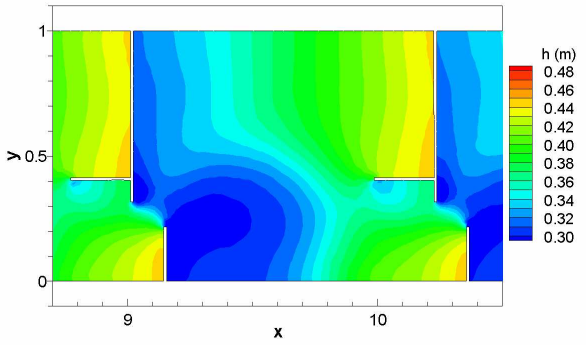

(f) $h(m)$. Roe order 2.

Figure 8.20: Influence of the numerical scheme on the velocity and water depth fields. Design T1. Q=$65l/s$. ML model.

by Hubbard and García-Navarro [62], is addressed as *order 2*.

The first order scheme is too diffusive, and it is not able to reproduce the upper recirculation eddy (Figures 8.20(a) and 8.22(a)). The excessive diffusion is due to the numerical scheme, since the eddy viscosity fields obtained with all the schemes are similar (Figure 8.21). No significant differences in the velocity field, neither in the water depth field, appear in the results obtained with the hybrid first/second order scheme and with the fully second order scheme. This shows the

importance of using a second order discretisation of the unit discharges, which removes most of the first order scheme's numerical diffusion. The results given by the van Leer's and Roe's schemes do not show any significant difference.

The water depth fields obtained with the first and second order schemes show some differences downstream the inlet slot, where the second order schemes produce a stronger depression in the water surface elevation (Figures 8.20(b,d,f)).

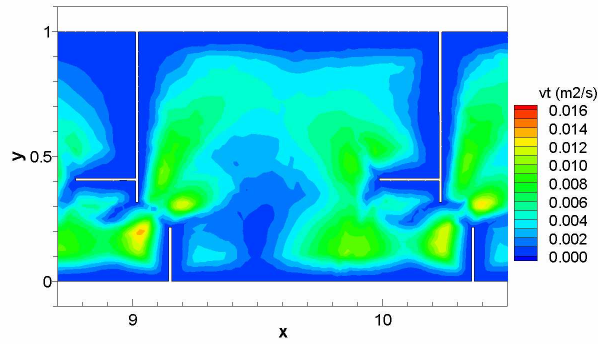

(a) Eddy viscosity $\nu_t(m^2/s)$. van Leer order 1.

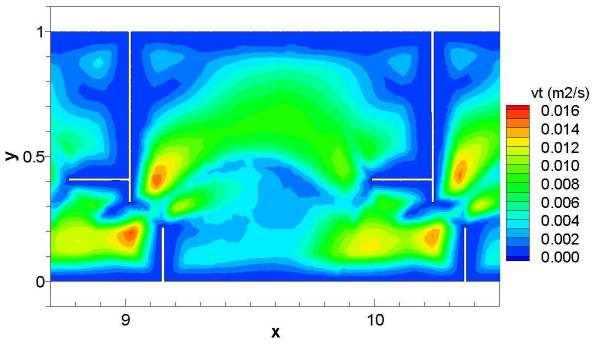

(b) Eddy viscosity $\nu_t(m^2/s)$. van Leer order 122.

Figure 8.21: Influence of the numerical scheme on the eddy viscosity field. Design T1. Q=$65l/s$. ML model.

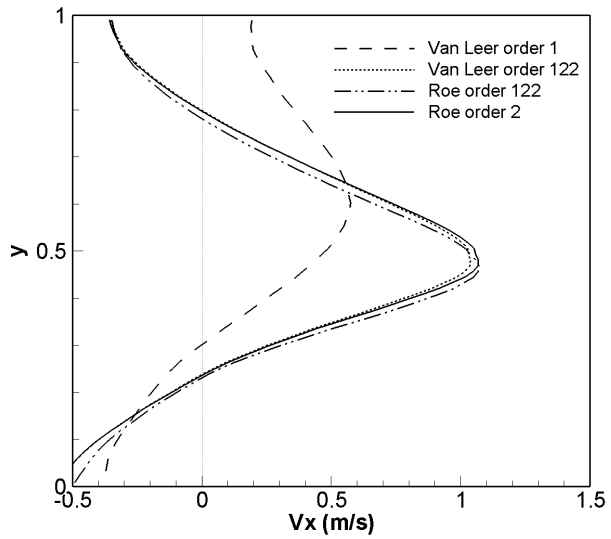

(a) Longitudinal velocity $V_x(m/s)$ at $x = 0.4m$.

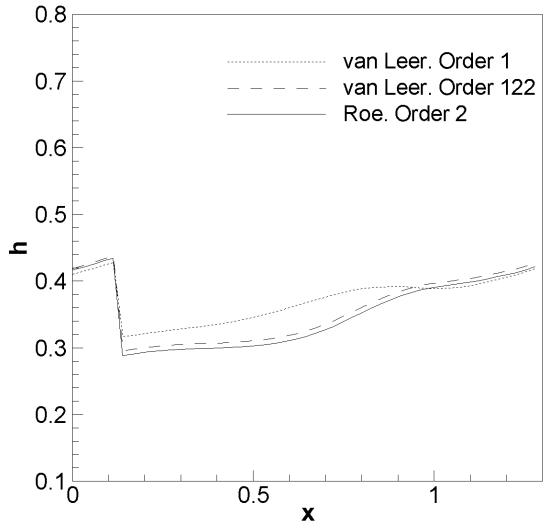

(b) Water depth $h(m)$ at $y = 0.16m$.

Figure 8.22: Influence of the numerical scheme on the velocity and water depth. Design T1. Q=$65l/s$. ML model.

8.5.6 Unsteady solutions

Most of the simulations have converged to a steady solution, which is the expected behaviour in RANS computations. However, in some cases the numerical solution shows periodical oscillations, specially when the ASM is used. Unsteady solutions have been found in the design T2 for the discharges of $35l/s$ and $65l/s$ with the ASM, and in the design T1 for the discharge of $35l/s$ with both the ASM and the $k-\varepsilon$ models (Figure 8.23). The magnitude of the oscillations is larger for the $35l/s$ discharge. In all those cases an unsteady computation with a constant time step has been done, in the same way as it is done in URANS simulations. Figure 8.23 shows the time evolution of the longitudinal velocity at the spatial points defined in Figure 8.4 for the discharge of $35l/s$. The strongest oscillations occur at the points P5 and P4, followed by the points P3, P2 and P1.

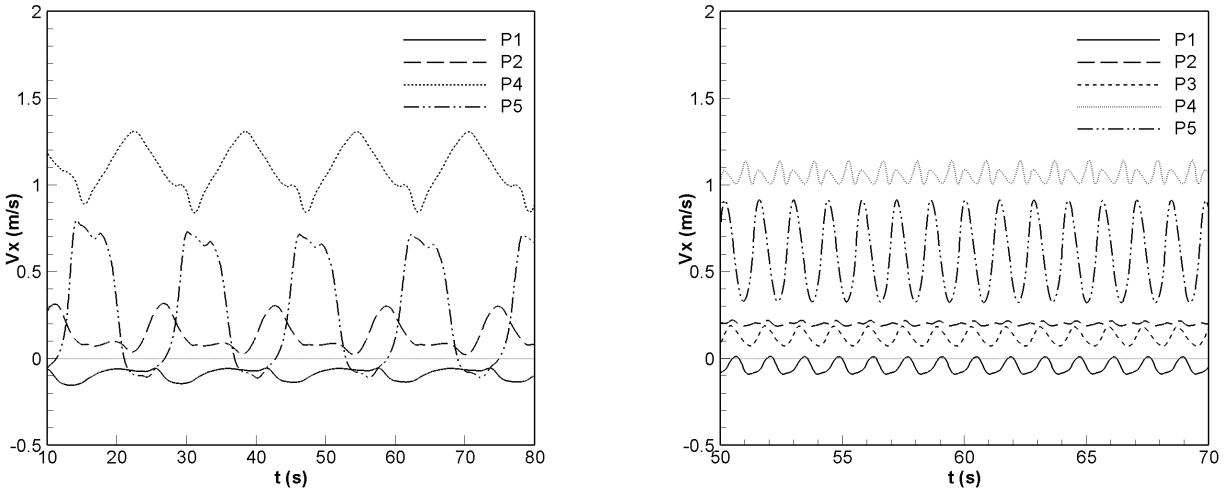

(a) Design T2.

(b) Design T1.

Figure 8.23: Time evolution of the longitudinal velocity $V_x(m/s)$ at the points defined in Table 8.2 and in Figure 8.4. Designs T1 and T2. Q=$35l/s$. ASM.

The physical interpretation of these unsteady solutions is not clear. They occur because the flow has strong separation regions which enhance the growth of instabilities. When the turbulence energy produced by the turbulence model is not large enough to damp these instabilities, the solution shows a periodical oscillation. Numerically, these oscillations might be interpreted as the unsteady solutions found in URANS computations. However, their physical interpretation should not be done in a URANS basis for several reasons. First, because it is not obvious the physical meaning of URANS oscillations obtained from the depth averaged shallow water equations, specially considering that the water depth in the fishway is of the same order of magnitude as the pool length. Second, because the turbulence in the fishway is strongly three-dimensional, and therefore, the intrinsic physics of the oscillations should be simulated with a 3D model. A URANS interpretation would be reasonable if the water depth was much smaller than the amplitude of the oscillations, which is not the case in the present simulations.

It is more likely to have unsteady solutions with the ASM than with the $k-\varepsilon$ model because the latter one overpredicts systematically the turbulent energy in the presence of stagnation points and recirculation regions. Why the unsteady oscillations are stronger as the water depth diminishes is not so clear. It may have to do with the fact that the Froude number increases as the water depth diminishes, reaching values larger that 1 in the slot region for the discharge of $35l/s$ (Figure 8.24). The change in the flow conditions from subcritical to supercritical, and again to subcritical in approximately $15cm$, probably enhances the growth of instabilities in the flow. All the results relative to the unsteady simulations have been time averaged in order to obtain a steady flow field. For the reasons exposed above, no additional interpretation has been done of the unsteady oscillations.

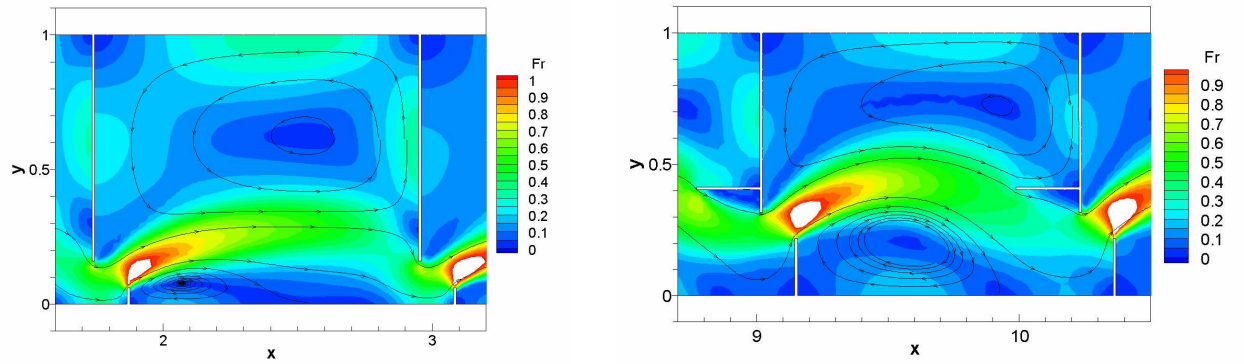

(a) Design T2. (b) Design T1.

Figure 8.24: Froude number field. Designs T1 and T2. Q=$35l/s$. ASM.

Figure 8.25 shows a one cycle time sequence of the ASM unsteady solution for the design T1 with a discharge of $65l/s$. It clearly shows a movement of the main jet, as well as variations in the velocity peak value.

8.6 Numerical results and experimental validation

8.6.1 Results in Section 1 - Design T2

All the results presented in this section have been obtained with the numerical mesh T2m1 (Figures 8.16(a) and 8.18(a)), whose characteristics are presented in Table 8.8. For the discharges of $35l/s$ and $65l/s$, the ASM results have been obtained as a time average of the unsteady numerical solution.

All the flow field plots shown in this section are referred to the system of reference used in Figure 8.16(a). All the cross section plots are referred to the system of reference defined in Figure 8.4(b). The only difference between both systems of reference is an offset of $1.74m$ in the origin of the x - axis.

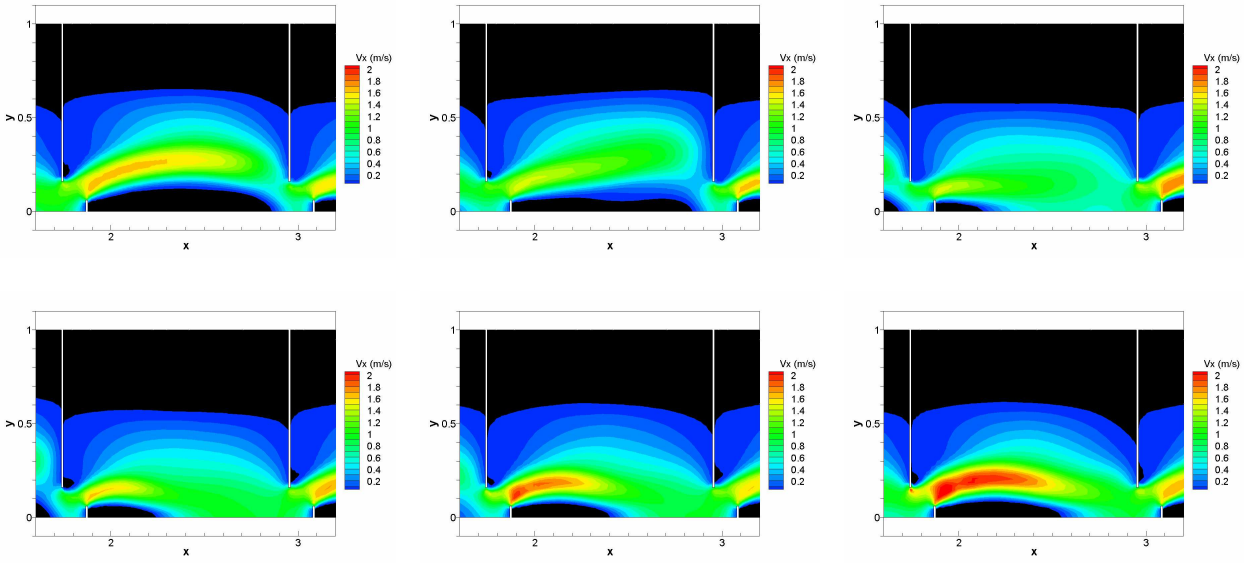

Figure 8.25: Six snapshots of the longitudinal velocity $V_x(m/s)$ over one unsteady oscillation. Design T2. Q=$65l/s$. ASM.

Velocity field in the design T2

The dependence of the velocity field on the total discharge is shown in Figure 8.26. Both the $k-\varepsilon$ model and the ASM predict recirculation regions which are rather insensitive to the total discharge, which is in direct agreement with the experimental results. The maximum velocity given by the $k-\varepsilon$ model is almost independent of the total discharge. On the other hand, the maximum velocity in the slot given by the ASM increases when the discharge is increased from $35l/s$ to $65l/s$. The velocity field obtained with the mixing length model (ML) is slightly more sensitive to the total discharge. This is because the turbulent length scale used to compute the eddy viscosity with the ML model depends directly on the water depth (Equation 2.69). Therefore, the turbulent stresses (diffusive forces) increase with the water depth, and the velocity profiles become more flattened. This is not the case in the ASM and $k-\varepsilon$ models, where the turbulent length scale is given by the turbulent kinetic energy and the dissipation. The dependence of the eddy viscosity on the total discharge is shown in Figure 8.27. While the ML model almost triplicates the value of the eddy viscosity when increasing the discharge from $35l/s$ to $105l/s$, the eddy viscosity field obtained with the $k-\varepsilon$ model is very insensitive to the total discharge. Figures 8.26(a-c) and 8.27(a,b) show that similar velocity fields are obtained with different eddy viscosity fields, which is a characteristic feature of RANS models.

A comparison of the depth averaged longitudinal velocity at several cross sections reveals a satisfactory agreement between the experimental and numerical results (Figure 8.28). The experimental velocity in Figure 8.28 has been computed as a weight average of the velocity at several elevations (2 elevations for Q=$35l/s$, 3 elevations for Q=$65l/s$ and 5 elevations for Q=$105l/s$). The ASM and $k-\varepsilon$ models predict fairly well the width of the recirculation eddies, as well as

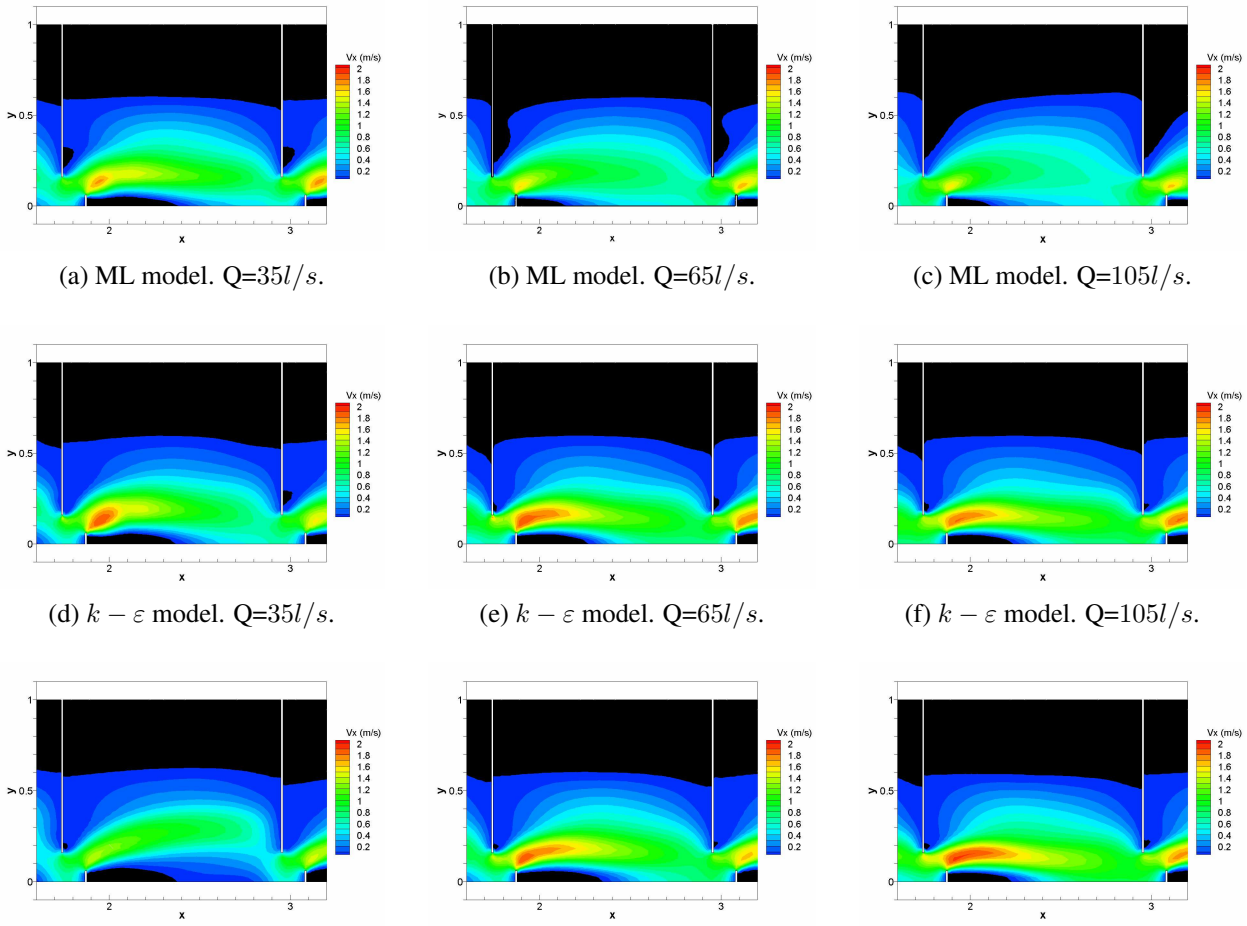

(a) ML model. Q=35l/s. (b) ML model. Q=65l/s. (c) ML model. Q=105l/s.

(d) $k-\varepsilon$ model. Q=35l/s. (e) $k-\varepsilon$ model. Q=65l/s. (f) $k-\varepsilon$ model. Q=105l/s.

(g) ASM. Q=35l/s. (h) ASM. Q=65l/s. (i) ASM. Q=105l/s.

Figure 8.26: Depth averaged longitudinal velocity fields $V_x(m/s)$. Design T2. Several discharges. Several turbulence models. The black region represents negative longitudinal velocities.

the evolution of the jet as the flow crosses the pool. Although both models give slightly different results, none of them can be considered in better agreement with the experimental data. The predictions of the ML model are somewhat worse, specially as the discharge increases. The width of the upper recirculation region is still in good agreement with the experiments, but the size of the lower eddy is underpredicted. The velocity profiles are too flattened, specially for the discharges of $65l/s$ and $105l/s$.

For the discharge of $35l/s$ the ML and $k-\varepsilon$ models give a very similar definition of the main jet. On the other hand, the ASM gives a slightly different position of the jet centreline, and a somewhat smaller peak velocity (Figures 8.28(a-c)). The best agreement with the experimental data for this discharge is given by the $k-\varepsilon$ and ML models. For the $65l/s$ and $105l/s$ discharges, the ASM and $k-\varepsilon$ models give better predictions than the ML model.

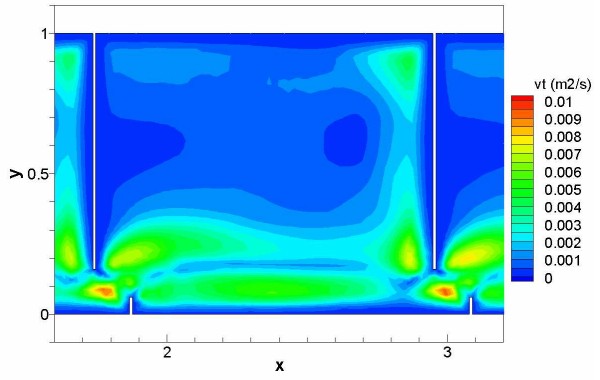

(a) ML model. Q=$35l/s$.

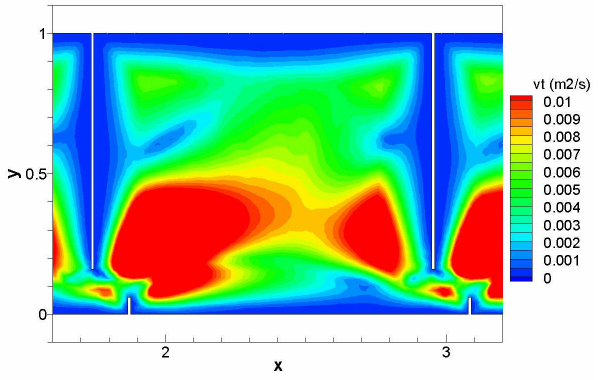

(b) ML model. Q=$105l/s$.

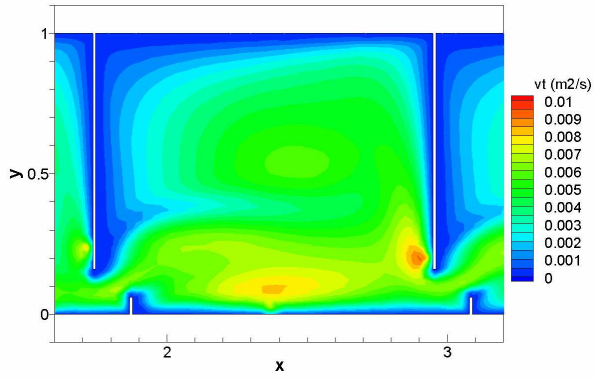

(c) $k-\varepsilon$ model. Q=$35l/s$.

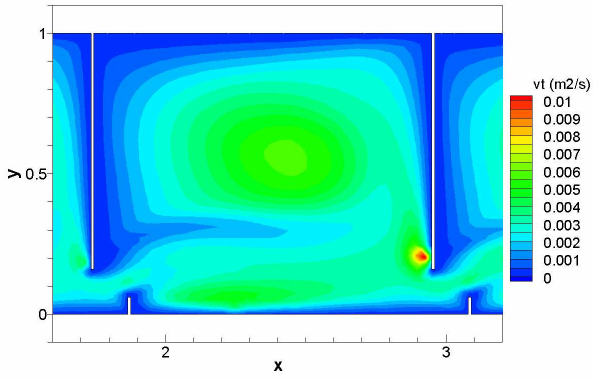

(d) $k-\varepsilon$ model. Q=$105l/s$.

Figure 8.27: Dependence of the eddy viscosity $\nu_t(m^2/s)$ on the total discharge. Design T2.

Water depth field in the design T2

The ASM and $k-\varepsilon$ models predict similar water depths in all the pool except in the depression area which appears downstream the inlet slot, where the $k-\varepsilon$ model gives a lower water depth (Figure 8.29). Since there are not many experimental data points in that area, it is difficult to assess from Figure 8.29 which model is in better agreement with the experimental results. The ML model gives slightly worse results, specially near the downstream baffle, where it predicts a too large water depth.

Figure 8.30 shows several longitudinal sections of the water depth. The best agreement with the experimental data is usually given by the ASM and $k-\varepsilon$ models, except for the $35l/s$ discharge, where the ASM results are somewhat poorer. Figure 8.31(a) shows the relation between the total discharge and the water depth in the middle of the pool ($x=0.6m, y=0.5m$). For the considered range of discharges the model gives an almost linear relation, which is in complete agreement with the experiments.

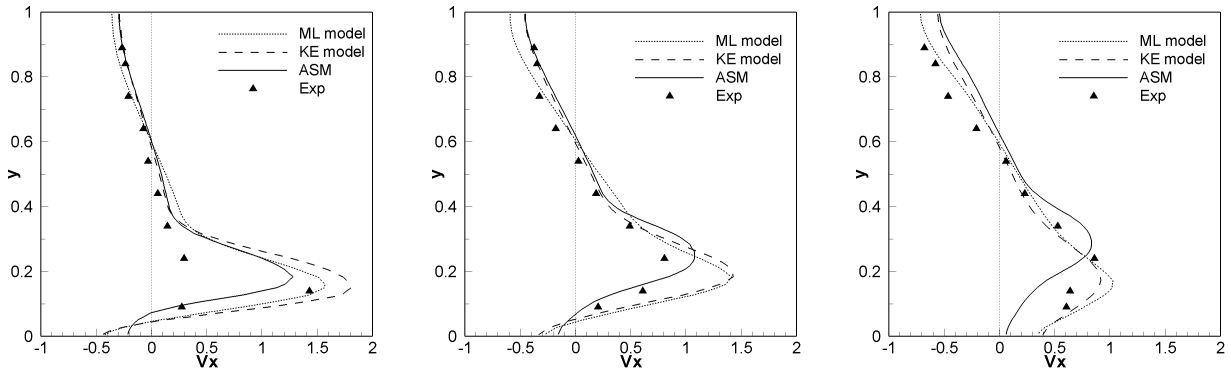

(a) Q=$35l/s$. $x = 0.26m$. (b) Q=$35l/s$. $x = 0.46m$. (c) Q=$35l/s$. $x = 0.86m$.

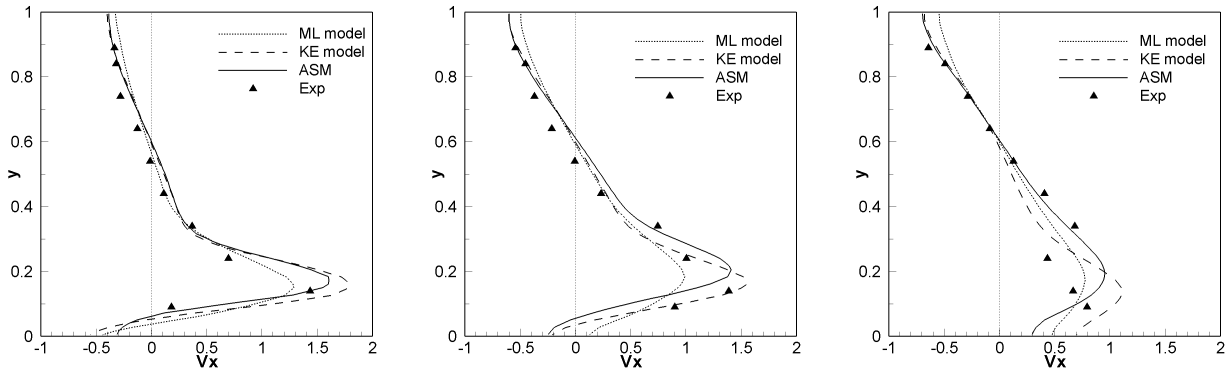

(d) Q=$65l/s$. $x = 0.26m$. (e) Q=$65l/s$. $x = 0.46m$. (f) Q=$65l/s$. $x = 0.86m$.

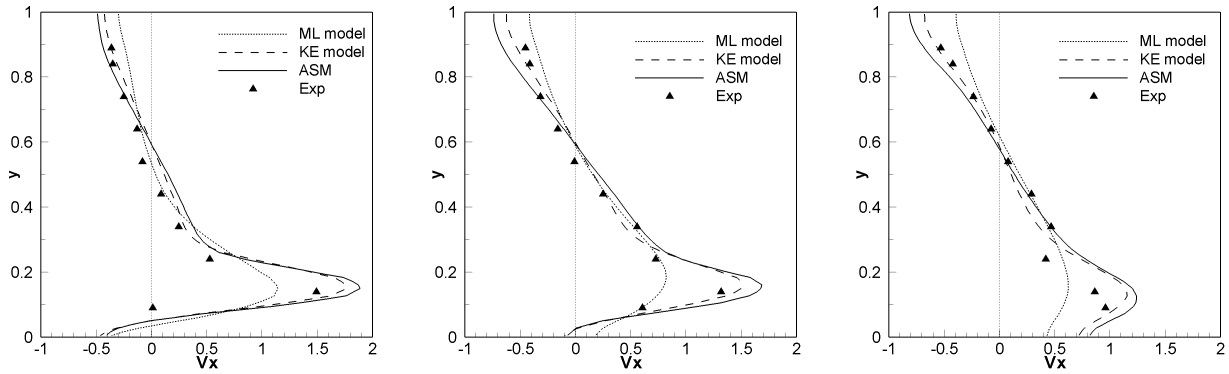

(g) Q=$105l/s$. $x = 0.26m$. (h) Q=$105l/s$. $x = 0.46m$. (i) Q=$105l/s$. $x = 0.86m$.

Figure 8.28: Numerical and experimental depth averaged longitudinal velocity $V_x(m/s)$ at several cross sections. Design T2.

Turbulence field in the design T2

As it has been pointed out by many researchers [46, 30, 110], the turbulence field is extremely important in the performance of any fishway design, since it has a big influence on the swimming costs of fishes. The fact of obtaining rather accurate velocity fields does not necessarily imply that the turbulence field has been correctly computed. The turbulent kinetic energy and Reynolds stresses given by RANS models are usually less accurate than the mean velocity results, specially

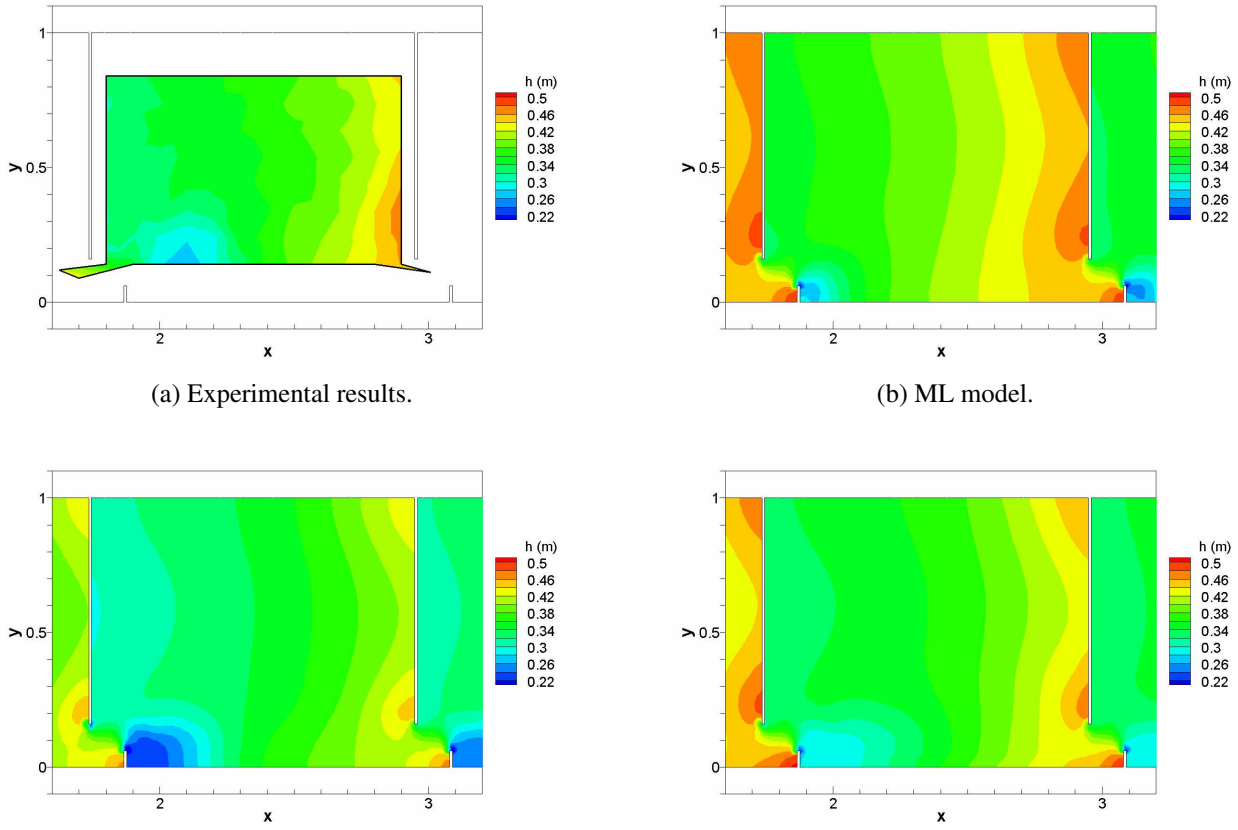

(a) Experimental results.

(b) ML model.

(c) $k-\varepsilon$ model.

(d) ASM model.

Figure 8.29: Water depth field $h(m)$. Design T2. Q=$65l/s$.

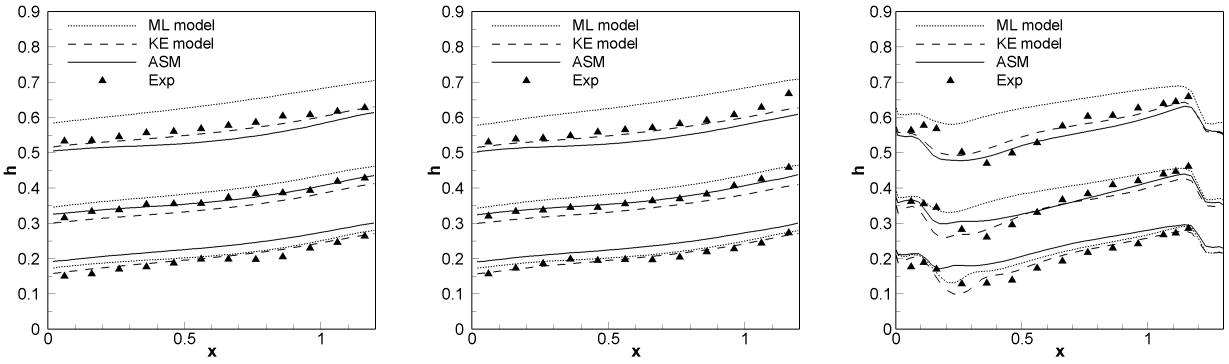

(a) $y = 0.74m$.

(b) $y = 0.44m$.

(c) $y = 0.14m$.

Figure 8.30: Numerical and experimental water depth at several longitudinal sections. Q=$35l/s, 65l/s, 105l/s$. Design T2.

in anisotropic recirculating flows. In the following plots the Reynolds stresses given by the $k-\varepsilon$ model have been computed with the Boussinesq assumption, using the eddy viscosity, the turbulent kinetic energy and the mean velocity given by the model. The ML model does not compute the turbulent kinetic energy, and therefore, it is not considered in this section.

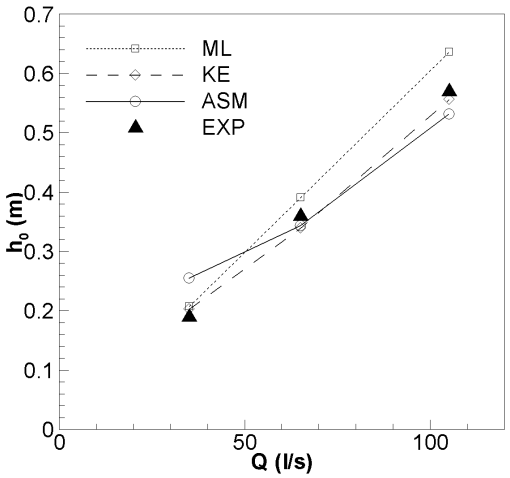

(a) Design T2.

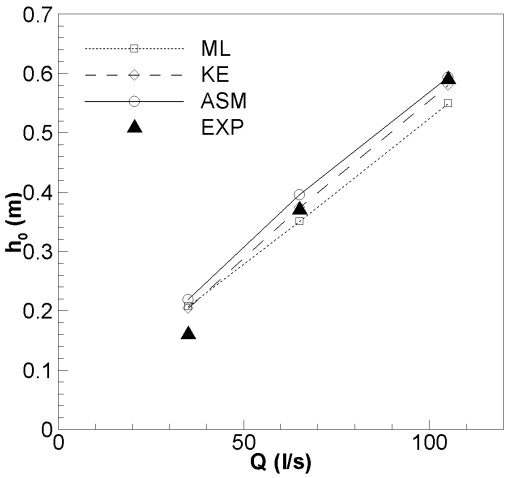

(b) Design T1.

Figure 8.31: Discharge-water depth relations. h_0: water depth at the middle of the pool.

The global agreement between the experimental and numerical results is rather satisfactory, specially considering the flow pattern in the pool. The ASM systematically predicts lower turbulence levels than the $k-\varepsilon$ model. The largest differences between both models occur in the main jet stream, where the ASM underpredicts the turbulent energy, while the $k-\varepsilon$ model overpredicts it (Figure 8.32). Near the outlet slot both models overpredict the turbulent energy (Figure 8.32(c)). The excessively large turbulence levels given by the $k-\varepsilon$ model just downstream the inlet slot (Figures 8.32(a) and 8.34(a)) are caused by the strong shear strain, with velocity gradients of the order of $20s^{-1}$. The flow conditions in that region, with a very strong swirl as well as separation and reattachment in a very short distance, are beyond the capabilities of the eddy viscosity models.

The largest source of turbulence in the pool is due to the strong shear strain in the inlet slot and in the lower eddy (Figure 8.33). Although in the $k-\varepsilon$ model the turbulence production near stagnation points is controlled by the production limiter (Equation 2.88) and by the realizability condition (Equation 2.93), the ASM still gives lower values of the turbulent kinetic energy in the slot region and in the lower recirculation eddy (Figure 8.34). On the other hand, the production levels given by the ASM extend further downstream (Figure 8.33), which is clearly shown in the turbulent kinetic energy fields (Figure 8.34). The peak value of the turbulent energy given by the $k-\varepsilon$ model is inside the lower eddy, with values around $0.24m^2/s^2$. With the ASM the peak values are lowered to $0.18m^2/s^2$ and moved downstream.

The anisotropy between the longitudinal and transverse Reynolds stresses downstream the inlet slot is well predicted by the ASM model (Figure 8.35(a,b)). While the longitudinal component ($\overline{u'^2}$) is slightly underpredicted, probably due to the effects of the air bubbles and of the 3D flow features in the slot region, which are not considered in the model, the transverse component ($\overline{v'^2}$) is rather accurately computed. On the other hand, the $k-\varepsilon$ model overpredicts both components in this region, specially the transverse one ($\overline{v'^2}$). Near the outlet slot both models give poorer

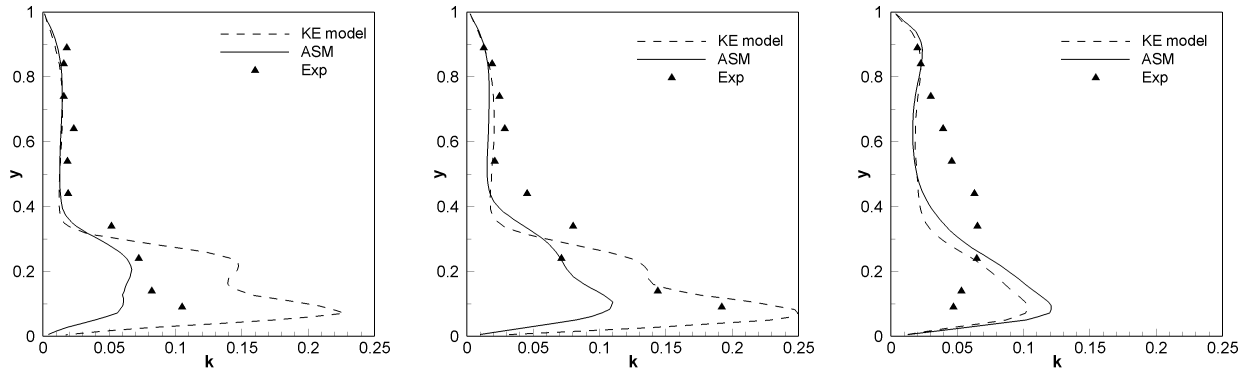

(a) $x = 0.26m$. (b) $x = 0.46m$. (c) $x = 0.86m$.

Figure 8.32: Numerical and experimental turbulent kinetic energy $k(m^2/s^2)$ at several cross sections. Design T2. Q=$65l/s$.

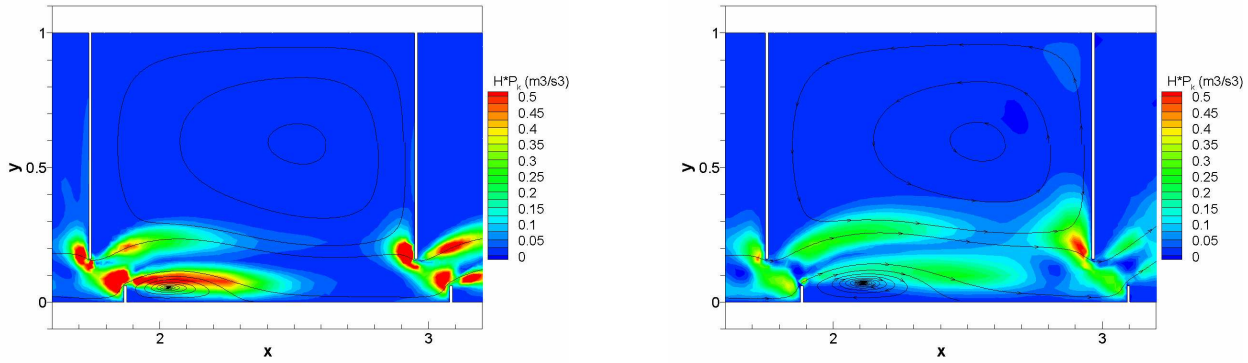

(a) $k - \varepsilon$ model. (b) ASM.

Figure 8.33: Production of turbulent kinetic energy due to horizontal strain $hP_k(m^3/s^3)$. ASM and $k - \varepsilon$ models. Design T2. Q=$65l/s$.

predictions. It seems that the production of turbulence given by both models in the reattachment region ($x \approx 2.3m$ in Figure 8.33) is excessively high.

8.6.2 Results in Section 2 - Design T1

All the results relative to the design T1 have been obtained with the numerical mesh T1m1 (Figures 8.16(b) and 8.18(b)), whose characteristics are defined in Table 8.7. Unsteady solutions have been obtained only for the $35l/s$ discharge, with both the ASM and the $k - \varepsilon$ models. In those cases a time average of the numerical solution has been computed in order to compare with the experimental results.

All the flow field plots shown in this section are referred to the system of reference defined in Figure 8.16(b). All the cross section plots are referred to the system of reference defined in Figure 8.4(a). The only difference between both systems of reference is an offset of $9.0m$ in the origin of the x - axis.

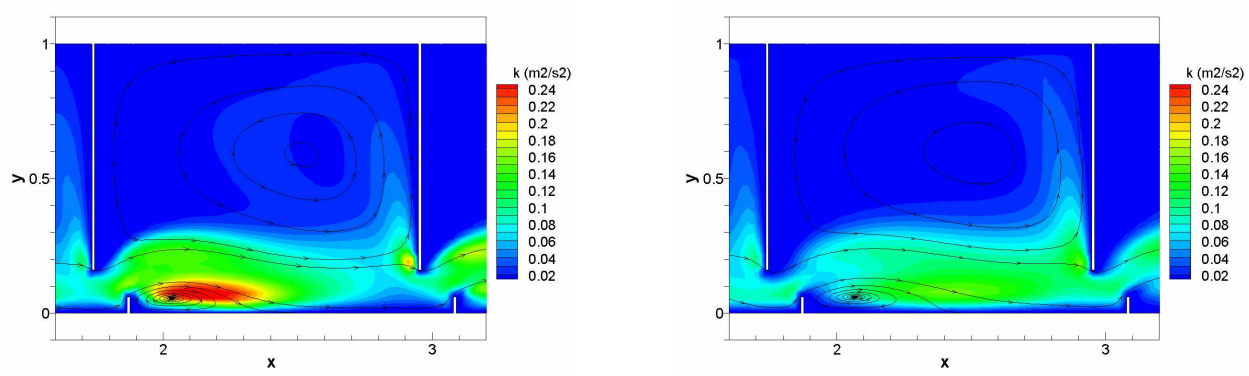

(a) $k-\varepsilon$ model. (b) ASM.

Figure 8.34: Turbulent kinetic energy field $k(m^2/s^2)$. ASM and $k-\varepsilon$ models. Design T2. Q=$65l/s$.

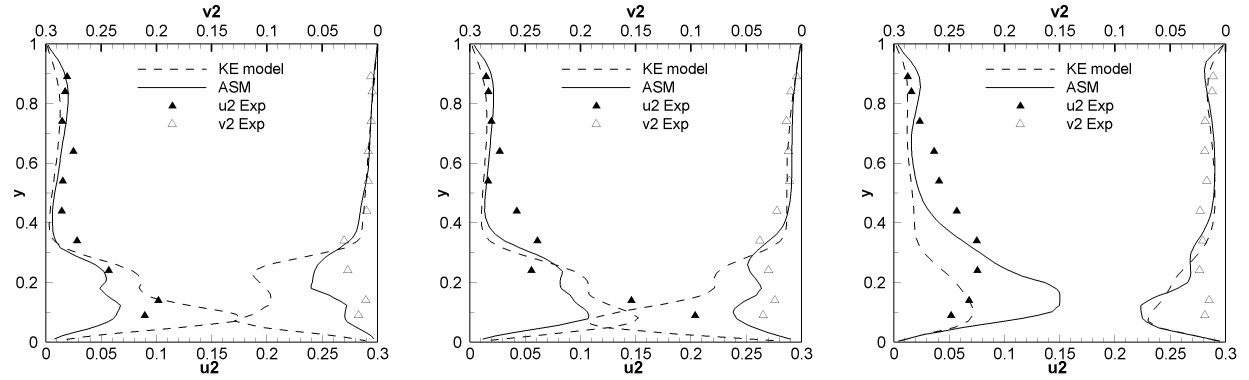

(a) Q=$65l/s$. $x=0.26m$. (b) Q=$65l/s$. $x=0.46m$. (c) Q=$65l/s$. $x=0.86m$.

Figure 8.35: Numerical and experimental horizontal Reynolds stresses $\overline{u'^2}$ and $\overline{v'^2}(m^2/s^2)$ at several cross sections. Design T2. Q=$65l/s$.

Velocity field in the design T1

The flow pattern in the pool design T1 is also rather independent of the total discharge. The main differences between the velocity fields in the designs T1 and T2 are the size of the lower recirculation eddy and the curvature of the main jet. Figure 8.36 shows the longitudinal velocity fields obtained with the 3 turbulence models for the 3 flow discharges used in the numerical computations. The ML model results are very dependent on the total discharge, and fail to predict the size of the recirculation eddies. This is specially true for the discharge of $105l/s$, where the upper recirculation region completely disappears. Both the upper and lower recirculation eddies given by the ASM and $k-\varepsilon$ models are almost independent of the total discharge, which is in good agreement with the experiments. The size of both eddies is similarly predicted by both models. The maximum velocity in the slot increases slightly from the $35l/s$ discharge to the $65l/s$ discharge, and then it remains almost constant up to the $105l/s$ discharge. The ASM gives slightly higher velocities than the $k-\varepsilon$ model in the slot region.

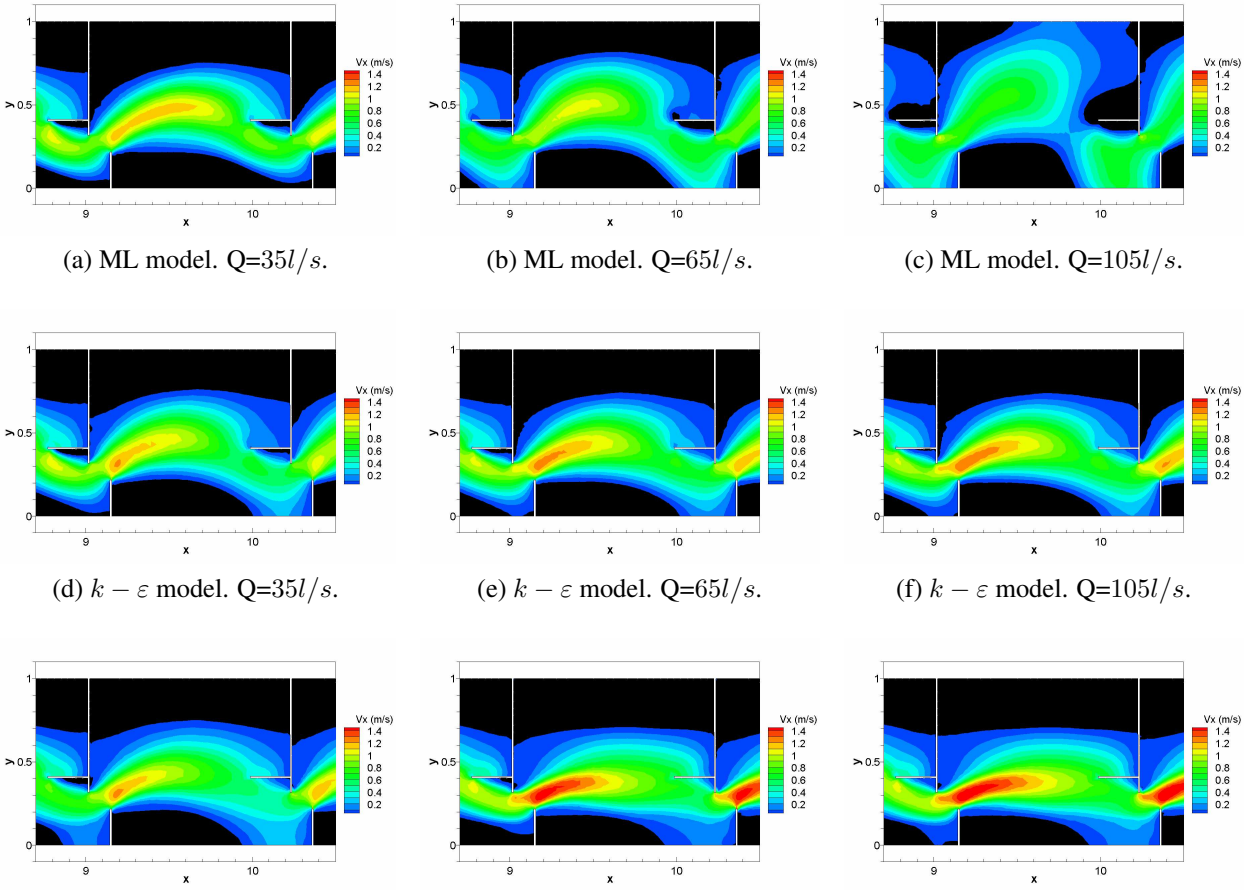

(a) ML model. Q=$35l/s$. (b) ML model. Q=$65l/s$. (c) ML model. Q=$105l/s$.

(d) $k-\varepsilon$ model. Q=$35l/s$. (e) $k-\varepsilon$ model. Q=$65l/s$. (f) $k-\varepsilon$ model. Q=$105l/s$.

(g) ASM. Q=$35l/s$. (h) ASM. Q=$65l/s$. (i) ASM. Q=$105l/s$.

Figure 8.36: Depth averaged longitudinal velocity fields $V_x(m/s)$. Design T1. Several discharges. Several turbulence models. The black region represents negative longitudinal velocities.

The comparison of the numerical and experimental depth averaged longitudinal velocity at several cross sections (Figure 8.37) shows a good agreement when using the ASM and $k-\varepsilon$ models. As it occurs in the pool design T2, both the ASM and $k-\varepsilon$ models give somewhat different results, but a similar level of agreement with the experimental data. The models give a good definition of both the upper and lower eddies. The excessive turbulent diffusion produced by the ML model is clearly shown in the flattened velocity profiles obtained for the $105l/s$ discharge (Figures 8.37(g-i)).

Water depth field in the design T1

The agreement between the numerical and experimental water depth in the pool design T1 is rather good for the $65l/s$ and $105l/s$ discharges. For the discharge of $35l/s$ the numerical model overpredicts the water depth in all the pool (Figure 8.38). Both the ML and $k-\varepsilon$ models give similar water depths in this design, still the $k-\varepsilon$ model agrees slightly better with the experimental data for the discharge of $105l/s$. The ASM predicts slightly larger water depths, specially for the

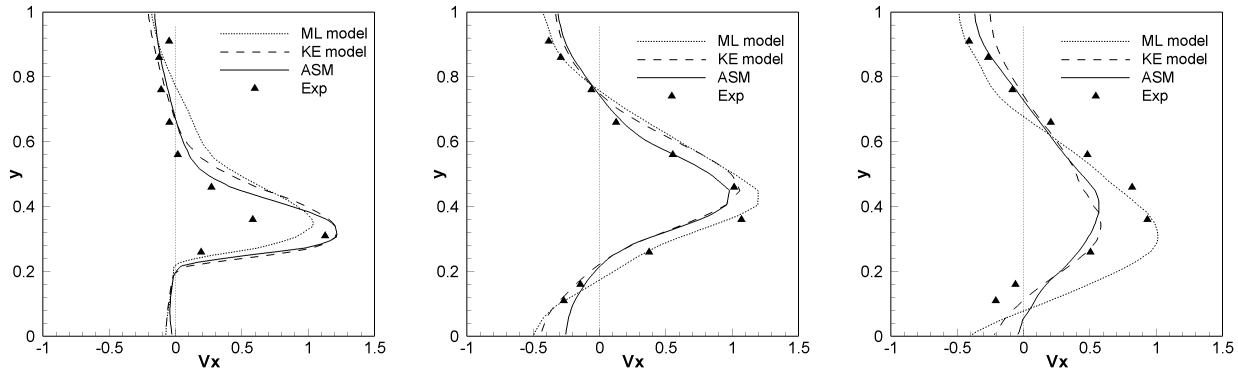

(a) Q=$35l/s$. $x = 0.16m$. (b) Q=$35l/s$. $x = 0.46m$. (c) Q=$35l/s$. $x = 0.86m$.

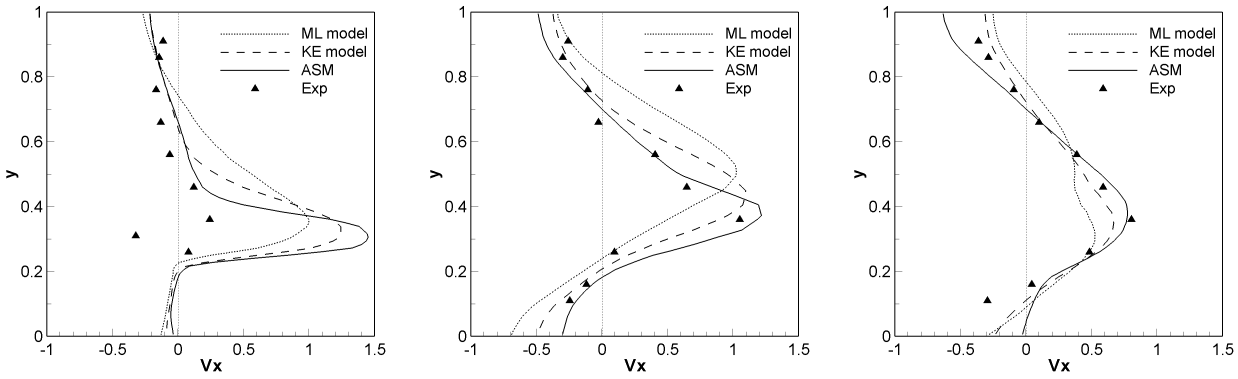

(d) Q=$65l/s$. $x = 0.16m$. (e) Q=$65l/s$. $x = 0.46m$. (f) Q=$65l/s$. $x = 0.86m$.

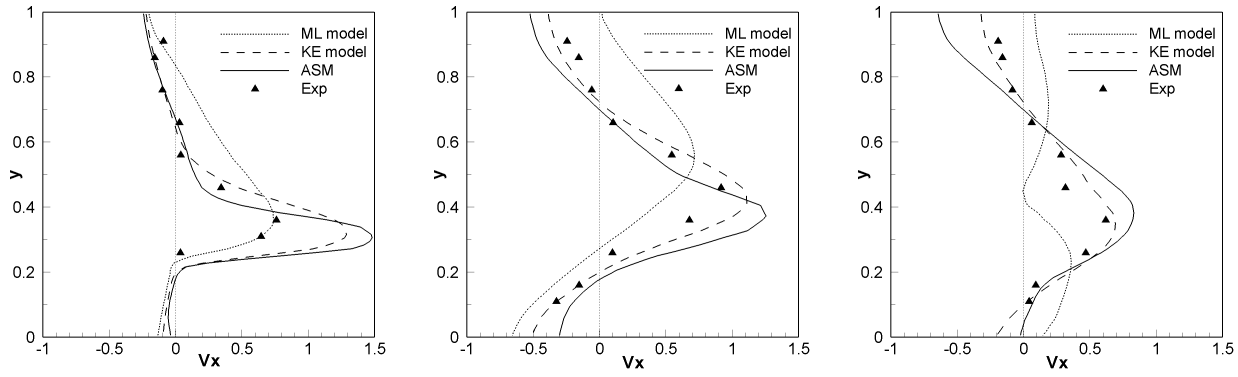

(g) Q=$105l/s$. $x = 0.16m$. (h) Q=$105l/s$. $x = 0.46m$. (i) Q=$105l/s$. $x = 0.86m$.

Figure 8.37: Numerical and experimental depth averaged longitudinal velocity $V_x(m/s)$ at several cross sections. Design T1.

discharge of $35l/s$.

Turbulence field in the design T1

The ASM gives better predictions of the turbulence field than the $k-\varepsilon$ model, specially regarding the Reynolds stresses. As is happens in the pool design T2, the turbulent kinetic energy peak near the inlet slot is underpredicted by the ASM, while overpredicted by the $k-\varepsilon$ model (Fig-

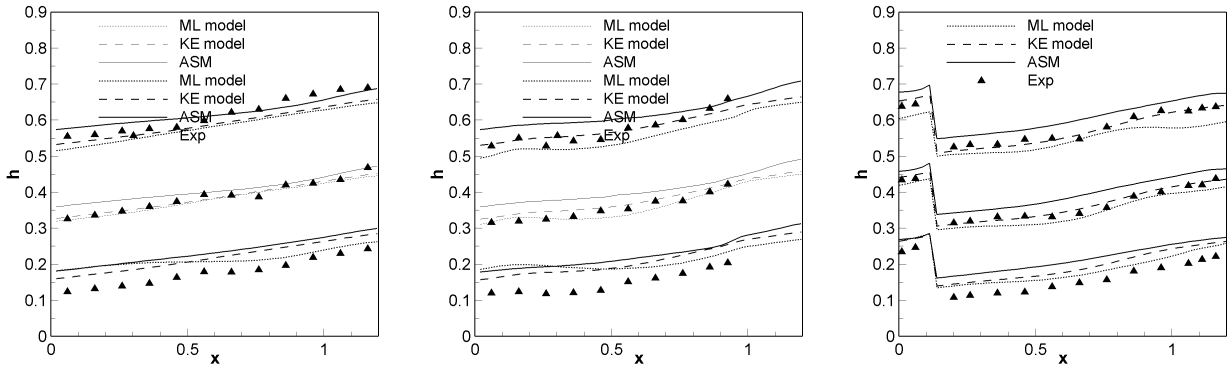

(a) $y = 0.76m$. (b) $y = 0.46m$. (c) $y = 0.16m$.

Figure 8.38: Numerical and experimental water depth at several longitudinal sections. Q=$35l/s, 65l/s, 105l/s$. Design T1.

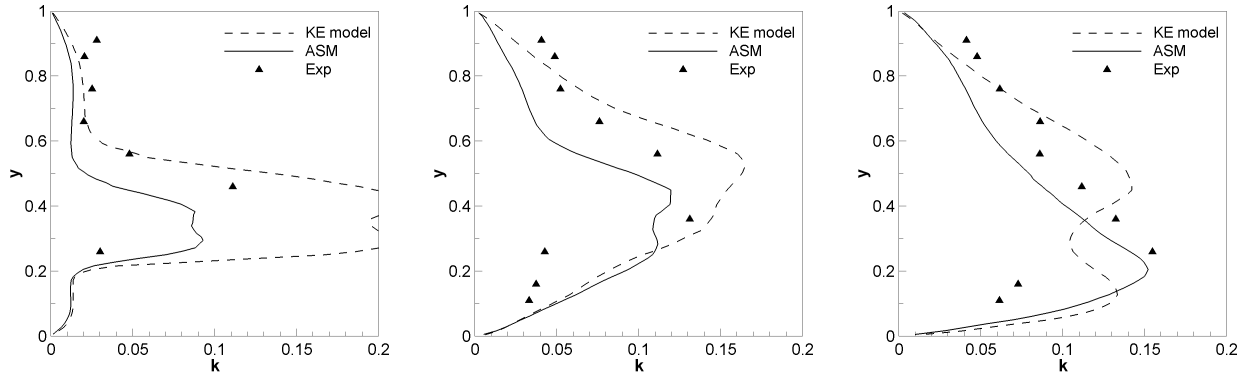

(a) Q=$65l/s$. $x = 0.16m$. (b) Q=$65l/s$. $x = 0.46m$. (c) Q=$65l/s$. $x = 0.86m$.

Figure 8.39: Numerical and experimental turbulent kinetic energy $k(m^2/s^2)$ at several cross sections. Design T1. Q=$65l/s$.

ure 8.39(a,b)). Near the outlet slot the ASM is in very good agreement with the experiments (Figure 8.39(c)).

As it could be expected, the $k - \varepsilon$ model fails to predict the anisotropy between the two horizontal Reynolds stresses, and gives excessively large values of the transverse component $\overline{v'^2}$ (Figure 8.40). On the other hand, the agreement between the ASM predictions of $\overline{v'^2}$ and the experimental data is remarkable. It should be noticed that near the inlet slot the experimental peak in the longitudinal normal stress ($\overline{u'^2}$) is underpredicted by the ASM, while the transverse stress ($\overline{v'^2}$) is in much better agreement with the experimental data. This feature was also found in the design T2, and, as it has been argued, it might be explained to certain degree by the large amount of air bubbles which are present in this region of the pool, and by the 3D flow features in the slot.

In the upper part of the pool, which is a quiet area with a relatively low turbulence level, both models give similar results, in good agreement with the experimental data. In the lower part of the pool, where the maximum velocity and largest turbulence levels occur, the ASM performs better.

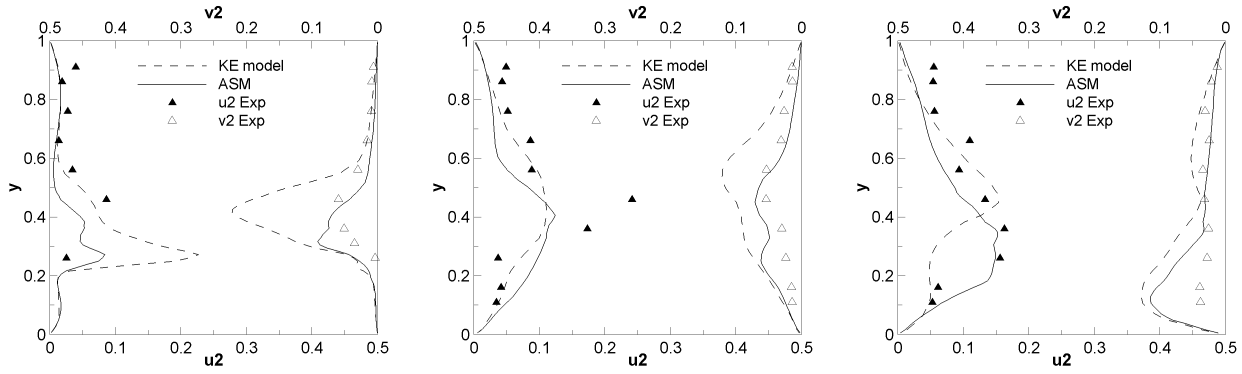

(a) Q=$65l/s$. $x = 0.16m$. (b) Q=$65l/s$. $x = 0.46m$. (c) Q=$65l/s$. $x = 0.86m$.

Figure 8.40: Numerical and experimental horizontal Reynolds stresses $\overline{u'^2}$ and $\overline{v'^2}(m^2/s^2)$ at several cross sections. Design T1. Q=$65l/s$.

8.7 Concluding remarks

The numerical and experimental results presented in this chapter suggest that the depth averaged shallow water equations, with a suitable turbulence model, might be used in order to compute the free surface flow in vertical slot fishways. Although there are several regions in the flow where the modelling assumptions are broken, specially near the slot region, the numerical results show a satisfactory global agreement with the experiments. The size of the recirculation regions is well predicted, and the velocity fields are fairly independent of the water discharge, which is a characteristic feature of vertical slot fishways [30]. The velocity field is more accurately computed than the turbulent kinetic energy field, as it usually occurs in RANS modelling.

The numerical results can be considered as a useful complementary tool for fishway design purposes. Nevertheless, depending on the specific pool design and on the flow conditions, the equations of the model might be in their limit of application. Therefore, special care should be taken when analysing the numerical results. In more complex pool designs, and for bed slopes larger than 10%, the numerical predictions are expected to deteriorate rapidly. On the other hand, it should be said that a slope of 10% is in the upper limit of the most frequently used slopes in vertical slot fishways [30, 76].

According to the numerical results, the bed friction does not have any influence on the mean flow, nor on the turbulent energy field. The bed shear stress in the mean flow equations is negligible when compared to the bed slope and turbulent diffusion. In the same way, the production of turbulent kinetic energy due to bed friction is several orders of magnitude smaller than the production due to horizontal shear strain. For this reason, in the fishway flow the depth averaged ASM and $k - \varepsilon$ models become the respective original 2D models.

The importance of a correct turbulence modelling follows directly from the numerical and experimental results. The large values of the turbulent kinetic energy give it a very important role

in the mean flow equations. Although the ASM gives slightly better predictions of the turbulent kinetic energy, the level of agreement with the experiments is generally similar for the ASM and $k - \varepsilon$ models. However, the Reynolds stresses are better predicted by the ASM. The accuracy of the results is as expected when applying a RANS turbulence model to a strong recirculating flow. A significant improvement in the results may only be achieved by a 3D simulation rather than a more complex depth averaged turbulence model.

The influence on the mean flow of the large amount of air bubbles present in the slot region has not been directly checked, but it is probably responsible for some of the differences between the numerical and experimental results near the inlet slot.

Conclusions

As a result of this work, a finite volume solver for the unsteady depth averaged shallow water equations (2D-SWE) coupled with several RANS turbulence models has been developed and applied to several free surface flows. Special attention has been placed in the modelling of turbulent flows and in the treatment of wet-dry fronts. In all the cases the numerical results have been compared with experimental data, obtaining satisfactory results.

Three depth averaged turbulence models have been used in the applications: a mixing length model (ML), a $k - \varepsilon$ model, and an algebraic stress model (ASM). The depth averaged mixing length and $k - \varepsilon$ models are commonly used in the simulation of turbulent shallow flows. Additional limiters to the production of turbulence proposed by Menter [88] and Durbin [45] have been introduced in the original models in order to control the excessively large turbulence production given by eddy viscosity models in stagnation regions. The depth averaged algebraic stress model has been proposed in this work as an extension of the 2D algebraic stress model, with additional source terms which account for the production of Reynolds stresses due to vertical shear. The computational cost and numerical stability of the proposed ASM are similar to those of the $k - \varepsilon$ model.

The numerical solver includes the first order upwind schemes of Roe and van Leer, as well as their second order extension. In all the numerical simulations the importance of using a second order upwind spatial discretisation has been checked. A first order scheme may give rather good predictions of the water depth, but it introduces too much numerical diffusion, and therefore, it excessively smooths the velocity profiles. This is specially important when comparing different turbulence models, since the numerical diffusion introduced by a first order upwind scheme may be of the same order of magnitude as the turbulent diffusion. In order to avoid spurious oscillations when the bathimetry is irregular, an upwind discretisation of the bed slope term is used in the solver, with second order corrections proposed by Hubbard and García-Navarro [62]. In this way a fully second order upwind scheme free of spurious oscillations is obtained.

Alternatively to the fully second order scheme, a rather simple, free of spurious oscillations and stable scheme, which reduces the numerical diffusion in a significant way, has been proposed in this work, by just using a second order discretisation for the two unit discharge components, whilst keeping a first order discretisation for the water depth and bed elevation. The resulting hybrid

scheme has been used in the practical applications, giving accurate and stable results. Nevertheless, it is important to remark that the water depth gradient in all the applications was quite smooth. In other flow conditions with very steep water depth gradients, a fully second order scheme is expected to produce more accurate results than the hybrid scheme.

The treatment of wet-dry fronts proposed in section 3.9 is based on the ideas of Brufau et al. [19], with a slight modification in the reflection condition. It has been tested with satisfactory results in the simulation of long shallow waves generated by bed movements (chapter 5), and tidal waves in coastal regions (chapter 6). The wet-dry condition used in the solver is numerically stable, even with a very irregular bathimetry, and it does not generate spurious oscillations which could contaminate the numerical results. In chapter 6 it has been used to model the flooding and drying of tidal flats in the Crouch estuary, without producing any significant instability in the numerical results. In addition, the wet-dry treatment is not diffusive, even in the presence of discontinuities in the bed elevation. For this reason it can be used to model overtopping vertical walls inside the numerical domain, by just introducing a discontinuity in the bed elevation (chapter 5). However, in such a case it should be considered that the shallow water equations neglect the vertical accelerations, and assume an hydrostatic pressure distribution, which is not physically correct when modelling the runup of waves in very steep walls. For this reason, even though the wet-dry condition works well in the sense that it is numerically stable and it does not diffuse the wave until it overtops the wall, the runup on vertical walls is underestimated and the high frequency water level oscillations, which are caused by the vertical accelerations near the wall, are not resolved by the model. A possible line of future work to improve the runup predictions using the 2D-SWE is to include an additional term in the momentum equations in order to account for the non-hydrostatic pressure distribution when the vertical accelerations are important.

The 1D-SWE have been applied in chapter 5 to model the generation of long waves by the horizontal movement of a slanted paddle. The generation of the wave is achieved numerically by a moving bed. At the same time the wet-dry condition participates in the generation process, modelling the runup of the generated wave in the slanted paddle. The results are rather satisfactory, but again, when the paddle slope is too large the vertical accelerations produce high frequency oscillations which are not resolved by the model. These oscillations are small when the paddle slope is 45^o, and somewhat larger when the paddle slope is increased to 60^o. A moving boundary condition was used in order to compute the wave generated by a vertical paddle (90^o). In this case, the vertical accelerations are very important and the maximum wave height is underpredicted by the model.

The numerical modelling of the Crouch estuary (chapter 6) showed that the turbulence model does not have a big influence on the velocity and water depth fields, and its importance might be reduced to local flow features. This is because the turbulence level in the estuary is low, and the diffusive forces are smaller than the convective forces in the momentum equations. The results are

somewhat more sensitive to the bed friction coefficient, but the dependence is still low. Both the ASM and $k-\varepsilon$ models give very similar turbulent kinetic energy fields. This is because the main source of turbulence in the estuary is the bed friction, and both models account in a similar way for this process. Nonetheless, some differences appear in the Reynolds stresses predicted by the ASM and $k-\varepsilon$ models. The comparison of the numerical predictions with experimental turbulence data might be a useful future work in order to assess the models performance.

The numerical modelling of the flow in vertical slot fishways (chapter 8) was proposed as a future line of research in previous works by various researchers (see for example [105]), and was accomplished in this thesis. The comparison between the numerical and experimental results showed that the depth averaged shallow water equations, coupled with a suitable turbulence model, may be used in order to compute the free surface flow in vertical slot fishways. Although there are several regions in the flow where the modelling assumptions are broken, specially near the slot region, the numerical results show a satisfactory global agreement with the experiments. The most important features of the flow field (maximum velocity in the pool, size of the recirculation regions, turbulence level, dependence of the solution on the total discharge ...) are well predicted by the solver. This is an interesting finding because from the nature of the fishway flow (3D turbulence, water depth similar to the horizontal length scale, 3D mean flow features in the slot region, ...), it seems that only a 3D model approach would give successful and accurate results. However, as shown in chapter 8, a depth average model can give very satisfactory predictions with a relatively low computational cost.

The importance of a correct turbulence modelling in the fishway was confirmed by the numerical results. The ML model failed to predict the velocity field accurately, specially for large water discharges, because the model assumes a turbulent length scale proportional to the water depth, which is not correct in the fishway flow. The ASM and $k-\varepsilon$ models give fairly accurate velocity fields. The original purpose of using the algebraic stress model was to account for the effects of the anisotropic Reynolds stresses in the flow. When compared to the $k-\varepsilon$ model, which assumes an isotropic eddy viscosity, the ASM improves the prediction of the turbulent stresses. On the other hand, no improvement has been found in the water depth and velocity fields, which are predicted with a similar degree of accuracy with either the ASM or the $k-\varepsilon$ model. Probably the main disagreements between the experimental and numerical results are due to the approximations assumed in the depth averaged equations, and may only be improved by using a 3D model rather than implementing more complex depth averaged turbulence models.

As it often happens in CFD, no conclusion can be drawn about which is the most suitable turbulence model to be generally used. The ASM gives a better representation of the anisotropic turbulence than the $k-\varepsilon$ model, and both of them are much more complex and realistic than the ML model. On the other hand, the computational cost and numerical instabilities increase with the complexity of the model. Therefore, considering all these factors (accuracy, stability

and computational cost), sometimes it might be worth using a simple turbulence model (or even neglect the turbulent effects, as it has been done in the propagation of shallow waves in chapter 5). Nevertheless, it should be remarked that even in those situations in which turbulence plays a little role in the mean flow field, a more sophisticated model will always give more accurate predictions of the turbulence field, which is very important in pollutant and sediment transport processes. In other flows, as for example in vertical slot fishways, the turbulent effects are extremely important in the momentum conservation equations, and a complex turbulence model is needed.

References

[1] AKANBI, A. A., AND KATOPODES, N. D. Model for flood propagation on initially dry land. *J. Hydraul. Eng. 114*, 7 (1988), 689–706.

[2] ALTAI, S., ZHANG, J., AND CHU, V. H. Shallow turbulent flow simulation using two-length-scale model. *J. Eng. Mech. 125*, 7 (1999), 780–788.

[3] BABARUTSI, S., AND CHU, V. H. A two-length-scale model for quasi-two-dimensional turbulent shear flows. In *Proc. 24th Congr. of IAHR, Vol. C, Madrid, Spain* (1991), Int. Assoc.for Hydr. Res., pp. 51–60.

[4] BABARUTSI, S., AND CHU, V. H. Modelling transverse mixing layer in shallow open-channel flows. *J. Hydraul. Eng. 124*, 7 (1998), 718–727.

[5] BABARUTSI, S., NASSIRI, M., AND CHU, V. H. Computation of shallow recirculating flow dominated by friction. *J. Hydraul. Eng. 122*, 7 (1996), 367–372.

[6] BALDWIN, B., AND LOMAX, H. Thin layer approximation and algebraic model for separated turbulent flows. *AIAA Paper* (1978), 78–257.

[7] BATCHELOR, G. K. Computation of the energy spectrum in homogeneous two-dimensional turbulence. *Phys. Fluids Suppl.II* (1969), 233–239.

[8] BELLOS, C. V., SOULIS, J. V., AND SAKKAS, J. G. Computation of two-dimensional dam break induced flows. *Adv. Water Res. 14*, 1 (1991), 31–41.

[9] BENZI, R., PALADIN, G., AND VULPIANI, A. Power spectra in two-dimensional turbulence. *Phys. Rev. A 42*, 6 (1990), 3654–3656.

[10] BERMÚDEZ, A., AND VÁZQUEZ-CENDÓN, M. E. Upwind methods for hyperbolic conservation laws with source terms. *Comput. Fluids 23*, 8 (1994), 1049.

[11] BERMÚDEZ, A., DERVIEUX, A., DESIDERI, J. A., AND VÁZQUEZ-CENDÓN, M. E. Upwind schemes for the two-dimensional shallow water equations with variable depth using unstructured meshes. *Comput. Methods Appl. Mech. Eng. 155* (1998), 49–72.

[12] BIJVELDS, M. D. J. P., KRANENBUTG, C., AND STELLING, G. S. 3D numerical simulation of turbulent shallow-water flow in square harbor. *J. Hydraul. Eng. 125*, 1 (1999), 26–31.

[13] BONILLO, J. Un modelo de transporte de sustancias solubles para flujos turbulentos en lámina libre. Tesis doctoral. Área de Ingeniería Hidráulica. Universidad de A Coruña, 2000.

[14] BOOIJ, R. Depth-averaged $k-\varepsilon$ modelling. In *Proc. 23rd IAHR Congr., Delft, The Netherlands* (1989), vol. A, IAHR, pp. 198–206.

[15] BRADFORD, F., AND SANDERS, B. F. Finite-volume model for shallow-water flooding of arbitrary topography. *J. Hydraul. Eng. 128*, 3 (2002), 289–298.

[16] BRADSHAW, P., FERRISS, D., AND ATWELL, N. Calculation of boundary layer development using the turbulent energy equation. *J. Fluid Mech.*, 28 (1967), 593–616.

[17] BRUFAU, P. Simulación bidimensional de flujos hidrodinámicos transitorios en geometrías irregulares. Tesis doctoral. Área de Mécanica de Fluidos. Universidad de Zaragoza, 2000.

[18] BRUFAU, P., AND GARCÍA-NAVARRO, P. Two-dimensional dam break flow simulation. *Int. J. Numer. Meth. Fluids 33* (2000), 35–57.

[19] BRUFAU, P., VÁZQUEZ-CENDÓN, M. E., AND GARCÍA-NAVARRO, P. A numerical model for the flooding and drying of irregular domains. *Int. J. Numer. Meth. Fluids 39* (2002), 247–275.

[20] CEA, L., FERREIRO, A., VÁZQUEZ-CENDÓN, M. E., AND PUERTAS, J. Experimental and numerical analysis of solitary waves generated by bed and boundary movements. *Int. J. Numer. Meth. Fluids 46*, 8 (2004), 793–813.

[21] CEA, L., VÁZQUEZ-CENDÓN, M. E., PUERTAS, J., AND PENA, L. Numerical treatment of turbulent and mass source terms in the shallow water equations for channels with irregular section. In *Prooceedings of the* 4^{th} *European Congress on Computational Methods in Applied Sciences and Engineering, Jyväskylä, Finland* (2004), ECCOMAS.

[22] CEBECI, T., AND SMITH, A. *Analysis of Turbulent Bounday Layers*. McGraw-Hill, New York, 1974.

[23] CHACÓN, T., FERNÁNDEZ, E. D., AND DOMÍNGUEZ, A. Well balanced schemes for shallow water equations with sediment transport. In *Prooceedings of the* 4^{th} *European Congress on Computational Methods in Applied Sciences and Engineering, Jyväskylä, Finland* (2004), ECCOMAS.

[24] CHEN, D., AND JIRKA, G. H. Experimental study of plane turbulent wakes in a shallow water layer. *Fluid Dyn. Res. 16* (1995), 11–41.

[25] CHEN, D., AND JIRKA, G. H. Absolute and convective instabilities of plane tubulent wakes in a shallow water layer. *J. Fluid Mech. 338* (1997), 157–172.

[26] CHEN, D., AND JIRKA, G. H. Linear instability analysis of turbulent mixing layers and jets in shallow water layers. *J. Hydraul. Res. 36*, 5 (1998).

[27] CHIEN, K. Predictions of channel and boundary layer flows with a low-Reynolds-number turbulence model. *AIAA Journal 20* (1982), 33–38.

[28] CHU, V. H., AND BABARUTSI, S. Confinement and bed-friction effects in shallow turbulent mixing layers. *J. Hydraul. Eng. 114*, 10 (1988), 1257–1274.

[29] CHU, V. H., WU, J. H., AND KHAYAT, R. E. Stability of transverse shear flows in shallow open channels. *J. Hydraul. Eng. 117*, 10 (1991), 1370–1388.

[30] CLAY, C. H. *Design of fishways and other fish facilities*. Boca Ratón, Lewis Publishers, 1995.

[31] COMPTE-BELLOT, G., AND CORRSIN, S. Simple eulerian time correlation of full- and narrow-band velocity signals in grid-generated, 'isotropic' turbulence. *J. Fluid Mech. 48*, part 2 (1971), 273–337.

[32] DAVIDSON, L. Implementation of a $k - \varepsilon$ model and a Reynolds Stress Model into a multiblock code. Tech. Rep. CRS4-APPMATH-93-21, Aplied Mathematics and Simulation Group CRS4, Cagliary, Italy, 1993.

[33] DAVIDSON, L. Prediction of the flow around an airfoil using a Reynolds Stress Transport Model. *J. Fluids Eng. 117* (1995), 50–57.

[34] DAVIDSON, L. An introduction to turbulence models. Tech. Rep. 97/2, Dept. of Thermo and Fluid Dynamics, Chalmers University of Technology, 1997.

[35] DAVIES, A. M., JONES, J. E., AND XING, J. Review of recent developments in tidal hydrodynamic modeling. II: Turbulence energy models. *J. Hydraul. Eng. 123*, 4 (1997), 278–292.

[36] DE WAAL, J. P., AND VAN DER MEER, J. W. Wave runup and overtopping on coastal structures. In *Proc.* 23^{rd} *Int. Conf. Coastal Eng.* (1992), ASCE, pp. 1758–1771.

[37] DERVIEUX, A., AND DESIDERI, J. A. Compressible flow solvers using unstructured grids. Rapports de Recherche 1732, INRIA, 1992.

[38] DHI. *MIKE21C, user guide and scientific documentation*. Danish Hydraulic Institute, Horsholm, Denmark, 1998.

[39] DING, Y., JIA, Y., AND WANG, S. S. Y. Identification of Manning's roughness coefficients in shallow water flows. *J. Hydraul. Eng. 130*, 6 (2004), 501–510.

[40] DODD, N. Numerical model of wave run-up, overtopping, and regeneration. *J. Waterw., Port, Coastal, Ocean Eng. 124*, 2 (1998), 73–81.

[41] DONG, C. M., AND HUANG, C. J. Generation and propagation of water waves in a two-dimensional numerical viscous wave flume. *J. Waterw., Port, Coastal, Ocean Eng. 130*, 3 (2004), 143–153.

[42] DRACOS, T., GIGER, M., AND JIRKA, G. H. Plane turbulent jets in a bounded fluid layer. *J. Fluid Mech. 241* (1992), 587–614.

[43] DUAN, J. G. Simulation of flow and mass dispersion in meandering channels. *J. Hydraul. Eng. 130*, 10 (2004), 964–976.

[44] DURBIN, P. Separated flow computations using the $k-\varepsilon-\overline{v^2}$ model. *AIAA J. 33*, 4 (1995), 659.

[45] DURBIN, P. On the $k-\varepsilon$ stagnation point anomaly. *Int. J. Heat Fluid Flow 17* (1996), 89–90.

[46] ENDERS, E. C., BOISCLAIR, D., AND ROY, A. G. The effect of turbulence on the cost of swimming for juvenile atlantic salmon. *Can. J. Fish. Aquat. Sci 60*, 9 (2003), 1149–1160.

[47] FERNÁNDEZ-NIETO, E. D. Aproximación numérica de leyes de conservación hiperbólicas no homogéneas. Aplicación a las ecuaciones de aguas someras. Tesis doctoral. Universidad de Sevilla, 2003.

[48] FINNIE, J., AND JEPPSON, R. Solving turbulent flows using finite elements. *J. Hydraul. Eng. 117*, 11 (1991), 1513–1530.

[49] FRANCCAROLLO, L., AND TORO, E. F. Experimental and numerical assessment of the shallow water model for two-dimensional dam-break problem. *J. Hydraul. Res. 33* (1995), 843–864.

[50] GARCÍA-NAVARRO, P., HUBBARD, M. E., AND PRIESTLEY, E. Genuinely multidimensional upwinding for the 2D shallow water equations. *J. Comput. Phys. 121*, 1 (1995), 79–93.

[51] GARCÍA-NAVARRO, P., AND VÁZQUEZ-CENDÓN, M. E. On numerical treatment of the source terms in the shallow water equations. *Comput. Fluids 29* (2000), 951–979.

[52] GATSKI, T., AND SPEZIALE, C. On explicit algebraic stress models for complex turbulent flows. *J. Fluid Mech.*, 154 (1993), 59–78.

[53] GEORGE, W. K. Insight into the dynamics of coherent structures from a proper orthogonal decomposition. In *International seminar on wall turbulence, May 16-20, 1988, Dubrovnik* (1988).

[54] GEORGE, W. K., ABRAHAMSSON, H., ERIKSSON, J., KARLSSON, R. I., LÖFDAHL, L., AND WOSNIK, M. A similarity theory for the turbulent plane wall jet without external stream. *J. Fluid Mech. 425* (2000), 367–411.

[55] GEORGE, W. K., BEUTHER, P. D., AND LUMLEY, J. L. Processing of random signals. In *Proceedings of the Dynamic Flow Conference* (1978), pp. 757–800.

[56] GIGER, M., DRACOS, T., AND JIRKA, G. H. Entrainment and mixing in plane turbulent jets in shallow water. *J. Hydraul. Res. 29*, 4 (1991), 615–643.

[57] HARTEN, A., LAX, P., AND VAN LEER, A. On upstream differencing and Godunov-type schemes for hyperbolic conservation laws. *SIAM Rev. 25* (1983), 35–61.

[58] HEINRICH, P. Nonlinear water waves generated by submarine and aerial landslides. *J. Waterw., Port, Coastal, Ocean Eng. 118*, 3 (1992), 249–266.

[59] HSIEH, T. Y., AND YANG, J. C. Investigation on the suitability of two-dimensional depth-averaged models for bend-flow simulation. *J. Hydraul. Eng. 129*, 8 (2003), 597–612.

[60] HU, K., MINGHAM, C. G., AND CAUSON, D. M. Numerical simulation of wave overtopping of coastal structures using the non-linear shallow water equations. *Coast. Eng. 41* (2000), 433–465.

[61] HUBBARD, M. E., AND DODD, N. A 2D numerical model of wave runup and overtopping. *Coast. Eng. 47* (2002), 1–26.

[62] HUBBARD, M. E., AND GARCÍA-NAVARRO, P. Flux difference splitting and the balancing of source terms and flux gradients. *J. Comput. Phys. 165* (2000), 89–125.

[63] HUNT, J. C. R. Developments in computational modelling of turbulent flows. In *Proc. ERCOFTAC Work* (1990), Cambridge University Press.

[64] INGRAM, R. G., AND CHU, V. H. Flow around islands in Rupert Bay: An investigation of the bottom friction effect. *J. Geophys. Res. 92(C13)* (1987), 14521–14533.

[65] JIA, Y., AND WANG, S. S. Y. Numerical model for channel flow and morphological change studies. *J. Hydraul. Eng. 125*, 9 (1999), 924–933.

[66] JIRKA, G. H. Large scale flow structures and mixing processes in shallow flows. *J. Hydraul. Res. 39*, 6 (2001), 567–573.

[67] JONES, W. P., AND LAUNDER, B. The prediction of laminarization with a two-equation model of turbulence. *Int. J. Heat Mass Transfer 15* (1972), 301–314.

[68] KAMULA, R. Flow over weirs with application to fish passage facilities. Academic dissertation, Univ. of Oulu, Finland, 2001.

[69] KAWANISI, K. Structure of turbulent flow in a shallow tidal estuary. *J. Hydraul. Eng. 130*, 4 (2004), 360–370.

[70] KOBAYASHI, N., DE SILVA, G., AND WATSON, K. Wave transformation and swash oscillations on gentle and steep slopes. *J. Geophys. Res. 94* (1989), 951–966.

[71] KOBAYASHI, N., OTTA, A. K., AND ROY, I. Wave reflection and run-up on rough slopes. *J. Waterw., Port, Coastal, Ocean Eng. 113*, 3 (1987), 282–298.

[72] KOBAYASHI, N., AND TEGA, Y. Numerical prediction of solitary wave runup on vertical walls by finite-amplitude shallow-water model, 1996.

[73] KOLMOGOROV, A. N. The local structure of turbulence in incompressible viscous fluid for very large Reynolds numbers. *Dokl. Akad. Nauk SSSR 30. Translated by V. Levin. Reprinted in Proc. R. Soc. Lond A 434, 9-13. (1991)* (1941).

[74] KRAICHNAN, R. H. Preliminary calculation of the Kolmogorov turbulence spectrum. *Phys. Fluids 8* (1965), 995–997.

[75] KRAICHNAN, R. H. Inertial ranges in two-dimensional turbulence. *Phys. Fluids 10* (1967), 1417.

[76] LARINIER, M., PORCHER, J. P., TRAVADE, F., AND GOSSET, C. *Passes a poissons. Expertise conception des ouvrages de franchissement*. Collection Mise Au Point Conseil Superior de la Péache Paris, 1998.

[77] LAUNDER, B., REECE, G., AND RODI, W. Progress in the development of a Reynolds-stress turbulence closure. *J. Fluid Mech. 68* (1975), 537–566.

[78] LAUNDER, B., AND SHARMA, B. Application of the energy dissipation model of turbulence to the calculation of flow near a spinning disc. *Lett. Heat Mass Transfer 1* (1974), 131–138.

[79] LEVEQUE, R. J. High resolution finite volume methods on arbitrary grids via wave propagation. *J. Comput. Phys. 78* (1988), 36–63.

[80] LEVEQUE, R. J. *Numerical Methods for Conservation Laws*. Birkhäuser, Basel/Boston/Berlin, 1990.

[81] LIEN, H. C., HSIEH, T. Y., YANG, J. C., AND YEH, K. C. Bend-flow simulation using 2D depth-averaged model. *J. Hydraul. Eng. 125*, 10 (1999), 1097–1108.

[82] LIN, P., CHANG, K., AND LIU, P. L. Runup and rundown of solitary waves on sloping beaches. *J. Waterw., Port, Coastal, Ocean Eng. 125* (1999), 247–255.

[83] LIU, P. L., CHO, Y., BRIGGS, M. J., KANOGLU, U., AND SYNOLAKIS, C. E. Runup of solitary waves on circular island. *J. Fluid Mech. 302* (1995), 259–285.

[84] LLOYD, P. M., AND STANSBY, P. K. Shallow water flow around model conical islands of small side slope. Part 1: Surface piercing. *J. Hydraul. Eng. 123* (1997), 1057–1067.

[85] LLOYD, P. M., AND STANSBY, P. K. Shallow water flow around model conical islands of small side slope. Part 2: Submerged. *J. Hydraul. Eng. 123* (1997), 1068–1077.

[86] LLOYD, P. M., STANSBY, P. K., AND CHEN, D. Wake formation around islands in oscillatory laminar shallow water flows. Part 1. Experimental investigation. *J. Fluid Mech. 429* (2001), 217–238.

[87] LOHRMANN, A., CABRERA, R., AND KRAUS, N. C. Acoustic doppler velocimeter (ADV) for laboratory use. In *Proc. Symp. on Fundamentals and Advancements on Hydr. Measurements and Experimentation* (1994), ASCE, pp. 351–365.

[88] MENTER, F. R. Zonal two-equation $k-\omega$ turbulence models for aerodynamic flows. AIAA Paper 93-2906, 1993.

[89] MENTER, F. R. Two-equation eddy-viscosity turbulence models for engineering applications. *AIAA Journal 32*, 8 (1994), 269–289.

[90] MENTER, F. R., AND ESCH, T. Elements of industrial heat transfer predictions. In *16^{th} Brazilian Congress of Mechanical Engineering (COBEM), Uberlandia, Brazil* (2001).

[91] MENTER, F. R., KUNTZ, M., AND BENDER, R. A scale-adaptive simulation model for turbulent flow predictions. AIAA paper, AIAA 2003-0767, 2003.

[92] MINH-DUC, B., WENKA, T., AND RODI, W. Numerical modeling of bed deformation in laboratory channels. *J. Hydraul. Eng. 130*, 9 (2004), 894–904.

[93] MOLLS, T., AND CHAUDHRY, M. H. Depth-averaged open-channel flow model. *J. Hydraul. Eng. 121*, 6 (1995), 453–465.

[94] MOSER, R. D., KIM, J. D., AND MANSOUR, N. N. Direct numerical simulation of turbulent channel flow up to $R_\tau = 590$. *Phys. of Fluids 11* (1999), 943–945.

[95] NI, H. Current status and development of prediction of water engineering turbulence models. In *Proceedings of the 3^d conference on turbulent flow and refined modelling in engineering, Shangai, China* (2000), pp. 184–197.

[96] NIKORA, V. I., AND GORING, D. G. ADV measurements of turbulence: can we improve their interpretation? *J. Hydraul. Eng. 124*, 6 (1998), 630–634.

[97] OLSEN, N. R. B. Two-dimensional numerical modelling of flushing processes in water reservoirs. *J. Hydraul. Res. 37*, 1 (1999), 3–16.

[98] OLSEN, N. R. B., AND KJELLESVIG, H. M. Three-dimensional numerical flow modelling for estimation of spillway capacity. *J. Hydraul. Res. 36*, 5 (1998), 775–784.

[99] OLSEN, N. R. B., AND MELAAEN, M. C. Three-dimensional calculation of scour around cylinders. *J. Hydraul. Eng. 119*, 9 (1998), 1049–1054.

[100] PAN, Y., AND BANERJEE, S. A numerical study of free-surface turbulence in channel flow. *Phys. Fluids 7*, 7 (1995), 1649–1664.

[101] PARÉS, C., AND CASTRO-DÍAZ, M. J. On the well-balanced property of Roe's method for nonconservative hyperbolic systems. Applications to shallow-water systems. In *Prooceedings of the 4^{th} European Congress on Computational Methods in Applied Sciences and Engineering, Jyväskylä, Finland* (2004), ECCOMAS.

[102] PATANKAR, S. V. *Numerical Heat Transfer and Fluid Flow*. McGraw-Hill, New York, 1980.

[103] PATEL, V., RODI, W., AND SCHEUERER, G. Turbulence models for near-wall and low Reynolds number flows: A review. *AIAA J.*, 23 (1985), 1308–1319.

[104] PELTIER, E., DUPLEX, J., LATTEUX, B., PECHON, P., AND CHAUSSON, P. Finite element model for bed-load transport and morphological evolution. *Computer modelling in Ocean Engineering 91* (1991).

[105] PENA, L. Estudio hidráulico en modelo de escalas de peixes de fenda vertical e de fenda profunda aliñadas. Aproximación á avaliación experimental da enerxía cinética turbulenta. Tesis doctoral. Universidad de A Coruña, 2004.

[106] PENA, L., CEA, L., AND PUERTAS, J. Turbulent flow: An experimental analysis in vertical slot fishways. In *Fifth International Symposium on Ecohydraulics, Madrid* (2004), IAHR, pp. 881–888.

[107] PHILLIPS, N. G. A coordinate system having some special advantages for numerical forecasting. *J. Meteorology 24* (1957), 184–185.

[108] PLAYÁN, E., WALKER, W. R., AND MERKLEY, G. P. Two-dimensional simulation of basin irrigation I: Theory. *J. Irrig. Drain. Eng. 120*, 5 (1994), 837–856.

[109] POPE. A more general effective-viscosity hypothesis. *J. Fluid Mech.*, 472 (1975), 331–340.

[110] POWERS, P., AND ORSBORN, J. New concepts in fish ladder design: Analysis of barriers to upstream fish migration, Volume IV of IV; Investigation of the physical and biological conditions affecting fish passage success at culverts and waterfalls. Final Report 1982-1984. BPA Report DOE/BP-36523-1 Project No. 198201400, Bonneville Power Administration, 1984.

[111] PUERTAS, J., PENA, L., AND TEIJEIRO, T. An experimental approach to the hydraulics of vertical slot fishways. *J. Hydraul. Eng. 130*, 1 (2004), 10–23.

[112] RAHMAN, M., AND SIIKONEN, T. Improved low-Reynolds-number $k-\varepsilon$ model. *AIAA J.*, 38 (2000), 1298–1300.

[113] RAJARATNAM, N., KATOPODIS, C., AND SOLANSKI, S. New designs for vertical slot fishways. *J. Hydraul. Eng. 19*, 3 (1992), 402–414.

[114] RAJARATNAM, N., VAN DER VINNE, G., AND KATOPODIS, C. Hydraulics of vertical slot fishways. *J. Hydraul. Eng. 112*, 10 (1986), 909–927.

[115] RAMESHWARAN, P., AND SHIONO, K. Computer modelling of two-stage meandering channel flows. *Water and Maritime Engineering 156*, 4 (2003), 325–339.

[116] RASTOGI, A. K., AND RODI, W. Predictions of heat and mass transfer in open channels. *Journal of the Hydraulics Division HY3* (1978), 397–420.

[117] RODI, W. Simulation approaches for turbulent flows. Computational Fluids Dynamics '94. S.Wagner et al, John Wiley and Sons, 1994.

[118] ROE, P. L. Discrete models for the numerical analysis of time-dependent multidimensional gas dynamics. *J. Comput. Phys. 63* (1986), 458–476.

[119] RUTGERS, M. A. Forced 2D turbulence: Experimental evidence of simultaneous inverse energy and forward enstrophy cascades. *Physical Review Letters 81*, 11 (1998), 2244–2247.

[120] SAUVAGET, P., DAVID, E., AND SOARES, C. G. Modelling tidal currents on the coast of Portugal. *Coastal Engineering 40* (2000), 393–409.

[121] SCHLICHTING, H. *Boundary layer theory*. McGraw Hill Book Co., New York, 1960.

[122] SHIRAZI, S. A., AND TRUMAN, C. R. Simple turbulence models for supersonic flows: Bodies at incidence and compression corner. *AIAA J. 29*, 11 (1991), 1850–1859.

[123] SLEIGH, P. A., GASKELL, P. H., BERZINS, M., AND WRIGHT, N. G. An unstructured finite-volume algorithm for predicting flow in rivers and estuaries. *Comput. Fluids 27*, 4 (1998), 479–508.

[124] SMITH, B. R. The $k - kl$ turbulence model and wall layer model for compressible flows. AIAA Paper 90–1483 21^{st} Fluid and Plasma Dynamics Conference – Seattle, Washington, July 18–20 1990.

[125] SMITH, B. R. A near wall model for the $k - l$ two equation turbulence model. AIAA Paper 94–2386 25^{th} Fluid Dynamics Conference - Colorado Springs, Colorado, June 20-23 1994.

[126] SPALART, P. R. Strategies for turbulence modelling and simulations. *Int. J. Heat Fluid Flow 21* (2000), 252–263.

[127] SPALART, P. R., AND ALLMARAS, S. R. A one-equation turbulence model for aerodynamic flows. *La Recherche Aérospatiale*, 1 (1994), 5–21.

[128] STANSBY, P. K., AND LLOYD, P. M. Wake formation around islands in oscillatory laminar shallow-water flows. Part2. Three-dimensional boundary-layer modelling. *J. Fluid Mech. 429* (2001), 239–254.

[129] STOCKSTILL, R. L., BERGER, R. C., AND NECE, R. E. Two-dimensional flow model for trapezoidal high-velocity channels. *J. Hydraul. Eng. 123*, 10 (1997), 844–852.

[130] SUMER, B. M., CHUA, L. H. C., CHENG, N. S., AND FREDSOE, J. Influence of turbulence on bed load sediment transport. *J. Hydraul. Eng. 129*, 8 (2003), 585–596.

[131] SYNOLAKIS, C. E., LIU, P. L., Y.CHO, AND BRIGGS, M. J. Runup of solitary waves on a circular island. *J. Fluid Mech 302* (1995), 259–285.

[132] THOMAS, F. O., AND GOLDSCHMIDT, V. W. Structural characteristics of developing turbulent planar jet. *J. Fluid Mech. 63* (1986), 227–256.

[133] TORO, E. F. *Riemann Solvers and Numerical Methods for Fluid Dynamics. A Practical Introduction*. Springer-Verlag, New York, 1997.

[134] TORO, E. F. *Shock-capturing Methods for Free-Surface Shallow Flows*. Wiley, Chichester, West Sussex PO19 1UD, England, 2001.

[135] TRAVIN, A., SHUR, M., SPALART, P. R., AND STRELETS, M. On URANS solutions with LES-like behaviour. In *Proceedings of the* 4^{th} *European Congress on Computational Methods in Applied Sciences and Engineering, Jyväskylä, Finland* (2004), ECCOMAS.

[136] UIJTTEWAAL, W. S. J., AND BOOIJ, R. Effects of shallowness on the development of free-surface mixing layers. *Phys. Fluids 12*, 2 (2000), 392–402.

[137] UIJTTEWAAL, W. S. J., AND GIRKA, G. H. Grid turbulence in shallow flows. *J. Fluid Mech. 489* (2003), 325–344.

[138] UIJTTEWAAL, W. S. J., AND TUKKER, J. Development of quasi two-dimensional structures in a shallow free-surface mixing layer. *Exp. Fluids 24* (1998), 192–200.

[139] UITTENBOGAARD, R., AND VAN VOSSEN, B. 2D-DNS of quasi-2D turbulence in shallow water. In *3rd AFOSR International Conference on Direct Numerical Simulation and Large Eddy Simulation (TAICDL)* (2001), University of Texas at Arlington.

[140] VAN LEER, B. Towards the ultimate conservative difference scheme III. Upstream-centered difference schemes for ideal compressible flow. *J. Comput. Phys. 23* (1977), 263–275.

[141] VAN PROOIJEN, B. C., BOOIJ, R., AND UIJTTEWAAL, W. S. J. Measurement and analysis methods of large scale horizontal coherent structures in a wide shallow channel. In 10^{th} *International Symposium on Applications of Laser Techniques to Fluid Mechanics, Calouste Gulbenkian Foundation, Lisbon, Portugal* (2000).

[142] VAN RIJN, L. C. Sediment transport, Part III: Bed forms and alluvial roughness. *J. Hydraul. Eng. 110*, 12 (1984), 1733–1754.

[143] VÁZQUEZ-CENDÓN, M. E. Estudio de esquemas descentrados para su aplicación a las leyes de conservación hiperbólicas con términos fuente. Tesis doctoral. Departamento de Matemática Aplicada. Universidad de Santiago de Compostela, 1994.

[144] VÁZQUEZ-CENDÓN, M. E. Improved treatment of source terms in upwind schemes for the shallow water equations in channels with irregular geometry. *J. Comput. Phys. 148* (1999), 497–526.

[145] WATTS, P. Tsunami features of solid block underwater landslides. *J. Waterw., Port, Coastal, Ocean Eng. 126*, 3 (2000), 144–152.

[146] WIEGEL, R. L. Laboratory studies of gravity waves generated by the movement of a submerged body. *Trans. American Geophysical Union 36* (1955), 759–774.

[147] WILCOX, D. C. Reassessment of the scale-determining equation for advanced turbulence models. *AIAA J. 26*, 11 (1988), 1299–1310.

[148] WILCOX, D. C. *Turbulence Modeling for CFD*. D. C. Wilcox, DCW Industries, 1993.

[149] WILSON, C. A. M. E., BATES, P. D., AND HERVOUET, J. M. Comparison of turbulence models for stage-discharge rating curve prediction in reach-scale compound channel flows using two-dimensional finite element methods. *J. Hydrology 257* (2002), 42–58.

[150] WINTERWERP, J. C., WANG, Z. B., VAN KESTER, A. T. M., AND VERWEIJ, J. F. Far-field impact of water injection dredging in the Crouch River. *Water and Maritime Engineering 154*, 4 (2002), 285–296.

[151] WOLANSKI, E., IMBERGER, J., AND HERON, M. L. Island wakes in shallow coastal waters. *Journal of Geophysical Research 89* (1984), 10553–10569.

[152] WU, W. Depth-averaged two-dimensional numerical modeling of unsteady flow and nonuniform sediment transport in open channels. *J. Hydraul. Eng. 130*, 10 (2004), 1013–1024.

[153] WU, W., RODI, W., AND WENKA, T. 3D numerical modeling of flow and sediment transport in open channels. *J. Hydraul. Eng. 126*, 1 (2000), 4–15.

[154] YE, J., AND MCCORQUODALE, J. A. Depth-averaged hydrodynamic model in curvilinear collocated grid. *J. Hydraul. Eng. 123*, 5 (1997), 380–388.

[155] YOON, T. H. Finite volume model for two-dimensional shallow water flows on unstructured grids. *J. Hydraul. Eng. 130*, 7 (2004), 678–688.

[156] ZIENKIEWICZ, O., AND TAYLOR, R. *The finite element method*. Mac-Graw Hill, New York, EEUU, 1989.